[Faculty of Science]
[Department of Chemistry]

Plasma catalysis: Study of CO_2 reforming of CH_4 in a DBD reactor

Proefschrift voorgelegd tot het behalen van de graad van
doctor in de wetenschappen: chemie
aan de Universiteit Antwerpen
te verdedigen door
Jinxin Wang

Supervisors: Prof. dr. Vera Meynen; Prof. dr. Annemie Bogaerts

Antwerp, 2022

Table of contents

Acknowledgments

The first day I came to Belgium seems not long ago, but actually I have stayed here for over 4 years. This PhD is an experience I will never forget. This work has been complete with the support and help of many people, and I would like to express my gratitude to them.

First of all, I would like to thank my supervisors, Prof. Vera Meynen and Prof. Annemie Bogaerts. Thank you for giving me the opportunity to work with you. You gave me the freedom to do my research, and your guidance and discussions with me always point me in the right direction whenever I get stuck. Four years ago, I was just a novice in the world of science. It was your help and advice that made me to grow into a qualified and mature researcher.

I also grateful acknowledge for the financial support given by the China Scholarship Council (No. 201806060123) and the VLAIO Catalisti transition project CO2PERATE (HBC.2017.0692). I especially would also like to thank the following people:

Prof. Pegie Cool, your knowledge and insights in the field of plasma catalysis have helped me a lot during the many meetings we have held together, especially during my first year of Ph.D. Thanks for your guidance.

Gert Nuyts, Safiyye Kavak and Prof. Sara Bals, thank you for the SEM and STEM measurements for many times of my samples and discussions with me, which helped me find the right direction for synthesis. Also Alexander Vansant and Dr. Steven Mullens of VITO, thanks for your contributions to the DLS measurements.

Prof. Anne-Marie De Wilde of VITO, thank you very much for the mercury intrusion measurements and answers to my questions, which were very important to my research.

I'm not a very social person, but thanks to all the colleagues in the group. It was a pleasure working with them. And I also learned and grew a lot from them.

Rui, my colleague who started the Ph.D program at the same time as me. Your help in my life is invaluable. I was new to Europe for the first time and was not familiar with almost everything, and thanks to your help I was able to quickly adapt to it all.

Wencong, we often discussed scientific issues together. In addition, our travels and chats together are also good memories that I will not forget over the years.

Karen and Saskia, you are probably the people who have helped me the most with my research besides my supervisors. You are always the first people I think of when I have any problem. I learned a lot from your experience and knowledge. I sincerely thank you for your selfless and earnest help to me.

Jeroen, Ravi, Stefano, Sander and Wouter, all of you gave a lot of help to me during the past four years, much appreciate for that.

Mitra, Diana, Valeria, Radu, Jan, Lore, Hilde, Zhiyuan, Shangkun and Jian, happy to be colleagues and be friendes with you all.

My parents and sister, it is a pity that you cannot come here to witness my graduation because of the epidemic, but thank you for your unconditional love and support. I love you!

Finally, I would like to thank my wife and colleague, Kaimin. Thank you for being in my life. You have given me the courage to face all difficulties and hardships, and everything I have spent with you is a good memory for me. You are the driving force for me to study abroad for a Ph.D., and the source of courage to persist until today, not to mention the help you have given me in my life and work. I love you forever!

List of abbreviation

AC	alternating current
APGD	atmospheric pressure glow discharge
BET method	Brunauer–Emmett–Teller method
BJH method	Barrett-Joyner-Halenda method
DC	direct current
DLS	dynamic light scattering
DME	dimethyl ether
DRM	dry reforming of methane
EDX	energy dispersive X-ray spectroscopy
EE	energy efficiency
EY	energy yield
FID	flame ionization detector
GA	gliding arc
GC	gas chromatograph
GDP	gross domestic product
GWP	global warming potential
H_2-TPR	hydrogen-temperature programmed reduction
HAADF-STEM	high angle annular dark field scanning transmission electron microcopy
IPC	in-plasma catalysis

MOF	metal–organic framework
NLDFT	non-local density functional theory
O_2-TPO	oxygen-temperature programmed oxidation
PC	personal computer
PPC	post-plasma catalysis
SEI	specific input energy
SEM	scanning electron microcopy
STEM	scanning transmission electron microcopy
TCD	thermal conductivity detector
TEOS	tetraethyl orthosilicate
UV	ultraviolet
XRD	X-ray powder diffraction

List of symbols

Symbol	Description	Unit
C_{cell}	capacitance of dielectric barrier discharge reactor	pF
C_{diel}	capacitance of dielectric barrier	pF
f	discharge fraction in the DBD reactor	%
I_{RMS}	root mean square current	mA
P_{dis}	power of the plasma	W
P_{sply}	power provided by the power supply	W
Q_{dis}	displaced charge of discharges	nC
U_{bur}	burning voltage to sustain the plasma	kV
U_{pp}	peak-to-peak voltage of the alternating current	kV

General introduction

The emission of greenhouse gases and the resulting climate change is a major issue for mankind. A lot of technologies are being studied for conversion of greenhouse gases and utilization of renewable resources, such as CO_2 hydrogenation and biomass conversion. Among them, CO_2 reforming of methane (dry reforming) is an attractive procedure since it simultaneously utilizes two greenhouse gases (CH_4 and CO_2), which can come from sustainable resources such as biogas, to produce chemical products and clean fuels.

However, a large amount of energy is needed to activate the CH_4 and CO_2 because of their high stability. For example, the classic thermocatalytic reaction always need a high temperature, which will lead to catalyst deactivation, and it is not flexible enough to integrate with fluctuating renewable energy generation. Non-equilibrium plasma catalysis is considered to be promising to overcome these problems, since CH_4 and CO_2 can be activated at a relatively low temperature (lower than 250 °C). The accelerated electrons with high energy in plasma are able to break the stable CH_4 and CO_2 molecules, while the other species with larger mass keep the overall kinetic temperature at a low level. Among the various types of non-equilibrium plasma reactors, the dielectric barrier discharge (DBD) reactor is one of the easiest to be combined with catalysts, as it has a simple structure and operates at close to ambient temperature and atmospheric pressure.

Nevertheless, the conversion of CH_4 and CO_2 and the energy yield (i.e., the amount of CO_2 and CH_4 converted per unit energy input) in DBD reactors is limited, and the existing catalysts also barely improved the performance, since catalysts for conventional thermal dry reforming were used in most studies. In the majority of dry reforming studies with undiluted feed gases, the conversion of CH_4 and CO_2 with fully packed IPC fixed bed packings or catalysts were lower than in the empty reactor at the same flow rate and plasma power. Based on previous simulations, we believe that conventional catalysts for thermal dry reforming may not be suitable for plasma reactions due to the more complex interactions between plasma and catalyst. It is necessary to study catalysts suitable for plasma dry reforming in DBD reactors. Therefore, the main work in this PhD is to study the structural properties of catalysts suitable for plasma dry reforming in DBD reactors through the controllable synthesis of catalysts with specific structures, and to realize the improvement of the dry reforming performance. In addition to the catalysts, the design of the DBD reactor was also improved.

Chapter 1: Introduction

In this first chapter, an introduction to plasma-based dry reforming in DBD reactors is given. Several techniques for CO_2 conversion are described and compared with the plasma-based dry reforming. Several plasma reactors are also introduced and their advantages and disadvantages are discussed,

Chapter 2: Modifying the Stöber Process: Is the Organic Solvent Indispensable?

In the second chapter, a modified Stöber process is developed to synthesize uniform silica particles which can be used as catalyst supports or templates. This modified process eliminates the addition of organic solvents and is more economical and environmentally friendly than the original Stöber method. The role of organic solvents in Stöber method are discussed.

Chapter 3: Three Dimensional Porous Catalysts for Plasma-Catalytic Dry Reforming of Methane: How Does the Pore Size Affect the Plasma Catalytic Performance?

In the third chapter, 3D porous Cu and CuO catalysts with different pore sizes are prepared using uniform silica particles synthesized in chapter 2 as templates. The effect of catalyst pore size on the plasma-catalytic dry reforming are studied. The pore size of the catalyst have a significant influence on the performance of plasma-catalytic dry reforming, and the influence trends shown by the experimental results are different from those in previous thermal processes and simulation studies.

Chapter 4: Plasma-based Dry Reforming of Methane in a Dielectric Barrier Discharge Reactor: Importance of Uniform (Sub)Micron Packing/Catalysts to Enhance the Performance

In the fourth chapter, (sub)micron SiO_2 spheres (with or without supported metal) are used as packings and catalysts supports for plasma-based dry reforming, and the effect of different particle sizes are studied. The uniform (sub)micron particles greatly improve the performance of plasma-based dry reforming, and the particle size shows a significant effect.

Chapter 5: Dry Reforming in a Dielectric Barrier Discharge Reactor with Non-uniform Discharge Gap: Effects of Metal Rings on the Discharge Behavior and Performance

In the fifth chapter, some stainless steel rings are put over the inner electrode rod of the DBD reactor to change the local discharge gap and electric field, and study the dry reforming performance. This design change improve the energy yield of DBD reactors due to its effects on the discharge.

Chapter 1 Introduction

1.1 Background

1.1.1 Environmental challenges

Desert expansion, glacier retreat, sea level rise, and frequent extreme weather such as storms and droughts, all of which show that climate change is an imminent problem facing all mankind [1-5]. Human activity, especially greenhouse gas emissions, is the main reason for the rapid climate change since the 1800s [6,7]. The greenhouse effect has already affected various aspects of human society and ecosystems [8-11]. Since the first World Climate Conference in 1979, climate protection has become an increasingly important topic of international conferences [12]. Although the world still has not reached a consensus on the measures to be taken to manage climate change, the idea that the greenhouse effect must be controlled has been widely accepted.

The main greenhouse gases are water vapor (H_2O), carbon dioxide (CO_2), methane (CH_4), nitrous oxide (N_2O), sulfur hexafluoride (SF_6), hydrofluorocarbons (HFCs) and perfluorocarbons (PFCs). Their presence in the atmosphere makes the Earth like a glass-covered greenhouse, maintaining a suitable temperature by absorbing the heat radiated from the ground at night when it is not exposed to the sun. Without the greenhouse effect, the temperature difference between day and night on Earth would be too large for human beings to survive. However, as human activities increase the content of greenhouse gases in the atmosphere, the Earth is able to retain more heat, leading to the global warming and a series of climate changes. Figure 1.1 shows the global surface temperature changes caused by human & natural factors (1850-2020). Since 1950, the human-driven unnatural global surface temperature has risen around 1.2 °C. The ability of different gases to increase the greenhouse effect, known as the Global Warming Potential (GWP), is different. SF_6, HFCs and PFCs have a higher GWP than other greenhouse gases. However, although the GWP of CO_2 and CH_4 is relatively low, their contribution to the global warming is the largest (more than 90%) due to their larger emissions, see Figure 1.2 [13]. The emissions of CO_2 and CH_4 account for about 90% of the total greenhouse gas emissions, and in 2016 they accounted for 74,4% and 17.3% of the total emissions, respectively [14].

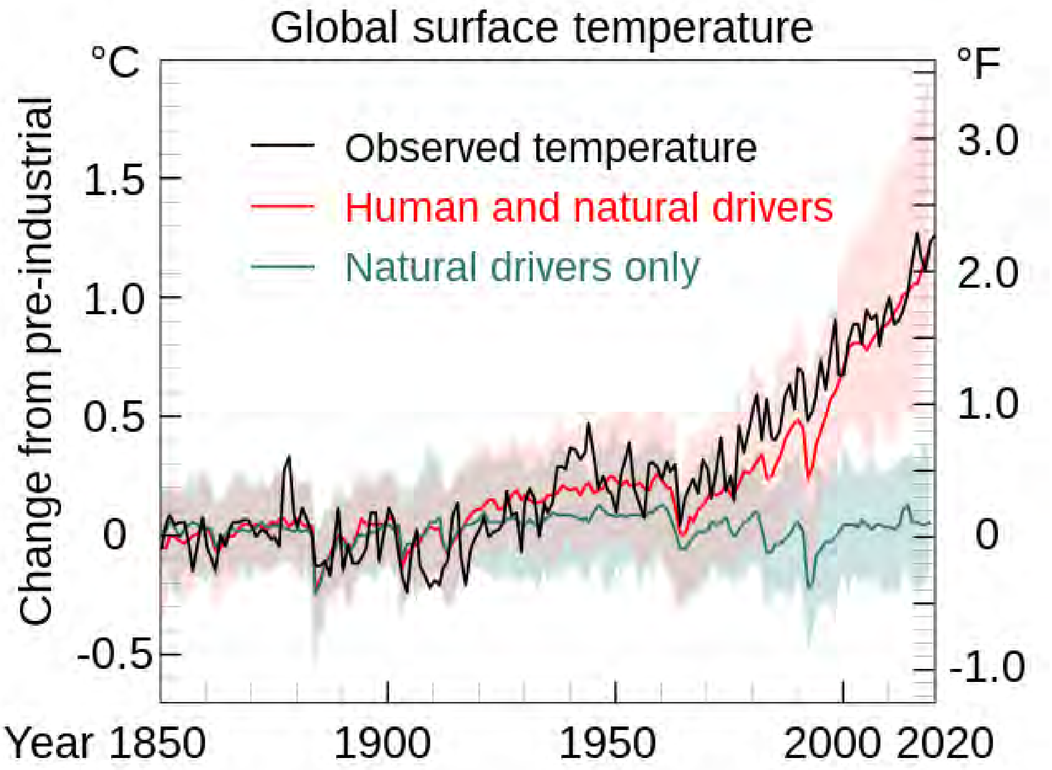

Figure 1.1. Change in global surface temperature (annual average) as observed and simulated using human & natural and only natural factors (both 1850–2020). Reproduced from [13], with permission from the United Nations Framework Convention on Climate Change.

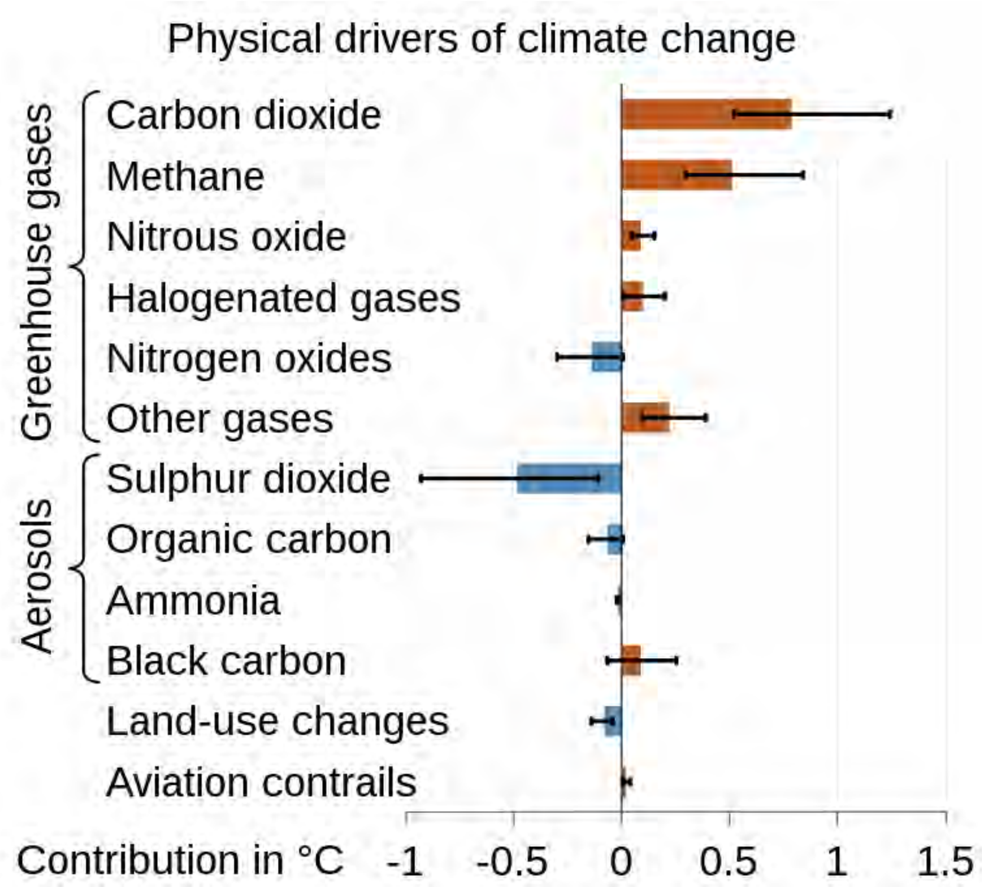

Figure 1.2. Radiative forcing (warming influence) of different contributors to climate change in 2019. Reproduced from [13], with permission from the United Nations Framework Convention on Climate Change.

The emissions of greenhouse gases are from different sectors of the economy. One of the main sources is the energy sector, including the energy use in industry, transportation, and buildings, etc., accounting for about 70% of total greenhouse gas emissions [14]. This is because the extensive use of fossil fuels, such as methane leaks from petroleum and coal mining, greenhouse gas by-products in petrochemical processes, and exhaust gas from direct combustion of fossil fuels. Every step in the application of fossil fuels is accompanied by the release of large amounts of greenhouse gases [15-17]. In addition, the land use, livestock & manure, and cement production, etc. in the agricultural and industrial sectors all contribute to global greenhouse gas emissions. Figure 1.3 shows the detailed sources of greenhouse gas emissions in 2020. It can be seen that the sources of greenhouse gases are diverse and involve all aspects of modern society, which means that controlling greenhouse gas emissions will be difficult and complicated.

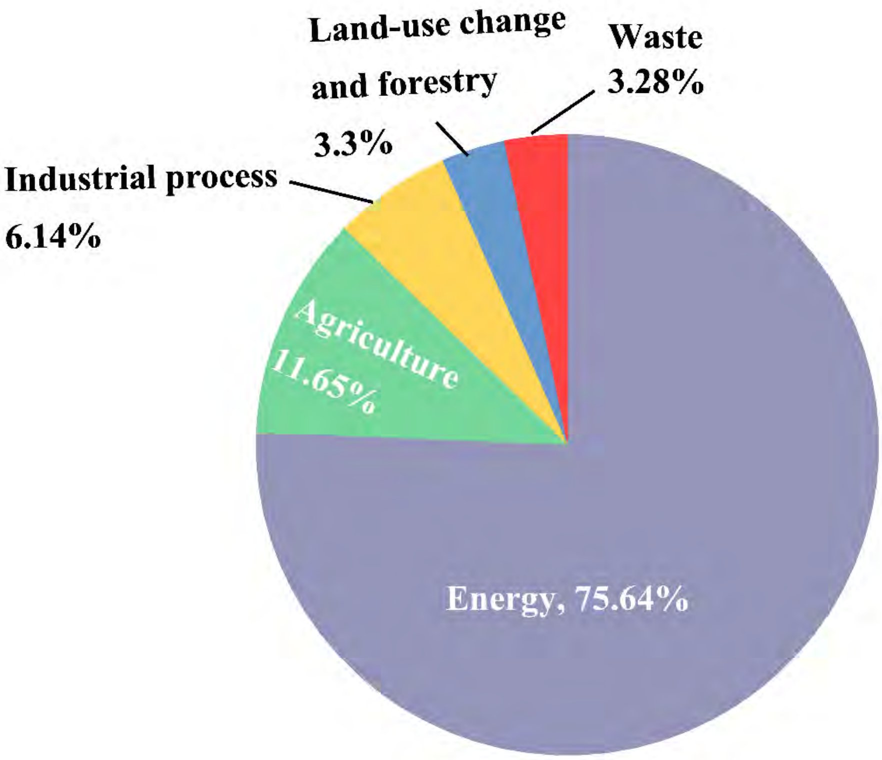

Figure 1.3. Global greenhouse gas emissions by sector in 2020.

The 2015 Paris Agreement set a goal of limiting global warming to below 2°C and preferably 1.5°C [18]. Many countries have developed their own emission reduction plans to deal with climate problems. However, with current emissions and future plans, reaching the goals of the Paris Agreement is almost impossible [19]. Greater reductions in emissions are needed in countries around the world. The more developed the countries, such as countries in Europe and North America, the higher per capita greenhouse gas emissions. In recent decades, as the industries in Asian countries have grown, their per capita greenhouse gas emissions have risen significantly, and total emissions have surpassed those of Europe and the North Americas due to Asia's larger population. Under the existing industrial technology, emissions almost correlate to the level of development and people's living standards. This is why countries are unwilling and unable to minimize greenhouse gas emissions. Therefore, it is difficult to reduce emissions simply by reducing economic activity, and developing sustainable technologies is a viable way to control climate change.

1.1.2 Resource challenges

Another worldwide problem is resource shortages [20]. On the one hand, as the world population is still increasing rapidly, the demand for various resources is increasing; on the other hand, economic development and technological progress also lead to an increase in the rate of resource consumption. Therefore, limited natural resources have become a limiting factor for the further development of society.

One of the most important natural resources is petroleum. It is not only an energy source, but also a chemical raw material. The petrochemical base chemicals such as olefins, aromatic hydrocarbons and synthesis gas are obtained by steam cracking, reforming and separation of petroleum. With these chemicals, more than 200 kinds of organic chemical intermediates can be produced, which are used to produce petrochemical derived products such as fertilizers, adhesives, detergents and building materials. Commodities produced by petrochemicals have already spread across all fields of our lives [21]. Petroleum is so important to our industrial society in its current configuration that it is called the life-blood of modern civilization [22]. As shown in Figure 1.4, the world GDP growth is closely related to oil price. However, as a non-renewable resource, its limited reserves are a problem that the petrochemical industry has to face [23]. The proven oil reserves can only last about 50 years at current oil extraction [24], although the oil reserves that can be detected and utilized will increase as technology advances [25,26]. Nevertheless, finding alternatives to petroleum is still critical due to its non-renewable nature and increased mining and use costs.

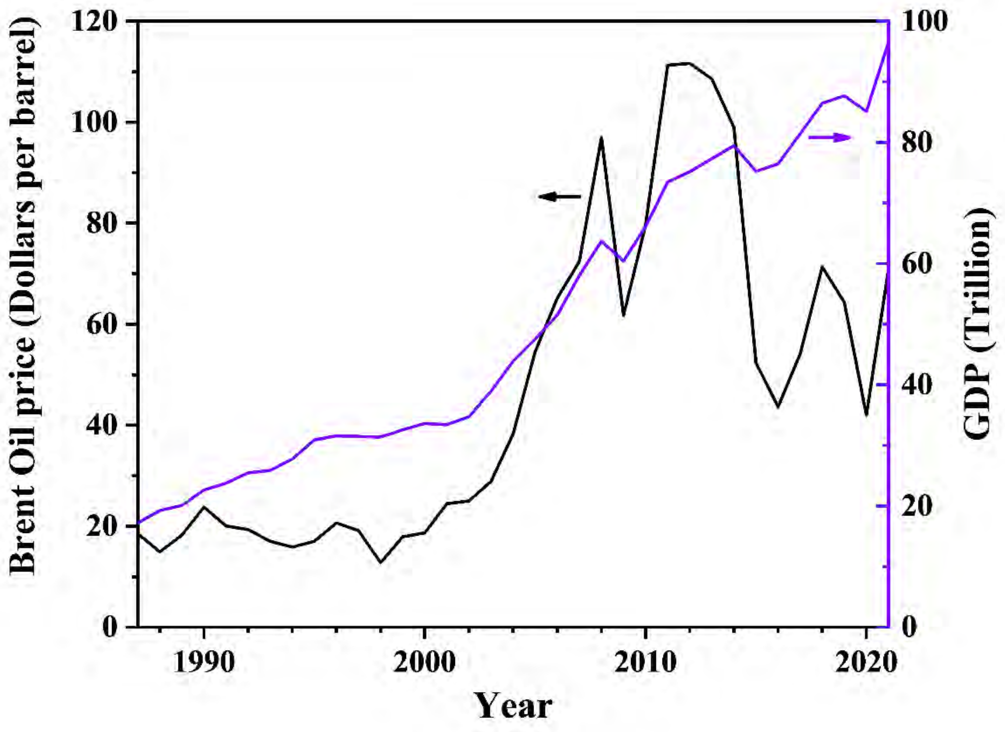

Figure 1.4. World GDP growth and Brent oil price.

1.1.3 Technologies to address environmental and resource issues

1.1.3.1 Renewable energy

Due to the above environmental and resource issues, a lot of technologies are being studied and applied. For example, in order to reduce carbon dioxide emissions and deal with climate change, renewable energy sources have been massively studied in recent years, to replace polluting and non-renewable fossil energy sources [27]. In fact, renewable energy has a longer history of use than fossil energy. In ancient production and life, the combustion of traditional biomass such as wood and agricultural waste was the most typical application of renewable energy. In theory, the use of such conventional renewable energy sources is carbon-neutral, since the CO_2 emissions from combustion form a carbon cycle with the CO_2 captured from the atmosphere by photosynthesis during biomass growth. However, as the current climate problem is already severe, and this traditional biomass, especially wood, needs a long growth time to capture CO_2, the greenhouse gas emissions generated by their combustion will aggravate the greenhouse effect in the short term. Therefore, it is not suitable as one of the solutions to deal with climate change. Modern renewable energy that is being widely promoted to replace fossil energy is basically clean and emission-less. Solar power, wind power, hydropower, geothermal power and tidal power are all typical modern renewable energy sources. Figure 1.5 shows the global renewable energy generation from 1965 to 2021 [27]. As shown in the figure, from the oil crisis in the 1970s, which is the beginning of the large-scale application of renewable energy, to present, hydropower has always been the most dominant way of renewable energy generation. The amount of hydroelectric power generation is much more than other renewable energy sources, and it still maintains a considerable growth rate. In the past 20 years, the application of other renewable energy sources has also begun to increase significantly, especially solar and wind power. They do not emit greenhouse gases and do not cause climate change. With the advancement of technology, the cost of using renewable energy will gradually decrease, while the price of fossil energy will increase with the reduction of reserves. Figure 1.6 shows change of the global levelized cost of electricity from renewable power generation technologies from 2010 to 2020 [28]. Based on these advantages, some countries are considering relying 100% on renewable energy sources, rather than just supplementing nuclear and fossil energy sources [29].

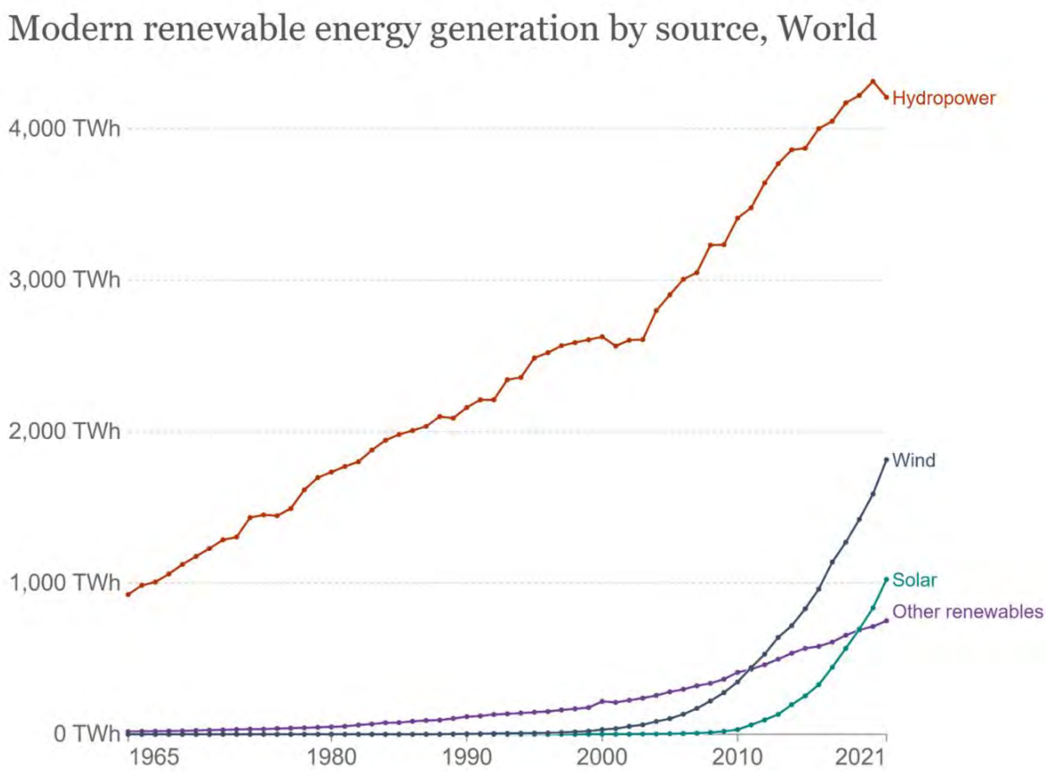

Figure 1.5. Renewable energy generation worldwide from 1956 to 2021. 'Other renewables' refers to renewable sources including geothermal, biomass, waste, wave, and tidal. Reproduced from [27], with permission from the Our World in Data.

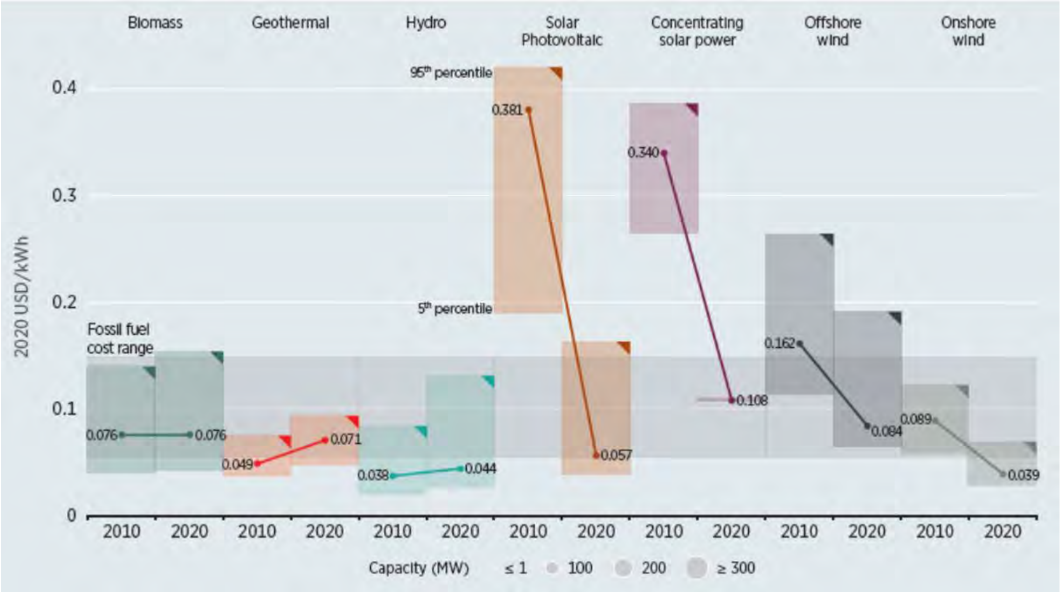

Figure 1.6. Global levelized cost of electricity from newly commissioned, utility-scale renewable power generation technologies, 2010-2020. Reproduced from [28], with permission from the International Renewable Energy Agency.

However, renewable energy is far from perfect. First, although the process of renewable energy generation is carbon-neutral, the whole application cycle is not. The manufacture of windmills, the production of solar panels, the concrete pouring of dams, etc. consume a lot of energy and costs, and emit large amounts of carbon dioxide and even toxic pollutants [30]. In addition, most renewable energy facilities have a limited lifespan, and their disposal and recycling is also an energy and cost-intensive process. Of course, these manufacturing and recycling processes produce far less greenhouse gas emissions than their application can reduce, so they can still be considered carbon-neutral technologies. Second, most renewable power generation requires huge installations to get as much natural energy as possible, such as large windmill generators, solar photovoltaic arrays and dams. These facilities take up a lot of land and will cause irreversible damage to the local environment. Windmill generators destroy bird habitats and even collide with birds resulting in death. Large dams cause large areas of land upstream to be submerged, fragmenting biological habitats; downstream soil erosion; hinder the migration and reproduction of aquatic organisms. Although renewable energy installations have a limited lifespan, their damage and impact on the environment is much longer term. Third, renewable energy is limited by natural conditions and is often unstable, unable to match the energy consumption needs of people [31]. Areas with abundant renewable energy may be remote from human society, such as wind-rich offshore and solar-rich deserts. It is difficult to build renewable energy power plants in these areas, and the electricity generated is difficult to store and transport. Moreover, even those renewable power plants built close to human settlements also have to face a mismatch between supply and demand. For example, solar power generation relies on light and can only work during the day. If there is no suitable energy storage method, it will not be able to meet the power consumption at night. Winds are also intermittent in many places. During times of the day or during seasons of the year when power demand is high, it can be a time of lack of wind. A similar problem exists with hydropower. In areas that rely heavily on hydropower for power supply, power shortages can occur when water flows decrease during dry seasons.

However, when the wind or water flow is large, the power supply will exceed the demand, and the power generation will usually be stopped for safety. Figure 1.7 shows the seasonal variation in wind, solar and electricity load in Europe [32]. It can be seen from the figure that both wind power generation and solar power generation cannot match the electricity load, and the intensity of their seasonal changes is greater than that of the electricity load, which means that there will always be oversupply and undersupply. As human electricity consumption is not constant, but a curve that fluctuates daily and monthly, grid balancing is an important issue even if only fossil fuels are used to generate electricity. The addition of renewable energy sources with intermittent supplies will make the problem much more complicated. In order to meet the needs of industrial electricity, power must remain operational 24/7 to maintain a stable and reliable minimum output, which is also difficult to achieve with renewable energy sources [33]. For the above reasons, it is impossible to completely replace fossil energy with renewable energy worldwide in a long future [34]. Therefore, more technologies are still needed to advance the resolution of environmental and resource issues. Conversion and utilization of greenhouse gases is a feasible path, which can not only reduce the greenhouse gas content in the atmosphere to slow down climate change, but also the products can be used as fuel or chemical raw material to reduce the dependence on fossil fuels. Furthermore, the excess energy produced by renewable energy sources at peak times can also be converted into chemical energy, which can be stored and transported, through greenhouse gas conversion reactions.

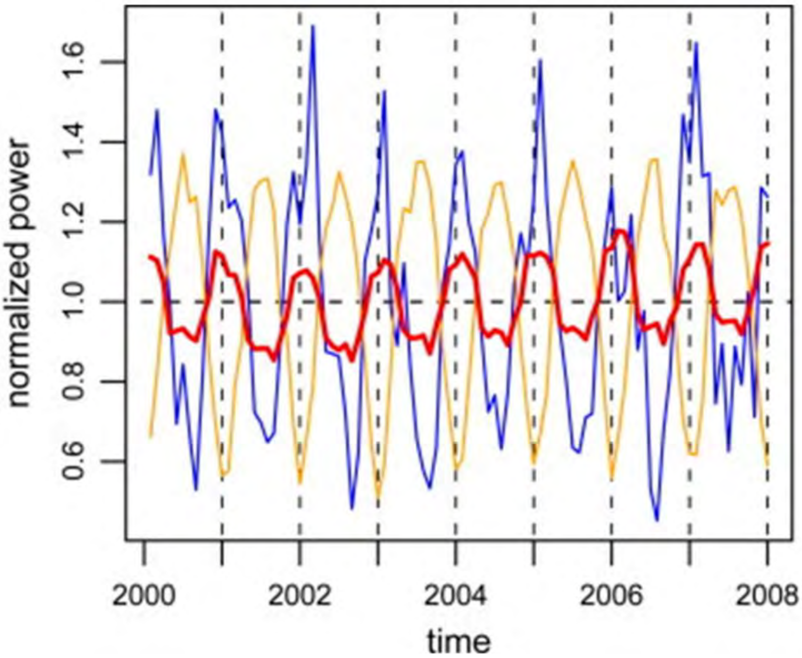

Figure 1.7. Normalized wind power generation (blue), solar power generation (orange) and load (red) time series aggregated over Europe. Each series is shown in one-month resolution and is normalized to its 8 years average. Reproduced from [32], with the permission from the Elsevier.

1.1.3.2 CO_2 utilization

For the problem of CO_2 emissions, one solution is CO_2 capture and long-term storage [35,36]. The CO_2 is first separated out with an absorbent, then compressed and transported to safe geological storage sites. This process has additional costs, and it could be a viable means of mitigating climate change, but clearly not a permanent solution. Converting carbon dioxide into valuable chemicals or fuels is more attractive and sustainable [37]. However, CO_2, the most oxidized state of carbon, is in an extremely low energy state, which means that its conversion requires a high energy input.

In nature, carbon dioxide is converted into organic matter by photosynthesis of plants using solar energy. In the process, solar energy is converted into chemical energy and stored. The utilization of CO_2 is to follow a similar path to complete the carbon cycle in industrial production. Limited by current technology, photosynthesis cannot be directly applied in industry, and other similar reactions need to be found. The CO_2 conversion with potential for industrial application can be mainly divided into two directions. The first is the conversion of CO_2 for polymer/fine chemical production. There have been many studies on the production of various chemicals from CO_2 as feedstock. The production of various polymers/fine chemicals involving CO_2 has been studied as shown in Figure 1.8 [37]. For example, CO_2 could be used as an oxidant in hydrocarbon dehydrogenation reactions, and could also be coupled with epoxides, olefins, alkanes and alcohols to form various value-added chemicals [38]. Moreover, the reaction of CO_2 and ammonia can produce urea, an important chemical product. The direct coupling of glycerol with CO_2 is also a subject of great interest in the industry, as glycerol is a by-product produced in large quantities during the production of biodiesel [39].

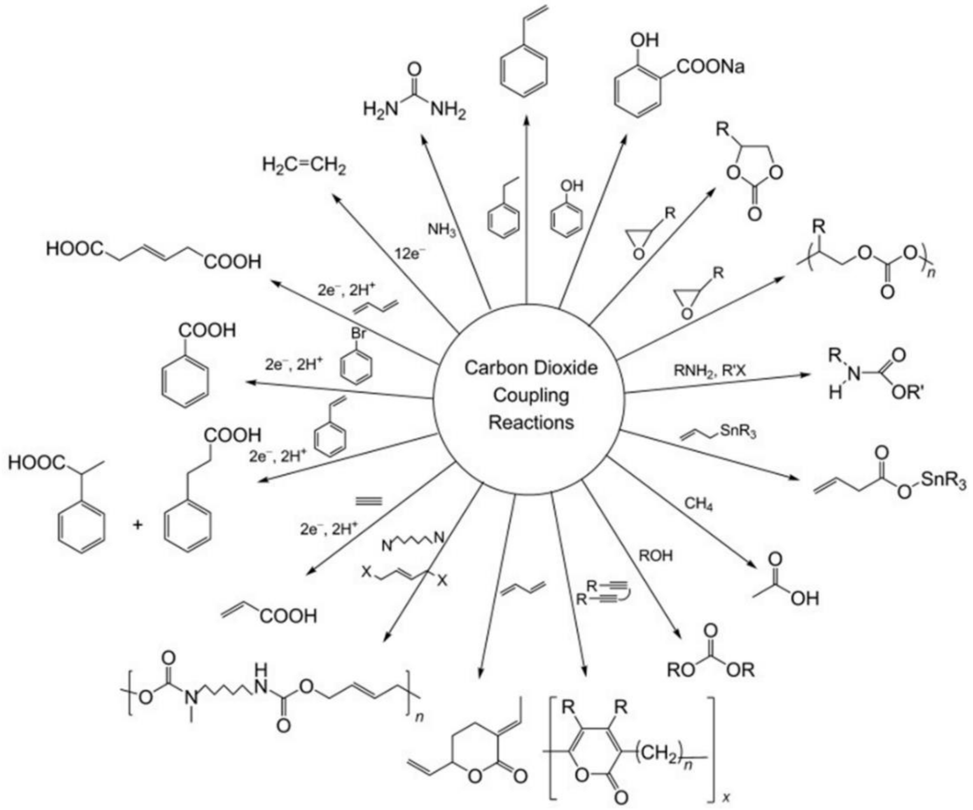

Figure 1.8. Fixation of carbon dioxide to give various chemicals. Reproduced from [37], with the permission of Wiley.

Considering the order of magnitude of CO_2 emissions, the CO_2 demand for the production of fine chemicals is too small to make a big difference in carbon-neutrality. Converting CO_2 to fuel is another direction of the CO_2 conversion and utilization. It has a greater impact on reducing greenhouse gas emissions because of the high global demand for the fuel. This part is explained in more detail in the next section.

1.2 Conversion of CO_2 to fuels

Converting CO_2 into fuel can not only solve the problem of CO_2 emissions, but also solve the problem of intermittent power generation from renewable energy. The energy required for the CO_2 conversion reaction can be supplied by energy generated at the peak of renewable energy, converting electrical energy into chemical energy for storage, and then use these fuels for power generation when renewable energy is low, to maintain a certain minimum power supply. There are several possibilities of CO_2 conversion, detailed in the next paragraphs.

1.2.1 CO_2 splitting

CO_2 can be directly split into CO and O_2, as shown in the following reaction:

$$\mathrm{CO_2(g)} \longrightarrow \mathrm{CO(g)} + \frac{1}{2}\mathrm{O_2(g)} \quad \Delta\mathrm{H}^0 = +283\ \mathrm{kJ\ mol^{-1}} \tag{1}$$

As mentioned above, CO_2 molecules are thermodynamically stable and high energy is required to break the chemical bond between C and O. In conventional CO_2 conversion, this energy is provided by thermal energy. However, thermal splitting of CO_2 is less feasible in practical applications. Figure 1.9 shows the theoretical conversion and energy efficiency of CO_2 thermal splitting without catalyst [40]. The energy efficiency (EE) of CO_2 splitting was calculated by the following formula:

$$\mathrm{EE}\ (\%) = \frac{\Delta\mathrm{H}\ (\frac{kJ}{mol})\cdot \mathrm{n}_{\mathrm{CO_2}\ (mol)}}{\mathrm{E}\ (\mathrm{kJ})} \tag{2}$$

ΔH is the reaction enthalpy of CO_2 dissociation, n_{CO2} is the amount of CO_2 converted, and E is the thermal energy expressed in kJ for the reaction. At 2000 K, the conversion of CO_2 is only 1.5%, although the conversion can reach 80%–100% at 3500 K–5000 K, and the highest energy efficiency of 47% is reached at about 80% conversion, this temperature is too high for industrial operation to be successfully applied. Solar thermal CO_2 splitting and plasma CO_2 splitting, which have recently attracted attention, can react without extra heating, finding new possibilities for this process [41,42].

In addition, next to the energy requirement, another drawback of CO_2 splitting is that the products CO and O_2 are difficult to be separated and used directly in the next step of liquid fuels production. Moreover, the explosion of CO in O_2 at high temperatures must be prevented. The gases need to be separated by some processes, such as membrane separation, for application. The separated CO is usually combined with H_2 from other sources to form syngas, which is an important intermediate in the process of producing liquid fuels such as methanol or hydrocarbons via Fischer-Tropsch synthesis.

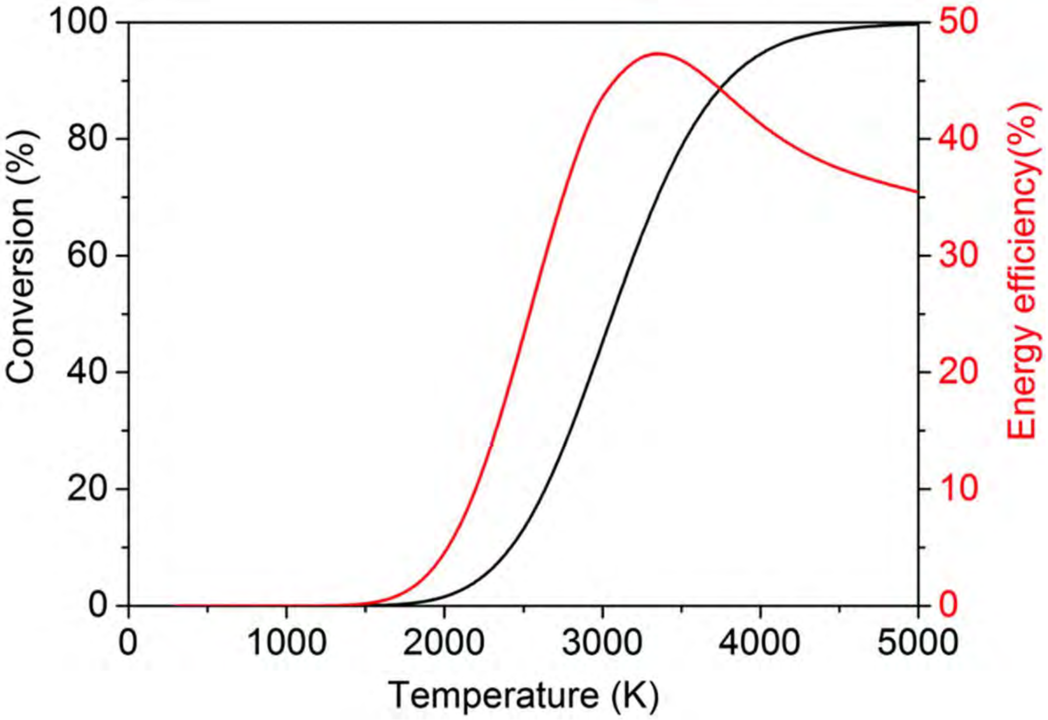

Figure 1.9. Theoretical conversion and energy efficiency as a function of temperature for thermal splitting of CO_2 into CO and O_2. Reproduced from [40], with permission from the Royal Society of Chemistry.

1.2.2 CO_2 hydrogenation

The reaction of CO_2 with H_2 is a more thermodynamically favorable process than the splitting of pure CO_2. formula (3) and (4) are the reactions of CO_2 hydrogenation to methane and methanol:

$$\mathrm{CO_2(g) + 4H_2(g) \rightleftharpoons CH_4(g) + 2H_2O(g)} \quad \Delta H^0 = -165.3\ \mathrm{kJ\ mol^{-1}} \tag{3}$$

$$\mathrm{CO_2(g) + 3H_2(g) \rightleftharpoons CH_3OH(g) + H_2O(g)} \quad \Delta H^0 = -49.9\ \mathrm{kJ\ mol^{-1}} \tag{4}$$

Due to the presence of multiple products, improving product selectivity is very important for this process. This can be achieved by selecting a suitable catalyst. For example, 100% methane selectivity has been obtained using Ni-based catalysts at a temperature of 700 K [43]. However, hydrogen is not an inexpensive raw material, and most of the H_2 currently used in industry comes from the steam reforming of methane. Therefore, the reaction of CO_2

and H_2 to produce methane is not an economically viable process. Compared with methane, methanol is a more economically competitive CO_2 hydrogenation product. It can be used both as a liquid fuel and for the production of value-added chemicals. As a liquid fuel, its energy density (4.33 kWh/L) is much greater than that of gaseous fuels (0.021 kWh/L for methane), and it is easier to transport [44]. Methanol can be a good alternative to fossil fuels, especially in the transportation sector, if available from renewable and sustainable sources. Cu, Pd and In are reported as optional catalytic active components to enhance the selectivity of methanol for CO_2 hydrogenation [45]. However, although CO_2 selective hydrogenation to methanol has been an industrially successful CO_2 reforming process, it still has the defect that 1/3 of the H_2 is wasted and converted into H_2O as by-product [40].

1.2.3 Combined conversion of CO_2 and H_2O

In traditional thermal conversion processes, the combined conversion of CO_2 and H_2O has rarely been studied. However, H_2O is often used as a hydrogen source in photocatalytic or electrocatalytic CO_2 conversion. Depending on the reaction conditions, syngas and various organics can be products of this reaction.

$$\mathrm{CO_2(g) + H_2O(g) \rightleftharpoons CO(g) + H_2(g) + O_2} \qquad \Delta H^0 = +525\ \mathrm{kJ\ mol^{-1}} \tag{5}$$

1.2.4 CO_2 reforming of CH_4 (dry reforming)

The reaction of CH_4 and CO_2, also known as dry reforming of methane (DRM), produces CO and H_2 as the main products:

$$\mathrm{CO_2(g) + CH_4(g) \rightleftharpoons 2CO(g) + 2H_2(g)} \qquad \Delta H^0 = +247\ \mathrm{kJ\ mol^{-1}} \tag{6}$$

The DRM also requires energy input to break the chemical bonds of CO_2 and CH_4, but the temperature requirement is much lower than that of CO_2 splitting. The energy efficiency (EE) of CO_2 reforming of CH_4 was calculated by the following formula:

$$\mathrm{EE}\ (\%) = \frac{\Delta \mathrm{H}\ (\frac{kJ}{mol})\cdot(\mathrm{n}_{\mathrm{CO}_2\,(mol)}+n_{CH_4(mol)})}{\mathrm{E}\ (\mathrm{kJ})} \tag{7}$$

ΔH is the reaction enthalpy, n_{CO2} and n_{CH4} are the amount of CO_2 and CH_4 converted, and E is the thermal energy expressed in kJ for the reaction. As shown in Figure 1.10, thermal DRM without catalysts reaches the maximum conversion and energy efficiency at around 1000 K. Compared with the above two processes, DRM may have more advantages for industrial applications. First, the products of it are mainly CO and H_2 (i.e. syngas), and by combining with Fischer-Tropsch synthesis, it is relatively easy to further synthesize liquid fuels such as methanol and liquid hydrocarbons. Second, methane, another feedstock gas besides CO_2, can be obtained directly from abundant natural gas at a lower cost than H_2 and oil. Converting it into liquid fuels and value-added chemicals is economically feasible. Moreover, as mentioned above, CH_4 itself is also an important greenhouse gas, and its contribution to the global greenhouse effect is second only to CO_2. The promotion and application of the dry reforming will reduce the emission of two greenhouse gases at the same time. Additionally, the feed gas for DRM has a sustainable source.

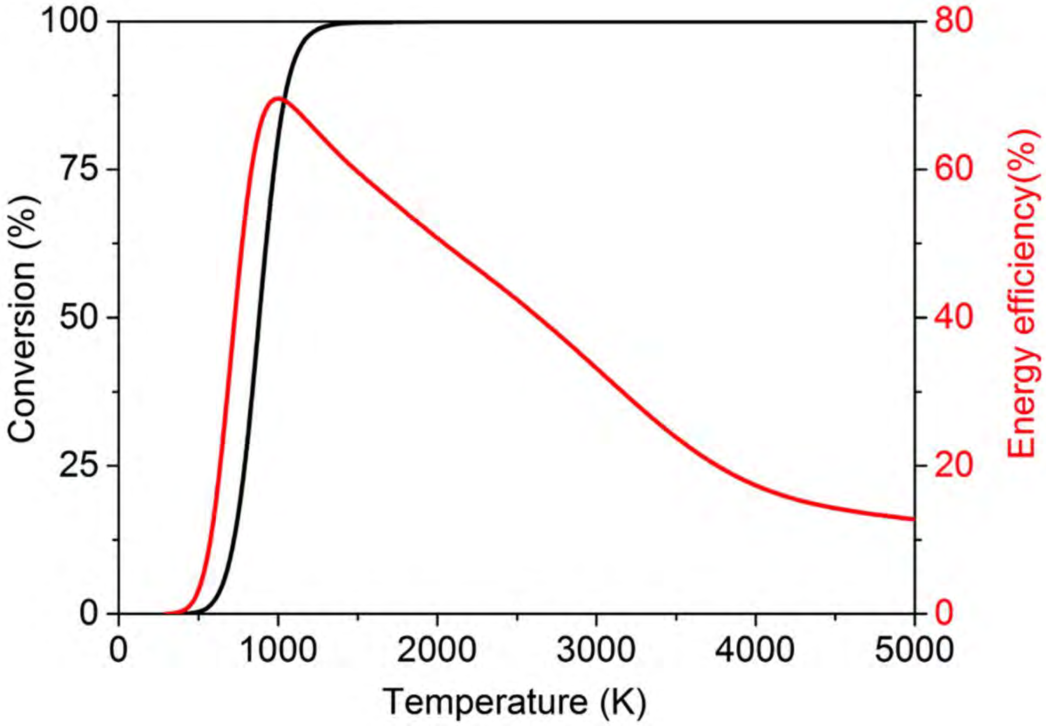

Figure 1.10. Theoretical conversion and energy efficiency as a function of temperature for thermal dry reforming of CH_4 into CO and H_2[40]. Reproduced from [40], with permission from the Royal Society of Chemistry.

Figure 1.11 shows the sources of global methane emissions in 2010 [46]. As can be seen from the figure, more than half of the methane emissions come from agriculture, including crop cultivation, fertilizer management and livestock raising. However, the agricultural sector has received far less attention than the industrial sector in greenhouse gas reduction measures in all countries. Enteric fermentation and manure of ruminants, such as cattle and sheep, are the largest sources of agricultural emissions. These methane emissions from livestock will further increase because population growth and economic development have boosted human demand for animal protein. The second largest source of agricultural emissions is the fermentation of crops and their wastes in an anaerobic environment. The direct emission of this methane into the atmosphere would contribute significantly to the greenhouse effect due to the high GWP of methane. As we all know, CH_4 itself can be used as a fuel, and agricultural production of methane is a sustainable and renewable process. Therefore, if the methane produced by these agricultural sectors can be utilized effectively, it will not only directly reduce greenhouse gas emissions, but also find a relatively stable and clean alternative to fossil energy. Since it is derived from agricultural waste, the low cost makes it economically advantageous. There are already a lot of related factories that are in production for power generation or fuel [47,48]. In addition, these gases from the decay of organic/waste are not pure methane, but a mixed gas, biogas. The main components of biogas are CH_4 (50–75%) and CO_2 (25%–50%), exactly the feed gas for DRM, and may contain small amounts of H_2S, H_2 and moisture [49,50]. Depending on the biomass from which the biogas is produced, the ratio of CH_4 and CO_2 is different. Compared to burning directly as a gaseous fuel, it may be more valuable to industry of biogas to use biogas as feed gas of DRM to produce value-added chemicals or liquid fuels. It can not only improve its economic potential, but also enhance environmental benefits. At present, the application scale of biogas is still relatively small, and there is large room for improvement. The DRM will further increase the demand for biogas, which is beneficial to the expansion of the biogas production industry.

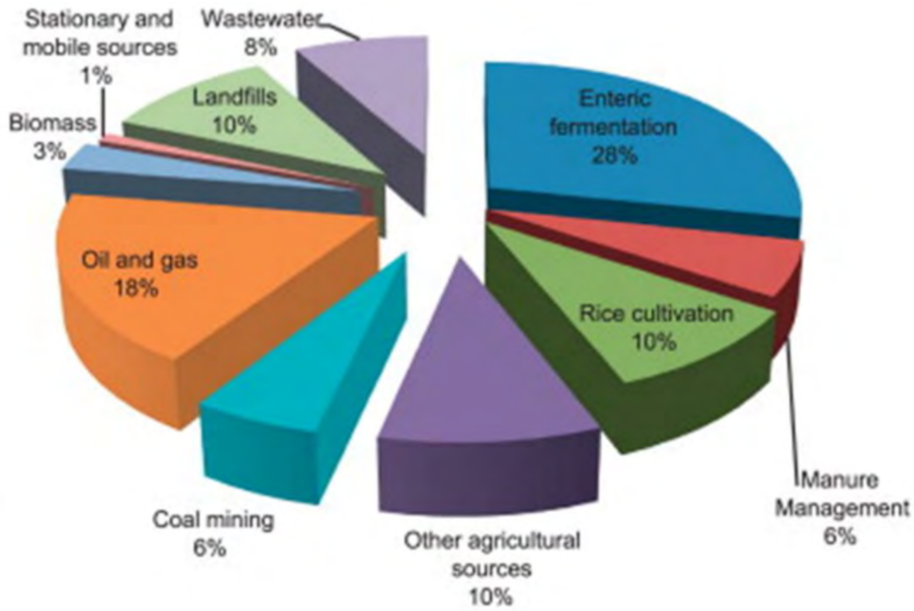

Figure 1.11. Anthropogenic methane emissions by source. Reproduced from [46], with permission from the Elsevier.

Although DRM has these advantages and is almost the key to solving some problems, it has not been widely applied in industry so far. This is because it has a major drawback, carbon deposition and catalyst deactivation at high temperatures in the process. This defect also exists in other CO_2 thermal conversion processes. Some studies have attempted to solve this problem by improving catalysts. Another route is to use other forms of energy instead of thermal input to activate gas molecules for CO_2 conversion.

1.2.5 Novel approaches for CO_2 conversion

Traditionally, as mentioned above, the energy required for the CO_2 conversion reaction is provided by thermal energy. However, a serious disadvantage of thermal conversion of CO_2 is coking and catalyst deactivation at high temperatures (> 800 °C for dry reforming, for example), limiting the industrial development of these processes. Moreover, renewable energy is a potential energy source for CO_2 conversion, but using renewable energy for thermal conversion processes cannot work efficiently. First, large thermal reactors take a long time to start and preheat, which has a certain hysteresis and energy loss. It cannot be started and stopped frequently, otherwise the cost loss will be huge. However, as mentioned above, renewable energy sources are unstable due to natural conditions, and their utilization is more suited to a technology with quick on-off-switching capacities. Secondly, the traditional thermal conversion process needs to go through too many energy conversion processes, which may be first from renewable energy to electricity, then from electricity to thermal energy, and finally from thermal energy to chemical energy. These conversion processes may bring about a large amount of energy loss and lead to a lower energy efficiency. In particular, thermal energy is a low grade energy, with a low energy conversion efficiency. It would be more economical to reduce these steps and convert directly from renewable energy or electrical energy to chemical energy. Some new CO_2 conversion technologies, such as photochemical, solar thermochemical, biochemical, (photo)electrochemical and plasma technologies, which are expected to solve the problems in the CO_2 conversion, and will work better with renewable energy.

1.2.5.1 Photochemical conversion and solar thermochemical conversion

The photochemical conversion of CO_2 is an imitation of photosynthesis in nature. Semiconductors are often used as photocatalysts for this process. The principle is shown in Figure 1.12 [51]. Photocatalysts absorb light energy, and electrons in the valence band are excited to the conduction band, leaving an electron hole in the valence band. If the potential of the conduction band of the photocatalyst is higher than the redox potential of CO_2 and its reduction products, the photogenerated electrons in the conduction band are transferred from the catalyst surface to the adsorbed CO_2 species, which are then converted into organic chemicals, fuels or other products. The hydrogen in the product is often provided by H_2O, which reacts with positively charged holes in the valence band to generate O_2 and protons. Carbon monoxide, formic acid, formaldehyde, methanol, methane, ethylene, ethane and ethanol are all possible products of the photochemical processes [52]. However, most of the current research on photocatalysts is carried out using ultraviolet (UV) light, and the commonly used photocatalysts have poor responsiveness to visible light. The energy of UV accounts for a small proportion (~4%) of solar energy, which means that the conversion efficiency of solar energy by current photochemical processes is low. The development of photocatalysts with higher visible light efficiency is a long-standing challenge for this process [52].

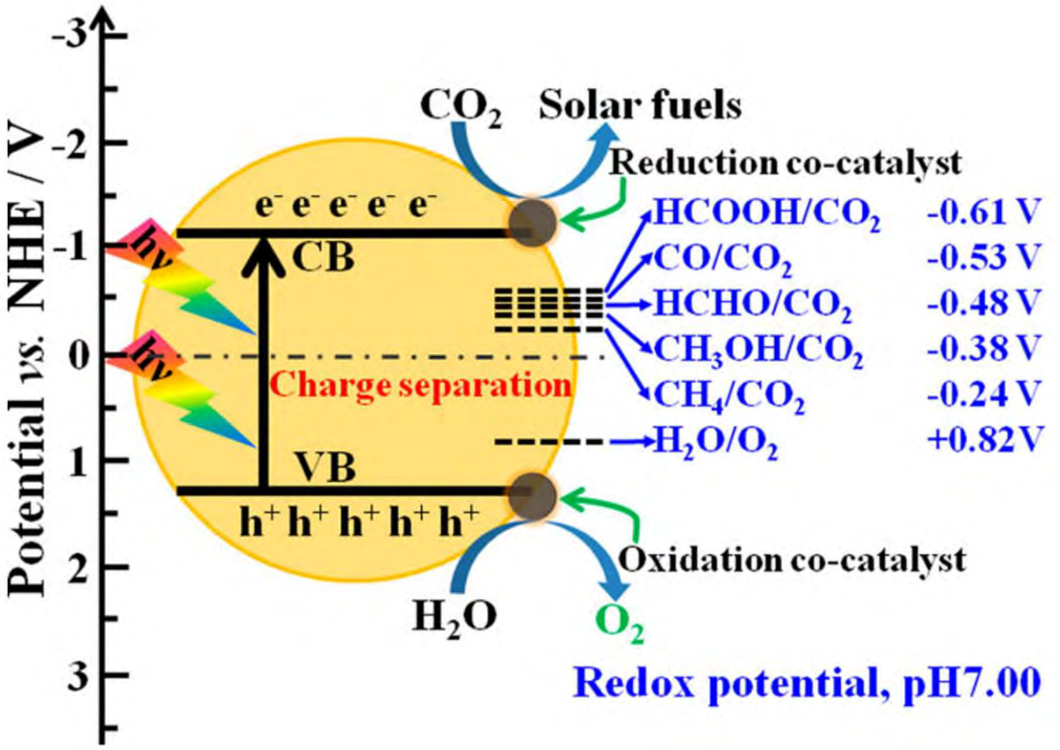

Figure 1.12. Photochemical conversion of CO_2 and H_2O on a semiconductor. Reproduced from [51], with permission from the American Chemical Society.

Solar thermochemical conversion has attracted a lot of attention recently. It differs from photochemical conversion in the utilization of different forms of solar energy. Figure 1.13 shows a schematic of a typical solar thermochemical reactor and a two-step solar thermochemical cycle for CO_2 splitting [53,54]. The energy of the process is actually provided in the form of thermal energy, but the heat source is concentrated sunlight. The advantage is that the direct utilization of solar heat saves a lot of energy loss in the energy conversion process. As mentioned above, the temperature required for CO_2 thermal splitting is too high for industrial applications. The introduction of metal oxides (typically CeO_2) divides this process into two steps, making it possible to proceed at relatively low temperatures. The metal oxide is solar thermally reduced in the first step, and then it is oxidized by CO_2 in the second step. O_2 and CO are the products of the first and second steps, respectively. This process is still in research phase. The building cost of the solar concentrator, the moderate temperature (< 2000 K) efficiency of the metal oxide material, and its stability in redox cycles are the research priorities.

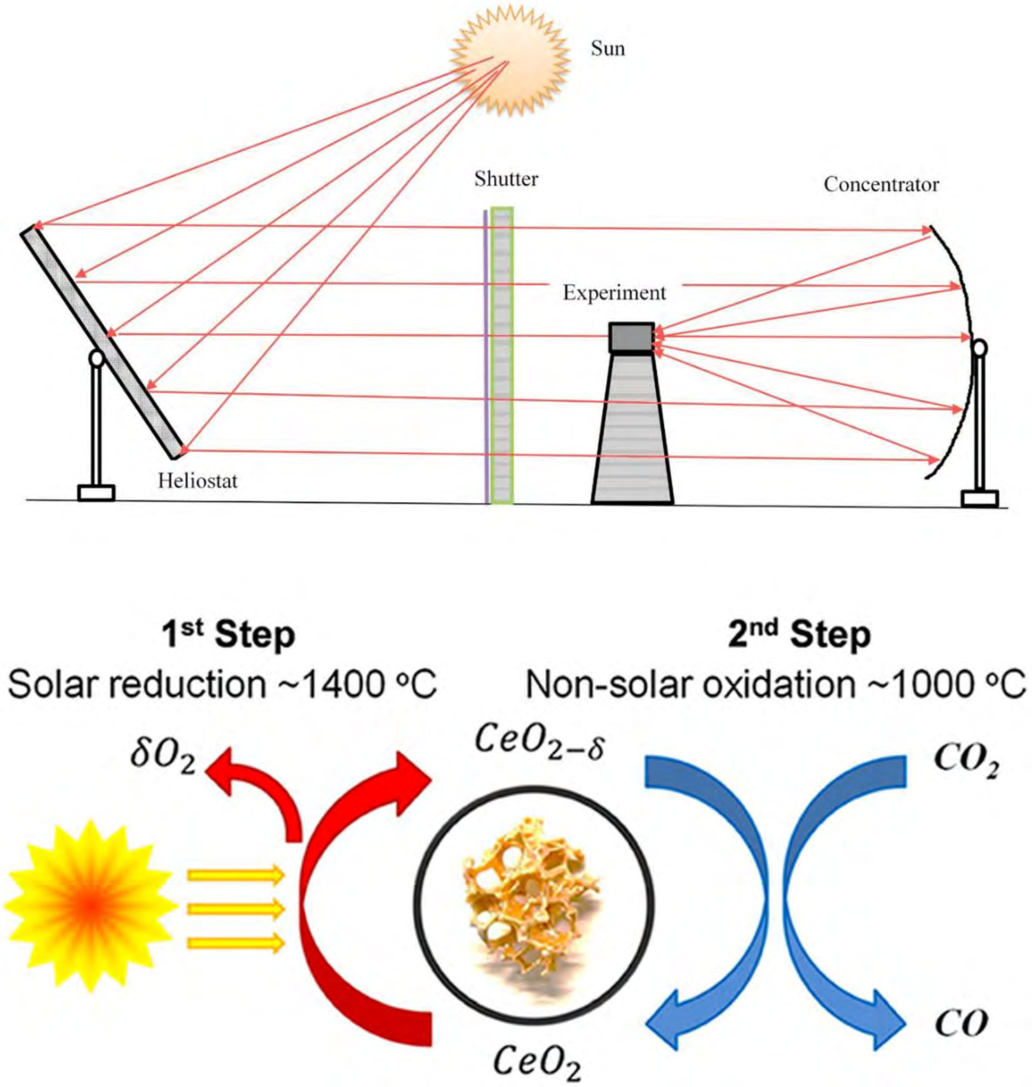

Figure 1.13. schematic of a typical solar thermochemical reactor and a two-step solar thermochemical cycle for CO_2 splitting. Reproduced from the [53], with permission of the Elsevier and the [54], with permission of the Frontiers Media SA.

1.2.5.2 Biochemical CO_2 conversion

Biochemical techniques are the direct use of photosynthesis. Biomass is cultivated and used for fuel production. Similar to the use of traditional biomass, the biochemical CO_2 conversion process is in theory carbon-neutral. The CO_2 emitted in the process comes from the CO_2 absorbed from the atmosphere during photosynthesis. The most studied biomass is microalgae, because it does not occupy land for agriculture and has a short growth period, relatively low cost, and less water consumption [55]. Figure 1.14 shows the process of microalgae biochemical CO_2 conversion technology [56]. In addition to fuels, such as methane, methanol, ethanol, hydrogen and biodiesel, the process also produces high-value by-products such as biopolymers, animal feed and fertilizers. However, the cultivation of biomass in biochemical technology and the process of extracting complex molecules from algae to make value-added products are expensive [56]. The current technology is still not suitable for commercialization. In addition, the nitrogen fertilizers required in the algae production process are derived from fossil fuels, which is not sustainable.

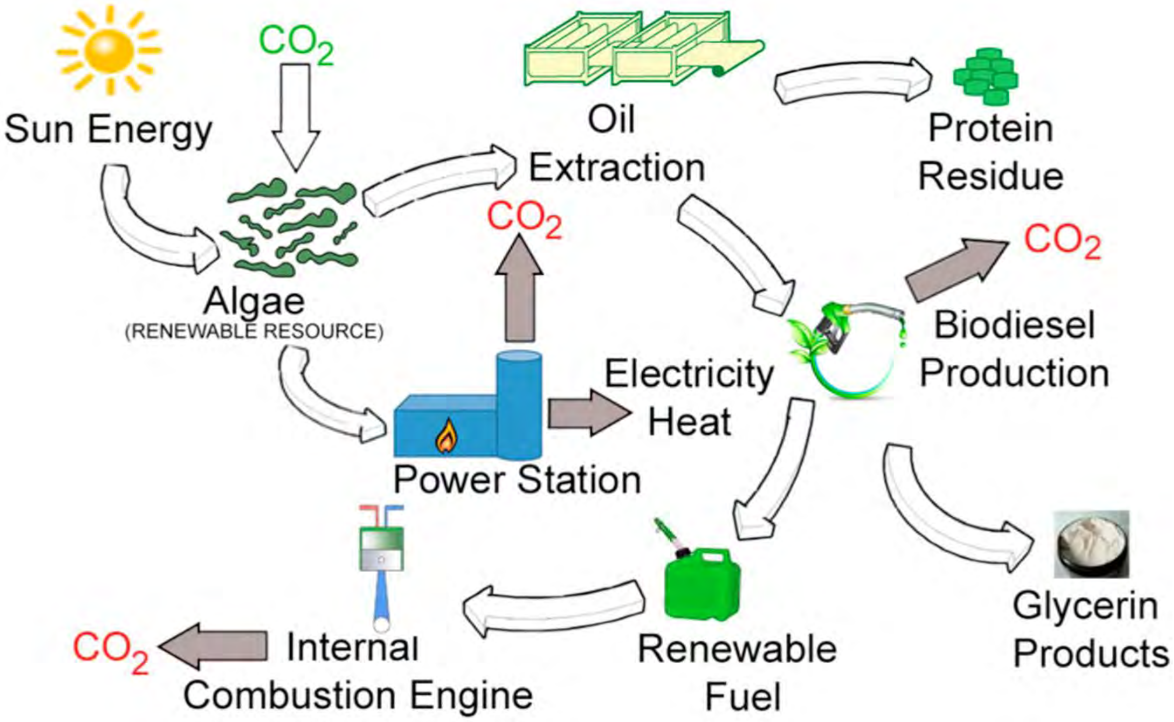

Figure 1.14. The process of algal biochemical conversion of CO_2. Reproduced from [56], with permission from the Elsevier.

1.2.5.3 Electrochemical CO_2 conversion

Electrochemical technology is not a direct conversion of renewable energy (e.g. solar energy), but relies on electrical energy. Although this causes energy loss in the power generation, it also makes this technology applicable to more types of renewable energy.

Figure 1.15 shows a schematic of an electrochemical cell for the conversion of CO_2 to CO [57]. The conversion of CO_2 can be carried out under mild conditions by applying a potential difference between the two electrodes. Beside CO, liquid fuels and chemicals such as formic acid, formaldehyde, methanol, oxalic acid, and ethanol can all be the products of the electrochemical conversion of CO_2 by adjusting the experimental conditions or catalyst [58]. The research on electrochemical conversion of CO_2 has made great progress, but there are still some problems. For example, it is difficult to increase production due to the limitation of the solubility of CO_2 in water (1.449 g/L at room temperature). The composition of the product is complex and the separation is difficult. In addition, the activity and long-term stability of catalysts are also challenges for electrochemical conversion. Due to these factors, to date, this technology has not been widely applied on an industrial scale so far.

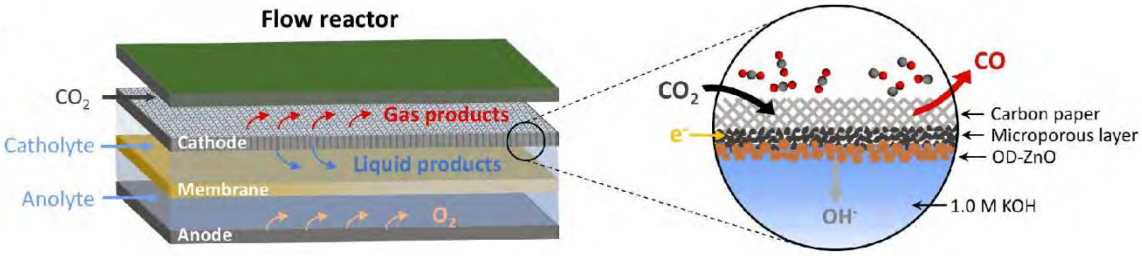

Figure 1.15. Electrochemical cell for the reduction of CO_2 to CO. Reproduced from [57], with permission from the Elsevier.

1.3 Plasma technology for dry reforming of methane

As can be seen from the previous section, CO_2 conversion is rapidly developing as a promising approach to solve the environmental and resource problems. Various reactions and techniques have been studied. Taking economic and environmental benefits into consideration, dry reforming is one of the most promising reactions for successful industrialization, as mentioned above. The problems limiting its promotion are mainly caused by high reaction temperatures (> 800 °C). The new technologies introduced in the previous section to replace high temperature can not only work better with renewable energy, but may also solve the problems existing in high temperature reactions. However, these techniques are not applicable to all CO_2 conversion reactions. For example, CO_2 splitting is often studied in solar thermal chemistry, but it is difficult to combine it with photocatalysis [52]. In recent years, an emerging technology, plasma technology, has received extensive attention for CO_2 conversion. Various CO_2 conversion reactions have been studied with plasma technology, including CO_2 splitting, dry reforming, and co-conversion of CO_2 with H_2 or H_2O. As a technology still under research, it has its own advantages, but still faces many problems.

1.3.1 General plasma properties

Plasma, although the term was not introduced until 1928 by I. Langmuir [59], is not uncommon. Conversely, despite being relatively rare on Earth, more than 99% of the matter in the visible universe is plasma. Stars, such as the sun, are made of hot plasma. Interstellar medium is also essentially in the weakly ionized plasma state. In addition, the aurora, lightning (Figure 1.16), etc. that we can see on Earth are also natural plasmas.

Figure 1.16. Natural plasma on Earth. (a) lightning, reproduced from [60], with permission of Springer Nature (b) aurora, reproduced from [61], with permission of the GeoScienceWorld.

Plasma can be created by adding energy to a gas (and other aggregation states), such as by heating, applying an electric field, or adiabatic compression. This process is like phase transitions of matter, such as transforming a solid into a liquid and then into a gas by heating. This is why, although inaccurately, plasma is often referred to as the "fourth state of matter." The introduced energy causes some electrons to leave the gas molecules and become free electrons, a process called ionization. Plasma is a partially or fully ionized substance consisting of electrons, positive and negative ions, and neutral molecules, atoms, and radicals, etc..

Plasma has a lot of interesting properties. Due to the presence of charged particles, a plasma is excited conductive. It is quasi-neutral because over the entire plasma volume, the positive and negative charges are equal. Collisions between the moving particles produce excited molecules, and photons released by their radiative relaxation are the source of the light of the plasma. In addition, a plasma cannot be simply regarded as just charged gas. There is a collective effect between the charged particles of the plasma due to the plasma approximation. Each charged particle affects many nearby charged substances, not just the closest one. Therefore, the interactions between plasma particles are stronger and more complex than that of gas molecules.

Due to the complex composition and properties of plasmas, they are of interest for applications in various fields [62]. For example, smelting, spraying, welding, medical applications, chip manufacturing and display manufacturing have all been studied to apply the plasma technology. Figure 1.17 shows two application examples of plasma medicine and welding. The application of plasma technology in CO_2 conversion (including dry reforming) is also a subject worth studying. Due to the presence of energetic electrons and reactive species and their interaction, plasma has higher reactivity than non-ionized gases. Therefore, the CO_2 conversion reaction in this state may bring new discoveries and breakthroughs to this field.

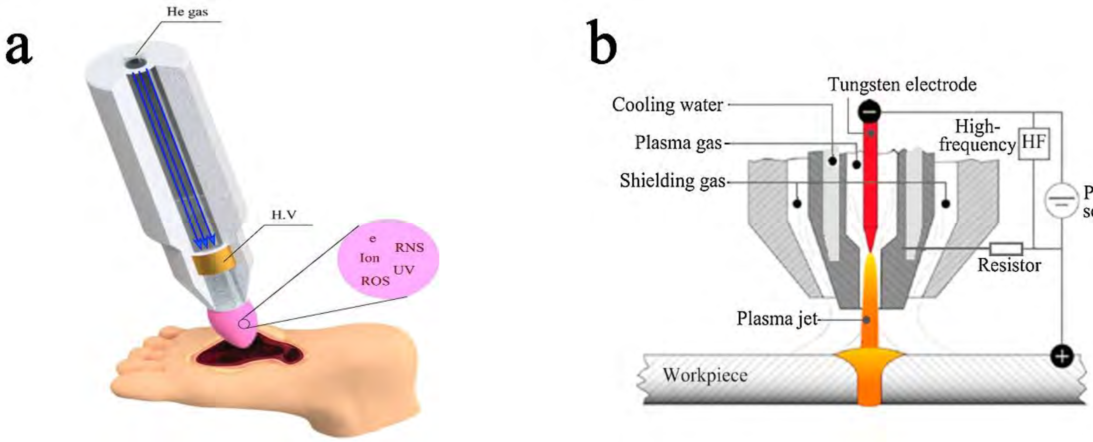

Figure 1.17. (a) Schematic of helium atmospheric plasma wound healing system, reproduced from [63], with permission of the Springer Nature. (b) Schematic of plasma arc welding torch, reproduced from [64], with permission of the Elsevier.

An important parameter for plasmas is temperature, usually expressed in Kelvin or electron volts. According to the temperature, plasmas can be divided into high temperature plasmas and low temperature plasmas. Different with other substances, as a multicomponent system, plasma may have more than one temperature. So another way of classifying is based on whether the plasma is in thermal equilibrium. If all the components in the plasma (electrons, ions and neutral particles) are in local thermal equilibrium, the plasma is called thermal plasma. Due to the difference in the mass of electrons and heavy particles (ions and neutral particles), sometimes the temperature of the components in the plasma can be very different. Plasmas in this non-thermal equilibrium are called non-thermal plasma.

Non-equilibrium plasma components are easy to obtain in artificial plasmas. For example, in a typical way, passing a gas through an electric field composed of two parallel electrodes with a potential difference, and when the voltage reaches a certain threshold, the gas is broken down. The movement and collision of electrons and other particles in the plasma leads to ionization, excitation, and secondary electron emission, and the released electrons will collide with more atoms, forming a chain reaction. This is called an electron avalanche and is the key to the breakdown process. Gas molecules are partially ionized into electrons and ions, forming a plasma. In this case, the ionization is incomplete, and most of the gas molecules remain neutral. Electrons and ions are accelerated by the electric field towards the anode and cathode, respectively. In the same electric field, electrons and ions acquire very different accelerations because of their very different masses. Therefore, in the case of insufficient energy exchange between electrons and heavy particles, their velocities are very different, i.e. their temperatures are very different. Electrons in non-thermal plasmas typically reach temperatures of 10^4–10^5 K, while other species remain around room temperature.

The collision and energy exchange between electrons and other particles in the plasma lead to the generation of highly reactive radicals, the transfer of energy, and the destruction and formation of chemical bonds. This is the principle by which non-thermal plasma technology can replace CO_2 thermal conversion and thermal dry reforming. Inactive CO_2 and CH_4 molecules that require activation by heating in thermal reactions, can be activated by energetic electron collisions at close to room temperature (< 250 °C) in non-thermal plasmas. The resulting radicals and ions react with each other to form new compounds. This technique avoids many problems of high temperature processes. First, the problem of catalyst sintering deactivation at high temperature can be avoided in non-thermal plasma. Second, without long warm-up and cool-down, non-thermal plasma technology is a process with quick on-off-switching capacities. As mentioned above, this is critical for working with fluctuating supplies of renewable electricity. In addition, same as electrochemical conversion technology, electric-driven plasma technology is more adaptable to a variety of renewable energy sources. And because of the simple structure of some reactors, their low construction cost and strong scalability, makes it easier to expand it from laboratory scale to large-scale industrial equipment. However, the high reactivity and complex mixture of free radicals and ions in non-thermal plasmas, forming various products, has poor selectivity. For plasma dry reforming, in addition to syngas, a large amount of other hydrocarbons and oxygenates are also formed. Improving product selectivity (whether syngas or (higher) hydrocarbons or oxygenates) is one of the current research directions for plasma dry reforming.

Compared to non-thermal plasmas, thermal plasmas usually have a higher temperature or pressure to allow enough collisions between particles [65]. More collisions between particles lead to more efficient energy exchange between electrons and heavy particles to maintain their temperature balance. The temperature of thermal plasma can reach 20,000 K and above [40]. It is mainly applied in fields such as coating technology, metallurgy, etc. that require the high temperatures [65]. Few thermal plasmas are suitable as a new technology for CO_2 conversion improvement due to their too high temperatures, and the types of plasmas (both thermal and non-thermal) that can be applied to CO_2 conversion are described below.

1.3.2 Plasma reactors for dry reforming

Based on the above-mentioned generation principle of plasma, various plasma reactors suitable for gas chemical reaction have been designed and studied. Volatile Organic Compounds (VOCs) decomposition, NH_3 synthesis and CO_2 conversion, including of course dry reforming, are commonly studied processes.

1.3.2.1 Dielectric barrier discharge (DBD)

Dielectric barrier discharge, also known as "silent discharge", is one of the most typical non-thermal plasma generation methods. The structure of it is simple, a common type shown in Figure 1.18, consisting of two parallel electrodes with a dielectric barrier inserted [66]. The two electrodes are applied with a potential difference to create a uniform electric field, and the dielectric barrier is used to limit the current to prevent the formation of sparks and arcs. Also other forms of DBD reactors exist with the same discharge principle, such as the reactor with coaxially arranged tubular electrodes and tubular dielectric baffles. Since a DBD device for ozone generation was first reported by Siemens in 1857, it has been used in a wide variety of fields such as pollution control, surface modification, and synthesis of fuels and chemicals [67-69].

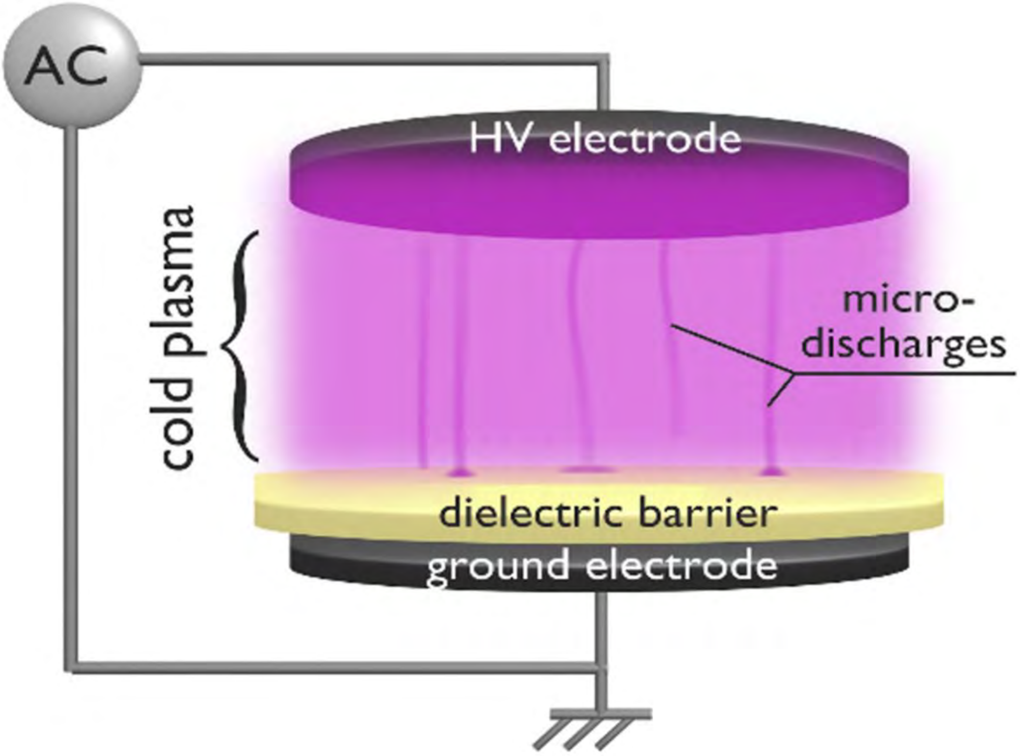

Figure 1.18. Schematic of a type of DBD reactor. Reproduced from [66], with permission from the Elsevier.

DBD reactors can work at 0.1–10 atmospheres [65]. The threshold of the voltage applied between the electrodes to break down the gas, the so-called breakdown voltage, is determined by the distance between two electrodes, the gas pressure and the type of gas, known as Paschen’s law. Alternating current (AC) is typically applied in the experiments to prevent the accumulation of too much charge on the dielectric barrier of a DBD reactor and causing the plasma to extinguish. The amplitude of the AC is 1–100 kV and the frequency is 50 Hz–500 kHz [70-75]. A Q-U graph, known as a Lissajous figure, can be plotted using the voltage and charge data to study the discharges in a DBD reactor. Figure 1.19 shows a typical Lissajous figure of the plasma in a DBD reactor. The slopes of the sides of the Lissajous figure represent the equivalent capacitance of the DBD reactor at different phases, since dQ/dU = C. In the AB and CD phases when the reactor is not discharged, the entire DBD reactor, including the dielectric barrier and discharge gap, behaves as a capacitor. Therefore, the slope of the AB and CD phases in the Lissajous figure is the capacitance of the capacitor formed by the dielectric barrier and the discharge gap in series. Plasma occurs in the BC and DA phases. During the discharge, a part of the discharge gap behaves like a resistor due to the breakdown of the reactive gas, while the dielectric barrier and another part of the discharge gap still behave as a capacitor (because the entire gap is not fully discharged in a DBD reactor). Therefore, the slope of the BC and DA phases represents the capacitance, including the dielectric barrier and the undischarged gap. The discharging areal fraction, burning voltage (U_{bur}), which is the minimum voltage to sustain the plasma in the reactor, and the displaced charge of the plasma can be calculated from the slopes and points in the Lissajous figure (See the experimental section in chapters below for the specific calculation method) [76,77].

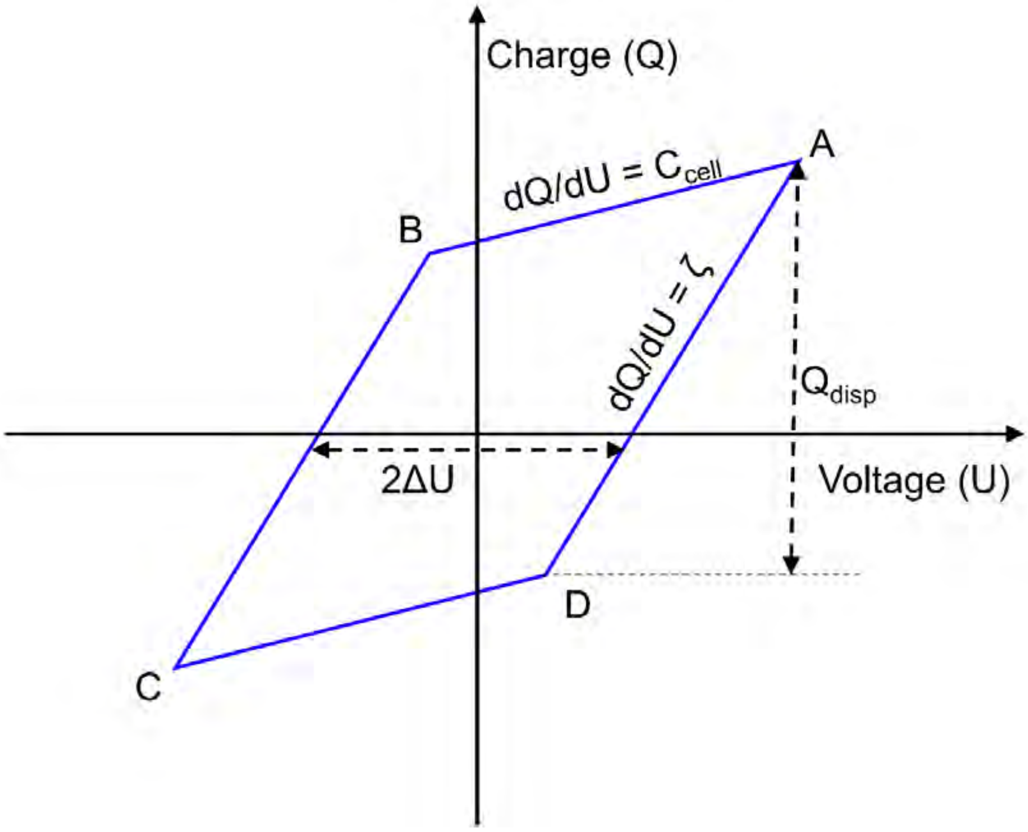

Figure 1.19. Typical Lissajous figure of a discharge in a DBD reactor.

Typically, the filamentary discharge mode is the main discharge mode in DBD reactors. During the discharge process, a large number of micro-discharge filaments form a non-uniform plasma (Figure 1.18). The diameter of discharge filaments is about 100 μm and their lifetime is only a few nanoseconds. The number of micro-discharges and filament distribution are affected by a number of factors, including the structure of the reactor, the properties of the packing in the reactor, and even the physical properties of the dielectric barrier [78]. Electrons with high energy exist only in these filaments. Compared with other non-thermal plasmas (such as glow discharge and corona discharge), the kinetic energy of electrons inside the filament in filamentary discharge is higher, up to 10 eV. However, the volume of the micro-discharge filaments is only 1–10% of the total gas volume [79]. More of the gas is not ionized and is "heated" by the dissipated energy. Only some long-lived species such as some free radicals generated in micro-discharges, may diffuse into the gas and react. This may be one of the reasons that the energy yield (i.e., the amount of CO_2 and CH_4 converted per unit energy input) of the DBD reactor is lower than that of other reactors [80]. Moreover, the energy of electrons in filaments are too high for vibrational excitation, and mainly causing electronic excitation – dissociation. This process requires more energy than strictly needed for bond breaking, and this extra energy is simply wasted [80,81].

The advantages of DBD reactors is that they can be operated at ambient temperature and pressure. Moreover, it is straightforward to add a catalyst to the discharge zone. Benefiting from the simple structure, the DBD reactor is easily scaled up for industrial production. Figure 1.20 is an example of a large DBD ozone generator [82].

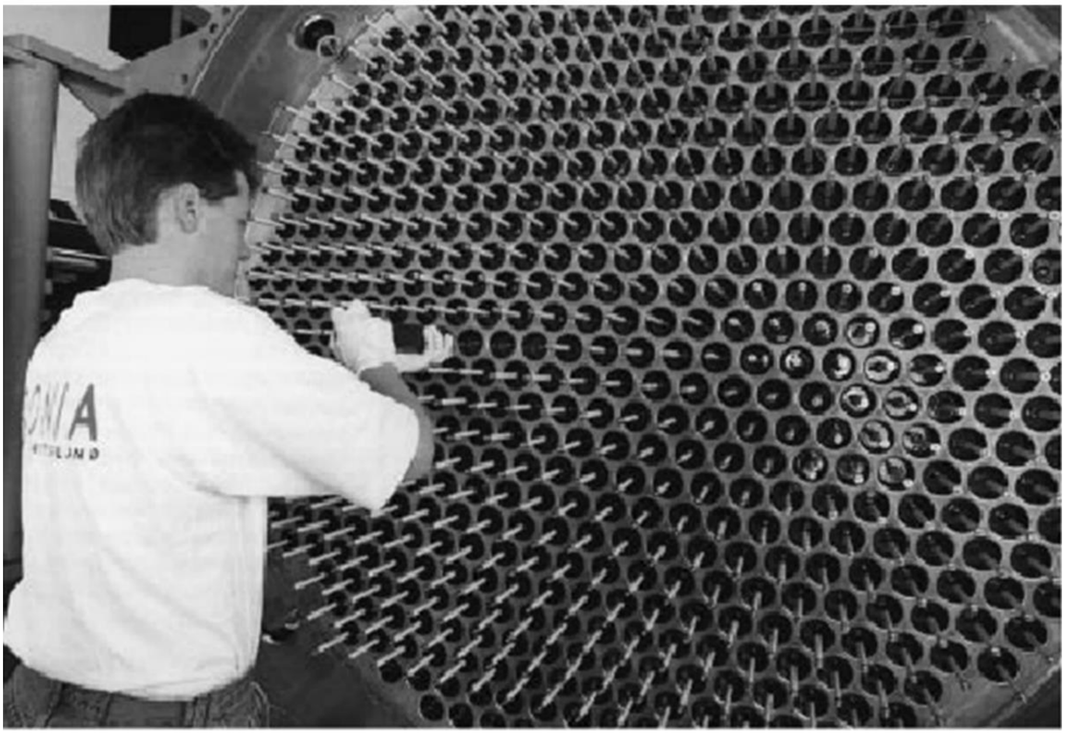

Figure 1.20. Photo of large DBD ozone generator [82].

1.3.2.2 Gliding arc (GA) discharge

A gliding arc is another commonly used type of plasma reactor. Figure 1.21 shows a photograph and structural schematic of a typical gliding arc reactor [83]. The gas flow passes through the gap between two knife-shaped electrodes from the bottom. A voltage is applied on the electrodes, creating a small arc at the bottom of the electrodes (the narrowest part of the discharge gap). The arc moves towards the top with the gas flow and gradually elongates as the electrode gap increases, until it is no longer sustained. The plasma in the arc is in local thermal equilibrium, but cannot be maintained after the arc length exceeds its critical value. Since the energy provided by the electric field at this time is less than the heat loss of the plasma, the temperature of the heavy particles cools down rapidly, but the electrons still maintain a relatively high temperature (~1 eV). The plasma remains conductive in this non-thermal equilibrium state and continues to move with the gas flow until it is extinguished. A new arc will then be created and a new cycle will start [84]. This transition from thermal equilibrium to non-thermal equilibrium is rapid, possibly completed in nanoseconds [85]. Therefore, the plasma in the non-equilibrium region can consume more discharge energy, about 75–80%, and electrons around 1 eV in this state are considered suitable for the vibrational excitation of CO_2.[86]

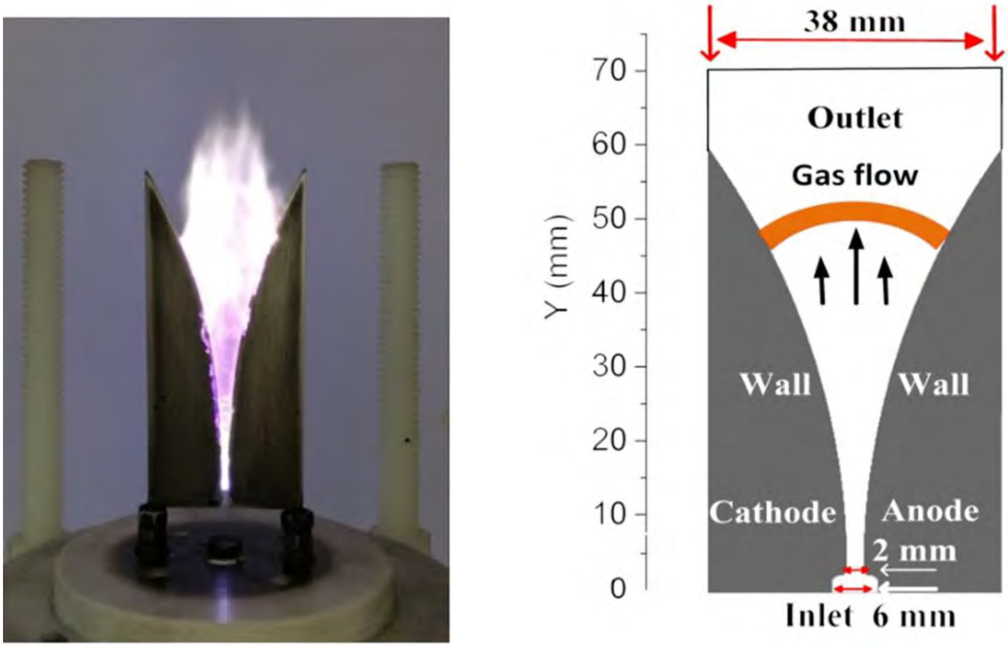

Figure 1.21. Photo (left) and structural schematic (right) of a typical 2D gliding arc reactor. Reproduced from [83], with permission of Elsevier.

Because the gliding arc discharge combines thermal and non-thermal plasmas, it is sometimes referred to as a "warm plasma". The temperature of the gas is between thermal and non-thermal plasmas. In addition to the traditional knife-shaped GA reactor, many modified GA reactors have been studied, such as a 3D gliding arc plasmatron, a multiple-electrode gliding arc reactor, and a fluidized bed gliding arc reactor [40]. Figure 1.22 shows a photograph and schematic of a gliding arc plasmatron. The gas flow entering from the inlet on the side moves along the tangential direction of the arc, and drives the movement and elongation of the arc upward and then downward to the outlet until it is extinguished. The gas forms a vortex between the anode and cathode, and its contact and mixing with the plasma arc is more sufficient and uniform than that in a conventional flat knife-shaped reactor. GA reactors have been extensively studied for various CO_2 conversion reactions [87-89], and it was found to generally have a good conversion and energy yield for dry reforming. However, it has problems of carbon deposition, and is difficult to work with catalysts.

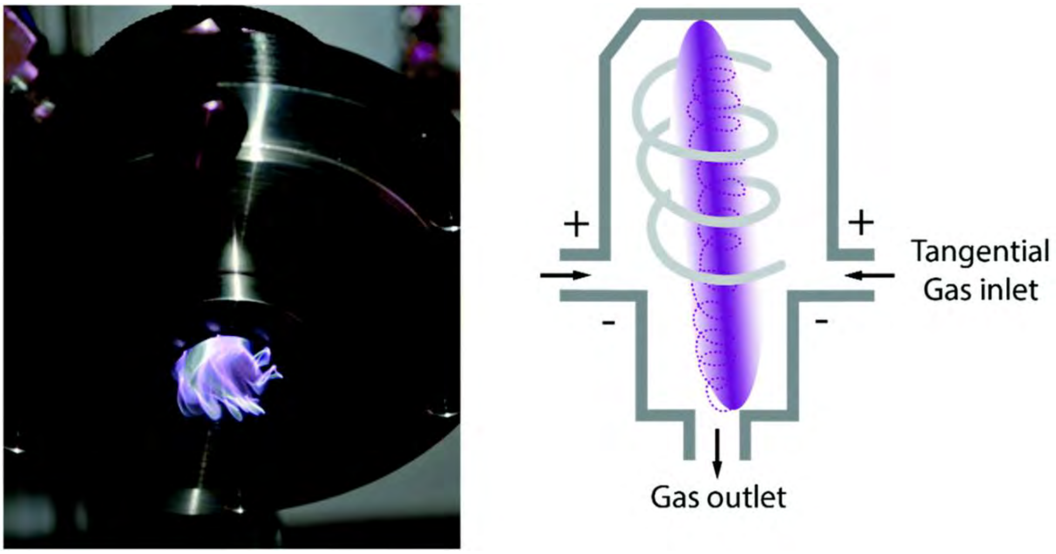

Figure 1.22. Photo (left) and structural schematic (right) of a gliding arc plasmatron. Reproduced from [40], with permission from the Royal Society of Chemistry.

1.3.2.3 Other discharge types

In addition to the two most commonly studied plasma discharge types above, there are several other plasma types that can be applied for dry reforming, including microwave discharge, glow discharge, corona discharge, spark discharge, etc.. A microwave discharge is also a kind of warm plasma. It has no electrodes, instead energy is dissipated into the gas in the form of electromagnetic waves. The electromagnetic waves have frequencies from 300 MHz to 10 GHz and can be supplied in pulsed or continuous mode. The plasma can absorb up to 90% of the energy provided by electromagnetic waves. Various forms of microwave discharges, including surface wave discharges, cavity induced discharges, freely expanding atmospheric plasma discharge torches and electron cyclotron resonance plasmas, have been studied for medicine, material synthesis, pollution treatment and CO_2 conversion [90]. Like gliding arc discharge as warm plasma, microwave discharge also has a relatively high energy yield in CO_2 conversion [91-93]. However, it can be rather complex and the rather high installation cost may hinder its extensive application [80,90].

A glow discharge is a discharge generated between two electrode plates without a dielectric barrier. It can operate under low pressure (0.1–10 mbar) but also atmospheric pressure. In a low-pressure rarefied gas, the charged particles have a longer mean free path and thus can obtain higher energies in an electric field. Different from the non-uniform filamentary discharge in the DBD, the glow discharge is a rather uniform discharge (although it consists of various spatial regions). However, the low pressure is a shortcoming for its application to CO_2 conversion. Achieving glow discharge at atmospheric pressure is an important research direction. In some studies, atmospheric pressure glow discharge (APGD) has been successfully applied to dry reforming to produce syngas [94-98].

If a reactor is with a large distance between the electrodes, sustaining a discharge is generally not easy. And if the electrode is sharp (with a small radius of curvature), a strong local electric field is created that causes the gas to be excited and ionized, producing a corona discharge. Corona discharge is a non-uniform discharge like DBD but without a dielectric barrier, and it is a typical filamentary discharge. Many plasma streamers extend from the electrode tip into the surrounding gas and eventually extinguish. Corona discharges are sometimes called single-electrode discharges because the plasma streamer cannot reach the other electrode. This is needed, or if the two electrodes would connect by a conductive path, a spark or arc would form instead of a corona discharge. Therefore, corona discharges are often in a pulsed mode to suppress the transition from streamer to spark. Due to the large discharge gap, corona discharge is suitable for processing large quantities of gas in large-scale applications. The discharge device is relatively simple, easy to set up and at low cost [99]. The application of corona discharge in dry reforming has been studied [99-102]. If the discharge streamer is gradually extended to connect the another electrode, it is transformed into a spark discharge. Different from arc discharge, spark discharge is limited by the supplied power and cannot maintain a stable arc, but it extinguishes within hundreds of microseconds. A complete spark discharge is a cycle of spark formation and extinction. Lightning in nature is a typical spark discharge.

Table 1.1 shows some of the reported performance of dry reforming in different types of plasma reactors [80]. The energy yield (EY) in the table is calculated by dividing the total CH_4 and CO_2 converted by the energy:

$$\mathrm{EY}\left(\frac{\mathrm{mmol}}{\mathrm{kJ}}\right) = \frac{n_{CH_4} \cdot X_{CH_4} + n_{CO_2} \cdot X_{CO_2}}{Pt} \cdot 1000\ \left(\frac{\mathrm{Ws}}{\mathrm{kJ}}\right) \tag{8}$$

where n is the milimoles of feed gas, X is the conversion, P is the power (in W), and t is the discharge time (in s). The energy yield and the conversion of CO_2 and CH_4 shown in the table can reflect the performance of the reactor. Both values are an important part to evaluate the economic and industrial feasibility of the plasma based process. As can be envisioned and observed from the data in the table, they are related. Increasing the input power or decreasing the flow rate can increase the conversion of CO_2 and CH_4, but lead to a lower energy yield, and conversely, reducing the input power to obtain higher energy yield leads to lower conversion. Although also other operating conditions or reactor configurations can have an influence, as can be observed from the first two lines in the table where a higher plasma power does not lead to higher conversion. Since various factors, such as space time, feed gas ratio, input power, etc. are different in different papers, as shown in the table, this makes it challenging to compare dry reforming performance within a certain type of plasma technology. Moreover, also differences in the type of plasma technology, causes significant differences, e.g. due to a changes in discharge behavior, temperature in the plasma, the amount of gas flowing through the plasma etc.. For this reason, literature data on plasma technology, even when the same plasma technology is applied, cannot be directly compared, and the comparison of a single conversion or energy yield is meaningless. However, from the table we can get at least an impression that the performance of a DBD reactor is generally lower than that of other plasma reactors. When comparing with other plasma reactors with similar conversions, such as DBD reactors in row 1 and 5 compared with microwave discharge reactors in row 11 and 12, and corona discharge reactors in row 20, the energy yield of the DBD reactor is lower than that of them. While when the energy yield is similar with that of other reactors, the conversion in a DBD reactor is much lower (e.g. compare the DBD reactor in row 6 with the spark discharge reactor in row 25), although there are exceptions.

Table 1.1. Comparison of dry reforming conversion achieved with various non-thermal plasmas.

	Reactor	Power supply	Frequency (Hz)	Plasma Power (W)	CH_4/CO_2	Total flow rate (mL/min)	Conversion (%)		Energy yield (mmol/kJ)	Reference
							CH_4	CO_2		
1	Dielectric barrier discharge	AC	7800	140	1.00	20.0	74	68	0.09	[103]
2		AC	7500	125.6	1.05	18.8	80	84	0.13	[104]
3		AC	3000	30	1.00	50.0	21	17	0.24	[105]
4		AC	3000	45	1.00	50.0	33	22	0.21	[106]
5		AC	7500	100	1.00	20.0	74	73.5	0.12	[107]
6		AC	50	2.1	1.00	30.0	12	5	1.00	[108]
7		AC	23500	100	1.00	50.0	33	23	0.09	[109]
8	Gliding arc	DC		500	0.33	10000	10	18	4.08	[110]
9		AC	50	520.7	0.50	12700	42	37	7.01	[111]
10		AC	50	95	0.43	5000	10	7	3.03	[112]
11	Microwave discharge	AC	2.45×10^7	60	1.50	200.0	71	69	1.74	[113]
12		AC	2.45×10^7	120	1.50	200.0	72	68	0.87	[90]
13	Atmospheric-pressure glow discharge	DC		104	0.54	500	66	86	2.63	[97]
14		AC	50	495	0.67	500	67	54	0.45	[114]
15		AC	4000	23	1.00	120	61	50	2.15	[95]
16		AC	50	66.7	0.67	4000	15	10	5.22	[96]
17	Corona discharge	DC	88	42	0.50	25.0	66	52	0.25	[115]
18		AC	1000	46.3	1.00	43.0	62	48	0.38	[116]
19		DC		63	0.50	63.0	94	78	0.62	[100]
20		AC	20000	45	0.50	60.0	75	60	0.64	[101]
21		DC		21	1.00	180.0	33	23	1.79	[102]
22		DC		10	0.50	100.0	66	44	3.82	[99]
23	Spark discharge	AC	5000	45	0.67	150	65	55	1.46	[117]
24		AC	4800	1344	1.50	150	75	70	0.06	[118]
25		DC		20	1.00	50.0	78	73	1.41	[119]

1.3.3 Combination of catalysis and plasma on DRM

In conventional thermal dry reforming, catalysts are always necessary to save energy by reducing the high activation energies for the conversion of CH_4 and CO_2. Furthermore, although theoretically the catalyst cannot change the equilibrium of the reaction, the catalyst can help the reaction to proceed faster, and a higher conversion therefore can be obtained within the same space time. Different catalyst components can also improve the selectivity of the corresponding products. For the application of plasma technology in dry reforming, although it is promising, the conversion, energy yield and selectivity still needs to be improved. This is especially true for the selectivity, because the product of plasma dry reforming is a complex mixture due to the presence of various reactive species in the plasma. Combining catalysts with plasma technology may be of great help in solving these problems and perfecting the application of plasma technology in DRM. The interaction of plasma and catalyst, and their possible synergistic effects, have been discussed in many studies [120-122]. How the plasma is combined with the catalyst is critical. Besides placing the catalyst in a plasma reactor to improve the performance of the reaction, the catalyst can also be pre-treated by plasma.

1.3.3.1 Pre-treatment of catalysts by non-thermal plasma

In some studies, the activity of the catalysts could be further enhanced by pre-treatment (heat treatment, ultrasound, etc.) before its application. Non-thermal plasma techniques can also be applied here. The catalytic performance is enhanced by the inelastic collision of kinetically energized particles in the plasma, including electrons, ions, radicals, and atoms, with the catalysts [123-125]. In different gas composition and discharge parameters, the catalysts could be oxidized, reduced, lattice reorganized, etc. in the plasma [126-129]. For example, before the use of dry reforming catalysts, the metal oxides on the prepared catalyst are usually reduced to metal active sites with low oxidation state to enhance dry reforming activity. This process can now be completed in H_2 plasma to replace traditional thermal reduction. Wu et al. pretreated Ni/γ–Al_2O_3 catalyst by H_2 plasma in a DBD reactor to reduce NiO/Ni^{2+} phase to Ni^0 [129].

The catalyst after plasma pre-treatment has better dispersion, which is beneficial to improve the performance of the catalyst. The reason of the improved dispersion was claimed to be electrons with high energy in non-thermal plasmas transferred energy to the catalyst metal clusters through inelastic collisions, and the local high temperatures on the metal clusters could induce them to re-agglomeration, producing smaller metal clusters [130,131]. Rahemi et al.[132] reported that the crystallite size of Ni on Ni/Al_2O_3 –ZrO_2 catalysts decreased from 35.5 nm to 18.5 nm after glow discharge treatment. In addition, some catalysts generate more oxygen vacancies after the metal sites were reduced [133,134]. The pore structure and size of the catalysts could also be altered by the plasma pretreatment due to collisions of energetic electrons with metals and supports. In the study of Shang et al., the mean pore size of the Ni/γ-Al_2O_3 catalyst was reduced from 9.8 nm to 6.9 nm by plasma treatment [135].

1.3.3.2 Hybrid plasma-catalysis reactor

There are two types of catalyst configurations that combine catalyst with plasma during the DRM process in the reactor, i.e., in-plasma catalysis (IPC) and post-plasma catalysis (PPC), which is based on placing catalyst in the discharge region and behind the discharge region, respectively. Figure 1.23 illustrates the two types of catalyst configurations. In a PPC configuration, the feed gases first react in the plasma and then pass through the catalyst bed. The catalysts can contact and interact only with stable molecules and long-lived active species generated from the plasma, and utilize the waste heat of the plasma, while most of the short-lived active species cannot reach the catalyst bed [136]. The lifetimes of vibrationally and electronically excited active species are only about 1–100 ns, while the lifetimes of ions and some radicals can reach 100 μs or even 1 s [137-139]. Sometimes the catalyst bed is heated to provide additional energy. In the IPC configuration, the species (including free radicals, photons, ions, electrons, etc.) in the non-thermal plasma can directly interact with the catalyst surface during the reaction process, which may be more helpful to improve the conversion of the DRM and the selectivity of specific products. The packing of the catalyst can affect the characteristics of the plasma and the species distribution, and the plasma can also affect the catalyst. Their interactions and effects are complex and interesting, and may be positive or negative for the progress of DRM. This IPC configuration is the most widely studied combination of catalyst and plasma, however, it is generally only suitable for DBD reactors. Other types of plasma reactors are less straightforward for applying IPC configurations either because of complex geometries or higher gas temperatures. This is also one of the reasons that DBD reactors are the most studied in dry reforming.

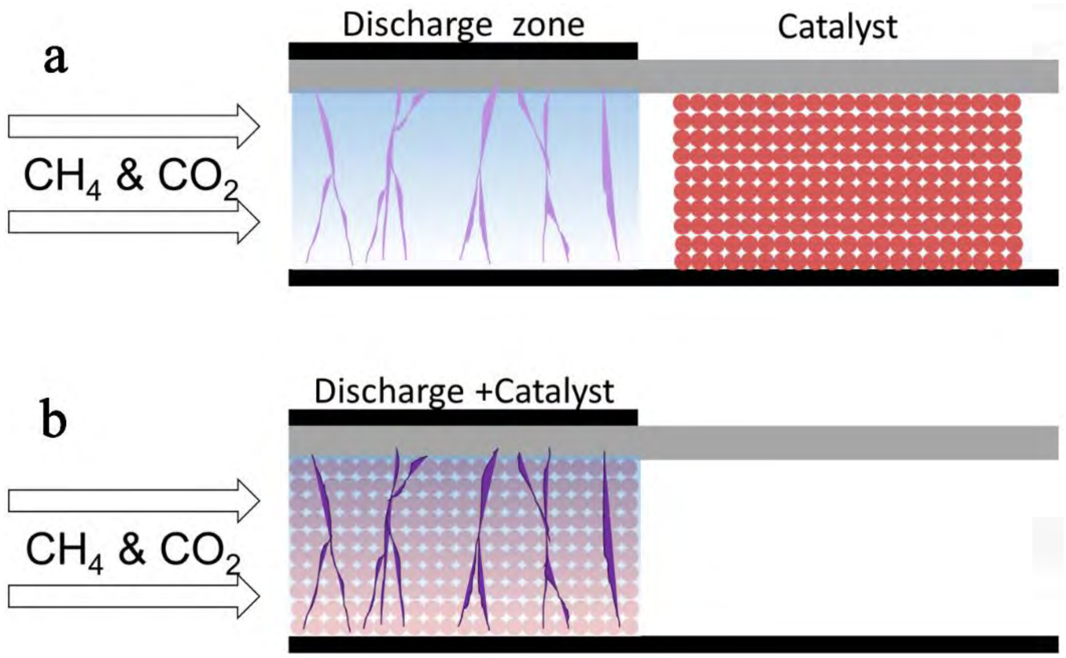

Figure 1.23. Schematic of the plasma-catalysis configurations: (a) Post-plasma catalysis (PPC); (b) In-plasma catalysis (IPC).

The plasma-catalyst interaction (mainly studied is the IPC configuration in the DBD reactor) can be divided into two categories, the influence of plasma on catalyst and the influence of catalyst on plasma. First, plasmas may alter the structure of catalysts, including structure of active metals and pores, through particle bombardment and thermal effects, as described above in the section of catalysts pre-treatment by plasma [140]. Plasma can make the catalyst have higher active metal dispersion, more adsorption sites and larger specific surface area, and thus have better adsorption and conversion performance for CO_2 and CH_4 [141]. Second, the energy transfer from the plasma to the catalyst can create hot spots on the catalyst surface, and the local electron temperatures can alter the crystal lattice of the catalyst. Both the lattice change and the plasma-induced valence state change of the active metals can lead to better oxygen affinity, which is important for improving CH_4 conversion and reducing carbon deposition in dry reforming [133,134,142]. Moreover, the adsorption of species in the plasma on the catalyst surface may change the reaction path of dry reforming, thereby affecting the conversion and selectivity. For example, the H atoms adsorbed on the surface of Ni-based catalysts was expected to promot the formation of methanol [143]. In addition, due to the semiconducting properties of some catalysts and supports, the photons generated by the radiative relaxation of excited species in plasmas might activate photocatalytic mechanism [144,145]. The packing of the catalyst also affects the discharge characteristics of the plasma, mainly causing physical effects. First, both the pores of the catalyst and the gaps between the catalyst particles are much smaller than the original discharge gap in the reactor, so the packing of the catalyst is bound to affect the micro-discharge paths and change their distribution. Second, the discharge mode is changed. The filamentary discharge in the DBD reactor may be partially transformed into surface discharge on the catalyst [146,147]. Moreover, the polarization of the catalyst particles provide an enhanced electric field, near the contact points between the particles, and subsequently produces electrons with higher temperature. The larger the dielectric constant of materials, the greater the produced electric field enhancement [146,148-150]. In addition, some active species may have longer residence time in the reaction zone due to adsorption on the packing/catalyst material.

In existing studies, metals were often used as active components of catalysts and were loaded on porous supports. As shown in Table 1.2, Pt, Au, Ag, Cu, Ni, etc. are typical active components of dry reforming catalysis, and the commonly used supports are mostly oxide materials, such as Al_2O_3, ZrO_2 and SiO_2. Noble metals such as Pt and Au usually have higher catalytic activity, but considering the cost of these catalysts and their presence on the critical raw material list, transition metals such as Cu and Ni are more promising research targets [106,108,151]. Packing the reactor with non-catalytically active materials such as SiO_2 can also change the performance of the plasma process, due to the complex interaction of the catalyst/packing with the plasma, as described above, such as the electric field enhancement caused by polarization of dielectric packings or supports in an electric field.

However, in the majority of dry reforming studies using undiluted feed gases and fully packed fixed beds (with packing materials or catalysts) in the discharge zone, the conversion of CH_4 and CO_2 was lower than in the empty reactor at the same flow rate and discharge power [73,108,152-154]. Table 1.2 shows a comparison of the conversion of CO_2 and CH_4 in empty and fully packed in-plasma catalysis (IPC) reactor configurations, obtained from literature, at the same gas flow rates. Although the conversions of CH_4 and CO_2 vary in different papers depending on the operating conditions, a common feature is that the performance of fully packed IPC reactors with packing/catalyst was not improved, and even more often decreased, compared to empty reactors. In some literature, the packing/catalyst could show a performance improvement for dry reforming by reducing the gas flow rate in fully packed IPC reactors to keep the same space time as the empty reactors [109,155]. However, the specific energy input (SEI), which is the ratio of input power to gas flow rate, was increased. The gas molecules thus obtained more energy input, and their conversion did not increase proportionally, and as a result, the energy yield was thus reduced.

Table 1.2. Comparison of conversion of CO_2 and CH_4 in empty and fully packed IPC DBD reactors at the same flow rate in literature of plasma-based dry reforming.

Performance of empty reactor		Performance of packed reactor			Reference
CO_2 conversion (%)	CH_4 conversion (%)	Packing/Catalyst	CO_2 conversion (%)	CH_4 conversion (%)	
22	33	γ-Al_2O_3	22	27	[106]
		Ag/γ-Al_2O_3	22	27	
		Pt/γ-Al_2O_3	22	33	
		Cu/γ-Al_2O_3	16	33	
15	18	γ-Al_2O_3	12	15	[151]
		Cu/γ-Al_2O_3	8	16	
		Au/γ-Al_2O_3	15	16	
		Pt/γ-Al_2O_3	13	17	
6	2	Ni-Mn/γ-Al_2O_3	2	4	[108]
20	37	ZrO_2	12	27	[109]
		SiO_2	18	22	
		α-Al_2O_3	22	33	
		$BaTiO_3$	20	13	
8	23	Quartz Wool	3	24	[156]
		γ-Al_2O_3	3	8	
		Zeolite 3A	2	3	

The reason for the unsatisfactory effect of catalysts and packing materials is that, although a lot of experimental or simulation studies have reported the interaction of packing materials with plasma and their effect on dry reforming, there are still many unknowns, including how the interplay and coinciding presence of different physical and chemical phenomena compensate or reinforce each other. The materials commonly used in the experimental studies are catalysts developed for thermal dry reforming, which may not be suitable for plasma-catalytic processes, due to the more complex nature of plasmas than heated gases. For example, when discussed on a relatively small scale, unlike the relatively weak forces between gas molecules in thermal catalysis, the electrostatic forces between charged particles in a plasma cause them to have a strong influence on each other, thereby affecting their propagation. On the other hand, on a larger scale, the plasma can be regarded as an electrically neutral fluid, because of the electric field screening effect in the plasma. This important parameter, reflecting the scale of charge interaction in the plasma, is the Debye length, which depends on the electron density and electron temperature in the plasma. This property will greatly affect the mass transfer in the plasma-based process. As reported in the literature [157-160], the plasma can only be generated or penetrated into pores larger than its Debye length, which is several hundreds of nanometers in typical plasma-catalytic conditions. However, porous materials used as catalyst supports in existing plasma catalysis studies usually only have micropores (< 2nm) or mesopores smaller than 10 nm, which are much smaller than the pore size in which the plasma would be able to propagate.

In addition, the effect of the packing material on the discharge, such as the polarization of the dielectric, the change of the discharge mode, etc., is also greatly affected by the particle size [76,109,161,162]. However, the particle size of the powder used in many studies was not controlled, hence is was not uniform and might not be suitable for the plasma process. Materials with unsuitable particle sizes can obstruct the discharge path and reduce the discharge volume, resulting in a reduction in the space-time of the gas.

There are too many differences in structure and properties between different catalysts/packings, which makes it challenging to find a clear relationship between material properties and dry reforming performance through the comparison of existing studies. For example, comparing the performance of zeolite and γ–Al_2O_3, it is difficult to find out which factors are important for the plasma-based processes. Although there have been some simulations to study the effect of pore size on plasma propagation inside pores, its effect may not be the same in experiments, and there is no relevant experimental study yet, especially in such a large pore size range (from commonly used micropores, mesopores to pores of micrometers or hundreds of nanometers close to the plasma Debye length). For the effect of particle size, the existing studies in literature were all in the millimeter range, which is relatively large for the gap dimensions (which are typically also in the millimeter range) of a common DBD reactor. Their positive effect on the discharge behavior, such as turning a filamentary discharges into surface discharges, may be small. In addition, in order to improve the discharge, not only the packing material can be studied, but also the design of the DBD reactor itself can be modified. In this PhD thesis, we will more systematically study the material properties and reactor structure affecting the performance of plasma dry reforming process in DBD reactors, to learn more about their specific impact with the purpose to provide insights how to improve the conversion and energy yield of plasma-based dry reforming.

1.4 Aim of this PhD work

The plasma-catalytic dry reforming in a DBD reactor is promising in chemical production. However, the reported studies of plasma-catalytic dry reforming in a DBD reactor normally use catalysts similar or the same as those for thermal processes instead of special catalysts for the plasma-based processes. This causes a series of problems, e.g. even lower performance of catalyst packed IPC reactions than in an empty reactor was observed at the same conditions (flow rate and discharge power). Due to the lack of customized catalysts, a systematic theory of the correlation of catalyst and the reaction performance has not been established, i.e. the relation of catalyst structure and property with the plasma-catalytic dry reforming performance is not clear, hampering the development of the dry reforming in a DBD reactor. Therefore, an in-depth study is required to correlate the catalyst structure and properties with the dry reforming performance in a DBD reactor. Apart from the problems of many unknowns related to the optimal catalyst, studies on the DBD reactor design are also still in their infancy. There is a lot of room for improvement in optimizing the reactor to improve the catalytic efficiency.

Based on the unknown impact of structure and properties of the catalysts, as well as the unknown impact of the reactor (design) on plasma catalysis, the aim of this PhD work is as follows: In this thesis, we investigated the plasma-catalytic dry reforming in a DBD reactor with an in-plasma catalysis (IPC) configuration. We developed a controllable synthesis of the morphology and structure of the silica packing material and porous catalysts template and applied these well-structured catalysts to the dry reforming tests in a DBD reactor. In addition, we designed and changed the DBD reactor to optimize the dry reforming performance. Hence, we first investigated a new process to synthesize uniform silica spheres without the use of organic solvents that could be used as catalyst supports or templates for plasma-catalytic DRM in Chapter 2. In Chapter 3, Cu and CuO catalysts with different pore sizes, crossing several orders of magnitude, were synthesized using the silica spheres synthesized by the new process in Chapter 2 as a template. These catalysts had uniform pore sizes (between ~2 nm and ~ 2000 nm nm) and the same structure. The use of these catalysts revealed the apparent effect of catalyst pore sizes on the plasma reaction. In Chapter 4, the plasma dry reforming performance of packing and catalysts associated with different particle sizes was investigated. Finally, Chapter 5 investigates the design of the reactor, i.e. we made some changes to the DBD reactor to study the effect of a non-uniform discharge gap and electric field caused by adding metal rings to the reactor, on the performance of plasma-based dry reforming. A summary of this work and an outlook for the future are also provided at the end of this PhD thesis.

1.5 References

[1] Huang, J.; Li, Y.; Fu, C.; Chen, F.; Fu, Q.; Dai, A.; Shinoda, M.; Ma, Z.; Guo, W.; Li, Z.; Zhang, L.; Liu, Y.; Yu, H.; He, Y.; Xie, Y.; Guan, X.; Ji, M.; Lin, L.; Wang, S.; Yan, H.; Wang, G. Dryland climate change: Recent progress and challenges. *Reviews of Geophysics* **2017**, *55*, 719-778.

[2] Huang, J.; Ji, M.; Xie, Y.; Wang, S.; He, Y.; Ran, J. Global semi-arid climate change over last 60 years. *Climate Dynamics* **2016**, *46*, 1131-1150.

[3] Dyurgerov Mark, B.; Meier Mark, F. Twentieth century climate change: Evidence from small glaciers. *Proceedings of the National Academy of Sciences* **2000**, *97*, 1406-1411.

[4] Kwadijk, J. C. J.; Haasnoot, M.; Mulder, J. P. M.; Hoogvliet, M. M. C.; Jeuken, A. B. M.; van der Krogt, R. A. A.; van Oostrom, N. G. C.; Schelfhout, H. A.; van Velzen, E. H.; van Waveren, H.; de Wit, M. J. M. Using adaptation tipping points to prepare for climate change and sea level rise: a case study in the Netherlands. *WIREs Climate Change* **2010**, *1*, 729-740.

[5] Coumou, D.; Rahmstorf, S. A decade of weather extremes. *Nature Climate Change* **2012**, *2*, 491-496.

[6] Mitchell, J. F. B. The “Greenhouse” effect and climate change. *Reviews of Geophysics* **1989**, *27*, 115-139.

[7] Manabe, S. Role of greenhouse gas in climate change. *Tellus A: Dynamic Meteorology and Oceanography* **2019**, *71*, 1620078.

[8] Sesana, E.; Gagnon, A. S.; Ciantelli, C.; Cassar, J.; Hughes, J. J. Climate change impacts on cultural heritage: A literature review. *WIREs Climate Change* **2021**, *12*, e710.

[9] De Frenne, P.; Lenoir, J.; Luoto, M.; Scheffers, B. R.; Zellweger, F.; Aalto, J.; Ashcroft, M. B.; Christiansen, D. M.; Decocq, G.; De Pauw, K.; Govaert, S.; Greiser, C.; Gril, E.; Hampe, A.; Jucker, T.; Klinges, D. H.; Koelemeijer, I. A.; Lembrechts, J. J.; Marrec, R.; Meeussen, C.; Ogée, J.; Tyystjärvi, V.; Vangansbeke, P.; Hylander, K. Forest microclimates and climate change: Importance, drivers and future research agenda. *Global Change Biology* **2021**, *27*, 2279-2297.

[10] Raupach, T. H.; Martius, O.; Allen, J. T.; Kunz, M.; Lasher-Trapp, S.; Mohr, S.; Rasmussen, K. L.; Trapp, R. J.; Zhang, Q. The effects of climate change on hailstorms. *Nature Reviews Earth & Environment* **2021**, *2*, 213-226.

[11] Ortiz-Bobea, A.; Ault, T. R.; Carrillo, C. M.; Chambers, R. G.; Lobell, D. B. Anthropogenic climate change has slowed global agricultural productivity growth. *Nature Climate Change* **2021**, *11*, 306-312.

[12] Zillman, J. W. A history of climate activities. *World Meteorological Organization (WMO) Bulletin* **2009**, *58*, 141.

[13] Masson-Delmotte, V.; Zhai, P.; Pirani, A.; Connors, S. L.; Péan, C.; Berger, S.; Caud, N.; Chen, Y.; Goldfarb, L.; Gomis, M. Climate change 2021: the physical science basis. *Contribution of working group I to the sixth assessment report of the intergovernmental panel on climate change* **2021**, 2.

[14] Ritchie, H.; Roser, M.; Rosado, P. CO_2 and greenhouse gas emissions. *Our world in data* **2020**.

[15] Lamb, W. F.; Wiedmann, T.; Pongratz, J.; Andrew, R.; Crippa, M.; Olivier, J. G. J.; Wiedenhofer, D.; Mattioli, G.; Khourdajie, A. A.; House, J.; Pachauri, S.; Figueroa, M.; Saheb, Y.; Slade, R.; Hubacek, K.; Sun, L.; Ribeiro, S. K.; Khennas, S.; de la Rue du Can, S.; Chapungu, L.; Davis, S. J.; Bashmakov, I.; Dai, H.; Dhakal, S.; Tan, X.; Geng, Y.; Gu, B.; Minx, J. A review of trends and drivers of greenhouse gas emissions by sector from 1990 to 2018. *Environmental Research Letters* **2021**, *16*, 073005.

[16] Rahman, S. M.; Al-Ismail, F. S. M.; Haque, M. E.; Shafiullah, M.; Islam, M. R.; Chowdhury, M. T.; Alam, M. S.; Razzak, S. A.; Ali, A.; Khan, Z. A. Electricity Generation in Saudi Arabia: Tracing Opportunities and Challenges to Reducing Greenhouse Gas Emissions. *IEEE Access* **2021**, *9*, 116163-116182.

[17] Chao, J. T.-H.; Cahill, A. G.; Van De Ven, C. J. C.; Beckie, R. D. Fate of Fugitive Natural Gas in Heterogeneous Near-Surface Sediments in a Region of Extensive Petroleum Resource Development. *Geophysical Research Letters* **2021**, *48*, e2021GL095200.

[18] Agreement, P. Paris agreement. In *Report of the Conference of the Parties to the United Nations Framework Convention on Climate Change (21st Session, 2015: Paris). Retrived December*; HeinOnline, 2015; pp 2017.

[19] Curry-Lindahl, K. United Nations Environment Programme. In *EARTHCARE: Global Protection of Natural Areas*. Routledge, 2019; pp 740-753.

[20] Saito, S. Role of nuclear energy to a future society of shortage of energy resources and global warming. *J. Nucl. Mater.* **2010**, *398*, 1-9.

[21] Carmen, S. Microbial capability for the degradation of chemical additives present in petroleum-based plastic products: A review on current status and perspectives. *J. Hazard. Mater.* **2021**, *402*, 123534.

[22] Hirsch, R. L. Mitigation of maximum world oil production: Shortage scenarios. *Energy Policy* **2008**, *36*, 881-889.

[23] Kjärstad, J.; Johnsson, F. Resources and future supply of oil. *Energy Policy* **2009**, *37*, 441-464.

[24] Worldometers Oil Left in the World. Worldometers Yorkville, IL, 2022.

[25] Maugeri, L. Oil: Never Cry Wolf--Why the Petroleum Age Is Far from over. *Science* **2004**, *304*, 1114-1115.

[26] Watkins, G. C. Oil scarcity: What have the past three decades revealed? *Energy Policy* **2006**, *34*, 508-514.

[27] Ritchie, H.; Roser, M.; Rosado, P. Renewable Energy. *Our World in Data* **2020**.

[28] IRENA Renewable Power Generation Costs in 2020. *International Renewable Energy Agency* **2021**.

[29] Delucchi, M. A.; Jacobson, M. Z. Meeting the world's energy needs entirely with wind, water, and solar power. *Bulletin of the Atomic Scientists* **2013**, *69*, 30-40.

[30] Pehl, M.; Arvesen, A.; Humpenöder, F.; Popp, A.; Hertwich, E. G.; Luderer, G. Understanding future emissions from low-carbon power systems by integration of life-cycle assessment and integrated energy modelling. *Nat. Energy* **2017**, *2*, 939-945.

[31] Rowe, D.; Sayeef, S.; Platt, G. Chapter 7 - Intermittency: It's the Short-Term That Matters. In *Future of Utilities Utilities of the Future*. F. P. Sioshansi, Ed.; Academic Press; Boston, 2016; pp 129-150.

[32] Heide, D.; von Bremen, L.; Greiner, M.; Hoffmann, C.; Speckmann, M.; Bofinger, S. Seasonal optimal mix of wind and solar power in a future, highly renewable Europe. *Renewable Energy* **2010**, *35*, 2483-2489.

[33] Lazar, J. *Teaching the" duck" to Fly*; Regulatory Assistance Project Montpelier VT, 2016.

[34] Moriarty, P.; Honnery, D. What is the global potential for renewable energy? *Renewable and Sustainable Energy Reviews* **2012**, *16*, 244-252.

[35] Boot-Handford, M. E.; Abanades, J. C.; Anthony, E. J.; Blunt, M. J.; Brandani, S.; Mac Dowell, N.; Fernández, J. R.; Ferrari, M.-C.; Gross, R.; Hallett, J. P. Carbon capture and storage update. *Energy & Environmental Science* **2014**, *7*, 130-189.

[36] Gibbins, J.; Chalmers, H. Carbon capture and storage. *Energy Policy* **2008**, *36*, 4317-4322.

[37] Yu, K. M. K.; Curcic, I.; Gabriel, J.; Tsang, S. C. E. Recent Advances in CO_2 Capture and Utilization. *ChemSusChem* **2008**, *1*, 893-899.

[38] Saito, M.; Kimura, H.; Mimura, N.; Wu, J.; Murata, K. Dehydrogenation of ethylbenzene in the presence of CO_2 over an alumina-supported iron oxide catalyst. *Appl. Catal. A: Gen.* **2003**, *239*, 71-77.

[39] Aresta, M.; Dibenedetto, A.; Nocito, F.; Pastore, C. A study on the carboxylation of glycerol to glycerol carbonate with carbon dioxide: The role of the catalyst, solvent and reaction conditions. *J. Mol. Catal. A: Chem.* **2006**, *257*, 149-153.

[40] Snoeckx, R.; Bogaerts, A. Plasma technology – a novel solution for CO_2 conversion? *Chem. Soc. Rev.* **2017**, *46*, 5805-5863.

[41] Furler, P.; Scheffe, J.; Gorbar, M.; Moes, L.; Vogt, U.; Steinfeld, A. Solar Thermochemical CO_2 Splitting Utilizing a Reticulated Porous Ceria Redox System. *Energy & Fuels* **2012**, *26*, 7051-7059.

[42] Berthelot, A.; Bogaerts, A. Modeling of CO_2 Splitting in a Microwave Plasma: How to Improve the Conversion and Energy Efficiency. *J. Phys. Chem. C* **2017**, *121*, 8236-8251.

[43] Aziz, M. A. A.; Jalil, A. A.; Triwahyono, S.; Ahmad, A. CO_2 methanation over heterogeneous catalysts: recent progress and future prospects. *Green Chemistry* **2015**, *17*, 2647-2663.

[44] Fischer, M.; Werber, M.; Schwartz, P. V. Batteries: Higher energy density than gasoline? *Energy Policy* **2009**, *37*, 2639-2641.

[45] Saeidi, S.; Najari, S.; Hessel, V.; Wilson, K.; Keil, F. J.; Concepción, P.; Suib, S. L.; Rodrigues, A. E. Recent advances in CO_2 hydrogenation to value-added products — Current challenges and future directions. *Prog. Energy Combust. Sci.* **2021**, *85*, 100905.

[46] Yusuf, R. O.; Noor, Z. Z.; Abba, A. H.; Hassan, M. A. A.; Din, M. F. M. Methane emission by sectors: A comprehensive review of emission sources and mitigation methods. *Renewable and Sustainable Energy Reviews* **2012**, *16*, 5059-5070.

[47] Aebiom, A. biogas road map for Europe. *European Biomass Association* **2009**.

[48] Coffey, M. Energy and power generation: Maximising biogas yields from sludge. *Filtration & Separation* **2009**, *46*, 12-15.

[49] Montzka, S. A.; Dlugokencky, E. J.; Butler, J. H. Non-CO_2 greenhouse gases and climate change. *Nature* **2011**, *476*, 43-50.

[50] Rasi, S. *Biogas composition and upgrading to biomethane*; University of Jyväskylä, 2009.

[51] Li, K.; Peng, B.; Peng, T. Recent Advances in Heterogeneous Photocatalytic CO_2 Conversion to Solar Fuels. *ACS Catalysis* **2016**, *6*, 7485-7527.

[52] Roy, S. C.; Varghese, O. K.; Paulose, M.; Grimes, C. A. Toward Solar Fuels: Photocatalytic Conversion of Carbon Dioxide to Hydrocarbons. *ACS Nano* **2010**, *4*, 1259-1278.

[53] Yadav, D.; Banerjee, R. A review of solar thermochemical processes. *Renewable and Sustainable Energy Reviews* **2016**, *54*, 497-532.

[54] Pullar, R. C.; Novais, R. M.; Caetano, A. P. F.; Barreiros, M. A.; Abanades, S.; Oliveira, F. A. C. A Review of Solar Thermochemical CO_2 Splitting Using Ceria-Based Ceramics With Designed Morphologies and Microstructures. *Frontiers in Chemistry* **2019**, *7*.

[55] Brennan, L.; Owende, P. Biofuels from microalgae—A review of technologies for production, processing, and extractions of biofuels and co-products. *Renewable and Sustainable Energy Reviews* **2010**, *14*, 557-577.

[56] Razzak, S. A.; Ali, S. A. M.; Hossain, M. M.; deLasa, H. Biological CO_2 fixation with production of microalgae in wastewater – A review. *Renewable and Sustainable Energy Reviews* **2017**, *76*, 379-390.

[57] Luo, W.; Zhang, Q.; Zhang, J.; Moioli, E.; Zhao, K.; Züttel, A. Electrochemical reconstruction of ZnO for selective reduction of CO_2 to CO. *Appl. Catal. B Environ.* **2020**, *273*, 119060.

[58] Qiao, J.; Liu, Y.; Hong, F.; Zhang, J. A review of catalysts for the electroreduction of carbon dioxide to produce low-carbon fuels. *Chem. Soc. Rev.* **2014**, *43*, 631-675.

[59] Tonks, L. The Birth of ``Plasma". *American Journal of Physics* **1967**, *35*, 857-858.

[60] Witze, A. Is lightning striking the Arctic more than ever before? *Nature* **2021**, *589*, 11-12.

[61] Tape, C.; Ringler, A. T.; Hampton, D. L. Recording the Aurora at Seismometers across Alaska. *Seismological Research Letters* **2020**, *91*, 3039-3053.

[62] Bogaerts, A.; Neyts, E.; Gijbels, R.; van der Mullen, J. Gas discharge plasmas and their applications. *Spectrochimica Acta Part B: Atomic Spectroscopy* **2002**, *57*, 609-658.

[63] Mirpour, S.; Fathollah, S.; Mansouri, P.; Larijani, B.; Ghoranneviss, M.; Mohajeri Tehrani, M.; Amini, M. R. Cold atmospheric plasma as an effective method to treat diabetic foot ulcers: A randomized clinical trial. *Scientific Reports* **2020**, *10*, 10440.

[64] Liu, Z. M.; Cui, S.; Luo, Z.; Zhang, C.; Wang, Z.; Zhang, Y. Plasma arc welding: Process variants and its recent developments of sensing, controlling and modeling. *Journal of Manufacturing Processes* **2016**, *23*, 315-327.

[65] Gomez, E.; Rani, D. A.; Cheeseman, C. R.; Deegan, D.; Wise, M.; Boccaccini, A. R. Thermal plasma technology for the treatment of wastes: A critical review. *J. Hazard. Mater.* **2009**, *161*, 614-626.

[66] Judée, F.; Simon, S.; Bailly, C.; Dufour, T. Plasma-activation of tap water using DBD for agronomy applications: Identification and quantification of long lifetime chemical species and production/consumption mechanisms. *Water Res.* **2018**, *133*, 47-59.

[67] Zhu, X.; Liu, S.; Cai, Y.; Gao, X.; Zhou, J.; Zheng, C.; Tu, X. Post-plasma catalytic removal of methanol over Mn–Ce catalysts in an atmospheric dielectric barrier discharge. *Appl. Catal. B Environ.* **2016**, *183*, 124-132.

[68] Wang, Y.; Craven, M.; Yu, X.; Ding, J.; Bryant, P.; Huang, J.; Tu, X. Plasma-Enhanced Catalytic Synthesis of Ammonia over a Ni/Al_2O_3 Catalyst at Near-Room Temperature: Insights into the Importance of the Catalyst Surface on the Reaction Mechanism. *ACS Catalysis* **2019**, *9*, 10780-10793.

[69] Chung, W.-C.; Mei, D.-H.; Tu, X.; Chang, M.-B. Removal of VOCs from gas streams via plasma and catalysis. *Catalysis Reviews* **2019**, *61*, 270-331.

[70] Zhou, L. M.; Xue, B.; Kogelschatz, U.; Eliasson, B. Nonequilibrium Plasma Reforming of Greenhouse Gases to Synthesis Gas. *Energy & Fuels* **1998**, *12*, 1191-1199.

[71] Zou, J.-J.; Zhang, Y.-p.; Liu, C.-J.; Li, Y.; Eliasson, B. Starch-Enhanced Synthesis of Oxygenates from Methane and Carbon Dioxide Using Dielectric-Barrier Discharges. *Plasma Chem. Plasma Process.* **2003**, *23*, 69-82.

[72] Wang, Q.; Yan, B.-H.; Jin, Y.; Cheng, Y. Dry Reforming of Methane in a Dielectric Barrier Discharge Reactor with Ni/Al_2O_3 Catalyst: Interaction of Catalyst and Plasma. *Energy & Fuels* **2009**, *23*, 4196-4201.

[73] Sentek, J.; Krawczyk, K.; Młotek, M.; Kalczewska, M.; Kroker, T.; Kolb, T.; Schenk, A.; Gericke, K.-H.; Schmidt-Szałowski, K. Plasma-catalytic methane conversion with carbon dioxide in dielectric barrier discharges. *Appl. Catal. B Environ.* **2010**, *94*, 19-26.

[74] Pan, K. L.; Chung, W. C.; Chang, M. B. Dry Reforming of CH_4 With CO_2 to Generate Syngas by Combined Plasma Catalysis. *IEEE Trans. Plasma Sci.* **2014**, *42*, 3809-3818.

[75] Chung, W.-C.; Pan, K.-L.; Lee, H.-M.; Chang, M.-B. Dry Reforming of Methane with Dielectric Barrier Discharge and Ferroelectric Packed-Bed Reactors. *Energy & Fuels* **2014**, *28*, 7621-7631.

[76] Uytdenhouwen, Y.; Van Alphen, S.; Michielsen, I.; Meynen, V.; Cool, P.; Bogaerts, A. A packed-bed DBD micro plasma reactor for CO_2 dissociation: Does size matter? *Chem. Eng. J.* **2018**, *348*, 557-568.

[77] Peeters, F. J. J.; van de Sanden, M. C. M. The influence of partial surface discharging on the electrical characterization of DBDs. *Plasma Sources Sci. Technol.* **2014**, *24*, 015016.

[78] Alliati, M.; Mei, D.; Tu, X. Plasma activation of CO_2 in a dielectric barrier discharge: A chemical kinetic model from the microdischarge to the reactor scales. *J. CO2 Utilzation* **2018**, *27*, 308-319.

[79] Bogaerts, A.; Wang, W.; Berthelot, A.; Guerra, V. Modeling plasma-based CO_2 conversion: crucial role of the dissociation cross section. *Plasma Sources Sci. Technol.* **2016**, *25*, 055016.

[80] Chung, W.-C.; Chang, M.-B. Review of catalysis and plasma performance on dry reforming of CH_4 and possible synergistic effects. *Renewable and Sustainable Energy Reviews* **2016**, *62*, 13-31.

[81] Bogaerts, A.; Centi, G. Plasma technology for CO_2 conversion: a personal perspective on prospects and gaps. *Frontiers in Energy Research* **2020**, *8*, 111.

[82] Kogelschatz, U.; Eliasson, B.; Egli, W. From ozone generators to flat television screens: history and future potential of dielectric-barrier discharges. *Pure Appl. Chem.* **1999**, *71*, 1819-1828.

[83] Wang, W.; Mei, D.; Tu, X.; Bogaerts, A. Gliding arc plasma for CO_2 conversion: Better insights by a combined experimental and modelling approach. *Chem. Eng. J.* **2017**, *330*, 11-25.

[84] Kolev, S.; Bogaerts, A. A 2D model for a gliding arc discharge. *Plasma Sources Sci. Technol.* **2014**, *24*, 015025.

[85] Sun, S. R.; Wang, H. X.; Mei, D. H.; Tu, X.; Bogaerts, A. CO_2 conversion in a gliding arc plasma: Performance improvement based on chemical reaction modeling. *J. CO2 Utilzation* **2017**, *17*, 220-234.

[86] Fridman, A.; Nester, S.; Kennedy, L. A.; Saveliev, A.; Mutaf-Yardimci, O. Gliding arc gas discharge. *Prog. Energy Combust. Sci.* **1999**, *25*, 211-231.

[87] Li, L.; Zhang, H.; Li, X.; Kong, X.; Xu, R.; Tay, K.; Tu, X. Plasma-assisted CO_2 conversion in a gliding arc discharge: Improving performance by optimizing the reactor design. *J. CO2 Utilzation* **2019**, *29*, 296-303.

[88] Zhu, F.; Zhang, H.; Yan, X.; Yan, J.; Ni, M.; Li, X.; Tu, X. Plasma-catalytic reforming of CO_2-rich biogas over Ni/γ-Al_2O_3 catalysts in a rotating gliding arc reactor. *Fuel* **2017**, *199*, 430-437.

[89] Zhang, H.; Li, L.; Li, X.; Wang, W.; Yan, J.; Tu, X. Warm plasma activation of CO_2 in a rotating gliding arc discharge reactor. *J. CO2 Utilzation* **2018**, *27*, 472-479.

[90] Zhang, J.-Q.; Zhang, J.-S.; Yang, Y.-J.; Liu, Q. Oxidative Coupling and Reforming of Methane with Carbon Dioxide Using a Pulsed Microwave Plasma under Atmospheric Pressure. *Energy & Fuels* **2003**, *17*, 54-59.

[91] Heijkers, S.; Snoeckx, R.; Kozák, T.; Silva, T.; Godfroid, T.; Britun, N.; Snyders, R.; Bogaerts, A. CO_2 Conversion in a Microwave Plasma Reactor in the Presence of N_2: Elucidating the Role of Vibrational Levels. *J. Phys. Chem. C* **2015**, *119*, 12815-12828.

[92] van Rooij, G. J.; van den Bekerom, D. C. M.; den Harder, N.; Minea, T.; Berden, G.; Bongers, W. A.; Engeln, R.; Graswinckel, M. F.; Zoethout, E.; van de Sanden, M. C. M. Taming microwave plasma to beat thermodynamics in CO_2 dissociation. *Faraday Discuss.* **2015**, *183*, 233-248.

[93] Chen, G.; Britun, N.; Godfroid, T.; Georgieva, V.; Snyders, R.; Delplancke-Ogletree, M.-P. An overview of CO_2 conversion in a microwave discharge: the role of plasma-catalysis. *J. Phys. D Appl. Phys.* **2017**, *50*, 084001.

[94] Ghorbanzadeh, A. M.; Norouzi, S.; Mohammadi, T. High energy efficiency in syngas and hydrocarbon production from dissociation of CH_4–CO_2 mixture in a non-equilibrium pulsed plasma. *J. Phys. D Appl. Phys.* **2005**, *38*, 3804-3811.

[95] Ghorbanzadeh, A. M.; Lotfalipour, R.; Rezaei, S. Carbon dioxide reforming of methane at near room temperature in low energy pulsed plasma. *Int. J. Hydrogen Energy* **2009**, *34*, 293-298.

[96] Li, D.; Li, X.; Bai, M.; Tao, X.; Shang, S.; Dai, X.; Yin, Y. CO_2 reforming of CH_4 by atmospheric pressure glow discharge plasma: A high conversion ability. *Int. J. Hydrogen Energy* **2009**, *34*, 308-313.

[97] Wanten, B.; Maerivoet, S.; Vantomme, C.; Slaets, J.; Trenchev, G.; Bogaerts, A. Dry reforming of methane in an atmospheric pressure glow discharge: Confining the plasma to expand the performance. *J. CO2 Utilzation* **2022**, *56*, 101869.

[98] Trenchev, G.; Nikiforov, A.; Wang, W.; Kolev, S.; Bogaerts, A. Atmospheric pressure glow discharge for CO_2 conversion: Model-based exploration of the optimum reactor configuration. *Chem. Eng. J.* **2019**, *362*, 830-841.

[99] Aziznia, A.; Bozorgzadeh, H. R.; Seyed-Matin, N.; Baghalha, M.; Mohamadalizadeh, A. Comparison of dry reforming of methane in low temperature hybrid plasma-catalytic corona with thermal catalytic reactor over Ni/γ-Al_2O_3. *Journal of Natural Gas Chemistry* **2012**, *21*, 466-475.

[100] Li, M.-w.; Xu, G.-h.; Tian, Y.-l.; Chen, L.; Fu, H.-f. Carbon Dioxide Reforming of Methane Using DC Corona Discharge Plasma Reaction. *J. Phys. Chem. A* **2004**, *108*, 1687-1693.

[101] Li, M.-W.; Tian, Y.-L.; Xu, G.-H. Characteristics of Carbon Dioxide Reforming of Methane via Alternating Current (AC) Corona Plasma Reactions. *Energy & Fuels* **2007**, *21*, 2335-2339.

[102] Seyed-Matin, N.; Jalili, A. H.; Jenab, M. H.; Zekordi, S. M.; Afzali, A.; Rasouli, C.; Zamaniyan, A. DC-Pulsed Plasma for Dry Reforming of Methane to Synthesis Gas. *Plasma Chem. Plasma Process.* **2010**, *30*, 333-347.

[103] Khoja, A. H.; Tahir, M.; Amin, N. A. S. Dry reforming of methane using different dielectric materials and DBD plasma reactor configurations. *Energy Convers. Manage.* **2017**, *144*, 262-274.

[104] Khoja, A. H.; Tahir, M.; Saidina Amin, N. A. Process optimization of DBD plasma dry reforming of methane over Ni/$La_2O_3MgAl_2O_4$ using multiple response surface methodology. *Int. J. Hydrogen Energy* **2019**, *44*, 11774-11787.

[105] Uytdenhouwen, Y.; Hereijgers, J.; Breugelmans, T.; Cool, P.; Bogaerts, A. How gas flow design can influence the performance of a DBD plasma reactor for dry reforming of methane. *Chem. Eng. J.* **2021**, *405*, 126618.

[106] Andersen, J. A.; Christensen, J. M.; Østberg, M.; Bogaerts, A.; Jensen, A. D. Plasma-catalytic dry reforming of methane: Screening of catalytic materials in a coaxial packed-bed DBD reactor. *Chem. Eng. J.* **2020**, *397*, 125519.

[107] Khoja, A. H.; Tahir, M.; Amin, N. A. S. Cold plasma dielectric barrier discharge reactor for dry reforming of methane over Ni/ɤ-Al_2O_3-MgO nanocomposite. *Fuel Process. Technol.* **2018**, *178*, 166-179.

[108] Ray, D.; Reddy, P. M. K.; Subrahmanyam, C. Ni-Mn/γ-Al_2O_3 assisted plasma dry reforming of methane. *Catal. Today* **2018**, *309*, 212-218.

[109] Michielsen, I.; Uytdenhouwen, Y.; Bogaerts, A.; Meynen, V. Altering Conversion and Product Selectivity of Dry Reforming of Methane in a Dielectric Barrier Discharge by Changing the Dielectric Packing Material. *Catalysts* **2019**, *9*.

[110] Cleiren, E.; Heijkers, S.; Ramakers, M.; Bogaerts, A. Dry Reforming of Methane in a Gliding Arc Plasmatron: Towards a Better Understanding of the Plasma Chemistry. *ChemSusChem* **2017**, *10*, 4025-4036.

[111] Bo, Z.; Yan, J.; Li, X.; Chi, Y.; Cen, K. Plasma assisted dry methane reforming using gliding arc gas discharge: Effect of feed gases proportion. *Int. J. Hydrogen Energy* **2008**, *33*, 5545-5553.

[112] Tu, X.; Whitehead, J. C. Plasma dry reforming of methane in an atmospheric pressure AC gliding arc discharge: Co-generation of syngas and carbon nanomaterials. *Int. J. Hydrogen Energy* **2014**, *39*, 9658-9669.

[113] Zhang, J.-Q.; Yang, Y.-J.; Zhang, J.-S.; Liu, Q. Study on the Conversion of CH_4 and CO_2 Using a Pulsed Microwave Plasma under Atmospheric Pressure. *ACTA CHIMICA SINICA-CHINESE EDITION-* **2002**, *60*, 1973-1980.

[114] Qi, C.; Wei, D.; Xumei, T.; Hui, Y.; Xiaoyan, D.; Yongxiang, Y. CO_2 Reforming of CH_4 by Atmospheric Pressure Abnormal Glow Plasma. *Plasma Science and Technology* **2006**, *8*, 181-184.

[115] Bin, D.; Xiu-ling, Z.; Wei-min, G.; Ren, H. Study on the Methane Coupling under Pulse Corona Plasma by Using CO_2 as Oxidant. *Plasma Science and Technology* **2000**, *2*, 577-580.

[116] Yang, Y. Methane Conversion and Reforming by Nonthermal Plasma on Pins. *Industrial & Engineering Chemistry Research* **2002**, *41*, 5918-5926.

[117] Li, X.-S.; Zhu, B.; Shi, C.; Xu, Y.; Zhu, A.-M. Carbon dioxide reforming of methane in kilohertz spark-discharge plasma at atmospheric pressure. *AlChE J.* **2011**, *57*, 2854-2860.

[118] Zhu, B.; Li, X.-S.; Shi, C.; Liu, J.-L.; Zhao, T.-L.; Zhu, A.-M. Pressurization effect on dry reforming of biogas in kilohertz spark-discharge plasma. *Int. J. Hydrogen Energy* **2012**, *37*, 4945-4954.

[119] Shapoval, V.; Marotta, E.; Ceretta, C.; Konjević, N.; Ivković, M.; Schiorlin, M.; Paradisi, C. Development and Testing of a Self-Triggered Spark Reactor for Plasma Driven Dry Reforming of Methane. *Plasma Processes and Polymers* **2014**, *11*, 787-797.

[120] Whitehead, J. C. Plasma–catalysis: the known knowns, the known unknowns and the unknown unknowns. *J. Phys. D Appl. Phys.* **2016**, *49*, 243001.

[121] Whitehead, J. C. Plasma-catalysis: Is it just a question of scale? *Frontiers of Chemical Science and Engineering* **2019**, *13*, 264-273.

[122] Tu, X.; Gallon, H. J.; Twigg, M. V.; Gorry, P. A.; Whitehead, J. C. Dry reforming of methane over a Ni/Al_2O_3 catalyst in a coaxial dielectric barrier discharge reactor. *J. Phys. D Appl. Phys.* **2011**, *44*, 274007.

[123] Zhu, B.; Jang, B. W. L. Insights into surface properties of non-thermal RF plasmas treated Pd/TiO_2 in acetylene hydrogenation. *J. Mol. Catal. A: Chem.* **2014**, *395*, 137-144.

[124] Jiang, Y.; Fu, T.; Lü, J.; Li, Z. A zirconium modified Co/SiO_2 Fischer-Tropsch catalyst prepared by dielectric-barrier discharge plasma. *Journal of Energy Chemistry* **2013**, *22*, 506-511.

[125] Estifaee, P.; Haghighi, M.; Babaluo, A. A.; Rahemi, N.; Jafari, M. F. The beneficial use of non-thermal plasma in synthesis of Ni/Al_2O_3–MgO nanocatalyst used in hydrogen production from reforming of CH_4/CO_2 greenhouse gases. *J. Power Sources* **2014**, *257*, 364-373.

[126] Zhang, M.; Zhu, X.; Liang, X.; Wang, Z. Preparation of highly efficient Au/C catalysts for glucose oxidation via novel plasma reduction. *Catal. Commun.* **2012**, *25*, 92-95.

[127] Tu, X.; Gallon, H. J.; Whitehead, J. C. Plasma-assisted reduction of a NiO/Al_2O_3 catalyst in atmospheric pressure H_2/Ar dielectric barrier discharge. *Catal. Today* **2013**, *211*, 120-125.

[128] Kim, H.-H.; Teramoto, Y.; Sano, T.; Negishi, N.; Ogata, A. Effects of Si/Al ratio on the interaction of nonthermal plasma and Ag/HY catalysts. *Appl. Catal. B Environ.* **2015**, *166-167*, 9-17.

[129] Wu, Y.-W.; Chung, W.-C.; Chang, M.-B. Modification of $Ni/\gamma\text{-}Al_2O_3$ catalyst with plasma for steam reforming of ethanol to generate hydrogen. *Int. J. Hydrogen Energy* **2015**, *40*, 8071-8080.

[130] Zhu, X.; Huo, P.; Zhang, Y.-p.; Cheng, D.-g.; Liu, C.-j. Structure and reactivity of plasma treated Ni/Al_2O_3 catalyst for CO_2 reforming of methane. *Appl. Catal. B Environ.* **2008**, *81*, 132-140.

[131] Hua, W.; Jin, L.; He, X.; Liu, J.; Hu, H. Preparation of Ni/MgO catalyst for CO_2 reforming of methane by dielectric-barrier discharge plasma. *Catal. Commun.* **2010**, *11*, 968-972.

[132] Rahemi, N.; Haghighi, M.; Babaluo, A. A.; Jafari, M. F.; Estifaee, P. Synthesis and physicochemical characterizations of Ni/Al_2O_3–ZrO_2 nanocatalyst prepared via impregnation method and treated with non-thermal plasma for CO_2 reforming of CH_4. *Journal of Industrial and Engineering Chemistry* **2013**, *19*, 1566-1576.

[133] Shkabko, A.; Aguirre, M. H.; Marozau, I.; Doebeli, M.; Mallepell, M.; Lippert, T.; Weidenkaff, A. Characterization and properties of microwave plasma-treated $SrTiO_3$. *Mater. Chem. Phys.* **2009**, *115*, 86-92.

[134] Roland, U.; Holzer, F.; Pöppl, A.; Kopinke, F. D. Combination of non-thermal plasma and heterogeneous catalysis for oxidation of volatile organic compounds: Part 3. Electron paramagnetic resonance (EPR) studies of plasma-treated porous alumina. *Appl. Catal. B Environ.* **2005**, *58*, 227-234.

[135] Shang, S.; Liu, G.; Chai, X.; Tao, X.; Li, X.; Bai, M.; Chu, W.; Dai, X.; Zhao, Y.; Yin, Y. Research on Ni/γ-Al_2O_3 catalyst for CO_2 reforming of CH_4 prepared by atmospheric pressure glow discharge plasma jet. *Catal. Today* **2009**, *148*, 268-274.

[136] Neyts, E. C.; Ostrikov, K.; Sunkara, M. K.; Bogaerts, A. Plasma Catalysis: Synergistic Effects at the Nanoscale. *Chem. Rev.* **2015**, *115*, 13408-13446.

[137] Chen, H. L.; Lee, H. M.; Chen, S. H.; Chao, Y.; Chang, M. B. Review of plasma catalysis on hydrocarbon reforming for hydrogen production—Interaction, integration, and prospects. *Appl. Catal. B Environ.* **2008**, *85*, 1-9.

[138] De Geyter, N.; Dubruel, P.; Morent, R.; Leys, C. Plasma-Assisted Surface Modification of Polymeric Biomaterials. In *Low Temperature Plasma Technology*. CRC Press, 2013; pp 413-430.

[139] Snoeckx, R.; Aerts, R.; Tu, X.; Bogaerts, A. Plasma-Based Dry Reforming: A Computational Study Ranging from the Nanoseconds to Seconds Time Scale. *J. Phys. Chem. C* **2013**, *117*, 4957-4970.

[140] Wang, Z.; Zhang, Y.; Neyts, E. C.; Cao, X.; Zhang, X.; Jang, B. W. L.; Liu, C.-j. Catalyst Preparation with Plasmas: How Does It Work? *ACS Catalysis* **2018**, *8*, 2093-2110.

[141] Guo, Y.-F.; Ye, D.-Q.; Chen, K.-F.; He, J.-C.; Chen, W.-L. Toluene decomposition using a wire-plate dielectric barrier discharge reactor with manganese oxide catalyst in situ. *J. Mol. Catal. A: Chem.* **2006**, *245*, 93-100.

[142] Kapokova, L.; Pavlova, S.; Bunina, R.; Alikina, G.; Krieger, T.; Ishchenko, A.; Rogov, V.; Sadykov, V. Dry reforming of methane over $LnFe_{0.7}Ni_{0.3}O_3{-}\delta$ perovskites: Influence of Ln nature. *Catal. Today* **2011**, *164*, 227-233.

[143] Shirazi, M.; Neyts, E. C.; Bogaerts, A. DFT study of Ni-catalyzed plasma dry reforming of methane. *Appl. Catal. B Environ.* **2017**, *205*, 605-614.

[144] Chen, J.; Xie, Z. Removal of H_2S in a novel dielectric barrier discharge reactor with photocatalytic electrode and activated carbon fiber. *J. Hazard. Mater.* **2013**, *261*, 38-43.

[145] Lifshits, E. V.; Kornilov, E. A. Measurement of the Correlation Functions of the Light-Emission Intensity in a Plasma-Beam Discharge. In *Recent Advances in*

Plasma Diagnostics / Diagnostika Plasmy / Диагностика Плазмы: Volume 3: Corpuscular, Correlation, Bolometric, and Other Techniques. V. T. Tolok, Ed.; Springer US; New York, NY, 1971; pp 55-60.

[146] Van Laer, K.; Bogaerts, A. Influence of Gap Size and Dielectric Constant of the Packing Material on the Plasma Behaviour in a Packed Bed DBD Reactor: A Fluid Modelling Study. *Plasma Processes and Polymers* **2017**, *14*, 1600129.

[147] Tu, X.; Gallon, H. J.; Whitehead, J. C. Electrical and spectroscopic diagnostics of a single-stage plasma-catalysis system: effect of packing with TiO_2. *J. Phys. D Appl. Phys.* **2011**, *44*, 482003.

[148] Van Laer, K.; Bogaerts, A. Fluid modelling of a packed bed dielectric barrier discharge plasma reactor. *Plasma Sources Sci. Technol.* **2015**, *25*, 015002.

[149] Gadkari, S.; Tu, X.; Gu, S. Fluid model for a partially packed dielectric barrier discharge plasma reactor. *Physics of Plasmas* **2017**, *24*, 093510.

[150] Mujahid, Z.-u.-I.; Hala, A. Plasma dynamics in a packed bed dielectric barrier discharge (DBD) operated in helium. *J. Phys. D Appl. Phys.* **2018**, *51*, 11LT02.

[151] Wang, L.; Yi, Y.; Wu, C.; Guo, H.; Tu, X. One-Step Reforming of CO_2 and CH_4 into High-Value Liquid Chemicals and Fuels at Room Temperature by Plasma-Driven Catalysis. *Angew. Chem. Int. Ed.* **2017**, *56*, 13679-13683.

[152] Tu, X.; Whitehead, J. C. Plasma-catalytic dry reforming of methane in an atmospheric dielectric barrier discharge: Understanding the synergistic effect at low temperature. *Appl. Catal. B Environ.* **2012**, *125*, 439-448.

[153] Song, H. K.; Choi, J.-W.; Yue, S. H.; Lee, H.; Na, B.-K. Synthesis gas production via dielectric barrier discharge over Ni/γ-Al_2O_3 catalyst. *Catal. Today* **2004**, *89*, 27-33.

[154] Eliasson, B.; Liu, C.-j.; Kogelschatz, U. Direct Conversion of Methane and Carbon Dioxide to Higher Hydrocarbons Using Catalytic Dielectric-Barrier Discharges with Zeolites. *Industrial & Engineering Chemistry Research* **2000**, *39*, 1221-1227.

[155] Uytdenhouwen, Y.; Bal, K. M.; Neyts, E. C.; Meynen, V.; Cool, P.; Bogaerts, A. On the kinetics and equilibria of plasma-based dry reforming of methane. *Chem. Eng. J.* **2021**, *405*, 126630.

[156] Gallon, H. J.; Tu, X.; Whitehead, J. C. Effects of Reactor Packing Materials on H_2 Production by CO_2 Reforming of CH_4 in a Dielectric Barrier Discharge. *Plasma Processes and Polymers* **2012**, *9*, 90-97.

[157] Zhang, Q.-Z.; Bogaerts, A. Plasma streamer propagation in structured catalysts. *Plasma Sources Sci. Technol.* **2018**, *27*, 105013.

[158] Zhang, Q.-Z.; Bogaerts, A. Propagation of a plasma streamer in catalyst pores. *Plasma Sources Sci. Technol.* **2018**, *27*, 035009.

[159] Zhang, Y.-R.; Van Laer, K.; Neyts, E. C.; Bogaerts, A. Can plasma be formed in catalyst pores? A modeling investigation. *Appl. Catal. B Environ.* **2016**, *185*, 56-67.

[160] Zhang, Q.-Z.; Wang, W.-Z.; Bogaerts, A. Importance of surface charging during plasma streamer propagation in catalyst pores. *Plasma Sources Sci. Technol.* **2018**, *27*, 065009.

[161] Michielsen, I.; Uytdenhouwen, Y.; Pype, J.; Michielsen, B.; Mertens, J.; Reniers, F.; Meynen, V.; Bogaerts, A. CO_2 dissociation in a packed bed DBD reactor: First steps towards a better understanding of plasma catalysis. *Chem. Eng. J.* **2017**, *326*, 477-488.

[162] El-Shafie, M.; Kambara, S.; Hayakawa, Y. Alumina particle size effect on H_2 production from ammonia decomposition by DBD plasma. *Energy Reports* **2020**, *6*, 25-30.

Chapter 2 Modifying the Stöber process: Is the organic solvent indispensable?

Abstract

The Stöber method is one of the most important and fundamental processes for the synthesis of inorganic (nano)materials, but has the drawback of using a large amount of organic solvent. Herein, we used ethanol as an example to explore if the organic solvent in a typical Stöber method can be omitted. We found that ethanol increases the particle size of the obtained silica spheres and aids the formation of uniform silica particles rather than forming a gel. Nevertheless, the results indicated that an organic solvent in the initial synthesis mixture is not indispensable. We discovered an initially immiscible synthesis method, which can replace the organic solvent-based Stöber method to successfully synthesize silica particles with the same size ranges as the original Stöber process without addition of organic solvents. Moreover, this process can be of further value to be extended to synthesis processes of other materials based on the Stöber process.

This chapter is accepted at:

J. Wang, K. Zhang, S. Kavak, S. Bals, V. Meynen, Modifying the Stöber Process: Is the Organic Solvent Indispensable?. Chem. Eur. J.

2.1 Introduction

In order to study the structure and properties of catalysts suitable for plasma catalysis, the controllable synthesis of catalysts is crucial. One of the most important methods for the controlled synthesis of inorganic materials and nanomaterials is the Stöber process, proposed by Stöber et al. in 1968 [1]. It was originally developed for the synthesis of uniform submicron silica spheres, but has now been expanded into a huge system by a lot of extension methods for synthesizing diverse materials with different morphologies and microstructures for a variety of applications, such as aerospace, drug delivery, adsorption, and catalysis [2-7]. For example, ordered mesoporous silica, with tunable pore size and high surface area, has been synthesized via modified Stöber processes [8,9]. Also silica materials with core-shell structure, yolk-shell structure, etc., and even carbon materials and metal oxide materials with different structures were prepared by extension of the Stöber method [10-14].

However, these classical or most modified methods always require the use of alcohols or other organic solvents to dissolve the silica precursors, which is neither economical nor environmentally friendly since a lot of organic solvent is wasted during the process. For example, the most typical Stöber process, using 0.28 mol/L of tetraethyl orthosilicate (TEOS) in ethanol solution, consumes about 1 L of ethanol to synthesize only 17 g of SiO_2 spheres [1]. Therefore, it is important to find a way to reduce the organic solvent consumption.

A lot of attempts have been made and reported. It was discovered that the formation of bio-silica in diatoms and sponges occurs in aqueous solutions with the aid of proteins, and subsequent studies found that silica with some specific structures could be synthesized without the addition of organic solvents in the presence of amino acids, surfactants, etc. [15-19]. Based on these studies, Davis et al. proposed to use a lysine aqueous solution as a catalyst to replace typical ammonia to synthesize silica spheres [20]. However, the particle size was only ~5 nm, much smaller than that obtained by the Stöber method. Yokoi et al. performed similar research at the same time and 15–44 nm silica spheres were obtained [21,22]. In order to extend the size range, multi-steps seed regrowth processes were proposed and particles up to 200 nm could be synthesized [23]. Nevertheless, these modified methods are either only able to synthesize silica with specific structures, or the size range of samples obtained from them is still too small to replace the classic Stöber process.

Although TEOS can also react with water without organic solvents to form silica particles in a classic ammonia (instead of amino acid) catalyzed process, the product is often non-uniform and uncontrollable, rather than controlled uniform particles. The role of solvents has been studied. It was found that the type of solvent influences the silica particle sizes [1,24]. Furthermore, it has been reported that the alcohols not only regulate the miscibility of the system, but also participate in the reaction [25,26]. Although a lot of research has been done on the influence of solvent over decades, it has not yet been discovered that addition of organic solvents can actually be omitted in the ammonia Stöber process.

In this work, we found that uniform silica spheres with much larger and adjustable diameters can be synthesized without any organic solvents or amino acids (denoted as organic solvent-free method), as long as the ratio of reagents is controlled in an appropriate range. The particle size of the silica spheres synthesized by this method is controllable at the sub-micron scale, the same as the Stöber method. Moreover, the catalyst is the ammonia solution, just like the classic Stöber method (also in similar amounts), which is inexpensive and saves additional costs of other additives such as amino acids. Due to the importance of the classical Stöber method for syntheses of inorganic materials, the success of this organic solvent-free controllable synthesis of silica can be of great significance in practical applications by extending it to other Stöber-based materials syntheses.

2.2 Experimental procedures

2.2.1 Synthesis of silica particles

The organic solvent-free process is similar to the Stöber method except there is no additional organic solvent added. Ammonia solution (wt % = 25%) and deionized water were mixed in a beaker and agitated at 400 rpm at room temperature. The calculation of the amount of water in the synthesis included the water content in the ammonia solution and the water directly added. Then, 50 mL of tetraethyl orthosilicate (TEOS) was added into it quickly. The mixture was kept stirring at room temperature for 24 h. The silica spheres were collected by centrifugation without washing. Subsequently, they were dried at 353 K for 24 h. The details on the volumes and amounts of reactants of all the organic solvent-free syntheses in this work are listed in Table A.1 in Appendix A.

The synthesis with ethanol, executed as a control experiment, is the classic Stöber method. Ammonia solution (wt % = 25%) and deionized water were dissolved in 300 mL of ethanol to prepare a solution A and agitated at 400 rpm at room temperature. An ethanol solution B containing 50 mL of TEOS was added into it quickly. The specific amounts of ethanol and reactants are shown in Table A.2 in Appendix A. The amount of ethanol in solution B is equal to the total amount of ethanol minus the amount of ethanol in solution A. For samples 34-39 in Table A.2, the amount of ethanol in the solutions during the synthesis was one-tenth that of the other samples. The mixture was kept stirring at room temperature for 24 h. The silica spheres were collected by centrifugation without washing, and subsequently the spheres were dried at 353 K for 24 h.

2.2.2 Characterization

The topography of silica particles larger than 100 nm was investigated by a field emission scanning electron microscope (FEI Quanta 250 SEM) operating at 20 kV. The sample powder was sputter-coated with gold before the SEM observation. The particles smaller than 100 nm were analyzed with high angle annular dark field scanning transmission electron microcopy (HAADF-STEM) using a Thermo Fisher Tecnai Osiris electron microscope operated at 200 kV and 60 pA beam current. For HAADF-STEM imaging, the powder was diluted with ethanol, then a few drops from the suspension was dropped on a carbon coated polymer film on a copper grid. The particle sizes were calculated by measuring all the visible particles in the SEM or STEM images and averaging them. To prevent beam damage on the samples, a fast tomography technique was used. Tomography series were acquired by using the Fischione model 2020 single-tilt tomography holder over a tilt range from −50° to +70°, with tilt increments of 2°. The reconstruction of the tilt series was performed using the Astra Toolbox. Visualization and segmentation were performed using Amira 5.4.0 software.

The conductivity was measured during the synthesis by a Metrohm 644 Conductometer.

Nitrogen sorption measurements were carried out at -196 °C on a Quantachrome Quadrasorb SI automated gas sorption system. Before the measurements, the samples were degassed for 16 h under high vacuum at a temperature of 200 °C.

Prior to DLS measurements, the powders were dispersed in deionized water to prepare a suspension. Then, the particle size and agglomeration was measured by dynamic light scattering using a Zetasizer NanoZS (Malvern, UK) analyzer.

2.3 Results and discussion

Examples of different sizes of SiO_2 spheres, as prepared by this organic solvent-free method, are shown in Figure 2.1. The amount of TEOS was fixed for all syntheses to 50 mL, whereas the size difference was induced by the use of different amounts of water and ammonia in the synthesis. The obtained silica spheres are uniform in size and shape when the sizes are in the range of approximately 100 nm–1 µm (Figure 2.1b–2.1e). An example of the particle size distribution obtained via SEM is shown in Figure A.1a in Appendix A. However, when trying to reach even larger diameter particles (>1 µm) by only adjusting the ratio of reactants, the spheres lose uniformity, represented by small satellite particles present in the samples (Figure 2.1a). In addition, when the synthesis is not performed at an appropriate reactant ratio like discussed in this paper, agglomerated and non-uniform silica gels (Figure 2.1f), rather than uniform spheres, are being obtained. The volume and amounts of reactants of all the organic solvent-free syntheses in this work are listed in Table A.1. Figure A.2 in Appendix A shows the electron microscope images of all the obtained samples. The entry numbers of Table A.1 and Figure A.2 correspond to each other. Figure 2.1a-e correspond to the samples with entry numbers 5, 7, 19, 17, and 23 in Table A.1, respectively. The amount of ammonia used in this process was in the same range as in a typical Stöber process, and its molar ratio to the resulting silica (NH_3/SiO_2) is 3.2–8.5, compared to 1–30 in the typical Stöber process [1,27].

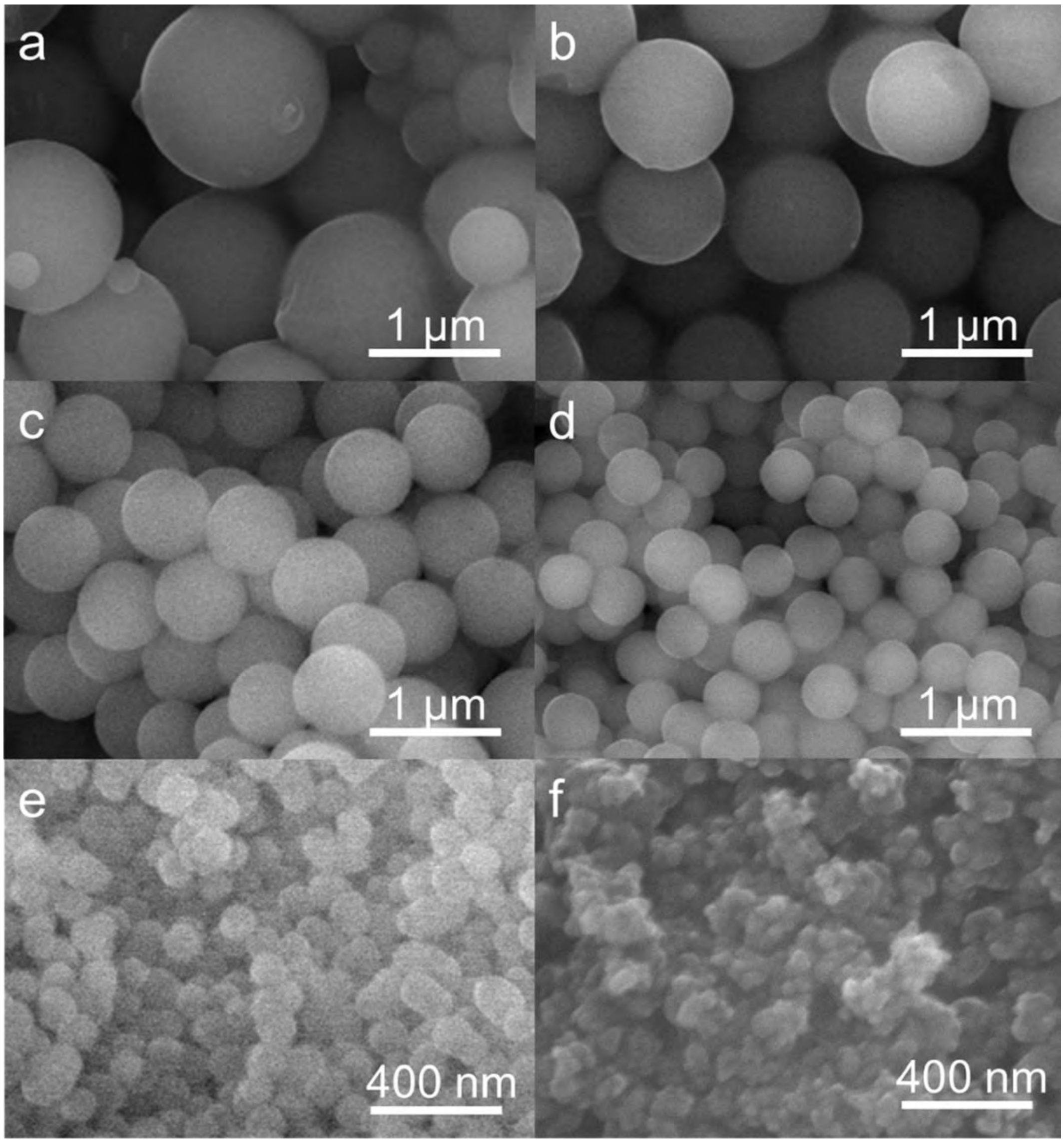

Figure 2.1. Scanning electron microcopy (SEM) images of silica with different sizes prepared by the organic solvent-free method. (a) Silica spheres with a diameter of ~1.3 µm. (b) Uniform silica spheres of ~1 µm. (c) Uniform silica spheres of ~710 nm. (d) Uniform silica spheres of ~430 nm. (e) Uniform silica spheres of ~100 nm. (f) Non-uniform and agglomerated silica gel.

The influence of the volume and molar ratios of water and ammonia, at constant volume of TEOS, on the silica sizes in the organic solvent-free method was studied. The results are shown in Figure 2.2. Since the concentration of the ammonia solution is 25%, the curve for each ammonia content has a corresponding minimum content of water instead of 0 mol. Additionally, only in a narrow range of water content, depending on the amount of ammonia added, this organic solvent-free method is able to prepare SiO_2 spheres. Otherwise a non-uniform gel is produced (yellow area in Figure 2.2). Another conclusion that can be deduced from the figure is that the lower the water content used in the synthesis, the larger the diameter of the SiO_2 spheres obtained. Ammonia contents below 1.33 mol allow a wider range of particle sizes than the higher ammonia contents. Comparing different curves along the Y-axis, it is found that in most cases, at a certain water content, increasing the amount of ammonia can increase the particle size. However, when the water content is small (~4 mol water), the particle size rises first and then drops with the increase of ammonia content. Some models of silica formation and growth in typical Stöber process have been proposed and studied [28-30]. Although there is no consensus yet on many details (e.g. the formation process of primary particles, the rate determining step of particle growth), it is generally accepted that different water and ammonia contents change important features, such as the solvation, electrostatic interactions, hydrolysis and condensation rates, that can influence the final particle size [28-32]. The equations for the hydrolysis and condensation of TEOS are shown in Figure A.3 in Appendix A. In the synthesis process, TEOS undergoes hydrolysis first, to produce monomers with one or more silanol groups and releasing ethanol into the solution (Figure A.3 (Eq. 1)). Then, the condensation between silanol groups (Figure A.3 (Eq. 2)) or between silanol groups and ethoxy groups (Figure A.3 (Eq. 3)) generates oligomers with siloxane bonds. The oligomers separate from the continuous phase to form nuclei, which become primary particles and grow further into the stable final particles through aggregation or monomers addition [31,32]. The influence of water content is that more water enables enhanced interactions between polymer segments and the continuous phase and dilutes the monomer concentration, which can reduce the final particle size. For the effect of ammonia, with increasing NH_3 concentration, there is a balance between the tendency to produce larger particles (due to the increase of charge shielding ability) and the tendency to produce smaller particles (due to the enhancement of solvation) [28,29]. This might be a reason for the apparent plateau value observed at low water content and with the increase of ammonia, where the particle size starts to drop after rising first. The particle size at high water content cannot reach this plateau value due to the limitation of the maximum ammonia concentration. As the effect of water and ammonia on the particle size shows a similar trend for the organic solvent-free process as for the typical Stöber method, they may have similar mechanisms and growth models, which need to be further studied and verified.

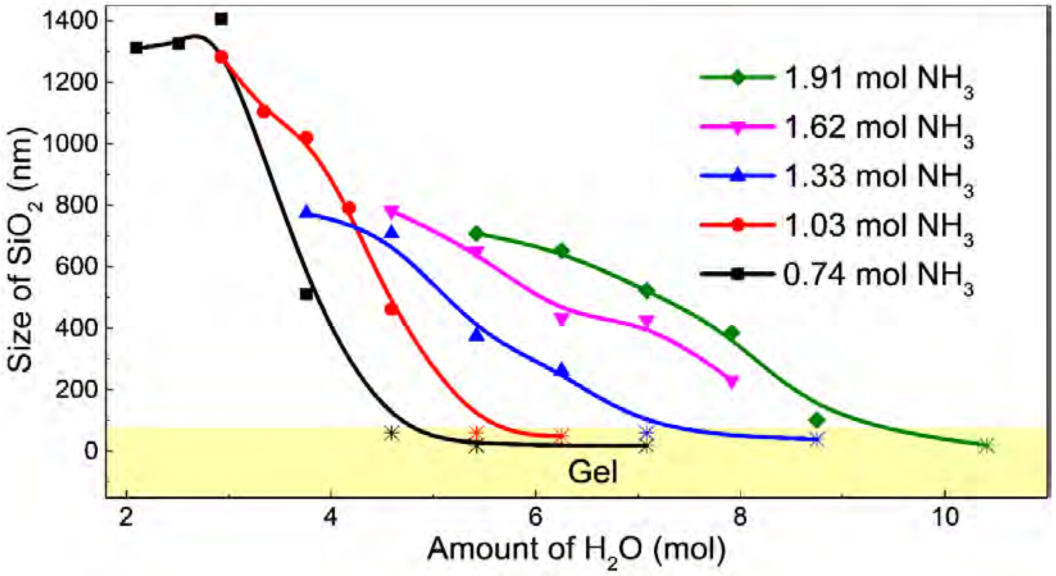

Figure 2.2. Particle sizes synthesized by the modified organic solvent-free Stöber method with different water and ammonia content. 50 mL of tetraethyl silicate (TEOS) is used with various amounts of water and ammonia without addition of ethanol. The amount of water includes the water content in the ammonia solution and the water directly added. Uniform spheres smaller than 100 nm cannot be synthesized in these cases, non-spherical and non-uniform gels are formed instead (yellow segment).

In order to study the influence of ethanol on the silica synthesis, the process without ethanol and typical Stöber method with ethanol were compared under the same conditions (Figure 2.3). The amount of ethanol varies with the amount of ammonia or water, but always dilutes the final concentration of TEOS to 0.28 mol/L as reported [1]. The specific amounts of ethanol and reactants used are shown in Table A.2. Another set of experiments presented in Figure 2.3b used 1/10 of the ethanol content of a typical process as a control experiment. As shown in Figure 2.3, the two processes with or without ethanol have similar trends in the effect of ammonia on the particle size, but with a broader size range in the organic solvent-free method (Figure 2.3a). However, for water the effect differs (Figure 2.3b). The particle size of silica in the presence of ethanol remains the same or slightly increases first and then decreases with the addition of water, which is consistent with reports in the literature of a typical Stöber process [29]. When only 1/10 of the classic ethanol amount is added, the size of the silica particles starts to decrease at a lower water content. However, in the organic solvent-free process, a monotonic decrease of particle size with the increase of water can be observed. Furthermore, in most cases, adding ethanol leads to larger particle sizes up to a certain particle size limit (similar to the maximum particle size of silica synthesized without ethanol).

The role of ethanol is complex [33]. It is difficult to study it as an independent variable since ethanol is both a solvent and a by-product of a reversible reaction (Eq. 1 in Figure A.3) [34]. The effects of the amount of reactants and the type of solvent have been extensively studied, but few studies have focused on the amount of solvent, and these few papers do not have a consistent conclusion [35,36]. However, as shown in Figure 2.3b, compared with the quite small effect on the variation in particle size when reducing the amount of ethanol with a factor of 10, the effect of the presence or absence of ethanol in the initial synthesis mixture is large. This suggests that, although there are other effects, the more important role of ethanol in the synthesis is as a solvent to dissolve two immiscible phases, TEOS and water, into one phase. Figure A.4 in Appendix A supports this hypothesis, as the process with ethanol added as a solvent has a shorter induction period (the part where the conductivity rises). The shorter induction period indicates that the dissolution of all reagents into one phase enables the reactant molecules to better contact and react with each other, improving the efficiency of hydrolysis and condensation, which could be one of the reasons for the larger particle size caused by ethanol [31]. In the organic solvent-free process, the hydrolysis of TEOS will gradually release ethanol, which can also dissolve the two phases of water and TEOS into one phase. This might also explain why at low water content, the particle size of silica prepared by the organic solvent-free process is similar to that of particles synthesized with the addition of ethanol. The particle prepared by the organic solvent-free process is much smaller at high water content, probably because the gradually released ethanol is too little relative to water to regulate the miscibility of water and TEOS. In addition to the above particle size measurements by electron microscopy, N_2-sorption and dynamic light scattering (DLS) measurement (see Figure A.5 and Figure A.6 in Appendix A) were used to prove that there is no structural difference (including particle size distribution width) between silica spheres synthesized with and without ethanol. The numbers in the figures correspond to the entry numbers of the samples in Table A.1 and S2. Comparing the silica spheres with similar particle size synthesized by the organic solvent-free process and the typical Stöber process, there is no significant difference in N_2-sorption and DLS results.

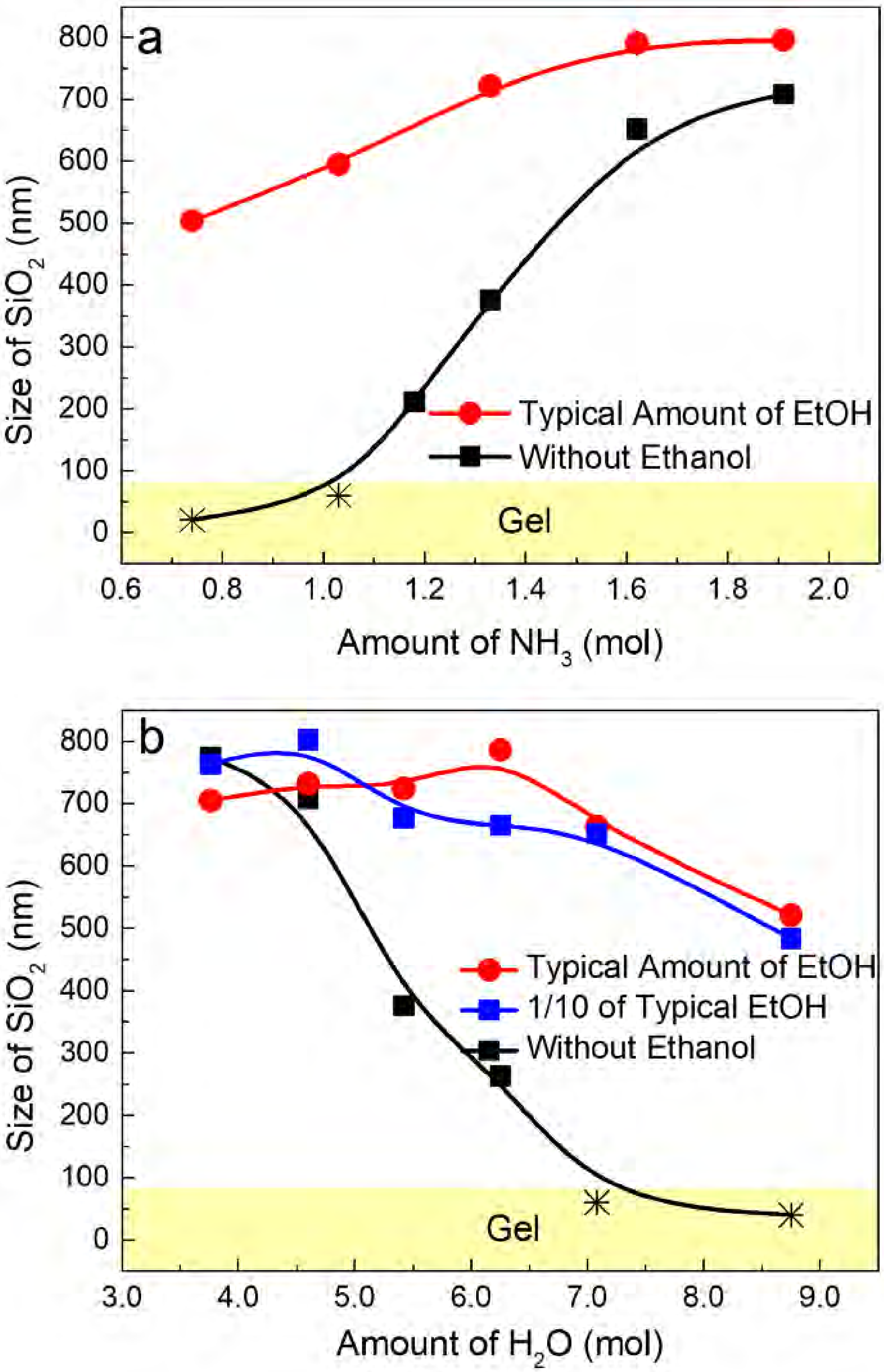

Figure 2.3. The comparison between the typical Stöber method with ethanol and the organic solvent-free method of this work. For syntheses with added ethanol, the typical amount of ethanol to dilute TEOS to 0.28 mol/L has been used as well as 1/10th of that amount. The amount of TEOS in all syntheses is 50 mL. (a) Particle sizes variation with NH_3 in 5.42 mol of H_2O. (b) Particle size variation with H_2O in 1.33 mol of NH_3.

It can also be observed in Figure 2.3 that compared to the typical Stöber method, the organic solvent-free process is only able to produce monodisperse silica spheres within a certain narrow range of water to ammonia ratio. At low ammonia or high water content, which is expected to produce particles smaller than 100 nm, a non-uniform gel is formed. Nevertheless, literature reported silica spheres as small as 50 nm could be produced via a typical Stöber process [1]. In those cases where small particles are produced such as at lower concentrations of ammonia, the hydrolysis of TEOS is less efficient, resulting in monomers with fewer silanol groups. These monomers tend to condense loosely to larger siloxane clusters and branched networks first, and then collapse into smaller and dense particles [31]. The two steps can be carried out well in ethanol solution. However, in the organic solvent-free process, it was observed that the liquid was absorbed by the polymer networks to form a non-flowing gel, so that the reaction cannot proceed to the next step to produce dense particles. We hypothesize that this is due to the much smaller liquid volume of the organic solvent-free process than the typical process with ethanol does not have sufficient space to accommodate and disperse the loose polymer networks formed at the beginning of the reaction, leading to the polymer segments and networks can contact and condense with each other. Therefore, based on the data, another proposed role of ethanol in the typical Stöber process seems to be the dispersion of the monomers, oligomers and nuclei produced by the reaction, to avoid the formation of non-flowing and non-uniform gels.

However, the role of ethanol is not indispensable. In the organic solvent-free process, although the reactants are immiscible, the initial reaction under stirring will gradually produce ethanol from hydrolyzed TEOS at the interphase of the two phases (Eq.1 and Eq.3 in Figure A.3) and dissolve the reactants progressively. Therefore, as long as the ratio and volume of water and ammonia are appropriate, uniform silica spheres larger than 100 nm are able to be produced. Moreover, keeping the above in mind, when synthesizing silica particles smaller than 100 nm, the problem of gel formation due to insufficient space can be avoided by reducing the concentration of TEOS to decrease the amount of monomers. Figure 2.4a shows the results of using the same amounts of ammonia and water while reducing the amount of TEOS. The process with lower TEOS concentration results in smaller relatively uniform particles. Furthermore, it confirms that particles smaller than 100 nm can indeed be obtained instead of formation of a gel network. High angle annular dark field scanning transmission electron microcopy (HAADF-STEM) and electron tomography were applied to study the morphology and size of these particles with a diameter smaller than 100 nm. As shown in Figure 2.4b1 and 4b2, the particle size is still relatively uniform (see also the Figure A.1b for the particle size distribution of ~50 nm particles), but the sphericity is lower than what was observed for larger particles. The 3D reconstruction obtained by electron tomography (Figure A.7 in Appendix A) shows that the particles with a diameter of ~50 nm are not perfect spheres, but have a rather oval shape in combination with aggregates of smaller (spherical) particles.

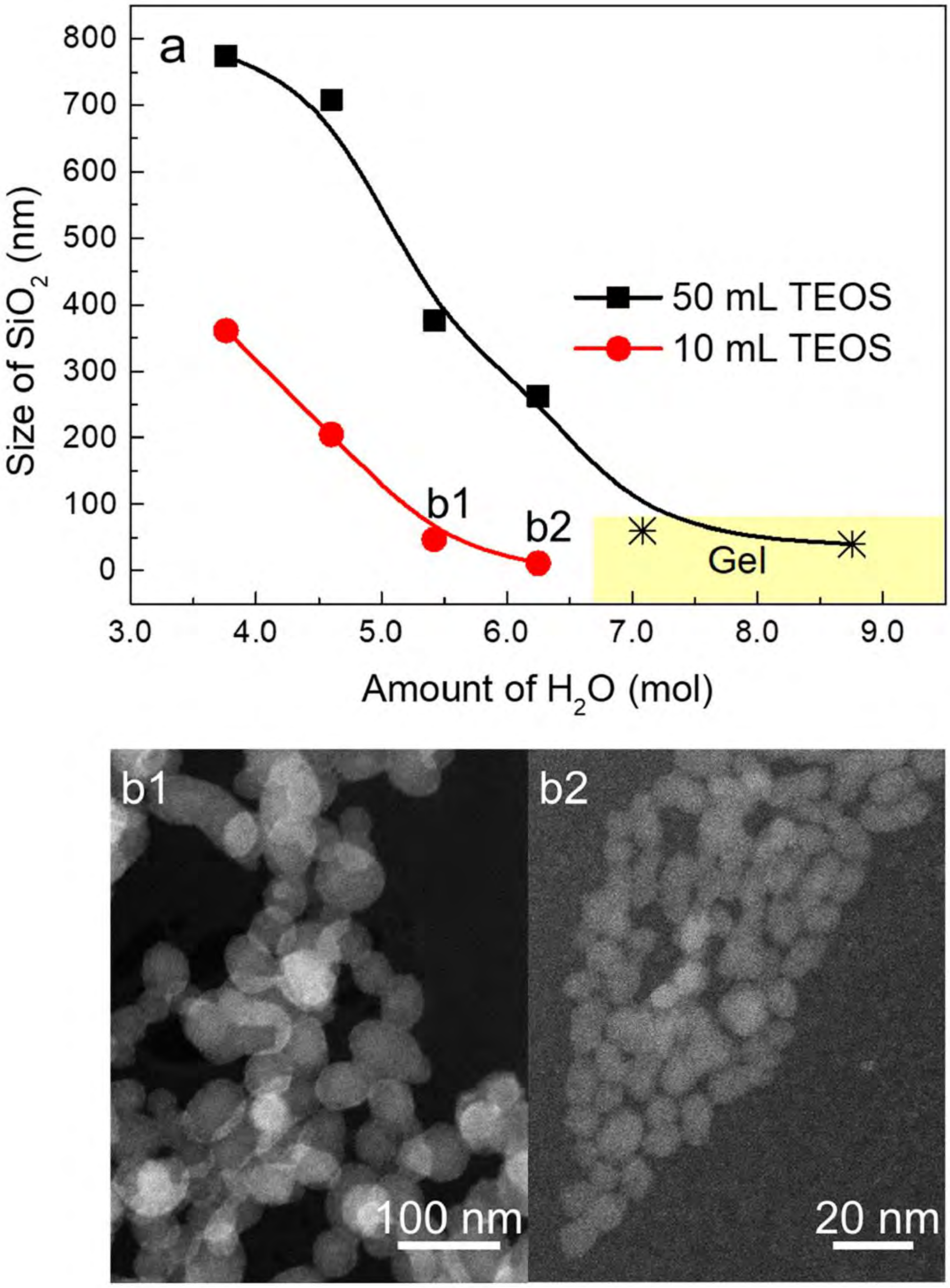

Figure 2.4. Experiments to synthesize silica particles smaller than 100 nm by the organic solvent-free method. (a) The particle sizes comparison of silica synthesized with two different amounts of TEOS by the organic solvent-free method. (b1, b2) HAADF-STEM images of silica particles with a diameter of ~50 nm (b1) and ~10 nm (b2) synthesized by the organic solvent-free method. The amount of NH_3 is 1.33 mol in all experiments. The b1 and b2 data points in Figure 2.4a correspond to Figure 2.4b1 and Figure 2.4b2, respectively.

The results thus show that particle size ranges of silica that can be prepared by the organic solvent-free process are the same as the typical Stöber method, which can be controlled between about tens of nm and 1 μm. The solid content obtained by the modified process for silica particles smaller than 100 nm is ~17 g/L to ~19 g/L, which is similar with that of the typical Stöber method. The larger particles, however, can be synthesized at a solid content of ~53 g/L to ~123 g/L, making it more suitable for large scale fabrication than the typical Stöber processes. In addition, Nagao et al. reported an extension of the Stöber method to synthesize silica particles larger than 1 μm, which introduced electrolytes in the hydrolysis of alkyl silicates [37]. We preliminary studied if this extended method of adding electrolytes still works in the organic solvent-free process. As shown in Figure A.8 in Appendix A, the diameters of silica increased from ~380 nm to ~1.8 μm and from ~710 nm to ~2 μm, respectively, by the addition of 0.1 g (4.14×10^{-4} mol) of $Cu(NO_3)_2 \cdot 3H_2O$, while still remaining uniform. It shows that this modification based on the Stöber method is also feasible for the organic solvent-free process. Therefore, it's a reasonable expectation that more syntheses of various other materials based on the typical Stöber method, such as porous materials, aerogels, carbon materials, and metal oxide materials, are also applicable to the organic solvent-free alternative method described here.

2.4 Conclusion

In summary, we found that although ethanol plays an important role in the Stöber method to control particle size and avoid gelation, it is not indispensable. A modification of the Stöber method was described, able to synthesize spherical silica particles with a controllable size without any organic solvents addition to the initial synthesis mixture. The particle size range of the SiO_2 spheres that can be prepared by this organic solvent-free process is the same as the typical Stöber method and even with a more sensitive particle size adjustment depending on the smart combination of water and ammonia content. This method can save a lot of organic solvent use and produces a higher solid content, which is more economical and environmentally friendly. Moreover, because the Stöber method is the foundation for materials synthesis of a variety of important structures, this organic solvent-free improvement will open new doors for all related fields when extended to other synthesis processes based on the Stöber method.

2.5 References

[1] Stöber, W.; Fink, A.; Bohn, E. Controlled growth of monodisperse silica spheres in the micron size range. *J. Colloid Interface Sci.* **1968**, *26*, 62-69.

[2] Parida, S. K.; Dash, S.; Patel, S.; Mishra, B. K. Adsorption of organic molecules on silica surface. *Adv. Colloid Interface Sci.* **2006**, *121*, 77-110.

[3] Seo, Y. D.; Lee, C.; Lee, K. J.; Jang, J. Fabrication of silica nanotubes with an anisotropic functionality as a smart catalyst supporter. *Chem. Commun.* **2016**, *52*, 9825-9828.

[4] Manzano, M.; Vallet-Regí, M. Mesoporous Silica Nanoparticles for Drug Delivery. *Adv. Funct. Mater.* **2020**, *30*, 1902634.

[5] Berg, H. S.; Seterdal, K. E.; Smetop, T.; Rozenvalds, R.; Brandtzaeg, O. K.; Vehus, T.; Lundanes, E.; Wilson, S. R. Self-packed core shell nano liquid chromatography columns and silica-based monolithic trap columns for targeted proteomics. *J. Chromatogr. A* **2017**, *1498*, 111-119.

[6] Wong, S.; Kitaev, V.; Ozin, G. A. Colloidal Crystal Films: Advances in Universality and Perfection. *J. Am. Chem. Soc.* **2003**, *125*, 15589-15598.

[7] Kwok, K. M.; Ong, S. W. D.; Chen, L.; Zeng, H. C. Transformation of Stöber Silica Spheres to Hollow Hierarchical Single-Crystal ZSM-5 Zeolites with Encapsulated Metal Nanocatalysts for Selective Catalysis. *ACS Appl. Mater. Interfaces* **2019**, *11*, 14774-14785.

[8] Wang, X.; Zhang, Y.; Luo, W.; Elzatahry, A. A.; Cheng, X.; Alghamdi, A.; Abdullah, A. M.; Deng, Y.; Zhao, D. Synthesis of Ordered Mesoporous Silica with Tunable Morphologies and Pore Sizes via a Nonpolar Solvent-Assisted Stöber Method. *Chem. Mater.* **2016**, *28*, 2356-2362.

[9] Teng, Z.; Zheng, G.; Dou, Y.; Li, W.; Mou, C.-Y.; Zhang, X.; Asiri, A. M.; Zhao, D. Highly Ordered Mesoporous Silica Films with Perpendicular Mesochannels by a Simple Stöber-Solution Growth Approach. *Angew. Chem. Int. Ed.* **2012**, *51*, 2173-2177.

[10] Li, W.; Zhao, D. Extension of the Stöber Method to Construct Mesoporous SiO_2 and TiO_2 Shells for Uniform Multifunctional Core–Shell Structures. *Adv. Mater.* **2013**, *25*, 142-149.

[11] Li, W.; Yang, J.; Wu, Z.; Wang, J.; Li, B.; Feng, S.; Deng, Y.; Zhang, F.; Zhao, D. A Versatile Kinetics-Controlled Coating Method To Construct Uniform Porous TiO_2 Shells for Multifunctional Core–Shell Structures. *J. Am. Chem. Soc.* **2012**, *134*, 11864-11867.

[12] Wong, Y. J.; Zhu, L.; Teo, W. S.; Tan, Y. W.; Yang, Y.; Wang, C.; Chen, H. Revisiting the Stöber Method: Inhomogeneity in Silica Shells. *J. Am. Chem. Soc.* **2011**, *133*, 11422-11425.

[13] Lu, A.-H.; Hao, G.-P.; Sun, Q. Can Carbon Spheres Be Created through the Stöber Method? *Angew. Chem. Int. Ed.* **2011**, *50*, 9023-9025.

[14] Liu, J.; Qiao, S. Z.; Liu, H.; Chen, J.; Orpe, A.; Zhao, D.; Lu, G. Q. Extension of The Stöber Method to the Preparation of Monodisperse Resorcinol–Formaldehyde Resin Polymer and Carbon Spheres. *Angew. Chem. Int. Ed.* **2011**, *50*, 5947-5951.

[15] Cha, J. N.; Stucky, G. D.; Morse, D. E.; Deming, T. J. Biomimetic synthesis of ordered silica structures mediated by block copolypeptides. *Nature* **2000**, *403*, 289-292.

[16] Kröger, N.; Deutzmann, R.; Sumper, M. Polycationic Peptides from Diatom Biosilica That Direct Silica Nanosphere Formation. *Science* **1999**, *286*, 1129.

[17] Hawkins, K. M.; Wang, S. S. S.; Ford, D. M.; Shantz, D. F. Poly-l-Lysine Templated Silicas: Using Polypeptide Secondary Structure to Control Oxide Pore Architectures. *J. Am. Chem. Soc.* **2004**, *126*, 9112-9119.

[18] Furlan, P. Y.; Furlan, A. Y.; Kisslinger, K.; Melcer, M. E.; Shinn, D. W.; Warren, J. B. Water as the Solvent in the Stober Process for Forming Ultrafine Silica Shells on Magnetite Nanoparticles. *ACS Sustainable Chemistry & Engineering* **2019**, *7*, 15578-15584.

[19] Kruk, M.; Jaroniec, M.; Ko, C. H.; Ryoo, R. Characterization of the Porous Structure of SBA-15. *Chem. Mater.* **2000**, *12*, 1961-1968.

[20] Davis, T. M.; Snyder, M. A.; Krohn, J. E.; Tsapatsis, M. Nanoparticles in Lysine−Silica Sols. *Chem. Mater.* **2006**, *18*, 5814-5816.

[21] Yokoi, T.; Sakamoto, Y.; Terasaki, O.; Kubota, Y.; Okubo, T.; Tatsumi, T. Periodic Arrangement of Silica Nanospheres Assisted by Amino Acids. *J. Am. Chem. Soc.* **2006**, *128*, 13664-13665.

[22] Wang, J.; Sugawara-Narutaki, A.; Fukao, M.; Yokoi, T.; Shimojima, A.; Okubo, T. Two-Phase Synthesis of Monodisperse Silica Nanospheres with Amines or Ammonia Catalyst and Their Controlled Self-Assembly. *ACS Appl. Mater. Interfaces* **2011**, *3*, 1538-1544.

[23] Hartlen, K. D.; Athanasopoulos, A. P. T.; Kitaev, V. Facile Preparation of Highly Monodisperse Small Silica Spheres (15 to >200 nm) Suitable for Colloidal Templating and Formation of Ordered Arrays. *Langmuir* **2008**, *24*, 1714-1720.

[24] Green, D. L.; Lin, J. S.; Lam, Y.-F.; Hu, M. Z. C.; Schaefer, D. W.; Harris, M. T. Size, volume fraction, and nucleation of Stober silica nanoparticles. *J. Colloid Interface Sci.* **2003**, *266*, 346-358.

[25] Bernards, T. N. M.; van Bommel, M. J.; Boonstra, A. H. Hydrolysis-condensation processes of the tetra-alkoxysilanes TPOS, TEOS and TMOS in some alcoholic solvents. *J. Non-Cryst. Solids* **1991**, *134*, 1-13.

[26] Bernards, T. N. M.; Janssen, M. J. C. H.; van Bommel, M. J. Influence of butanol on the hydrolysis-condensation behaviour of TEOS. *J. Non-Cryst. Solids* **1994**, *168*, 201-212.

[27] Bogush, G. H.; Tracy, M. A.; Zukoski, C. F. Preparation of monodisperse silica particles: Control of size and mass fraction. *J. Non-Cryst. Solids* **1988**, *104*, 95-106.

[28] Matsoukas, T.; Gulari, E. Dynamics of Growth of Silica Particles from Ammonia-Catalyzed Hydrolysis of Tetra-ethyl-orthosilicate. *J. Colloid Interface Sci.* **1988**, *124*, 252-261.

[29] Bogush, G. H.; Zukoski, C. F. Uniform silica particle precipitation: An aggregative growth model. *J. Colloid Interface Sci.* **1991**, *142*, 19-34.

[30] Wang, X.-D.; Shen, Z.-X.; Sang, T.; Cheng, X.-B.; Li, M.-F.; Chen, L.-Y.; Wang, Z.-S. Preparation of spherical silica particles by Stöber process with high concentration of tetra-ethyl-orthosilicate. *J. Colloid Interface Sci.* **2010**, *341*, 23-29.

[31] Han, Y.; Lu, Z.; Teng, Z.; Liang, J.; Guo, Z.; Wang, D.; Han, M.-Y.; Yang, W. Unraveling the Growth Mechanism of Silica Particles in the Stöber Method: In Situ Seeded Growth Model. *Langmuir* **2017**, *33*, 5879-5890.

[32] Ghimire, P. P.; Jaroniec, M. Renaissance of Stöber method for synthesis of colloidal particles: New developments and opportunities. *J. Colloid Interface Sci.* **2021**, *584*, 838-865.

[33] Fernandes, R. S.; Raimundo, I. M.; Pimentel, M. F. Revising the synthesis of Stöber silica nanoparticles: A multivariate assessment study on the effects of reaction parameters on the particle size. *Colloids Surf., A* **2019**, *577*, 1-7.

[34] Prabakar, S.; Assink, R. A. Hydrolysis and condensation kinetics of two component organically modified silica sols. *J. Non-Cryst. Solids* **1997**, *211*, 39-48.

[35] Shimura, N.; Ogawa, M. Preparation of surfactant templated nanoporous silica spherical particles by the Stöber method. Effect of solvent composition on the particle size. *J. Mater. Sci.* **2007**, *42*, 5299-5306.

[36] Chen, Q.; Ge, Y.; Granbohm, H.; Hannula, S.-P. Effect of Ethanol on Ag@Mesoporous Silica Formation by In Situ Modified Stöber Method. *Nanomaterials* **2018**, *8*.

[37] Nagao, D.; Satoh, T.; Konno, M. A Generalized Model for Describing Particle Formation in the Synthesis of Monodisperse Oxide Particles Based on the Hydrolysis and Condensation of Tetraethyl Orthosilicate. *J. Colloid Interface Sci.* **2000**, *232*, 102-110.

Chapter 3 Three dimensional porous catalysts for plasma-catalytic dry reforming of methane: How does the pore size affect the plasma catalytic performance?

Abstract

The effect of pore size on plasma catalysis is crucial but still unclear. Studies have shown plasma cannot enter micropores and mesopores, so catalysts for traditional thermocatalysis may not fit plasma catalysis. Here, 3D porous Cu and CuO with different pore sizes were prepared using uniform silica particles (10–2000 nm) as templates, and compared in plasma-catalytic dry reforming. In most cases, the smaller the pore size, the higher the conversion of CH_4 and CO_2. Large pores reachable by more electrons did not improve the reaction efficiency. We attribute this to the small surface area and large crystallite size, as indicated by N_2-sorption, mercury intrusion and XRD. While the smaller pores might not be reachable by electrons, due to the sheath formed in front of them, as predicted by modeling, they can still be reached by radicals formed in the plasma, and ions can even be attracted into these pores. An exception are the samples synthesized from 1 μm silica, which show better performance. We believe this is due to the electric field enhancement for pore sizes close to

the Debye length. The performances of CuO and Cu with different pore sizes can provide references for future research on oxide supports and metal components of plasma catalysts.

This chapter is in revision at:
J. Wang, A. Bogaerts, V. Meynen, 3D porous Catalysts for Plasma-Catalytic Dry Reforming of Methane: How Does the Pore Size Affect the Plasma Catalytic Performance? Chemical Engineering Journal

3.1 Introduction

As mentioned in Chapter 1, the dielectric barrier discharge (DBD) reactor is a popular type of non-equilibrium plasma reactor since it is straightforward to be combined with a catalyst. Moreover, it is easily to be applied in the chemical industry because it can be operated at ambient temperature and atmospheric pressure [1-5].

A DBD reactor operating in CO_2/CH_4 mixtures is typically in filamentary discharge mode, composed of a large number of independent micro-discharge filaments, which is greatly affected by the size and geometry of the reactor, as well as by the packing materials and catalysts filled in the reactor [6-9]. Therefore, the interaction between the plasma and the catalyst must be taken into account to study the plasma-catalytic dry reforming, not only the reaction process of feed gas molecules and the catalyst. Moreover, the reactant gas in the plasma state may exhibit quite different properties than in thermal reactions. Hence, the role played by the catalysts is more complicated than in thermal catalysis and is still not entirely clear.

The catalysts used in the existing studies are often the same as or slightly modified from the catalysts for traditional thermocatalytic dry reforming. Some studies reported that the catalyst had a synergistic effect with the plasma to promote the conversion of CH_4 and CO_2. For example, Vakili et al. [10] deposited Pt nanoparticles on the metal-organic framework material UiO-67 MOF as a catalyst, which enhanced the conversion of CH_4 and CO_2 in the diluted feed gases (5000 ppm). Zeng et al. [11] studied γ-Al_2O_3 supported transition metals (Ni, Mn, Co, Cu), and found that compared with only plasma in an empty reactor, filling pure γ-Al_2O_3 or γ-Al_2O_3 supported transition metal catalysts in the reactor yielded an improvement in the conversion of CH_4 (maximum increase was from ~14% to ~20%), although the conversion of CO_2 slightly decreased (from ~10% to ~9%). However, more studies showed inverse effects of the catalysts on plasma dry reforming, especially for those experiments using undiluted feed gases [12,13]. Wang et al. [14] also used a γ-Al_2O_3 support loaded with the same transition metal Cu as Zeng et al.. Moreover, also noble metals (Au, Pt), which are generally considered to be more active for dry reforming, were used as active ingredients [14,15]. However, due to the inhibition of the discharge by the catalysts, both the γ-Al_2O_3 with and without supporting metals reduced the conversion of CH_4 and CO_2 compared to the plasma reaction in an empty reactor, although the selectivity of some products was improved. Michielsen et al. [16] and Andersen et al. [17] reported that if keeping the same space time as the empty DBD reactor, packing materials and catalysts do have positive effects on the dry reforming (DRM) reaction. However, the (catalytic) packing material decreased the discharge volume in the reactor, leading to a shorter space time in the plasma. For some materials, the promotion of the DRM reaction due to the catalytic activity or electric field enhancement of the packing could not compensate for the decreased conversion caused by the loss in volume. In short, since there are so many factors affecting the interaction between catalyst and plasma, a wide variety of very different research results on plasma-catalytic dry reforming have been published in literature, even for similar packing materials. However, a general observation is that many porous catalysts did not show an improvement in plasma catalysis [18].

In order to study how porous materials affect the plasma in a DBD reactor, some researchers have simulated the behavior of plasma streamers in catalyst pores. Zhang et al. [19-22] studied by modeling whether plasma can enter catalyst pores. Their simulations showed that plasma could only be generated or penetrate into pores that are larger than the so-called Debye length, which is hundreds of nanometers at typical plasma-catalytic conditions. However, the porous materials applied as catalyst supports in the existing plasma-catalytic dry reforming studies were usually only with micropores or mesopores smaller than 10 nm. Hence, these are much smaller than the pore size in which plasma can be formed. Although microporous or mesoporous materials show good performance in traditional thermocatalytic dry reforming, because of their large specific surface area, the surface area resulting from the small pores might be ineffective for plasma reactions according to the simulation of Zhang et al. However, if the micropores and mesopores were ineffective for plasma reactions, the question arises what then caused the improved conversion in plasma-catalytic dry reforming, reported in those papers applying microporous or mesoporous catalysts [11,18,23,24]?

In many papers, only part of the DBD reactor space was packed with a little catalyst, to promote conversion of dry reforming by catalysts, although they might not mention or study this [11,23,24]. Tu et al. reported that instead of packing the catalyst particles into the entire discharge gap, packing a small amount of catalyst into a part of the gap improved the conversion of dry reforming [18]. Ray et al. studied the performance of Ni-Mn/γ-Al_2O_3 bimetallic catalyst for dry reforming, and found that the reactant conversion of full catalyst packing and 50% catalyst packing in a DBD reactor were similar to or even worse than that without catalyst, while 25% catalyst packing showed the best performance among all conditions [25]. They suggested that the reduction of discharge in DBD reactors, resulting from catalyst particle packing, is the reason that a partially packed or empty reactor has better performance than a full catalyst packed one. Furthermore, the conclusion of Zhang et al. [19-22] that the plasma cannot enter or be formed in the pores of microporous or mesoporous materials (e.g. γ-Al_2O_3) is another reason that a catalyst packing greatly reduces the plasma volume. It is reasonable that the more catalyst filling, the greater the negative effect on the plasma reaction. However, the dry reforming performance of some partially packed reactor (e.g. 25% Ni-Mn/γ-Al_2O_3 packing) is better than that of an empty reactor, which implies that the catalyst also has a positive effect on the plasma dry reforming in some way, even if the pores are unreachable to plasma. There is a balance between this positive effect and the negative effect of catalyst packing, which is the reason for the better conversion in partially packed reactors. However, this partial packing method is a compromise between catalyst and plasma. It reduces the negative effect of catalyst on the plasma, but also means that neither the plasma nor the catalyst can be fully utilized. Since one of the negative effects of catalysts on plasma is caused by the small pore size, a potential way is to apply catalysts with larger pores into which the plasma can enter, to see if it can maintain the positive effects of the catalysts while decreasing the negative effects of catalyst particles on plasma discharge. In addition, although the micropores and mesopores are ineffective for plasma discharge, their comprehensive effects on the plasma dry reforming processes are unknown. In order to truly combine the advantages of the catalyst and plasma reaction, and to know the right future research direction of the catalyst for plasma reactions, it is crucial to study the role of catalyst pores and the effect of pore size in plasma-catalytic dry reforming.

Some studies compared different catalyst supports that may possess different pore sizes, but they were limited to materials with pores of a few nanometers, while the larger plasma-reachable pores (which should be hundreds of nanometers) have rarely been studied [26-28]. Moreover, since the difference in materials, structures and properties of different supports resulted in too many interference factors, it is impossible to conclude the effect of the pore size on plasma dry reforming from these studies.

In the present paper, we thus synthesized catalysts of the same material with different pore sizes in the range of a few nanometers to micrometers and studied their performance for dry reforming in a DBD plasma reactor. Since the common porous supports or porous structure preparation process cannot adjust the pore sizes in such a large span, silica spheres with different diameters were prepared first as templates, assembled and then removed by etching to get 3D porous catalyst particles with different and controlled pore sizes, as shown in Figure 3.1. Copper was applied as the metal active ingredient because of its low cost and high activity, and unreduced copper oxide was also investigated as an example of a material with a certain dielectric constant. The porous structured samples consisted of pure copper or copper oxide without any support, so the influences of the supports (e.g. metal-support effects, alkalinity of the supports) do not have to be considered in this study, in contrast to literature studies using porous supported catalysts.

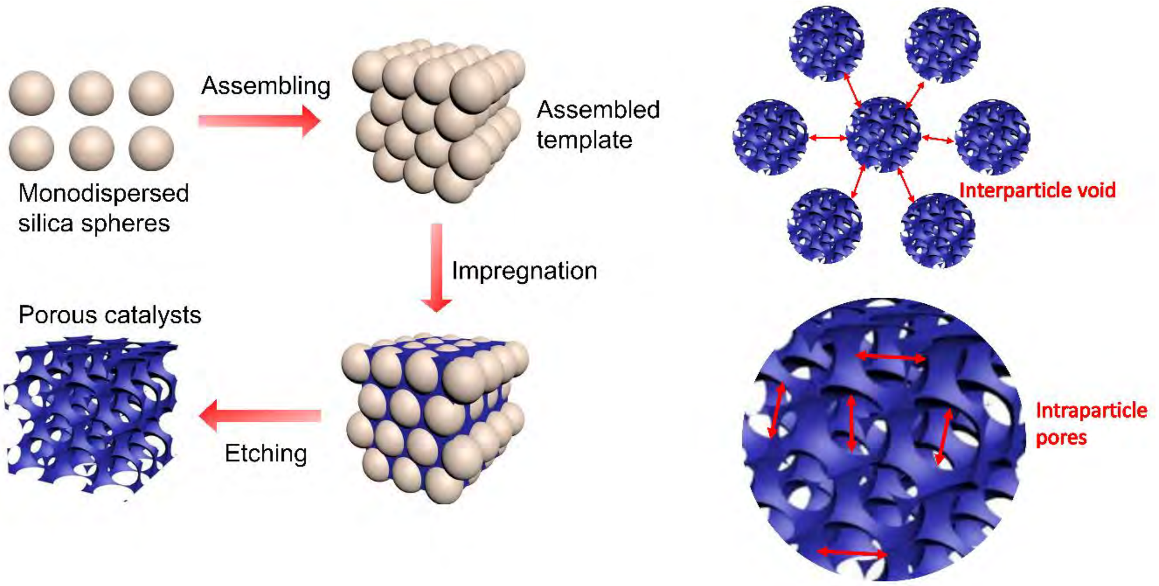

Figure 3.1. The process for the 3D porous catalysts synthesis (left), and explanation of the interparticle voids and intraparticle pores (right).

3.2 Experimental

3.2.1 Preparation of the 3D porous catalysts

Ammonia solution (wt % = 25 %), tetraethyl orthosilicate (TEOS) and ethanol were purchased from Sigma-Aldrich. Copper nitrate trihydrate was purchased from Acros.

3.2.1.1 Preparation of SiO_2 spheres template

The silica spheres were synthesized by a modified Stöber method. A certain amount of ammonia solution was dissolved in deionized water. The solution was agitated gently at 20 °C and 200 mL tetraethyl orthosilicate was added into it. Then, we kept stirring the mixture at the same temperature for 24 h. The silica spheres were obtained after centrifugation and drying at 80 °C for 24 h. The different ratios of ammonia to water were used to adjust the diameter of the silica spheres. Silica particles with diameters of about 10 nm, 50 nm, 100 nm, 600 nm, 1 and 2 μm were synthesized as templates for the next step of impregnation.

3.2.1.2 Impregnation and etching of metal ingredients

The silica samples were calcined at 800 ℃ for 12 h to interconnect the spheres. Excess copper nitrate (twice the mass of silica) was dissolved in ethanol and subsequently the silica was added. The mixture was left without agitation for 48 hours to complete the impregnation. Then, the solid product was dried in an oven at 80 ℃ for 24 h. The resulting sample was calcined in a crucible at 650 °C to decompose the nitrate species. Finally, the silica template was removed by etching with 2 M NaOH aqueous solution at 80 ℃ for 5 h. After washing to neutral and drying at 80 ℃, the 3D porous metal oxide particles were obtained.

The samples were denoted by the diameter of the silica particles used in the impregnation. For example, copper oxide synthesized using 10 nm and 2.5 μm silica particles as templates were denoted as CuO-10 and CuO-2500, respectively, and if reduced with H_2 before plasma testing, the catalysts are denoted as Cu-10 and Cu-2500 respectively.

3.2.2 Characterization of the catalysts

X-ray powder diffraction (XRD) was applied to characterize the crystal phases of all the CuO samples. The measurements were performed by a D8 advance Eco diffractometer with Cu-Kα radiation (λ= 1.5406 Å) at a scanning range of 10–80° 2θ and a scanning rate of 0.04°/4 s. The XRD patterns of all the samples were normalized by dividing every peak by the most intense peak to get relative intensities.

The scanning electron microscopy (SEM) and energy dispersive X-ray spectroscopy (EDX) were used to investigate the topography and surface composition of the samples. They were carried out by the FEI Quanta ESEM FEG 250 field emission microscope with an EDX detector operating at 20 kV.

Nitrogen sorption was used to study the pore size (< 50 nm) and specific surface area of the samples. The measurements were carried out on a Quantachrome Quadrasorb SI automated gas sorption system. The samples were degassed for 16 h under high vacuum at 200 ℃ before the N_2-sorption measurements. The temperature was kept at -196 ℃ by liquid nitrogen during the N_2-sorption. The surface area was determined by the multi-point Brunauer–Emmett–Teller (BET) method and the pore size distribution was determined by non-local density functional theory (NLDFT) on the adsorption branch.

Mercury porosimetry was applied to study the macropores (> 50 nm). The mercury porosimetry was executed on a Themo Electron Corporation Pascal 140 + 240 series, operating in 2 different pressure regimes. Prior to mercury intrusion the samples were vacuum dried for 10 minutes.

Hydrogen-temperature programmed reduction (H_2-TPR) and Oxygen-temperature programmed oxidation (O_2-TPO) were combined to check if the CuO samples were reduced completely in the tube furnace when Cu was needed for the dry reforming test. The measurements were carried out on the ChemStar TPX Chemisorption Analyzer. First, the samples were degassed at 350 ℃ for 2 h with 50 mL/min pure He flushing. After cooling down to 50 ℃, the first O_2-TPO was carried out from 50 ℃ to 800 ℃ with 10 ℃/min ramping rate, under 5% O_2/He at a flow rate of 50 mL/min. After cooling down to 50 ℃ again, the H_2-TPR was performed to 800 ℃ with 10 ℃/min ramping rate, under 50 mL/min of 5% H_2/Ar. The second O_2-TPO was done with the same procedure as the first one after cooling down.

3.2.3 Plasma-catalytic performance test of the catalysts

3.2.3.1 Set-up of the DBD reactor

A fixed bed DBD reactor as illustrated in Figure 3.2 was applied to study the plasma-catalytic performance for dry reforming of the catalysts with different pore sizes. The inner electrode was a stainless steel rod with outer diameter of 13 mm. An alumina dielectric tube with 21.8 mm outer diameter and 17.41 mm inner diameter was coaxially placed over the stainless steel rod as a dielectric barrier, so the discharge gap between the inner electrode and dielectric barrier was about 2.2 mm. A stainless steel mesh was used as outer electrode by tightly winding it on the outside of the alumina tube. The length of the outer electrode, which determines the length of the discharge zone, was 10 mm. 4 g of catalyst powder was filled in the whole plasma zone with 2 g glass wool at both sides to fix the powder.

The inner electrode was grounded, and the outer electrode was connected to a high voltage supplied by a function generator (Tektronix, AFG 2021) and a high voltage amplifier (TREK, Model 20/20C-HS). The generator provided a signal with a frequency of 3000 Hz, and the amplifier amplified the power of the input signal by 2000. A high-voltage probe (Tektronix, P6015A) was used to measure the voltage, and a Rogowski coil (Pearson 4100) was used to monitor the current. The current profile was filtered by applying a Savitzky-Golay filter of polynomial order 3 to exclude the signal noise [7]. The number of peaks per period in the current profile, after excluding signal noise, was used to study the number of micro-discharges in this study. It should be noted that this is not the exact number of discharges that occurred in the reactor, since the discharges might have occurred simultaneously, while only one peak of current was shown in the current profiles. In addition, some small discharges might be excluded as signal noise. However, multiple collections of current data and an average value of the number of current peaks can be used to compare and study the effects of different samples on the discharge even though the obtained numbers should not be interpreted as absolute but as apparent values. The charge in the plasma was monitored by a capacitor (10 nF) connected in series and a low-voltage probe (Picotech, TA150) connected in parallel with it. The displaced charge was obtained from it by taking the detected charge difference before and after discharge. All the signals were collected by an oscilloscope (Picotech, Picoscope 6402D) and shown on a PC. The data was calculated in real time to adjust the amplitude of the input signal from the amplifier, in order to keep the power of the power supply constant at 50 W. The calculation and counting of electrical parameters are done automatically by a MATLAB script.

3.2.3.2 Catalyst performance evaluation

The copper oxide was filled and tested directly in the reactor. However, to evaluate the copper samples, the copper oxide powder was reduced in a tube furnace (Carbolite Gero TF1 12/60/300) with 250 mL/min of 2% H_2/Ar gas flow at 450 °C for 8 h before being packed into the reactor. The reduction temperature of CuO was 450 °C which is determined by H_2-TPR.

For the plasma-catalytic dry reforming test, the feed gas consisted of 5 mL/min of CH_4 and 5 mL/min of CO_2, and the flow rate was controlled by mass flow controllers (Bronkhorst EL-FLOW Select). 10 mL/min of N_2 was added in the outlet gas as internal standard to exclude the impact of the gas expansion. The product gases from the reactor outlet were analyzed by an online gas chromatograph (Trace GC 1310, Interscience) equipped with a thermal conductivity detector (TCD) and a flame ionization detector (FID). After flushing the filled reactor with the feed gas for 30 minutes without plasma, the composition of the outlet gas was analyzed and recorded as blank measurements, and the concentrations of CO_2 and CH_4 were denoted as $CO_{2,in}$ and $CH_{4,in}$ respectively. Then the power was applied to generate plasma, and kept at 50 W for 30 minutes. The gases generated and unconverted feed gas after 30 min were analyzed and marked with “out”, i.e., $CO_{2,out}$, $CH_{4,out}$, $H_{2,out}$, CO_{out} and $C_xH_yO_{z,out}$. The conversion (X) of CO_2 and CH_4 are calculated by Eq. (1) and Eq. (2)

$$X_{CO_2} = \frac{CO_{2,in} - CO_{2,out}}{CO_{2,in}} \cdot 100\% \tag{1}$$

$$X_{CH_4} = \frac{CH_{4,in} - CH_{4,out}}{CH_{4,in}} \cdot 100\% \tag{2}$$

The selectivity (S) of the products are defined as Eq. (3) to Eq. (5)

$$S_{H_2} = \frac{H_{2,out}}{2(CH_{4,in} - CH_{4,out})} \cdot 100\% \tag{3}$$

$$S_{CO} = \frac{CO_{out}}{(CH_{4,in} - CH_{4,out}) + (CO_{2,in} - CO_{2,out})} \cdot 100\% \tag{4}$$

$$S_{C_xH_yO_z} = \frac{x \cdot C_xH_yO_{z,out}}{(CH_{4,in} - CH_{4,out}) + (CO_{2,in} - CO_{2,out})} \cdot 100\% \tag{5}$$

The DRM reaction produces CO, H_2 and various hydrocarbon products, resulting in the expansion with an unknown coefficient and pressure rise of the outlet gases. The GC always depressurizes the gases to ambient pressure during sampling, so the direct calculation of conversion and selectivity from gas_{out} and gas_{in} obtained by the GC will have systematic errors. Therefore, 10 mL/min N_2 flow was applied as the internal standard to reduce the errors [29].

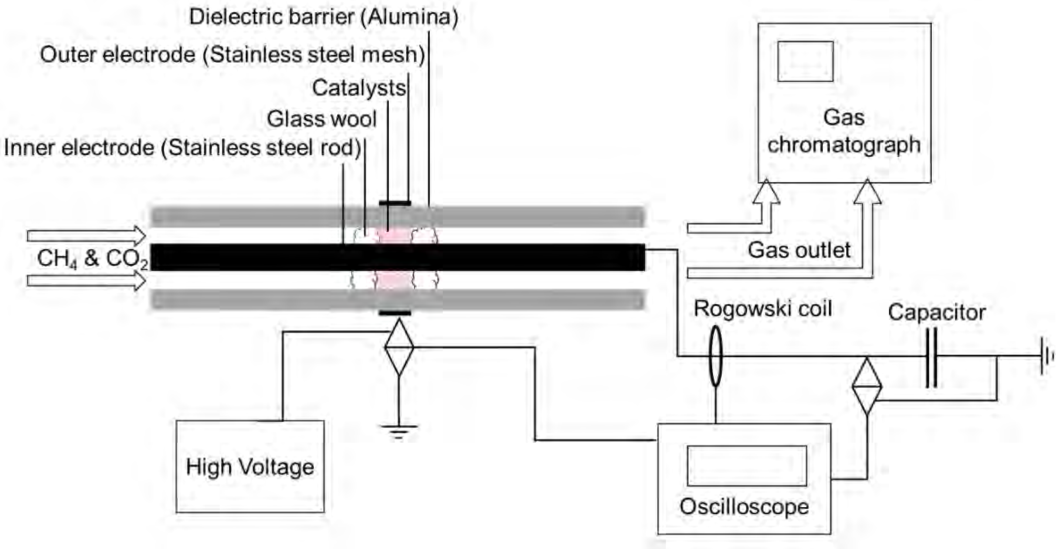

Figure 3.2. DBD reactor setup for the dry reforming of methane.

3.3 Results and discussion

3.3.1 Crystal phases of the catalysts

The XRD patterns of the 3D porous CuO samples, synthesized from silica particles of different sizes, are shown in Figure 3.3. A sample with copper oxide loading but without etching away the SiO_2 is also characterized by XRD for comparison. It is obvious that a broad peak attributed to (111) reflection of SiO_2 is detected at $2\theta = 21.60°$ in the sample without etching, while it is no longer present in all etched porous copper oxide samples. The diffraction peaks at other angles, such as the peaks at $2\theta = 32.51°$, 35.42°, 38.71°, 48.72°, 53.49°, 61.52°, 66.22°, 68.12°, 72.37°, and 74.98° are indexed to the (1 1 0), (0 0 2), (1 1 1), (2 0 -2), (0 2 0), (1 1 -3), (3 1 -1), (2 2 0), (3 1 1), and (0 0 4) crystal planes of Tenorite CuO (JCPDS 48-1548). These peaks get sharper with the increase of particle size of the applied SiO_2 template during the syntheses (from CuO-10 to CuO-600), suggesting that the crystallinity and crystal size of CuO is getting higher owing to the CuO sintering by calcination at 650 °C. When smaller silica particles are used as templates, the gaps between the particles are smaller, which restricts the growth of crystallites, resulting in smaller grains of copper oxide and thinner pore walls. On the contrary, thicker pore walls and larger copper oxide crystallites are obtained when larger silica particles are used as templates. The crystallinity and crystal size of the CuO-600, CuO-1000 and CuO-2000 is similar, and no longer increase significantly with increasing particle size of the SiO_2 template.

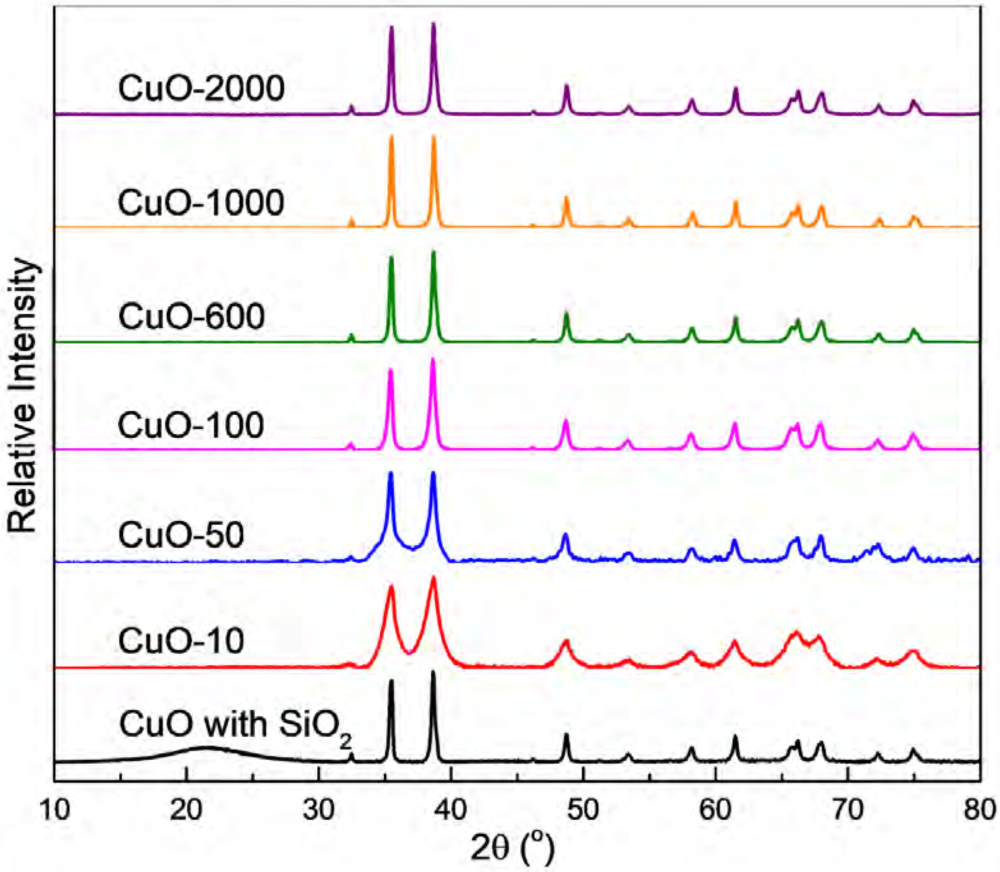

Figure 3.3. The normalized XRD patterns of the 3D porous CuO samples.

3.3.2 Pore structure of the catalysts

SEM measurements were carried out to observe the morphology and pore sizes of the 3D porous CuO samples, and the images are shown in Figure 3.4. All the samples in the figure show spherical pores with relatively uniform size. According to the design of the synthesis process shown in Figure 3.1, the pores should be connected, and the holes in the pore walls observed in Figure 3.4 fit that. EDX analysis proves that the silica particles can be etched away successfully by NaOH solution (see Table B.1 in Appendix B) as less than 0.5% Si is left on the surface of CuO. 30 measurable pores in the images were measured to get the average pore size of the samples, and it was found that the pore size of the samples were similar (slightly less) to the diameter of the corresponding silica particle templates used in the synthesis. The mean diameter of CuO-100, CuO-600, CuO-1000 and CuO-2000 are about 82 nm, 574 nm, 937 nm, and 1891 nm, respectively. The smaller diameter is probably caused by shrinkage of the pores during the calcination at 650°C and/or the etching of silica spheres. The pore size of CuO synthesized from 10 nm and 50 nm silica particles were too small to be observed by scanning microscopy, but their pore size can be characterized and calculated by N_2-sorption, by which more comprehensive pore diameter data of the samples can be obtained, including information of the bulk of the pores (adsorption branch) and the pore necks (desorption branch). A closer look inside the pores reveals that the junctions between the spherical pores (i.e. pore necks) are smaller in size than the diameter of the spherical pores themselves. This can be more clearly observed in the CuO SEM images of the larger pores. This is reasonable because the size of the contact surface between the template silica spheres was smaller than the diameter of the spheres themselves. The shape of the pores is a stack of multiple hollow spheres, rather than a cylindrical channel. The SEM images of CuO-100, CuO-600, CuO-1000 and CuO-2000 were only used to measure their diameter of the pore bodies, not the size of the pore necks. To measure the diameter of the pore necks more accurately, mercury intrusion porosimetry was applied.

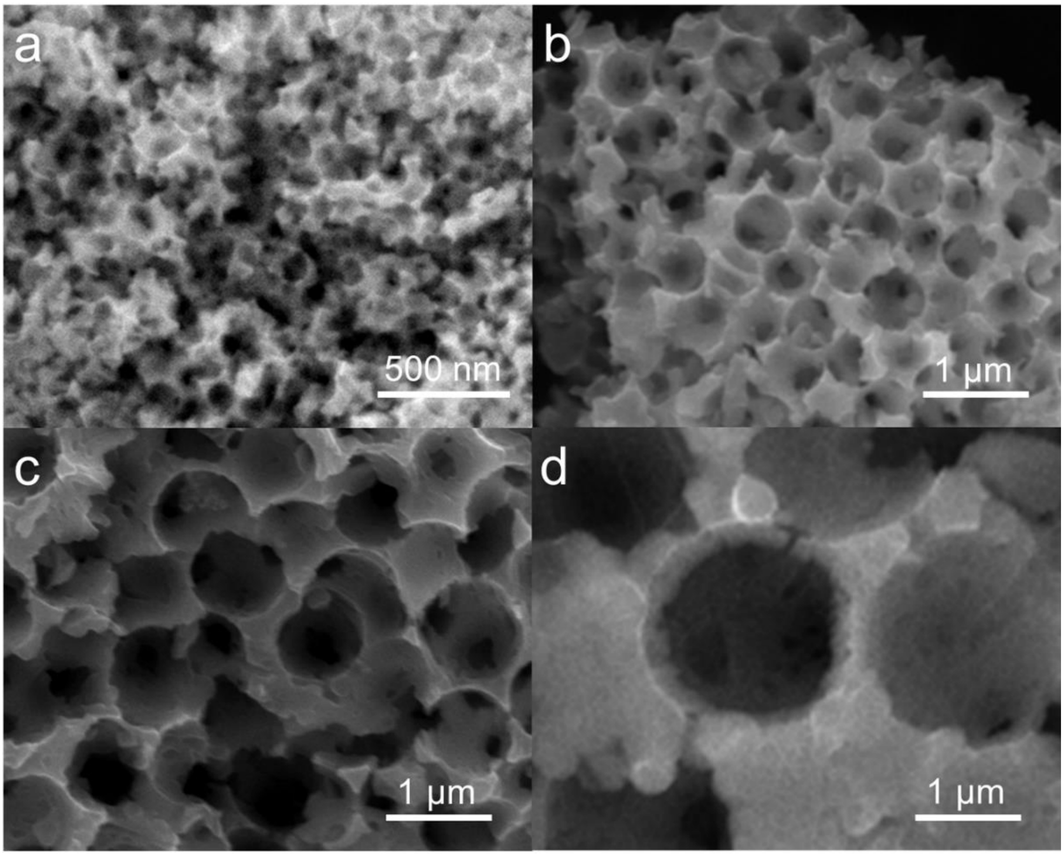

Figure 3.4. SEM images of 3D porous CuO. (a) CuO-100 synthesized from silica particles with a diameter of about 100 nm. (b) CuO-600 synthesized from silica particles with a diameter of about 600 nm. (c) CuO-1000 synthesized from silica particles with a diameter of about 1 μm. (d) CuO-2000 synthesized from silica particles with a diameter of about 2 μm.

Figure 3.5 displays the pore size distribution of the porous copper oxide samples based on N_2-sorption (NLDFT adsorption branch) and mercury intrusion porosimetry. The pore size distribution (calculated by BJH desorption branch) and N_2-soption isotherms of CuO-10 and CuO-50 are shown in Figure B.1 in Appendix B to obtain more complete pore structure information. Since nitrogen sorption and mercury intrusion porosimetery are applicable to different pore size ranges, the CuO-10 and CuO-50 samples were characterized by nitrogen sorption, and the other samples were determined by mercury intrusion porosimetry. Due to the different systematic errors of the two characterization methods, the pore size distribution of samples obtained by different methods cannot be accurately compared, but they are put into the same figure to roughly compare the pore size distributions and get an intuitive impression. Important to note is that, due to the ink-bottle effect, the pore size obtained by mercury intrusion is only the size of pore necks, which will be smaller than the actual bulk pore size (cf. SEM images, Figure 4) of the samples [30,31], while the pore size obtained by N_2-sorption includes both pore neck size (desorption branch, Figure B.1) and bulk pore size (adsorption branch, Figure 3.5). The pore size distribution of all samples suggest relatively uniform pores [30]. It is worth mentioning that because the synthesized CuO samples are powders with tens of µm particle size, there is another broad pore size distribution at the micrometer scale in the results of mercury intrusion (as shown in Figure B.2 in Appendix B), which reflects the size of the inter-particle voids rather than the bulk pore size [32,33].

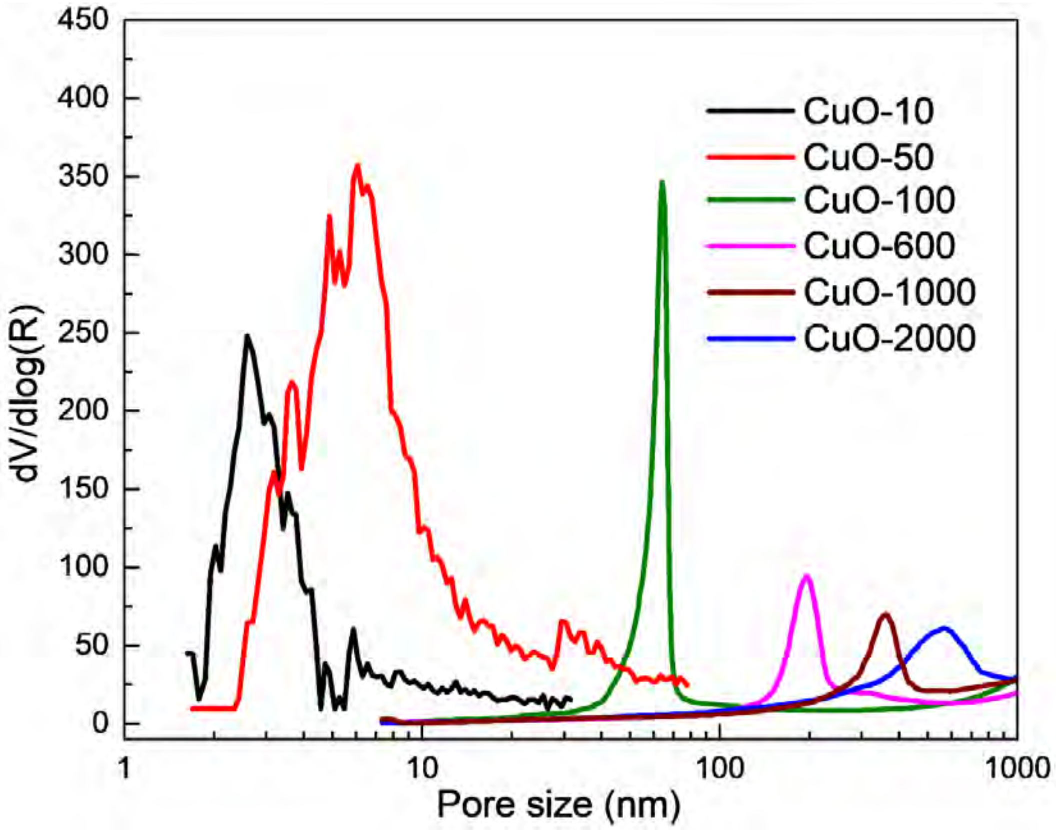

Figure 3.5. Pore size distribution of 3D porous CuO samples obtained by N_2-sorption (for CuO-10 and CuO-50) and mercury intrusion (for the other samples).

The maxima of the pore size distribution calculated from N_2-sorption and mercury intrusion porosimetry of all CuO samples are listed in Table 3.1. For CuO-10 and CuO-50, the pore size is much smaller than the diameter of the silica spheres used in the synthesis, which might be caused by shrinkage during thermal treatments [34]. In addition, consistent with the conclusions drawn from the SEM images, the pore neck size of CuO-100, CuO-600, CuO-1000, and CuO-2000 measured by mercury intrusion is smaller than the diameter of the silica spheres used in the synthesis. Although the pore size of all porous samples is not equal to the diameter of the silica spheres, it is obvious that there is a positive correlation with it, resulting in an increasing trend with the use of larger silica template particles. Hence, uniform pore catalysts with different pore sizes are indeed successfully prepared over a large pore size span. During the synthesis of porous samples, the silica templates were calcined to 800 °C, which slightly melts the contact surfaces between the silica spheres and connects the particles together. Silica with different particle sizes were calcined at the same temperature and for the same duration, while their surface melting degrees could be different, resulting in different particle connection surface sizes. This might be one of the reasons for the deviations in the pore neck diameter after etching, relative to the silica template size. For example, this calcination temperature and duration may be most suitable for 100 nm silica particles, so the pore neck diameter after etching is closest to the particle size. The apparent surface area determined using the Brunauer–Emmett–Teller (BET) theory by N_2-sorption is also listed in Table 3.1. Initially, it decreases rapidly with increasing pore size from CuO-10 to CuO-100. However, for the macroporous samples from CuO-100 to CuO-2000, the differences in specific surface area are very small as the pore size changes.

Table 3.1. Pore sizes, specific surface areas and mean particle size of 3D porous CuO samples obtained from N2-sorption, SEM and mercury intrusion.

Samples	Bulk pore diameter	Pore neck diameter	Specific surface area	Mean particle diameter[d]	Packing density	Packing density of reduced sample
CuO-10	2.6 nm[a]	/	236 m^2/g	8 μm	1.6 g/mL	1.7 g/mL
CuO-50	6.1 nm[a]	4.3 nm[a]	152 m^2/g	8 μm	1.7 g/mL	1.8 g/mL
CuO-100	82 nm[b]	64.0 nm[c]	8 m^2/g	10 μm	1.7 g/mL	1.7 g/mL
CuO-600	574 nm[b]	195.0 nm[c]	2 m^2/g	9 μm	1.6 g/mL	1.7 g/mL
CuO-1000	937 nm[b]	361.2 nm[c]	2 m^2/g	9 μm	1.6 g/mL	1.7 g/mL
CuO-2000	1891 nm[b]	565.6 nm[c]	1 m^2/g	10 μm	1.7 g/mL	1.8 g/mL

[a] Pore size characterized by N_2-sorption, including bulk pore diameter (deduced by NLDFT from the adsorption branch) and pore necks diameter (deduced by BJH from the desorption branch). [b] Bulk pore size measured and calculated by SEM images. [c] Pore size characterized by mercury intrusion, which is considered to only account for the size of the pore necks. [d] The particle distribution is broad (see the SEM images in Figure B.3), and this mean value is only present as a rough indication of differences in size between different powders but cannot be used to derive conclusion about e.g. void space due to the broad particle size distribution.

In addition, as shown in Figure B.3, the porous CuO particles synthesized by the method in this chapter are not uniform in shape and particle size. The particle diameters of the porous CuO particles range from ~5 μm to ~40 μm, and the average particle diameters calculated from measurements of more than 50 particles from the SEM images of Figure B.3 are summarized in Table 3.1. As shown in the table, compared with the large differences between the pore diameters (ranging from 2.6 to 1891 nm), the difference in mean particle diameter between the sample particles was relatively small, and the particle diameter did not show an obvious tendency to increase with increasing pore size. The average particle diameter of CuO-10 and CuO-50 was slightly smaller than for the other samples, because they included more small particles around 5 μm. Due to the similar mean particle diameters of the samples, their packing densities in the reactor, calculated from the weight of the particles packed in the discharge zone and the volume of the discharge space, as shown in Table 3.1, did not show significant variations with pore size. Nevertheless, it is important to realize that this (small) variation in particle diameter can also affect the performance results to some extent. Indeed, the packed bed in this study has a quite complex texture.

3.3.3 Dry reforming performance of catalysts with different pore sizes

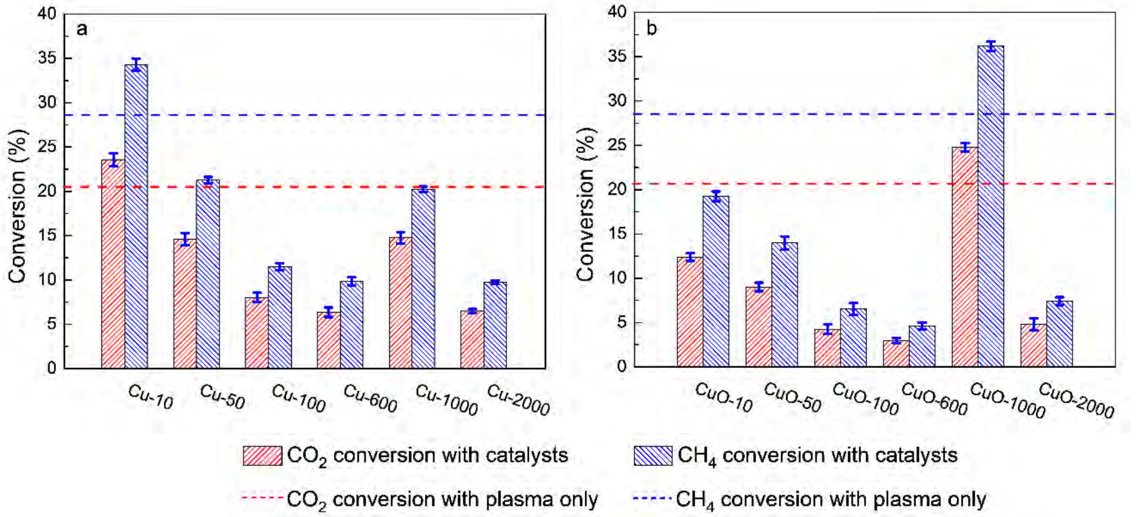

Figure 3.6. Conversion of CH_4 and CO_2 in plasma-catalytic dry reforming, of 3D porous (a) Cu and (b) CuO samples with different pore sizes. The dashed line is the conversion of the empty reactor only with plasma at the same gas flow rate. The error bars were obtained from standard errors based on three repeats.

Plasma-catalytic dry reforming tests were performed on porous samples with different pore sizes before and after reduction. Because the TPR in this chapter cannot accurately and quantitatively analyze the hydrogen consumption when the majority of the sample is reduced and only small amounts would be left as an oxide, a 2-cycle TPO with an intermediate TPR was used to determine whether the sample was completely reduced in the tube furnace. Figure B.4 in Appendix B shows the results of TPO-TPR-TPO of the samples after reduction. Although the TCD signal curves of the two TPOs are very different due to crystal changes caused by the sample being heated to 800 °C in the first cycle TPO and TPR, the integrated areas of the two TPOs are consistent. Therefore, the oxygen consumption of the two TPOs was the same, indicating that the CuO samples were completely reduced in the tube furnace. The conversions of CH_4 and CO_2 in the plasma-catalytic reaction are shown in Figure 3.6. The dashed lines in Figure 6 are the CH_4 and CO_2 conversions at the same gas flow in an empty reactor only with plasma. In most cases, similar to the results in the majority of literature on plasma dry reforming, the CH_4 and CO_2 conversions for the catalysts were lower than those in the empty reactor at the same flow rate. This is because the positive effects of catalysts are not enough to compensate for their negative effects, such as hindering discharge and reducing space time. However, the best performing samples for a certain pore size in Cu and CuO (i.e. Cu-10 and CuO-1000) exhibited higher conversion than the empty reactor, illustrating the importance of the pore size effect on the plasma catalytic process, and the positive effects of the fully packing catalyst with suitable properties in the plasma catalytic dry reforming can cover its negative effects. There are very similar trends in Figure 3.6a (reduced copper samples) and Figure 3.6b (unreduced copper oxide samples). The first trend is that among the samples with pore sizes smaller than Cu-1000 or CuO-1000, the smaller the pore size, the higher the obtained conversion. This seems normal from a thermocatalytic dry reforming point of view, because the smaller pore catalysts have a higher surface area (see specific surface area of the different samples in Table 3.1) to facilitate the adsorption and catalytic reaction at the surface. In a plasma reaction, however, it is unusual. Previous studies on pore size generally suggested that the high surface area in pores smaller than the Debye length of the plasma (~500 nm at typical plasma catalysis conditions [20]) was ineffective since the smaller the pore size, the fewer high energy electrons in the plasma can propagate into the pores during the discharge [19-21,35-38]. The direct comparison of the performance of catalysts with different pore sizes (Figure 3.6) shows results that are in contrast to the conclusions drawn from previously reported simulations or experimental studies of plasma propagation within catalyst pores [20,21,36,37]. The results suggests that although electrons may not be able to enter the smaller pores to activate gas molecules and interact with the catalyst surface inside the pores, the smaller pores still have some advantages, which are more important than the fact that plasma cannot enter inside these small pores.

1. The advantage of materials with large pores enabling more electrons to enter to react with the surface may not be as great. According to the data shown in Table 3.1, even if the pore size is large enough that the plasma streamer can propagate directly in it (CuO-1000 and CuO-2000), resulting in the effective surface area of plasma reaction equal to its total surface area, the specific surface area of the catalyst with macropores is so low that it could not bring much benefit to the catalytic reaction.

2. Although it is difficult for electrons in the plasma to enter the pores smaller than the Debye length to activate gas molecules due to the prevention of the plasma sheath, radicals or positively charged ions generated in the plasma will not be blocked. These plasma species may still diffuse into the pores, or even be accelerated out of the plasma into the pore, and thus react with the catalyst surface [38,39]. The lifetime of the free radicals will determine how deep they can penetrate into the pore.

3. For the catalysts with small pores (i.e., 500 nm or below), although the plasma can only propagate in the voids between the particles and cannot enter the pores, the high roughness of the outer surface resulting from the larger number of pores, causes electric field enhancement in the plasma, which creates more reactive plasma species that can interact with the catalyst.

4. The larger external surface area of the catalysts with small pores (again due to a higher number of pores at the surface), may be another reason for their better performance.

5. It can also be observed that the plasma power and the average filament charge show a clear correlation with the conversion of the reactants (refer to Table 3.2 later for more details) [22,40-42].

6. As mentioned before, the CuO-10 and CuO-50 particles had slightly (10−20%) smaller mean particle diameters (8μm versus 9−10μm). The void space between the particles and the contact points between particles might be different. This provides a complexity of positive and negative effects of performance that are difficult to estimate as they are mutually

interfering and are expected to have an optimum. But they might be a reason for the differences in conversion of CO_2 and CH_4 [43-45]. However, since the differences in mean particle diameter between the samples were small, and the packing densities did not show an obvious trend with pore size, it is difficult to estimate its role. Although the differences in particle sizes and packing densities are smaller than the 3 orders of magnitude differences in pore sizes, we cannot exclude its effect.

7. The large crystallinity of catalysts with large pores shown in Figure 3.3 is also unfavorable for the plasma catalytic dry reforming,[46] which may also explain the better performance of the catalysts with smaller pores.

In most cases, Cu with the same pore size exhibited better performance than CuO (cf. Figure 3.6a and 6b) as metals are the typical active components for dry reforming reactions [22,35]. An exception is observed for the samples synthesized from the 1 μm silica spheres, i.e., the conversion of CuO-1000 is higher than of Cu-1000. These samples are also exceptions to the trend that the smaller the pore size, the better the performance. Indeed, these samples show a higher conversion in plasma-based dry reforming than both the smaller and larger pore size samples, and CuO-1000 even shows the highest conversion among all the unreduced CuO samples. This can be attributed to the electric field enhancement in the pores with diameters close to the plasma Debye length (hundreds of nanometers at typical plasma catalysis conditions) [19,20]. This electric field enhancement enables Cu-1000 and CuO-1000 to perform better than the other samples. Since mainly surface discharges occur in DBD plasma packed with materials with relatively low dielectric constant,[22,35,47] such as CuO ($\varepsilon_r = 18.1$), the electric field enhancement of it due to surface charging is stronger than that of Cu-1000. Metals are in this context equivalent to a dielectric with infinite dielectric constant, and thus, the plasma will mainly be characterized by local filamentary microdischarges [22,35,47]. As samples with small pores can provide more and smaller discharge gaps for the local filamentary microdischarges, they are more favorable in Cu samples for the plasma reaction than the electric field enhancement of Cu-1000 [22,47]. The above factors together can explain why CuO-1000 shows the highest conversion of the unreduced CuO samples, while Cu-10 is the best among the reduced Cu samples.

Among the other macroporous samples with similar specific surface area, CuO-2000 showed better performance than CuO-600, while the performance of Cu-2000 is similar to that of Cu-600. This might also because the discharge mode dominated by surface discharges in CuO is more in line with the simulation of plasma propagation in pores,[20] which predicts that a larger pore size allows more electrons to enter. However, in case of metallic materials, the discharge mode (characterized by local filamentary micro-discharges) is different.

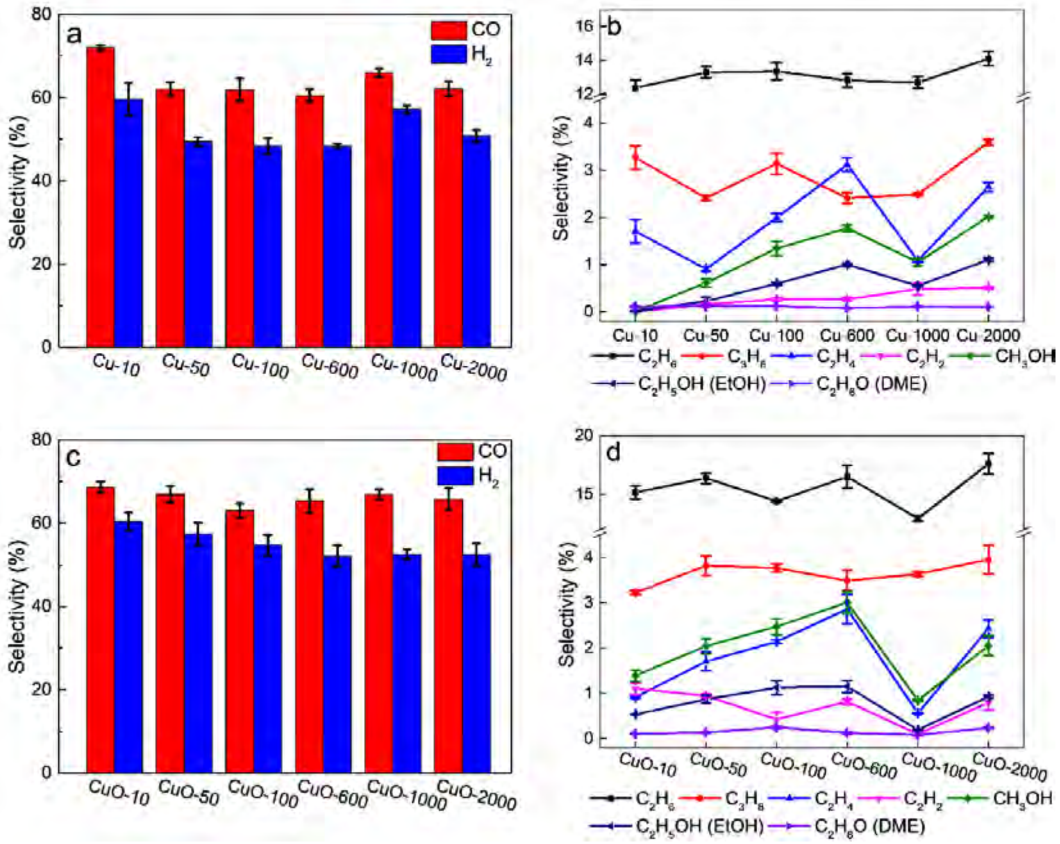

Figure 3.7. Product selectivities in plasma-catalytic dry reforming, for CO and H_2 of 3D porous Cu (a) and CuO (c) samples with different pore sizes, and for ethane, propane, ethylene, acetylene, methanol, ethanol and dimethyl ether of 3D porous Cu (b) and CuO (d) samples with different pore sizes. The error bars were obtained from standard errors based on three repeats.

The selectivities of the main components formed in plasma-catalytic dry reforming with the various 3D porous samples with different pore sizes are plotted in Figure 3.7. The carbon and hydrogen mass balance (shown in Figure B.5 in Appendix B) is not entirely 100%. Therefore there might still be a few possible liquid products and carbon deposits attached to the catalyst and the reactor, as well as the presence of other gaseous products that were not calibrated in the gas chromatograph, which cannot be counted. As shown in Figure 3.7a and Figure 3.7c, syngas is the predominant product in all experiments, and the CO selectivity is always higher than that of H_2. When comparing the samples with different pore sizes, some products do not differ significantly in selectivity, while others do. Interestingly, the difference in selectivity appears to correlate with the conversion of the reactants. A rough trend seems to be that samples exhibiting higher CH_4 and CO_2 conversions also have higher syngas (CO and H_2) selectivities, but lower selectivities for some unsaturated hydrocarbons and oxygenated organics, such as ethylene, methanol, and ethanol. The selectivity decrease is most striking for the Cu-1000 and CuO-1000 samples, and may be caused by the enhanced electric field in the samples, causing a higher conversion due to the higher energy input, and apparently a lower selectivity to these unsaturated hydrocarbons and oxygenates, in line with literature. [12,25] Besides the electric field enhancement, the reaction of radicals within the pores is another factor that might affects the selectivity. [38,39] The trends in selectivity for the various products are different, indicating a different impact of the pore size on the reaction paths of the radicals. For example, the selectivity towards acetylene is low in CuO-1000 but relatively high in CuO-10, although both of them show a high conversion of CO_2 and CH_4.

The electrical signals of the plasma experiments were recorded and collected by an oscilloscope. The fitted Lissajous figures (consisting of the slopes calculated from the Lissajous figures of multiple experiments) are shown in Figure B.6. Examples of raw data of the Lissajous figures are shown in Figure B.7. The collected and calculated electrical signal data from these are summarized in Table 3.2. As seen in the table, 26–28 kV peak-to-peak voltage (U_{pp}) was applied to achieve a constant 50 W supplied power. However, depending on some factors, such as the structure of the reactor and its internal packing materials, at the same supplied power, the distribution, number and intensity of the discharges are different, resulting in different plasma powers. The portion of the supplied power that was not converted to plasma power was lost in the circuit as heat or returned to the source as reactive power. A higher plasma power, such as for the Cu-10, CuO-10, and CuO-1000 samples, means higher energy input, which produces a more reactive plasma, leading to their higher conversion. The average number of micro-discharges per period is counted by the number of peaks in the normalized current profile after excluding signal noise. It may not be the exact number of micro-discharges, but subject to some system errors, as some discharges may coincide, or some may be too small and therefore are excluded as signal noise. By dividing the transferred charge by the number of micro-discharges in the same period, we obtain the average filament charge, which is a measure for the average strength of the discharge. Both a larger number of micro-discharges and more powerful discharges can have a positive effect on the conversion of plasma-based dry reforming. However, it is difficult for both to achieve relatively high values in the same reaction. As shown in Table 3.2, a higher average filament charge always corresponds with fewer discharges, and exhibits higher conversion, cfr. Figure 3.6. Therefore, our results suggest that the strength of the discharges has a larger effect on the conversion of plasma-based dry reforming than the number of micro-discharges.

However, most copper samples showed lower plasma power and discharge intensity than copper oxide with the same structure, despite they had a higher conversion of CO_2 and CH_4. The packing of the porous Cu powders in the reactor made some conductive particles to be directly connected to the grounded inner electrode to form an equipotential, which may cause most of the discharge to occur in the small gaps between the outermost particles (probably at the same potential as the electrode) and the dielectric barrier, and less point-to-point micro-discharges in the gaps between the other powders in the gap. Furthermore, surface discharges on the particles may not be present. Although the reduced Cu has a negative impact on the discharge, they showed better performance in most cases than the CuO samples with higher plasma power and more produced radicals and ions, probably due to its better dry reforming catalytic activity.

Table 3.2. Electrical characterization data measured and calculated from the recorded signals of the oscilloscope of the DRM experiments with the samples of different pore sizes.

Samples	U_{pp} (kV)	Power supplied (W)	Plasma power (W)	Number of micro-discharges (a.u./T)	Average filament charge (nC/disch.)
Cu-10	26.3	50.5	19.5	141	4.2
Cu-50	28.3	50.2	15.7	137	3.8
Cu-100	26.7	50.2	16.5	168	3.3
Cu-600	27.3	50.2	16.5	154	3.2
Cu-1000	28.0	50.1	15.7	139	4.1
Cu-2000	26.6	50.3	17.2	165	3.8
CuO-10	26.9	50.4	20.1	138	4.0
CuO-50	26.7	49.9	19.3	156	3.6
CuO-100	26.4	50.3	19.7	134	5.0
CuO-600	26.4	50.3	19.2	155	4.3
CuO-1000	26.0	50.6	24.4	85	7.2
CuO-2000	26.8	50.5	19.5	151	3.9

3.4 Conclusion

In this study, we investigated the effect of catalyst pore size on plasma-based dry reforming. The samples evaluated in this study were 3D porous Cu or CuO, synthesized from uniform silica particles in the range of 10 nm to 2 μm used as templates. Since the samples have the same pore structure, and consist of the same single chemistry without the interference of a support material, the plasma results can clearly show the influence of the catalyst pores in the plasma-based dry reforming.

Based on the conclusions drawn from previous simulation studies, we would expect that the larger the pore size, the better the catalyst performance, and the best results are obtained for catalyst pore sizes above the plasma Debye length (hundreds of nanometers at typical plasma catalysis conditions[19,20]). That is because the larger the pore size, the more electrons can propogate into it, and the pores larger than the Debye length allow the plasma streamer to penetrate inside the catalyst pores and thus generates a larger contact area between plasma and catalyst surface for chemical reactions. However, our results do not reveal that the larger catalyst pore size is more favorable for the plasma reaction, but they show the opposite trend in most cases, with the exception of CuO-1000 (Cu-1000 as well). This suggests that whether the electrons with high energy in the plasma can enter the catalyst pores or not is not the most important factor in plasma-catalytic reaction. Among the reduced Cu samples, Cu-10 showed the highest conversion of CH_4 and CO_2, while among the CuO samples, CuO-1000 showed the highest conversion. The higher the conversion of CH_4 and CO_2, the generally higher is the selectivity of syngas among the various product, and the lower is the selectivity of some unsaturated hydrocarbons and oxygenated organics. From the correlation with the electrical characteristics, we can conclude that the strength of the micro-discharges has an important effect on the conversion of CH_4 and CO_2 and the selectivity of the products, although not perfectly correlated.

In the 3D porous samples synthesized by the template method, the thickness of the pore wall varies with the pore size, resulting in changes in the crystallinity of the components. Samples with larger pore sizes have higher crystallinity, which is detrimental to the conversion of plasma-based dry reforming [46]. The difference in specific surface area for samples with pore sizes smaller than 100 nm and samples with larger pores is 2 orders of magnitude.

Therefore, even if the plasma streamers can propagate into the large pores and react with the entire surface of the sample, which is not possible for the pores smaller than the Debye length, they do not differ much in contact area with plasma thus will not bring much improvement. On the other hand, even if plasma streamers cannot propagate in the smaller pores, radicals or positively charged ions can still diffuse into these catalysts, and the effective contact area of these radicals and ions in small pores is much larger than for catalysts with larger pores.

In summary, catalysts with smaller pores were found to be generally better for plasma-based dry reforming, but there are exceptions depending on the properties of the materials. The possible electric field enhancement due to surface charging in the large pores of a certain pore size can greatly improve the reaction efficiency. This enhancement effect is strong for CuO, which is characterized by a relatively small dielectric constant, while it is weak for metallic catalytically active components. Therefore, in future research of catalysts for plasma reactions, macroporous supports with specific pore size (possibly several hundreds of nanometers) and metal active components with micropores (or the combination of both) are two potential feasible directions.

3.5 References

[1] Khoja, A. H.; Tahir, M.; Amin, N. A. S. Dry reforming of methane using different dielectric materials and DBD plasma reactor configurations. *Energy Convers. Manage.* **2017**, *144*, 262-274.

[2] Uytdenhouwen, Y.; Hereijgers, J.; Breugelmans, T.; Cool, P.; Bogaerts, A. How gas flow design can influence the performance of a DBD plasma reactor for dry reforming of methane. *Chem. Eng. J.* **2021**, *405*, 126618.

[3] Zhu, F.; Zhang, H.; Yan, X.; Yan, J.; Ni, M.; Li, X.; Tu, X. Plasma-catalytic reforming of CO_2-rich biogas over Ni/γ-Al_2O_3 catalysts in a rotating gliding arc reactor. *Fuel* **2017**, *199*, 430-437.

[4] Li, M.-w.; Xu, G.-h.; Tian, Y.-l.; Chen, L.; Fu, H.-f. Carbon Dioxide Reforming of Methane Using DC Corona Discharge Plasma Reaction. *J. Phys. Chem. A* **2004**, *108*, 1687-1693.

[5] Yi, Y.; Wang, X.; Jafarzadeh, A.; Wang, L.; Liu, P.; He, B.; Yan, J.; Zhang, R.; Zhang, H.; Liu, X.; Guo, H.; Neyts, E. C.; Bogaerts, A. Plasma-Catalytic Ammonia Reforming of Methane over Cu-Based Catalysts for the Production of HCN and H_2 at Reduced Temperature. *ACS Catalysis* **2021**, *11*, 1765-1773.

[6] Michielsen, I.; Uytdenhouwen, Y.; Pype, J.; Michielsen, B.; Mertens, J.; Reniers, F.; Meynen, V.; Bogaerts, A. CO_2 dissociation in a packed bed DBD reactor: First steps towards a better understanding of plasma catalysis. *Chem. Eng. J.* **2017**, *326*, 477-488.

[7] Uytdenhouwen, Y.; Van Alphen, S.; Michielsen, I.; Meynen, V.; Cool, P.; Bogaerts, A. A packed-bed DBD micro plasma reactor for CO_2 dissociation: Does size matter? *Chem. Eng. J.* **2018**, *348*, 557-568.

[8] Uytdenhouwen, Y.; Bal, K. M.; Michielsen, I.; Neyts, E. C.; Meynen, V.; Cool, P.; Bogaerts, A. How process parameters and packing materials tune chemical equilibrium and kinetics in plasma-based CO_2 conversion. *Chem. Eng. J.* **2019**, *372*, 1253-1264.

[9] Wang, B.; Mikhail, M.; Cavadias, S.; Tatoulian, M.; Da Costa, P.; Ognier, S. Improvement of the activity of CO_2 methanation in a hybrid plasma-catalytic process in varying catalyst particle size or under pressure. *J. CO2 Utilzation* **2021**, *46*, 101471.

[10] Vakili, R.; Gholami, R.; Stere, C. E.; Chansai, S.; Chen, H.; Holmes, S. M.; Jiao, Y.; Hardacre, C.; Fan, X. Plasma-assisted catalytic dry reforming of methane (DRM) over metal-organic frameworks (MOFs)-based catalysts. *Appl. Catal. B Environ.* **2020**, *260*, 118195.

[11] Zeng, Y.; Zhu, X.; Mei, D.; Ashford, B.; Tu, X. Plasma-catalytic dry reforming of methane over γ-Al_2O_3 supported metal catalysts. *Catal. Today* **2015**, *256*, 80-87.

[12] Tu, X.; Gallon, H. J.; Twigg, M. V.; Gorry, P. A.; Whitehead, J. C. Dry reforming of methane over a Ni/Al_2O_3 catalyst in a coaxial dielectric barrier discharge reactor. *J. Phys. D Appl. Phys.* **2011**, *44*, 274007.

[13] Song, H. K.; Choi, J.-W.; Yue, S. H.; Lee, H.; Na, B.-K. Synthesis gas production via dielectric barrier discharge over Ni/γ-Al_2O_3 catalyst. *Catal. Today* **2004**, *89*, 27-33.

[14] Wang, L.; Yi, Y.; Wu, C.; Guo, H.; Tu, X. One-Step Reforming of CO_2 and CH_4 into High-Value Liquid Chemicals and Fuels at Room Temperature by Plasma-Driven Catalysis. *Angew. Chem. Int. Ed.* **2017**, *56*, 13679-13683.

[15] Sentek, J.; Krawczyk, K.; Młotek, M.; Kalczewska, M.; Kroker, T.; Kolb, T.; Schenk, A.; Gericke, K.-H.; Schmidt-Szałowski, K. Plasma-catalytic methane conversion with carbon dioxide in dielectric barrier discharges. *Appl. Catal. B Environ.* **2010**, *94*, 19-26.

[16] Michielsen, I.; Uytdenhouwen, Y.; Bogaerts, A.; Meynen, V. Altering Conversion and Product Selectivity of Dry Reforming of Methane in a Dielectric Barrier Discharge by Changing the Dielectric Packing Material. *Catalysts* **2019**, *9*.

[17] Andersen, J. A.; Christensen, J. M.; Østberg, M.; Bogaerts, A.; Jensen, A. D. Plasma-catalytic dry reforming of methane: Screening of catalytic materials in a coaxial packed-bed DBD reactor. *Chem. Eng. J.* **2020**, *397*, 125519.

[18] Tu, X.; Whitehead, J. C. Plasma-catalytic dry reforming of methane in an atmospheric dielectric barrier discharge: Understanding the synergistic effect at low temperature. *Appl. Catal. B Environ.* **2012**, *125*, 439-448.

[19] Zhang, Q.-Z.; Bogaerts, A. Plasma streamer propagation in structured catalysts. *Plasma Sources Sci. Technol.* **2018**, *27*, 105013.

[20] Zhang, Q.-Z.; Bogaerts, A. Propagation of a plasma streamer in catalyst pores. *Plasma Sources Sci. Technol.* **2018**, *27*, 035009.

[21] Zhang, Y.-R.; Van Laer, K.; Neyts, E. C.; Bogaerts, A. Can plasma be formed in catalyst pores? A modeling investigation. *Appl. Catal. B Environ.* **2016**, *185*, 56-67.

[22] Zhang, Q.-Z.; Wang, W.-Z.; Bogaerts, A. Importance of surface charging during plasma streamer propagation in catalyst pores. *Plasma Sources Sci. Technol.* **2018**, *27*, 065009.

[23] Zheng, X.; Tan, S.; Dong, L.; Li, S.; Chen, H. $LaNiO_3$@SiO_2 core–shell nano-particles for the dry reforming of CH_4 in the dielectric barrier discharge plasma. *Int. J. Hydrogen Energy* **2014**, *39*, 11360-11367.

[24] Ray, D.; Nepak, D.; Vinodkumar, T.; Subrahmanyam, C. g-C_3N_4 promoted DBD plasma assisted dry reforming of methane. *Energy* **2019**, *183*, 630-638.

[25] Ray, D.; Reddy, P. M. K.; Subrahmanyam, C. Ni-Mn/γ-Al_2O_3 assisted plasma dry reforming of methane. *Catal. Today* **2018**, *309*, 212-218.

[26] Ray, D.; Nepak, D.; Janampelli, S.; Goshal, P.; Subrahmanyam, C. Dry Reforming of Methane in DBD Plasma over Ni-Based Catalysts: Influence of Process Conditions and Support on Performance and Durability. *Energy Technol.* **2019**, *7*, 1801008.

[27] Gao, X.; Lin, Z.; Li, T.; Huang, L.; Zhang, J.; Askari, S.; Dewangan, N.; Jangam, A.; Kawi, S. Recent Developments in Dielectric Barrier Discharge Plasma-Assisted Catalytic Dry Reforming of Methane over Ni-Based Catalysts. *Catalysts* **2021**, *11*.

[28] Xie, Q.; Zhuge, S.; Song, X.; Lu, M.; Yu, F.; Ruan, R.; Nie, Y. Non-thermal atmospheric plasma synthesis of ammonia in a DBD reactor packed with various catalysts. *J. Phys. D Appl. Phys.* **2019**, *53*, 064002.

[29] Pinhão, N.; Moura, A.; Branco, J. B.; Neves, J. Influence of gas expansion on process parameters in non-thermal plasma plug-flow reactors: A study applied to dry reforming of methane. *Int. J. Hydrogen Energy* **2016**, *41*, 9245-9255.

[30] Zhang, Y.; Yang, B.; Yang, Z.; Ye, G. Ink-bottle Effect and Pore Size Distribution of Cementitious Materials Identified by Pressurization–Depressurization Cycling Mercury Intrusion Porosimetry. *Materials* **2019**, *12*.

[31] Moro, F.; Böhni, H. Ink-Bottle Effect in Mercury Intrusion Porosimetry of Cement-Based Materials. *J. Colloid Interface Sci.* **2002**, *246*, 135-149.

[32] Mayer, R. P.; Stowe, R. A. Mercury porosimetry—breakthrough pressure for penetration between packed spheres. *J. Colloid Sci.* **1965**, *20*, 893-911.

[33] Palmer, H. K.; Rowe, R. C. The application of mercury porosimetry to porous polymer powders. *Powder Technol.* **1974**, *9*, 181-186.

[34] Feng, J.; Mo, W.; Ma, S.; Wang, Y.; Yang, J.; Su, X.; Wang, G.; Lin, M. Thermal shrinkage inhibition mechanism of fumed silica based thermal insulating composite. *Appl. Therm. Eng.* **2017**, *113*, 749-755.

[35] Bogaerts, A.; Zhang, Q.-Z.; Zhang, Y.-R.; Van Laer, K.; Wang, W. Burning questions of plasma catalysis: Answers by modeling. *Catal. Today* **2019**, *337*, 3-14.

[36] Kameshima, S.; Mizukami, R.; Yamazaki, T.; Prananto, L. A.; Nozaki, T. Interfacial reactions between DBD and porous catalyst in dry methane reforming. *J. Phys. D Appl. Phys.* **2018**, *51*, 114006.

[37] Hensel, K.; Katsura, S.; Mizuno, A. DC microdischarges inside porous ceramics. *IEEE Trans. Plasma Sci.* **2005**, *33*, 574-575.

[38] Snoeckx, R.; Aerts, R.; Tu, X.; Bogaerts, A. Plasma-Based Dry Reforming: A Computational Study Ranging from the Nanoseconds to Seconds Time Scale. *J. Phys. Chem. C* **2013**, *117*, 4957-4970.

[39] Loenders, B.; Engelmann, Y.; Bogaerts, A. Plasma-Catalytic Partial Oxidation of Methane on Pt(111): A Microkinetic Study on the Role of Different Plasma Species. *J. Phys. Chem. C* **2021**, *125*, 2966-2983.

[40] Neyts, E. C.; Bogaerts, A. Understanding plasma catalysis through modelling and simulation—a review. *J. Phys. D Appl. Phys.* **2014**, *47*, 224010.

[41] Woo Seok, K.; Jin Myung, P.; Yongho, K.; Sang Hee, H. Numerical study on influences of barrier arrangements on dielectric barrier discharge characteristics. *IEEE Trans. Plasma Sci.* **2003**, *31*, 504-510.

[42] Tilmatine, O.; Dascalescu, L.; Zeghloul, T.; Medles, K.; Fatu, A. Study of the Influence of the Different Parameters of the Atmospheric DBD Treatment on the Surface Roughness and the Electric Potential Distribution Generated After the Tribocharging of Polypropylene. *IEEE Trans. Ind. Appl.* **2021**, *57*, 4162-4169.

[43] Wang, W.; Butterworth, T.; Bogaerts, A. Plasma propagation in a single bead DBD reactor at different dielectric constants: insights from fluid modelling. *J. Phys. D Appl. Phys.* **2021**, *54*, 214004.

[44] Butterworth, T.; Allen, R. W. K. Plasma-catalyst interaction studied in a single pellet DBD reactor: dielectric constant effect on plasma dynamics. *Plasma Sources Sci. Technol.* **2017**, *26*, 065008.

[45] Kruszelnicki, J.; Engeling, K. W.; Foster, J. E.; Kushner, M. J. Interactions between atmospheric pressure plasmas and metallic catalyst particles in packed bed reactors. *J. Phys. D Appl. Phys.* **2020**, *54*, 104001.

[46] Rahemi, N.; Haghighi, M.; Babaluo, A. A.; Jafari, M. F.; Khorram, S. Non-thermal plasma assisted synthesis and physicochemical characterizations of Co and Cu doped Ni/Al_2O_3 nanocatalysts used for dry reforming of methane. *Int. J. Hydrogen Energy* **2013**, *38*, 16048-16061.

[47] Wang, W.; Kim, H.-H.; Van Laer, K.; Bogaerts, A. Streamer propagation in a packed bed plasma reactor for plasma catalysis applications. *Chem. Eng. J.* **2018**, *334*, 2467-2479.

Chapter 4 Plasma-based dry reforming of methane in a dielectric barrier discharge reactor: Importance of uniform (sub)micron packing/catalysts to enhance the performance

Abstract

Plasma catalysis in a dielectric barrier discharge (DBD) reactor is an attractive process for CO_2 reforming of methane (dry reforming). However, the improvement induced by catalysts or packing materials in plasma-based dry reforming in existing research is limited, and some packings even reduce the conversion and energy yield compared to an empty reactor. The particle diameter of the catalyst or packing is one of the important factors affecting the interaction between plasma and catalyst/packing. In this work, we used SiO_2 spheres of submicron and micron size (without or with supported metal, i.e. Cu, Fe, or Ni) to study their performance and the effect of different support particle sizes (120 nm–2.39 µm) on plasma-based dry reforming. We found that a uniform submicron and micron size SiO_2 packing improves the conversion and energy yield of plasma-based dry reforming due to its positive effects on the discharge, while the metal loading does not necessarily improve the performance, and even reduces the CH_4 and CO_2 conversion in most cases. The conversion of plasma-based dry reforming first increases and then decreases with increasing particle

size, due to the balance between the promoting and hindering effects of the particle filling in the plasma discharge. The best results were obtained with 740 nm SiO_2 packing with 5 wt % Ni loading, which improved the CO_2 and CH_4 conversion to 44% and 55%, respectively, compared to 20% and 27% in an empty reactor, at the same flow rate and operating conditions. The energy yield was improved from 0.116 mmol CO_2 and CH_4 converted per kJ to 0.271 mmol/kJ. The particle size affects not only the conversion, but also the selectivity of various products. The effect on the selectivities could be reduced by the metal loading. Using a suitable packing diameter is thus important for improving the conversion and product selectivity in plasma catalysis.

This chapter is in revision at:

J. Wang, A. Bogaerts, V. Meynen, Plasma-based dry reforming of methane in a dielectric barrier discharge reactor: Importance of uniform (sub)micron packing/catalysts to enhance the performance. Chemical Engineering Journal

4.1 Introduction

As already described in Chapter 1, the dielectric barrier discharge (DBD) reactor has the advantage that it is one of the easiest among the various types of non-equilibrium plasma reactors to be combined with catalysts, as it has a simple structure and operates at close to ambient temperature and atmospheric pressure [1-4]. Nevertheless, low conversion and energy yield in a DBD reactor are its main drawbacks [5-7]. Using alumina dielectric material, Khoja et al., demonstrated relatively good performance with an energy yield of 0.085 mmol/kJ [8]. Tu et al., reported an energy yield of 0.19 mmol/kJ by altering the catalyst packing method [7]. Although using a lower specific energy input (SEI) could provide a higher energy yield in some studies [7,9,10], the conversion of CH_4 and CO_2 was concomitantly reduced. Moreover, the existing catalysts and packing materials for DBD reactors have limited benefit in performance. As shown before in Table 1.2 in Chapter 1, in dry reforming studies with undiluted feed gases and fully packed fixed bed packings or catalysts, the conversion of CH_4 and CO_2 was lower than in the empty reactor at the same flow rate [7,9,11,12]. Some literature reported that catalysts or packings improved the dry reforming conversion compared to empty reactors [13,14], but since the processes were performed at a constant space time, the gas flow rate was reduced to exclude the volume reduction caused by the packings or catalysts, resulting in a significant increase in SEI. Hence, it was not clear whether the improvement in conversion came from the packing/catalyst or from the higher energy input [15].

A main challenge in the study of plasma catalysts in DBD reactors is that the effect of the catalyst is much more complex than in thermal reactors. It is not only the reaction between activated molecules and the active components of the catalyst, but it also includes the influence of the catalysts on the plasma discharge. Various properties of the catalyst, such as the dielectric properties, shape, size and structure, have an effect on the plasma filamentary discharge, which is the main discharge mode in the DBD reactor, consisting of a number of independent micro-discharge filaments [15-17]. Several studies have reported the effect of packing materials without active catalytic element on the plasma reaction, to investigate the effect of possible catalyst supports on the discharge and to distinguish the physical and chemical effects of the interaction between the plasma and the catalyst. In some studies, the catalytically inactive dielectric supports showed even a better performance in terms of conversion than the supports loaded with metal active components, due to the physical influence on the discharge [4,18]. Simulation studies found that one of the important physical effects of the catalyst was the polarization of the dielectric packing in the electric field of the DBD reactor, generating an enhanced electric field near the contact points of the packing [19]. It was also proven in experiments that this effect changes the discharges and enhances the conversion [20,21]. Furthermore, the packing partially changes the plasma discharge mode in DBD reactors from filamentary discharge to a surface discharge [22], which may also be beneficial for plasma-based dry reforming [5,23,24]. However, the packing also reduces the available discharge volume, and consequently the possible trajectories of micro-discharges, which has a negative effect on the plasma reaction [25]. In addition, for the same gas flow rate, it also reduces the space time of the feed gas in the plasma discharge area, which is also unfavorable for the conversion of the reagents [20,26].

These effects are greatly affected by the particle size of the packing materials and the catalysts. One of the reasons for the limited performance of the packings/catalysts might be that their positive effects are less important than negative effects, due to an inappropriate or non-uniform particle size [14,20]. There have been some studies on the size of the packing materials in plasma reactions, but the particle sizes in these studies were all in the millimeter range, which is relatively large for the gap dimensions (also in the millimeter range) of a common DBD reactor [14-16,27]. Therefore, their positive effect on the discharge behavior, such as turning filamentary discharges into surface discharges, may be small. Smaller particle sizes down to micron or submicron sizes have not yet been studied because they are considered to have too small void space and they are expected to reduce the space time too much, leading to too much negative effects in plasma catalysis, or even the prevention of plasma propagation between the particles [20,28,29]. However, in experiments, submicron or micron particles cannot achieve the closest packing in the reactor when loaded by tapping, so the void spaces and space times might not be too low.

Therefore, in this work, in order to improve the conversion and energy yield of dry reforming in DBD reactors, and to better understand the interaction of catalyst particles with the plasma and the influence of catalyst size, we use uniform silica spheres of submicron and micron size, to study the effect of support particles with different particle sizes on the plasma-based dry reforming. Furthermore, we also explore the changes after depositing a certain amount of catalytically active metal component on the silica support. All experiments were performed at constant gas flow rate and supplied power, so the applied specific energy was constant. The performance comparisons between the empty reactor and a packed bed reactor include the negative effects of fully packing the reactor, such as the greatly reduced space time.

4.2 Materials and methods

4.2.1 Preparation of samples

4.2.1.1 Preparation of silica spheres

Ammonia solution (25 wt %), tetraethyl orthosilicate (TEOS), and ethanol were purchased from Sigma-Aldrich. Silica spheres with average diameters of ~120 nm, ~460 nm, ~740 nm, and ~810 nm were synthesized by the traditional batch Stöber method [30], while silica spheres with average diameters of ~1.13 μm, ~1.8 μm and ~2.39 μm were synthesized by a semi-batch modified Stöber method [31]. For the Stöber method, a certain amount of ammonia solution and water were dissolved in ethanol (see [30] for their ratio). The solution was agitated at 400 rpm and 20 ℃, and 50 mL tetraethyl orthosilicate (TEOS) was added to it. Then, the solution was kept stirring at the same temperature for 24 h. Finally, it was centrifuged, and dried at 80 ℃ for 24 h to obtain silica spheres. In the semi-batch Stöber method proposed in the literature [31], 1.3 g of ~810 nm silica prepared by the batch Stöber method was dispersed in 22.6 mL ethanol solution with 0.7 mol/L NH_3 and 8 mol/L H_2O, as a seed suspension. TEOS/ethanol solution in a volume ratio of 1:2 was slowly added into the stirring seed suspension at room temperature. After centrifugation and drying, silica spheres with diameters larger than 1 μm were obtained. According to the average diameters of the silica spheres (in nm), the samples are denoted as Si-120, Si-460, Si-740, Si-810, Si-1130, Si-1800, and Si-2390, respectively.

4.2.1.2 Spheres Impregnation of metals on silica

Copper, iron, and nickel, as common dry reforming catalytically active metals, were supported on silica particles in this work. Copper nitrate trihydrate and ferric nitrate nonahydrate were purchased from Acros, and nickel nitrate hexahydrate was purchased from Sigma-Aldrich. The three metal nitrates were formulated into 100 mL separate precursor aqueous solutions. Then the silica spheres were dispersed in the precursor solutions with stirring for 5 h. The mass percentages of metal elements in solution relative to the SiO_2 used for impregnation were 0.2%, 1% and 5%, respectively. After drying the full solution at 40 ℃ and calcination at 650 ℃ for 6 h, the metal oxide loading on the silica particles was obtained. The samples were reduced at 800 ℃ for 6 h in a tube furnace with 250 mL/min 2% H_2/Ar, before testing their catalytic performance in plasma dry reforming. They are denoted as M_x/Si-Y, where x is the mass percentage of metal to silica and Y is the diameter of the silica spheres in nm. For example, the silica spheres with a diameter of 740 nm supporting 1 wt % Ni are denoted as Ni_1/Si-740.

4.2.2 Catalyst and plasma characterization

Scanning electron microscopy (SEM) was performed by the FEI Quanta 250 field emission scanning electron microscope at an operating voltage of 20 kV. The diameter of more than 30 silica spheres in the electron microscope images were measured and averaged.

Nitrogen sorption was carried out on an automated gas sorption system (Quantachrome Quadrasorb SI). Before the measurements, the samples were degassed under high vacuum at 200 °C for 16 h. During the sorption measurements, the temperature was kept at -196 °C by liquid nitrogen. The surface area was determined by the multi-point Brunauer–Emmett–Teller (BET) method.

The metal-loaded samples were characterized by X-ray diffraction (XRD) on a Panalytical Empyrean PRO MPD diffractometer using Co radiation. The scanning speed for the continuous mode measurements was 0.07^{o}/s. The XRD of all samples were measured after reduction at 800 °C. Some samples were re-calcined at 650 °C and then measured by XRD to compare their oxides, to prevent differences in the samples due to surface oxidation caused by storage in air.

Oxygen-temperature programmed oxidation (O_2-TPO) was performed for the metal-loaded samples on the ChemStar TPX Chemisorption Analyzer. The samples were degassed first at 200 °C for 1 h with 50 mL/min pure He flow. After cooling down to 50 °C, the O_2-TPO was carried out in 50 mL/min flow of 5% O_2/He, from 50 °C to 800 °C with 10 °C/min ramping rate.

Electrical characterization of the plasma was monitored by part of the setup shown in Figure 4.1. During the dry reforming test, the voltage was monitored by a high voltage probe (Tektronix, P6015A) and the current pulse was monitored by a Rogowski coil (Pearson

4100). The number of micro-discharges was obtained by counting the peaks per period in the current profile after excluding signal noise [15]. A capacitor (10 nF) was connected in parallel with a low voltage probe (Picotech, TA150) and in series with the reactor to measure the dissipated charge in the plasma. The displaced charge of the discharge is the detected charge difference before and after discharge. An oscilloscope (Picotech, Picoscope 6402D) was used to collect all the signals and to show them on a PC. A Q-U graph, also known as a Lissajous figure, was plotted with the applied voltage and dissipated charge as the horizontal and vertical axes, respectively. The counting and calculation of all electrical characteristics was completed by a MATLAB script [15].

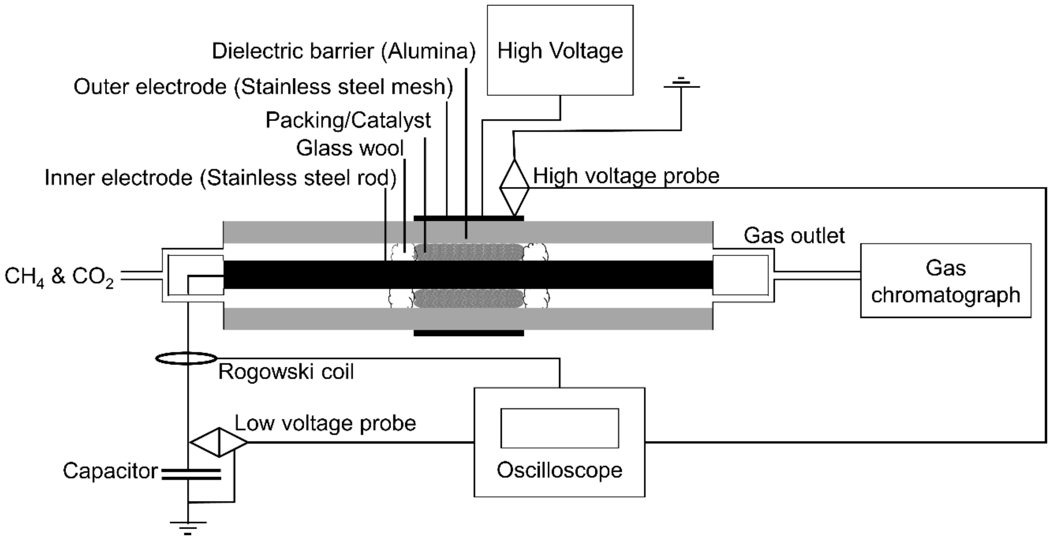

Figure 4.1. DBD plasma setup of the dry reforming tests.

4.2.3 Plasma dry reforming tests

A fixed bed DBD plasma reactor (illustrated in Figure 4.1) was applied to test the performance of the samples for plasma-based dry reforming. A grounded stainless steel rod with a diameter of 13 mm was used as the inner electrode. An alumina tube with an outer diameter of 21.8 mm and an inner diameter of 17.41 mm was coaxially placed around the stainless steel inner electrode as a dielectric barrier, so the spacing between the inner electrode and dielectric barrier, which is the discharge gap, was about 2.2 mm. A stainless steel mesh was tightly wound around the alumina tube as an outer electrode and connected to a high voltage, supplied by a function generator (Tektronix, AFG 2021) and a high voltage amplifier (TREK, model 20/20C-HS). The length of the outer electrode was 50 mm. The function generator provided an input signal with a frequency of 3 kHz, which was amplified by the amplifier. The electrical signals were collected by the oscilloscope and displayed on the PC to calculate the power in real time. The amplitude of the input signal from the amplifier was adjusted according to the calculation to keep the power of the power supply constant at 50 W. 6 g of silica spheres were filled in the entire plasma discharge space, and 2 g of glass wool was blocked at both sides to fix the spheres. The tapped volume of 6 g of silica spheres was larger than the volume of the discharge space (5.27 mL) for all particle sizes, to avoid the possible effect of glass wool on both sides on the discharge. Moreover, In order to measure the weight filled in the discharge space to calculate the packing density, the particles were repacked in an amount that just fills the discharge space of the reactor.

The silica spheres without supporting metal were tested directly in the DBD reactor. For the evaluation of silica with supporting metal, the samples were first reduced in a tube furnace (Carbolite Gero TF1 12/60/300) with 200 mL/min of 2% H_2/Ar gas flow rate at 800 ℃ for 6 h before being packed into the reactor. The feed gas entering the reactor consisted of 10 mL/min of CH_4 and 10 mL/min of CO_2 controlled by mass flow controllers (Bronkhorst EL-FLOW Select). An online gas chromatograph (Trace GC 1310, Interscience) with a thermal conductivity detector (TCD) and a flame ionization detector (FID) was used to analyze the composition of the outlet gas. The composition of the feed gas was determined by the GC after the reactor was flushed for 30 minutes and before the plasma was turned on. The concentrations of CO_2 and CH_4 (in %) in the feed gas were denoted as $CO_{2,in}$ and $CH_{4,in}$, respectively. The power was then turned on to generate plasma and maintained at 50 W for 30 min to allow plasma stabilization. After that, the concentrations of outlet gases (in %)

were analyzed with a GC and marked with "out", i.e., $CO_{2,out}$, $CH_{4,out}$, $H_{2,out}$, CO_{out} and $C_xH_yO_{z,out}$. The conversion of CO_2 and CH_4 were defined as Eq. (1) and Eq. (2)

$$X_{CO_2}(\%) = \frac{CO_{2,in} - CO_{2,out}}{CO_{2,in}} \cdot 100\% \tag{1}$$

$$X_{CH_4}(\%) = \frac{CH_{4,in} - CH_{4,out}}{CH_{4,in}} \cdot 100\% \tag{2}$$

The (H-based) selectivity of H_2, and the C-based selectivity of CO and of the other products were calculated by Eq. (3) to Eq. (5)

$$S_{H_2}(\%) = \frac{H_{2,out}}{2(CH_{4,in} - CH_{4,out})} \cdot 100\% \tag{3}$$

$$S_{CO}(\%) = \frac{CO_{out}}{(CH_{4,in} - CH_{4,out}) + (CO_{2,in} - CO_{2,out})} \cdot 100\% \tag{4}$$

$$S_{C_xH_yO_z}(\%) = \frac{x \cdot C_xH_yO_{z,out}}{(CH_{4,in} - CH_{4,out}) + (CO_{2,in} - CO_{2,out})} \cdot 100\% \tag{5}$$

The energy yield (EY) of dry reforming was defined as the amount of CO_2 and CH_4 that can be converted per kJ of energy input in the plasma, as shown in Eq. (6)

$$EY\ (mmol/kJ) = \frac{(V_{CO_2}X_{CO_2} + V_{CH_4}X_{CO_4})}{PV_m} \cdot \frac{1000}{60}\left(\frac{Wmin}{kJ}\right) \tag{6}$$

Where V_{CO2} and V_{CH4} are the volumetric flow rate of CO_2 and CH_4 in the feed gas (in mL/min), and X_{CO2} and X_{CH4} are the conversion of CO_2 and CH_4, respectively. P is the plasma power (in W) and V_m is the molar gas volume (24.4 mL/mmol). Finally, the 1000/60 (Wmin/kJ) stands for the conversion of Wmin to kJ, in order to obtain the same units as in the left-hand side. Dry reforming produces CO, H_2 and unknown amounts of various hydrocarbons from CO_2 and CH_4, causing an unknown coefficient of expansion and pressure increase in the outlet gas. The GC however always samples at a constant ambient pressure, so the gas composition analyzed by the GC has systematic errors. Therefore, 10 mL/min of N_2 was added into the outlet gas as an internal standard to correct for this and exclude the errors [32].

4.3 Results and discussion

4.3.1 Particle size effect of the dielectric packing on plasma-based dry reforming

The morphology and size of the silica particles were measured by SEM. As shown in Figure 4.2, all silica samples were of similar spherical shape with uniform diameters. The diameters of all measurable spheres (tens to over a hundred) on each SEM image were measured to calculate the average particle size and plot the particle size distribution. The mean particle sizes were 120 nm, 460 nm, 740 nm, 810 nm, 1130 nm, 1800 nm, and 2390 nm, respectively, and were used to name these samples. The particle size distribution shown in Figure 4.2h confirms that all samples were relatively uniform in size. The uniform size and shape made, these samples suitable for studying the effect of particle size in plasma-based dry reforming.

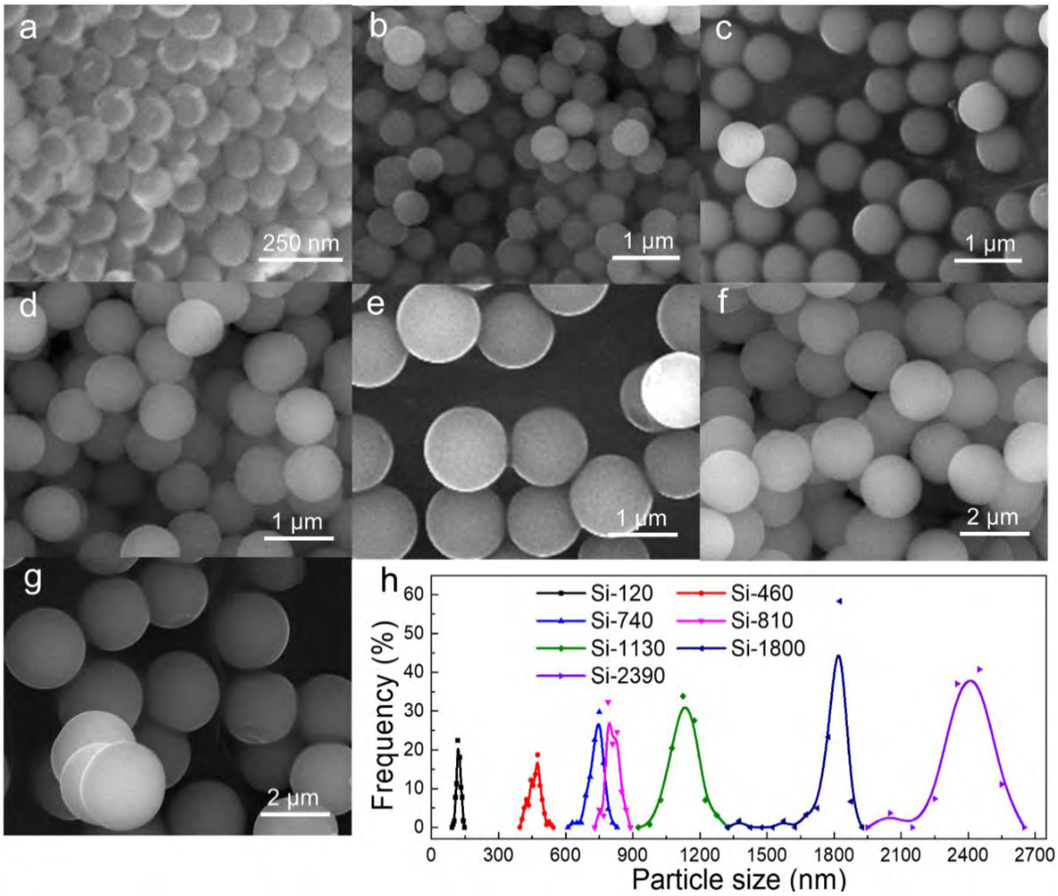

Figure 4.2. SEM images of (a) Si-120, (b) Si-460, (c) Si-740, (d) Si-810, (e) Si-1130, (f) Si-1800 and (g) Si-2390. (h) Particle size distribution of all samples.

Figure 4.3 shows the reforming conversion and energy yield for plasma-based dry for the empty reactor and the packed bed reactor with different sizes of silica spheres, at a constant 20 mL/min feed gas flow rate (1:1 of CH_4 to CO_2) and 50 W applied power. The specific values for conversion and energy yield are in Appendix C, Table C.1. In order to provide more industrially relevant information on the overall efficiency, in addition to the EY calculated from the discharge power (as shown in Figure 4.3), the EY calculated from the supplied power is also listed in Table C.1. Higher or at least comparable conversions of CH_4 and CO_2 were obtained for almost all diameters of the silica spheres compared to the empty reactor. This illustrates that the positive effects of the submicron and micron silica packing on the conversion were sufficient to compensate or even outweigh its negative effects (e.g., the reduction in space time) [7,15,16] Moreover, the conversions of CH_4 and CO_2 first increase and then decrease with increasing diameter of the silica spheres. The silica spheres with a diameter of about 740 nm showed the highest conversion. More specifically, the CO_2 and CH_4 conversion raised from 20% and 27% in the empty reactor, to 42% and 54%, respectively. Since the experiments were performed at a constant supplied power and the same gas flow rate (not the same space time), the specific supplied energy in the empty reactor and for all packed reactors was constant. The energy yield followed a similar trend as the conversion. Nevertheless, the energy yield was not exactly correlated to conversion due to the effect of the packing on the plasma power. For example, since the plasma power generated in the reactor with Si-120 was significantly lower than that of the other samples (see Table 4.1), and possibly also due to its larger specific surface area (the effect of which will be explained below), the energy yield of Si-120 was higher than that of Si-460, hence different from the conversion trend. The energy yield was improved from 0.116 mmol/kJ to a maximum of 0.252 mmol/kJ for the Si-740 packing. With such a large effect of the submicron and micron range particle sizes on the conversion and energy yield, it is clear that non-uniform or inappropriate particle sizes in some plasma-catalytic studies might have been an important reason for the poor performance of catalysts in plasma-catalytic conversion [7,11,12].

Dielectric packing materials such as SiO_2, which have been commonly used as supports and were not considered catalytically active in dry reforming, improve the conversion of plasma-based dry reforming due to two possible effects. One is the enhanced electric field around the contact points between the packing particles, resulting from the polarization of the dielectric, which has a promoting effect on the conversion of CH_4 and CO_2 [19,20,33]. Another is the surface discharge on the packing particles. It has been reported that the plasma discharge mode in the DBD reactor was partially changed by the packing from a filamentary discharge, which is not energy efficient, to a surface discharge [7,22,34]. Both effects work better for smaller particles, which have more contact points, smaller void spaces for filamentary discharge (determined by the particle size and packing density) and a larger external surface area in the same packing volume. The specific surface areas of the samples measured by N_2-sorption are in Table 4.1.

However, as mentioned above, the tested conversion and particle size of the SiO_2 packing did not exhibit a simple linear relationship. This is because of the coinciding negative effects of the packing, which are also more pronounced in smaller particles. Possibly smaller void spaces between smaller particles limit more the trajectories of the discharge [25]. If the samples were packed with the closest packing in the reactor, the void spaces between Si-120 samples, with the smallest particle size, might be only tens of nm, and the plasma cannot even be generated and propagated in it because it is smaller than the Debye length [28,29]. Although the (sub)micron particles cannot achieve the closest packing in the reactor by tapping as mentioned above, and the fact that we have conversion and we see electrical signals characteristic for a discharge in the Si-120 packed reactor also proves that plasma can be generated, either in the void space or as surface discharges, the propagation of the plasma between the smaller particles is still expected to be more restricted due to their smaller void spaces. Moreover, the packing reduces the volume of the discharge space and therefore the space time (< 11 s), which would lower conversion as is expected here [14,26]. At space times in the order of 20 seconds and less, small changes in space time are expected to decrease conversion substantially as it is further from partial equilibrium conditions [17]. The packing densities of SiO_2 particles, calculated from their weight in the discharge space and the volume of the discharge space in the reactor, are shown in Table 4.1. The smaller the SiO_2 particles, the more they are packed and the higher the packing density, resulting in a greater negative impact on the discharge. For the silica spheres with submicron and micron particle sizes used in this study, their positive effects on the discharge are dominant over the negative effects, so that higher energy yield and higher CH_4 and CO_2 conversion can be obtained at the same gas flow rate and power supply. The combined effect of the positive and negative effects of silica particles results in a first increase and then a decrease in conversion and energy yield with particle size.

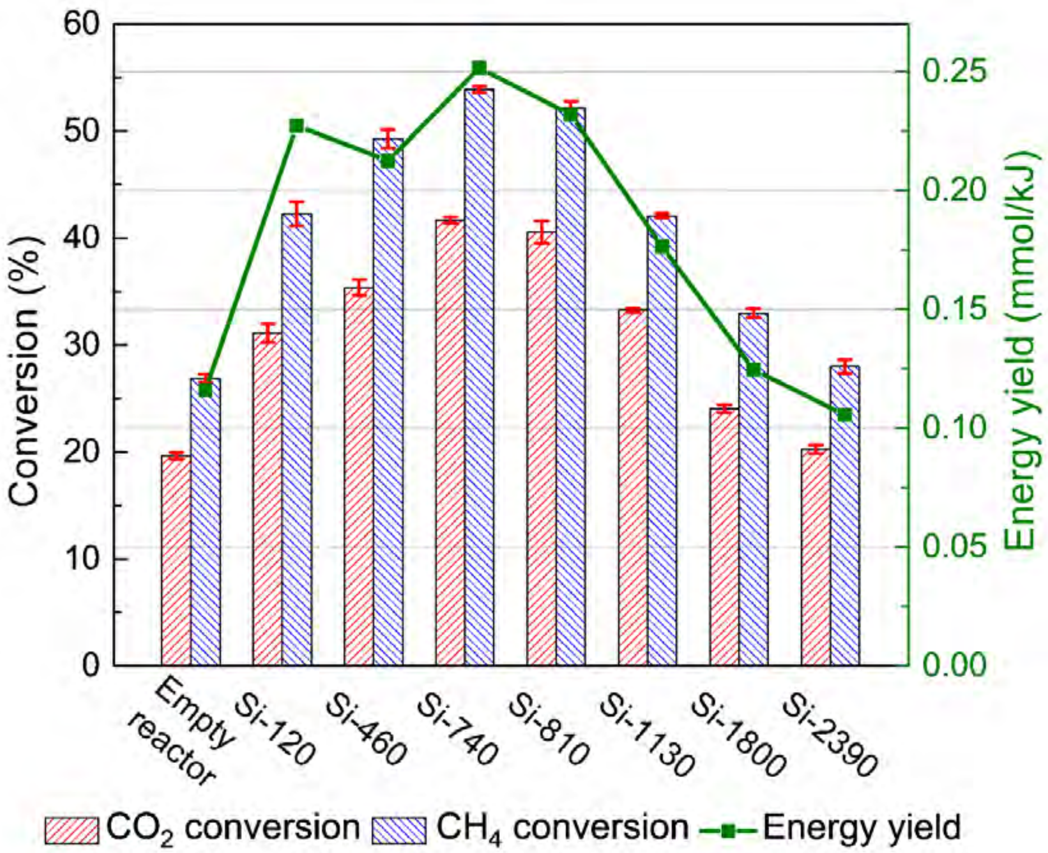

Figure 4.3. Conversion of CH_4 and CO_2 (left y-axis) and energy yield (right y-axis) in plasma-based dry reforming, in the empty DBD reactor and the packed reactor with different particle sizes of SiO_2 at the same gas flow rate. The error bars were obtained from standard errors based on three repeat repacking experiments.

Due to the limited measurement range of the PC connected oscilloscope system and the fluctuating discharge in the empty reactor, the connection between PC and oscilloscope was always broken. Hence, the displaced charge, and thus the Lissajous figures, of the empty reactor could not be obtained. The slopes of Lissajous figures obtained in the DBD reactor filled with SiO_2 particles with different sizes are shown in Appendix C, Figure C.1. More detailed data of the discharges, as obtained from the voltage, charge and current data are listed in Table 4.1. The plasma power was calculated by multiplying voltage and plasma current, and the average number of micro-discharges per period was the number of peaks in the normalized current profile after excluding signal noise [15]. The raw data of the Lissajous figures and voltage and current profiles for SiO_2 with different particle sizes in a period are shown in Figure C.2 and Figure C.3. As shown in Table 4.1, although the conversion in the empty reactor was lower than in the SiO_2 packed reactor, the root mean square current (RMS current) of the plasma was higher, and the applied peak-to-peak voltage (U_{pp}) required to achieve the same supply power was lower. The plasma power and number of micro-discharges were also higher in the empty reactor compared to the packed reactor filled with particles with diameter smaller than Si-810. This indicates that the SiO_2 packing hindered the plasma discharge and maybe partially changed the filamentary discharge mode to surface discharge [7,21,22,34], and that the plasma discharged more often and was more powerful in the empty reactor.

The negative effects decreased with increasing particle size, which is also reflected in the electrical signal data in Table 4.1. Although there are exceptions, from Si-120 to Si-2390, the plasma power, plasma current, and number of micro-discharges all have a tendency to increase with increasing SiO_2 particle size, and the required peak-to-peak voltage decreases accordingly. This means that there is a higher energy input and a higher chance of individual discharges in the packed reactor with larger particle sizes [35]. It can be noticed from the Lissajous figures that the displaced charge (vertical distance between two vertices on the right side of the parallelogram) during the discharge also increased with the particle size. Dividing it by the number of micro-discharges yields the average filament charge, which characterizes the strength of the discharge. The latter was also positively correlated with particle size. There was also a rough trend in the slopes on the left and right sides of the Lissajous figure, which increased slightly with particle size, indicating that the discharge fraction was larger in the reactor with large particles. These data verify that smaller particles are not conducive to discharge in DBD reactors, which is one of the reasons why the conversion and energy yield first increase with increasing particle size.

Table 4.1. Specific surface area and packing density of the SiO_2 spheres with different diameters in the DBD reactor, as well as the electrical characterization data measured and calculated from the recorded signals of the oscilloscope of the dry reforming experiments.

	Power supplied (W)	Specific surface area (m^2/g)	Packing density (g/cm^3)	U_{pp} (kV)	Plasma power (W)	RMS Current plasma (mA)	Number of micro-discharges (a.u./T)	Average filament charge (nC/disch.)
Empty reactor	50.4	/	/	18.8	27.4	24.5	75	/
Si-120	50.3	27	0.97	27.1	22.1	10.6	54	7.5
Si-460	50.5	6	0.96	23.2	27.2	12.6	70	8.4
Si-740	50.3	5	0.95	24.8	26.0	12.5	70	7.7
Si-810	50.7	4	0.95	24.3	27.3	10.8	76	7.0
Si-1130	50.1	4	0.91	21.0	29.2	16.2	72	10.5
Si-1800	50.3	3	0.85	20.3	31.3	14.4	80	10.4
Si-2390	49.7	3	0.84	20.0	31.2	14.3	74	11.0

The selectivities of the main products formed in plasma-based dry reforming with the SiO_2 spheres of different particle sizes are shown in Figure 4.4. It should be noted that the carbon and hydrogen mass balance calculated from the product selectivity does not reach 100% (shown in Figure C.4) because a few possible liquid products and carbon deposits attached to the catalyst and/or the reactor walls, as well as other gaseous products not calibrated in the gas chromatograph, could not be counted. As shown in Figure 4.4a, for all SiO_2 particle sizes, the main product was syngas (CO and H_2), and the CO selectivity was always higher than the H_2 selectivity. Comparing the empty reactor and the packed reactor with silica particles of different sizes, the syngas selectivity appears to be related to the CH_4 and CO_2 conversions. Although there was not an accurate correspondence, there was a general trend that the lower the conversion of CH_4 and CO_2, the greater the selectivity of CO and H_2, i.e., the selectivity decreases first and then increases with increasing particle size. The selectivities of C_2H_6, CH_3OH and C_2H_5OH (Ethanol, EtOH) also follow this trend (see Figure 4.4b and 4c). As shown in Figure 4.4b, the selectivity of C_3H_8 and C_2H_4 shows an increasing trend with increasing SiO_2 diameter, which might indicate that more micro-discharges or higher plasma power favor the formation of these two products. However, little C_3H_8, C_2H_4 and C_2H_2 (selectivity below 1%) were produced in the empty reactor despite it also having more micro-discharges and higher plasma power, probably due to the discharge mode in the empty reactor being different from the packed reactor.

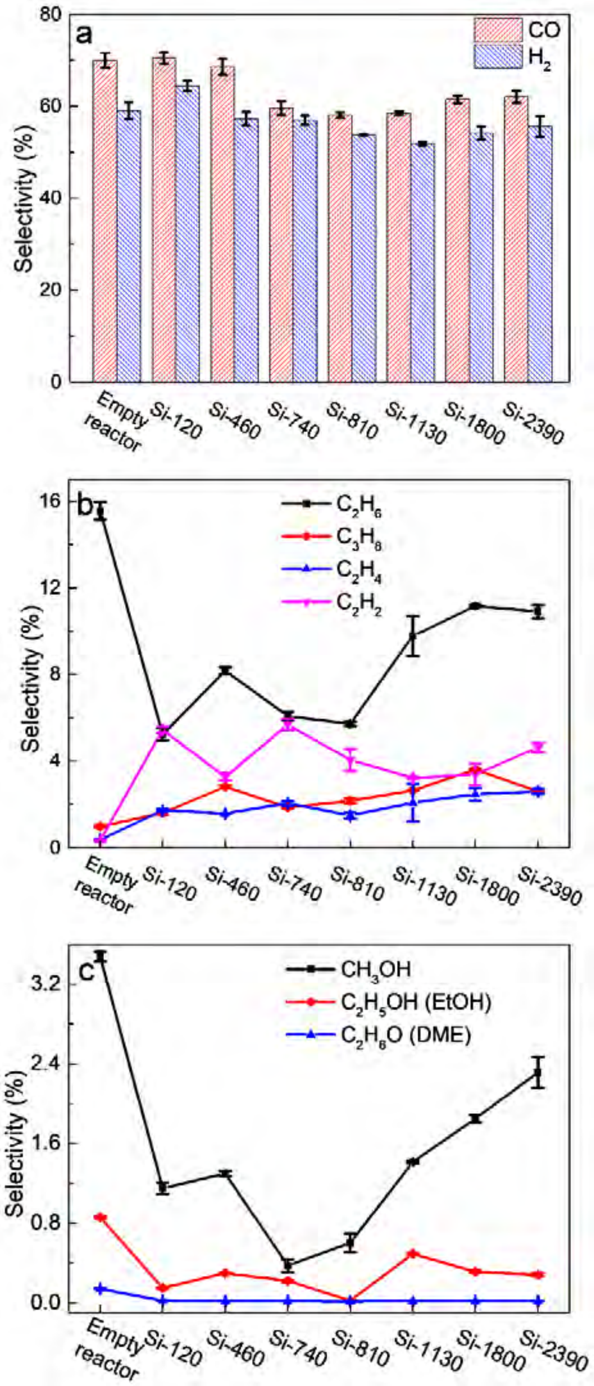

Figure 4.4. Product selectivities in plasma-based dry reforming, in the empty reactor and the packed reactor with different particle sizes of SiO_2 spheres, for (a) CO and H_2, (b) ethane, propane, ethylene, acetylene and (c) methanol, ethanol (EtOH) and dimethyl ether (DME). The error bars were obtained from standard errors based on three repeat repacking experiments.

4.3.2 Particle size effect of supported metal catalysts on plasma-based dry reforming

According to the above results, the SiO_2 spheres with a diameter of 740 nm show the highest conversion for both CO_2 and CH_4, resulting from the combination of the positive and negative effects of the packing on the discharge. Supported metal catalysts are common traditional dry reforming catalysts. Therefore, Si-740 was used as a support to prepare metal loaded catalysts of Cu, Fe and Ni to test their performance in plasma-based dry reforming. The XRD patterns of catalysts loaded with 5% of the different metals are shown in Figure C.5. The dry reforming test conditions were the same as in Figure 4.3. The obtained Lissajous figures and detailed electrical characteristics are shown Figure C.6, Figure C.7 and Table C.2, respectively. Interestingly, as shown in Figure 4.5, after loading with metal catalytic active components, the conversion of dry reforming was not improved in most samples, but decreased. This suggests that the interaction between metal and plasma may be adverse to the dry reforming reaction, and in the majority of cases the catalytic activity cannot compensate for it. Among these samples with different metals and different loadings, Ni_5/Si-740 exhibits relatively better performance, and it was the only sample that improves the conversion of both CH_4 and CO_2 compared to unloaded Si-740 particles, under the here applied conditions. Due to the catalytic activity of the metal and its interaction with the plasma, the role of the supported metal catalyst particles in the plasma-based dry reforming can be considered complex. Therefore, it is necessary to study whether the effect of the catalyst particle size on the plasma-based dry reforming is still following the same trend as the pure silica packing.

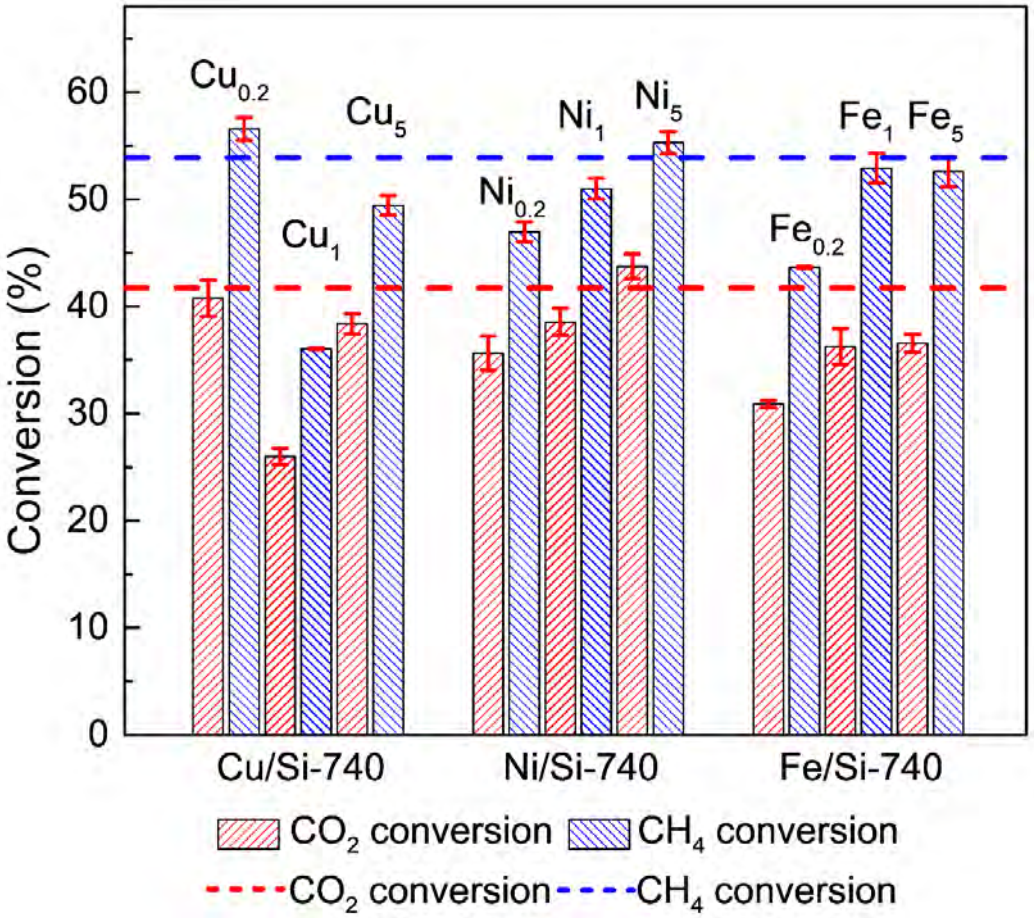

Figure 4.5. Conversion of CH_4 and CO_2 in plasma-based dry reforming of Si-740 without metal (benchmark – horizontal dashed line), and with different metals and loadings. The error bars were obtained from standard errors based on three repeat repacking experiments.

Silica spheres with all diameters were loaded with 5 wt % Ni and their catalytic performance for plasma-based dry reforming was tested. The test conditions were the same as in Figure 4.3. The XRD patterns and O_2-TPO of Ni-loaded samples are shown in Figure C.8 and Figure C.9, respectively, and they do not show an obvious difference and trend for different particle sizes. Hence, any differences observed in the plasma are most likely originating from differences in particles sizes. The variation of packing density (see Table 4.2 below) caused by the particle size is similar to that of the SiO_2 spheres without nickel loading. As shown in Figure 4.6, similar to the unloaded silica particles, the energy yield and conversion of CO_2 and CH_4 first increased and then decreased with increasing particle size. The catalyst with diameter of 740 nm still shows the best performance: it improves the CO_2 and CH_4

conversion from 20% and 27% in the empty reactor, to 44% and 55%, respectively. The energy yield reaches 0.271 mmol/kJ with the Ni_5/Si-740 catalyst. Furthermore, not all sizes of supported Ni/SiO_2 catalysts perform better than the unloaded silica particles. The conversion of dry reforming for Si-460, Si-740, and Si-1800 was improved after 5% Ni loading, but it decreased for Si-120, Si-810, Si-1130, and Si-2390 (relatively small changes for Si-120, Si-740 and Si-1800, less than 5%). The metal loading of differently sized particles not only changes the catalytic dry reforming activity of the silica particles, but also affects the plasma discharge [21,36]. The presence of the metal might enhance the electric field and electron density further in the proximity of the particle contact points, partially transforming the surface streamer discharges of the plasma on the dielectric into point-to-point local discharges [37-39]. Due to the size-dependent differences in properties, such as the number of contact points, void space and surface area, it could create a difference so that the effect of the interaction between metal and plasma was positive or negative on dry reforming, for particles with different diameters. Therefore, the change in conversion resulting from metal loading (i.e., the combined effect of metal catalytic activity and metal-plasma interaction) can be expected different for catalysts with different particle sizes. However, this change did not affect the trend of the material performance in function of particle diameters in our study. Which hints to a smaller, superimposed effect on plasma properties of the metal loaded packing compared to the impact of the size of SiO_2 support, while chemical effects can still play an important role (see the changes in selectivity). The particle diameter of the packing/support therefore is indeed an important factor in plasma-based dry reforming, even in supported metal catalysts.

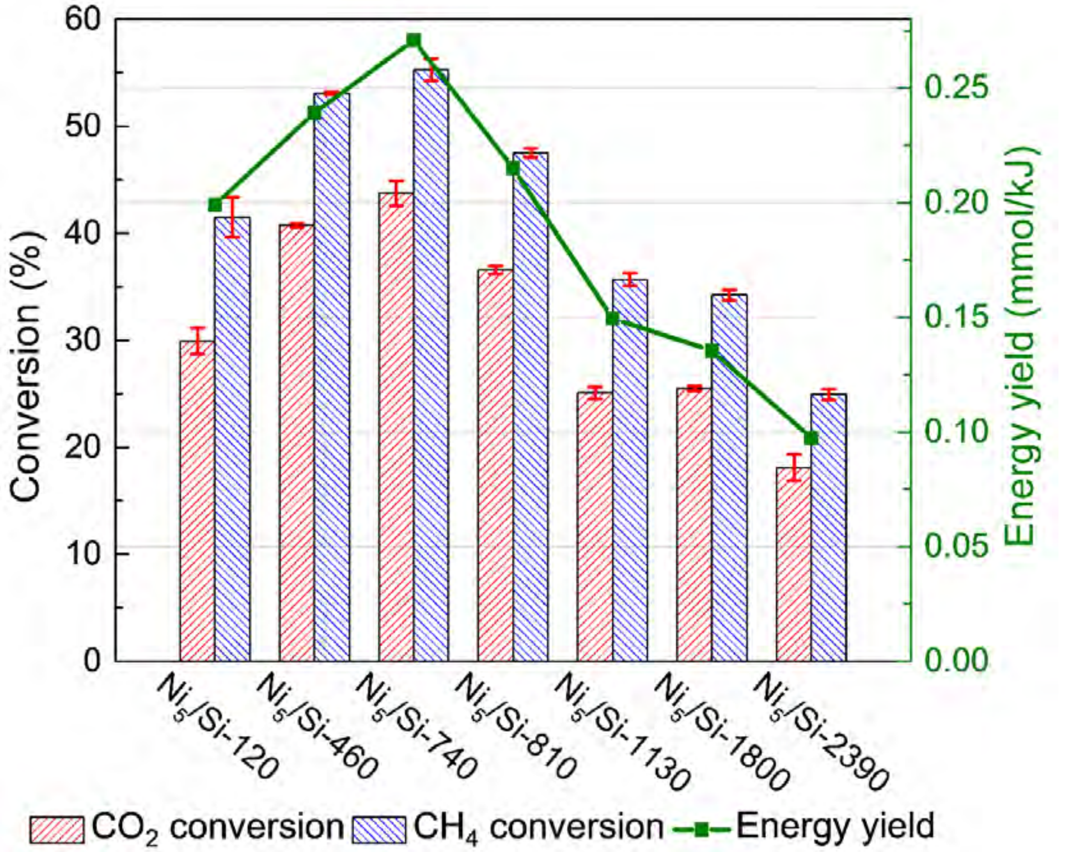

Figure 4.6. Conversion of CH_4 and CO_2 (left y-axis) and energy yield (right y-axis) in plasma-based dry reforming with 5 wt % Ni loading on different particle sizes of SiO_2. The error bars were obtained from standard errors based on three repeat repacking experiments.

The discharge data from the tests of the supported Ni catalysts in Figure 4.6 are listed in Table 4.2 (the raw voltage and current profiles are shown in Figure C.10), and the slopes and raw data of Lissajous figures are shown in Figure C.11 and Figure C.12. It can be noticed from the table that the plasma current and average filament charge have no obvious trend with particle size, while other parameters, including plasma power, number of micro-discharges and peak-to-peak voltage, still follow a similar trend to those of the unloaded SiO_2 support, but with smaller differences. That is, the hindering effect of catalyst packing on the filamentary discharge decreases, while less surface discharge might take place [7,21,22,34]. Compared with the pure SiO_2 support, the number of micro-discharges of the Ni-loaded SiO_2 catalyst particles increased for all sizes, which could be attributed to the change of the plasma discharge induced by the metal, i.e., from surface discharge to point-to-point local discharge [39,40].

Table 4.2. Packing density of SiO_2 particles in the DBD reactor and electrical characterization data measured and calculated from the recorded signals of the oscilloscope of the dry reforming experiments with 5 wt % Ni loading on different particle sizes of SiO_2.

	Power supplied (W)	Packing density (g/cm^3)	Upp (kV)	Plasma power (W)	RMS Current plasma (mA)	Number of micro-discharges (a.u./T)	Average filament charge (nC/disch.)
Ni_5/Si-120	50.6	0.93	25.2	24.5	11.9	75	8.0
Ni_5/Si-460	50.5	0.94	24.1	26.8	12.3	72	8.2
Ni_5/Si-740	50.0	0.92	25.4	25.0	11.4	79	6.4
Ni_5/Si-810	50.5	0.93	23.1	26.7	14.0	79	9.2
Ni_5/Si-1130	50.3	0.89	22.9	27.8	12.2	83	8.6
Ni_5/Si-1800	50.3	0.85	21.5	30.1	12.8	91	8.4
Ni_5/Si-2390	50.0	0.85	21.3	30.2	12.6	83	9.2

The product selectivities of Ni_5/SiO_2 catalysts with different particle sizes are shown in Figure 4.7, and the carbon and hydrogen mass balances calculated from the product selectivity are shown in Figure C.13. Compared with unloaded pure SiO_2, the selectivity trend of Ni_5/SiO_2 is not obvious. Although some products, such as C_2H_6 and CH_3OH, still roughly follow a similar selectivity trend to the unloaded SiO_2, the differences between catalysts with different diameters are not large (note the difference in Y-axis in Figure 4.7 versus Figure 4.4). This may be due to the reduced differences in electrical characteristic and the influence of metal catalytic activity on the reaction path [5,41-43]. The catalysts with different particle sizes support the same mass fraction of metal Ni, which might reduce the difference in product selectivity.

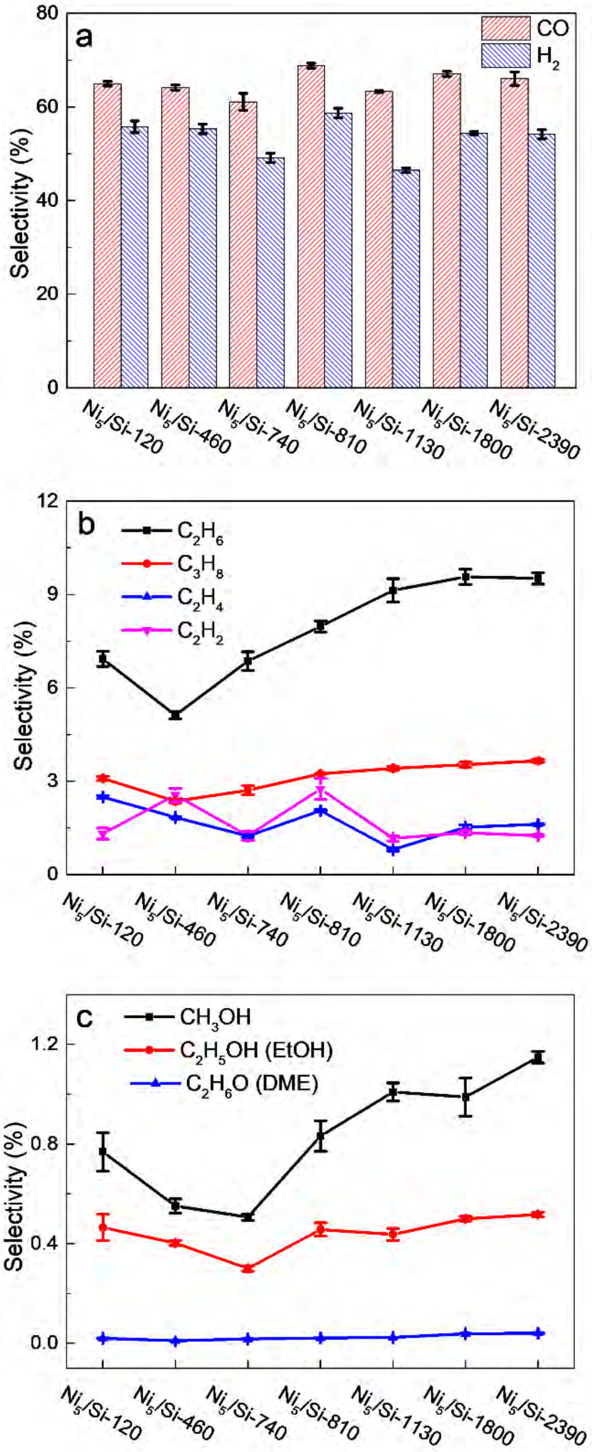

Figure 4.7. Product selectivities in plasma-based dry reforming with 5 wt % Ni loading on different particle sizes of SiO_2 spheres, for (a) CO and H_2, (b) ethane, propane, ethylene and acetylene, and (c) methanol, ethanol (EtOH) and dimethyl ether (DME). The error bars were obtained from standard errors based on three repeat repacking experiments.

4.4 Conclusion

In contrast to literature describing millimeter-sized packing materials, we synthesized uniform (sub)micron SiO_2 spheres, ranging from 120 nm to 2390 nm in diameter, to be used as packing in DBD plasma-based dry reforming, and we deposited metals on these SiO_2 particles to prepare supported catalysts. We found that due to their larger positive effect on the plasma discharge, packing the DBD reactor with uniform submicron and micron SiO_2 spheres (including both SiO_2 with or without metal loading) can improve both conversion and energy yield of plasma-based dry reforming, from 20% CO_2 conversion, 27% CH_4 conversion and 0.116 mmol/kJ energy yield in the empty reactor, to a maximum of 44% CO_2 conversion, 55% CH_4 conversion and 0.271 mmol/kJ energy yield. The metal loading does not necessarily improve the dry reforming performance, and it may even reduce the CH_4 and CO_2 conversion due to the interactions between metal and plasma, even at small wt%.

We investigated the influence of packing/catalyst particle size. We found that due to the balance between the promoting effects (e.g. enhancement of local electric field, change of discharge mode) and the hindering effects (e.g. restriction of the filament path and reduction of the space time) of the particle filling on the plasma discharge, the conversion of plasma-based dry reforming first increase and then decrease with increasing particle size. Both pure SiO_2 spheres and 5 wt % Ni-loaded SiO_2, particles with a diameter of 740 nm exhibit the best performance. The particle size affects not only the conversion, but also the selectivity of various products. The effect on the selectivities may be attenuated by the metal loading as less influence on selectivity in function of particle size was observed.

In summary, submicron and micron silica spheres show good performance for plasma-based dry reforming either as dielectric packings or catalyst supports, and the particle size exhibits an important effect. It is important for plasma catalysis reactions in general to find a suitable particle size, as this can largely affect the performance. A suitable catalyst/packing particle size for plasma-based processes in DBD reactors might be in the sub-micron range, due to its large modification to filamentary discharge, rather than the millimeter-scale particles commonly used in the literature and in industrial applications. Moreover, plasma-catalyst interactions and discharge effects must be taken into account in the selection of active elements, as important negative effects might be present after active element loading.

4.5 References

[1] Uytdenhouwen, Y.; Hereijgers, J.; Breugelmans, T.; Cool, P.; Bogaerts, A. How gas flow design can influence the performance of a DBD plasma reactor for dry reforming of methane. *Chem. Eng. J.* **2021**, *405*, 126618.

[2] Zhu, F.; Zhang, H.; Yan, X.; Yan, J.; Ni, M.; Li, X.; Tu, X. Plasma-catalytic reforming of CO_2-rich biogas over Ni/γ-Al_2O_3 catalysts in a rotating gliding arc reactor. *Fuel* **2017**, *199*, 430-437.

[3] Li, M.-w.; Xu, G.-h.; Tian, Y.-l.; Chen, L.; Fu, H.-f. Carbon Dioxide Reforming of Methane Using DC Corona Discharge Plasma Reaction. *J. Phys. Chem. A* **2004**, *108*, 1687-1693.

[4] Wang, L.; Yi, Y.; Wu, C.; Guo, H.; Tu, X. One-Step Reforming of CO_2 and CH_4 into High-Value Liquid Chemicals and Fuels at Room Temperature by Plasma-Driven Catalysis. *Angew. Chem. Int. Ed.* **2017**, *56*, 13679-13683.

[5] Chung, W.-C.; Chang, M.-B. Review of catalysis and plasma performance on dry reforming of CH_4 and possible synergistic effects. *Renewable and Sustainable Energy Reviews* **2016**, *62*, 13-31.

[6] Khoja, A. H.; Tahir, M.; Amin, N. A. S. Recent developments in non-thermal catalytic DBD plasma reactor for dry reforming of methane. *Energy Convers. Manage.* **2019**, *183*, 529-560.

[7] Tu, X.; Whitehead, J. C. Plasma-catalytic dry reforming of methane in an atmospheric dielectric barrier discharge: Understanding the synergistic effect at low temperature. *Appl. Catal. B Environ.* **2012**, *125*, 439-448.

[8] Khoja, A. H.; Tahir, M.; Amin, N. A. S. Dry reforming of methane using different dielectric materials and DBD plasma reactor configurations. *Energy Convers. Manage.* **2017**, *144*, 262-274.

[9] Ray, D.; Reddy, P. M. K.; Subrahmanyam, C. Ni-Mn/γ-Al_2O_3 assisted plasma dry reforming of methane. *Catal. Today* **2018**, *309*, 212-218.

[10] Ray, D.; Manoj Kumar Reddy, P.; Challapalli, S. Glass Beads Packed DBD-Plasma Assisted Dry Reforming of Methane. *Top. Catal.* **2017**, *60*, 869-878.

[11] Song, H. K.; Choi, J.-W.; Yue, S. H.; Lee, H.; Na, B.-K. Synthesis gas production via dielectric barrier discharge over Ni/γ-Al_2O_3 catalyst. *Catal. Today* **2004**, *89*, 27-33.

[12] Sentek, J.; Krawczyk, K.; Młotek, M.; Kalczewska, M.; Kroker, T.; Kolb, T.; Schenk, A.; Gericke, K.-H.; Schmidt-Szałowski, K. Plasma-catalytic methane conversion with carbon dioxide in dielectric barrier discharges. *Appl. Catal. B Environ.* **2010**, *94*, 19-26.

[13] Uytdenhouwen, Y.; Bal, K. M.; Neyts, E. C.; Meynen, V.; Cool, P.; Bogaerts, A. On the kinetics and equilibria of plasma-based dry reforming of methane. *Chem. Eng. J.* **2021**, *405*, 126630.

[14] Michielsen, I.; Uytdenhouwen, Y.; Bogaerts, A.; Meynen, V. Altering Conversion and Product Selectivity of Dry Reforming of Methane in a Dielectric Barrier Discharge by Changing the Dielectric Packing Material. *Catalysts* **2019**, *9*.

[15] Uytdenhouwen, Y.; Van Alphen, S.; Michielsen, I.; Meynen, V.; Cool, P.; Bogaerts, A. A packed-bed DBD micro plasma reactor for CO_2 dissociation: Does size matter? *Chem. Eng. J.* **2018**, *348*, 557-568.

[16] Michielsen, I.; Uytdenhouwen, Y.; Pype, J.; Michielsen, B.; Mertens, J.; Reniers, F.; Meynen, V.; Bogaerts, A. CO_2 dissociation in a packed bed DBD reactor: First steps towards a better understanding of plasma catalysis. *Chem. Eng. J.* **2017**, *326*, 477-488.

[17] Uytdenhouwen, Y.; Bal, K. M.; Michielsen, I.; Neyts, E. C.; Meynen, V.; Cool, P.; Bogaerts, A. How process parameters and packing materials tune chemical equilibrium and kinetics in plasma-based CO_2 conversion. *Chem. Eng. J.* **2019**, *372*, 1253-1264.

[18] Andersen, J. A.; Christensen, J. M.; Østberg, M.; Bogaerts, A.; Jensen, A. D. Plasma-catalytic dry reforming of methane: Screening of catalytic materials in a coaxial packed-bed DBD reactor. *Chem. Eng. J.* **2020**, *397*, 125519.

[19] Van Laer, K.; Bogaerts, A. Fluid modelling of a packed bed dielectric barrier discharge plasma reactor. *Plasma Sources Sci. Technol.* **2015**, *25*, 015002.

[20] Van Laer, K.; Bogaerts, A. Improving the Conversion and Energy Efficiency of Carbon Dioxide Splitting in a Zirconia-Packed Dielectric Barrier Discharge Reactor. *Energy Technol.* **2015**, *3*, 1038-1044.

[21] Wang, W.; Kim, H.-H.; Van Laer, K.; Bogaerts, A. Streamer propagation in a packed bed plasma reactor for plasma catalysis applications. *Chem. Eng. J.* **2018**, *334*, 2467-2479.

[22] Gallon, H. J.; Kim, H.; Tu, X.; Whitehead, J. C. Microscope–ICCD Imaging of an Atmospheric Pressure CH_4 and CO_2 Dielectric Barrier Discharge. *IEEE Trans. Plasma Sci.* **2011**, *39*, 2176-2177.

[23] Zhang, S.; Gao, Y.; Sun, H.; Fan, Z.; Shao, T. Charge transfer in plasma assisted dry reforming of methane using a nanosecond pulsed packed-bed reactor discharge. *Plasma Science and Technology* **2021**, *23*, 064007.

[24] Mei, D.; Zhu, X.; He, Y.-L.; Yan, J. D.; Tu, X. Plasma-assisted conversion of CO_2 in a dielectric barrier discharge reactor: understanding the effect of packing materials. *Plasma Sources Sci. Technol.* **2014**, *24*, 015011.

[25] Tu, X.; Gallon, H. J.; Twigg, M. V.; Gorry, P. A.; Whitehead, J. C. Dry reforming of methane over a Ni/Al_2O_3 catalyst in a coaxial dielectric barrier discharge reactor. *J. Phys. D Appl. Phys.* **2011**, *44*, 274007.

[26] Bogaerts, A.; Kozák, T.; van Laer, K.; Snoeckx, R. Plasma-based conversion of CO_2: current status and future challenges. *Faraday Discuss.* **2015**, *183*, 217-232.

[27] El-Shafie, M.; Kambara, S.; Hayakawa, Y. Alumina particle size effect on H_2 production from ammonia decomposition by DBD plasma. *Energy Reports* **2020**, *6*, 25-30.

[28] Zhang, Q.-Z.; Bogaerts, A. Propagation of a plasma streamer in catalyst pores. *Plasma Sources Sci. Technol.* **2018**, *27*, 035009.

[29] Zhang, Q.-Z.; Bogaerts, A. Plasma streamer propagation in structured catalysts. *Plasma Sources Sci. Technol.* **2018**, *27*, 105013.

[30] Stöber, W.; Fink, A.; Bohn, E. Controlled growth of monodisperse silica spheres in the micron size range. *J. Colloid Interface Sci.* **1968**, *26*, 62-69.

[31] Giesche, H. Synthesis of monodispersed silica powders II. Controlled growth reaction and continuous production process. *J. Eur. Ceram. Soc.* **1994**, *14*, 205-214.

[32] Pinhão, N.; Moura, A.; Branco, J. B.; Neves, J. Influence of gas expansion on process parameters in non-thermal plasma plug-flow reactors: A study applied to dry reforming of methane. *Int. J. Hydrogen Energy* **2016**, *41*, 9245-9255.

[33] Chen, H. L.; Lee, H. M.; Chen, S. H.; Chang, M. B. Review of Packed-Bed Plasma Reactor for Ozone Generation and Air Pollution Control. *Industrial & Engineering Chemistry Research* **2008**, *47*, 2122-2130.

[34] Gallon, H. J.; Tu, X.; Whitehead, J. C. Effects of Reactor Packing Materials on H_2 Production by CO_2 Reforming of CH_4 in a Dielectric Barrier Discharge. *Plasma Processes and Polymers* **2012**, *9*, 90-97.

[35] Herrera, F. A.; Brown, G. H.; Barboun, P.; Turan, N.; Mehta, P.; Schneider, W. F.; Hicks, J. C.; Go, D. B. The impact of transition metal catalysts on macroscopic dielectric barrier discharge (DBD) characteristics in an ammonia synthesis plasma catalysis reactor. *J. Phys. D Appl. Phys.* **2019**, *52*, 224002.

[36] Bogaerts, A.; Zhang, Q.-Z.; Zhang, Y.-R.; Van Laer, K.; Wang, W. Burning questions of plasma catalysis: Answers by modeling. *Catal. Today* **2019**, *337*, 3-14.

[37] Wang, W.; Butterworth, T.; Bogaerts, A. Plasma propagation in a single bead DBD reactor at different dielectric constants: insights from fluid modelling. *J. Phys. D Appl. Phys.* **2021**, *54*, 214004.

[38] Butterworth, T.; Allen, R. W. K. Plasma-catalyst interaction studied in a single pellet DBD reactor: dielectric constant effect on plasma dynamics. *Plasma Sources Sci. Technol.* **2017**, *26*, 065008.

[39] Kruszelnicki, J.; Engeling, K. W.; Foster, J. E.; Kushner, M. J. Interactions between atmospheric pressure plasmas and metallic catalyst particles in packed bed reactors. *J. Phys. D Appl. Phys.* **2020**, *54*, 104001.

[40] Van Laer, K.; Bogaerts, A. How bead size and dielectric constant affect the plasma behaviour in a packed bed plasma reactor: a modelling study. *Plasma Sources Sci. Technol.* **2017**, *26*, 085007.

[41] Sheng, Z.; Kim, H.-H.; Yao, S.; Nozaki, T. Plasma-chemical promotion of catalysis for CH_4 dry reforming: unveiling plasma-enabled reaction mechanisms. *PCCP* **2020**, *22*, 19349-19358.

[42] Sheng, Z.; Watanabe, Y.; Kim, H.-H.; Yao, S.; Nozaki, T. Plasma-enabled mode-selective activation of CH_4 for dry reforming: First touch on the kinetic analysis. *Chem. Eng. J.* **2020**, *399*, 125751.

[43] Shirazi, M.; Neyts, E. C.; Bogaerts, A. DFT study of Ni-catalyzed plasma dry reforming of methane. *Appl. Catal. B Environ.* **2017**, *205*, 605-614.

Chapter 5 Dry reforming in a dielectric barrier discharge reactor with non-uniform discharge gap: Effects of metal rings on the discharge behavior and performance

---

Abstract

The application of dielectric barrier discharge (DBD) reactors is promising in various environmental and energy processes, but is limited by its low energy yield. In this study, we put a number of stainless steel rings over the inner electrode rod of the DBD reactor to change the local discharge gap and electric field, and we studied the dry reforming performance. At 50 W supplied power, the metal rings mostly have a negative impact on the performance, which we attribute to the non-uniform spatial distribution of the discharges caused by the rings. However, at 30 W supplied power, the energy yield is higher than at 50 W and the placement of the rings improves the performance of the reactor. More rings and with a larger cross-sectional diameter can further improve the performance. The reactor with 20 rings with a 3.2 mm cross-sectional diameter exhibits the best performance in this study. Compared to the reactor without rings, it increases the CO_2 conversion from 7% to 16 %, the CH_4 conversion from 12% to 23%, and the energy yield from 0.05 mmol/kJ supplied power to 0.1 mmol/kJ (0.19 mmol/kJ if it was calculated from the plasma power),

respectively. The presence of the stainless steel rings increases the local electric field, the displaced charge and the discharge fraction, and also makes the discharge more stable and with more uniform intensity. It also slightly improves the selectivity to syngas (< 10%). The performance differences observed by placing stainless steel rings in this study form an interesting basis to evaluate also other plasma-based reactions, and the physical effects of metals might provide a reference for the study of metals on catalyst surfaces in plasma-catalytic processes.

This chapter is in revision at:
J. Wang, A. Bogaerts, V. Meynen, Dry reforming in a dielectric barrier discharge reactor with non-uniform discharge gap: Effects of metal rings on the discharge behavior and performance. Chemical Engineering Journal

5.1 Introduction

As mentioned above, the relatively low energy yield of the DBD reactor hinders its application prospects [1-3]. Khoja et al. studied the dry reforming of methane in DBD reactors with different dielectric materials and configurations, and a better energy yield of 0.085 mmol CO_2 and CH_4 converted per kJ plasma power was obtained for an alumina dielectric barrier [4]. Tu et al. [3] obtained an energy yield of 0.1 mmol/kJ in a DBD reactor combined with a catalyst, and this could be further improved to a maximum of 0.19 mmol/kJ by increasing the gas flow rate and reducing the specific energy input. Important to note that the energy yield in the above literature was calculated from the plasma power, and it could be about half to two-thirds of the value if it was calculated from the supplied power. The plasma discharge mode in a DBD reactor is mainly filamentary, and thus the plasma is not uniform in the whole space [5,6]. High-energy electrons exist almost exclusively in the discharge filaments [7,8]. The CH_4 and CO_2 molecules hit by the discharge filaments are dissociated upon electron collisions into various radicals, which can recombine into the dry reforming products within the filaments or afterglow [9-11]. The strength of the discharge filaments varies, which may result in poor product selectivity [12], and a too weak or too strong discharge causes energy waste, which may be one of the reasons for the lower energy yield of the DBD reactor [1,13].

Changing the design of the reactor is one method to improve the performance. DBD reactors with small discharge gaps (i.e., micro DBD reactors) may be able to increase the performance of dry reforming, due to the enhancement of the electric field [14,15]. Previous studies found that a reduced discharge gap did improve the conversion in DBD reactors at the same space time [16,17]. However, the same space time was maintained by reducing the gas flow rate, as the smaller gap reduced the discharge volume, and thus the energy yield of the conversion process is actually decreased.

In this study, we put a number of stainless steel rings with circular cross-sections over the stainless steel inner electrode rod of the reactor (see Figure 5.1). These rings reduce the local discharge gap and change the electric field, which may promote the discharge with less effect on the discharge volume. This may induce the discharge to take place on the rings, and although the rings will make the electric field distribution less uniform, they might make the discharge strength more uniform, thereby changing the performance of the plasma-based dry reforming. Since the material of the rings is similar to that of the stainless steel inner electrode, and the rings cause a quite limited increase in the surface area of the inner electrode, the possible catalytic effect of the stainless steel rings is not considered in this study. In addition, in a plasma-based process with a catalyst, the metal active components on the catalyst surface will also be in contact with the electrodes and might have a similar effect, but the performance caused by the physical and chemical (surface) effects cannot be distinguished in a catalyst. Therefore, the role of the metal rings in this study can also provide a reference for the study of catalysts with metal components.

5.2 Experimental

5.2.1 Set-up for plasma-based dry reforming

A coaxial cylindrical DBD reactor was applied for plasma-based dry reforming. The original inner electrode was a smooth stainless steel rod with a diameter of 8 mm. A number of stainless steel rings with an inner diameter of 8 mm were put over the inner electrode at even intervals, as illustrated in Figure 5.1. The cross-section of the rings is circular, and rings with two cross-sectional diameters, i.e., 1.6 mm and 3.2 mm, were used in this study.

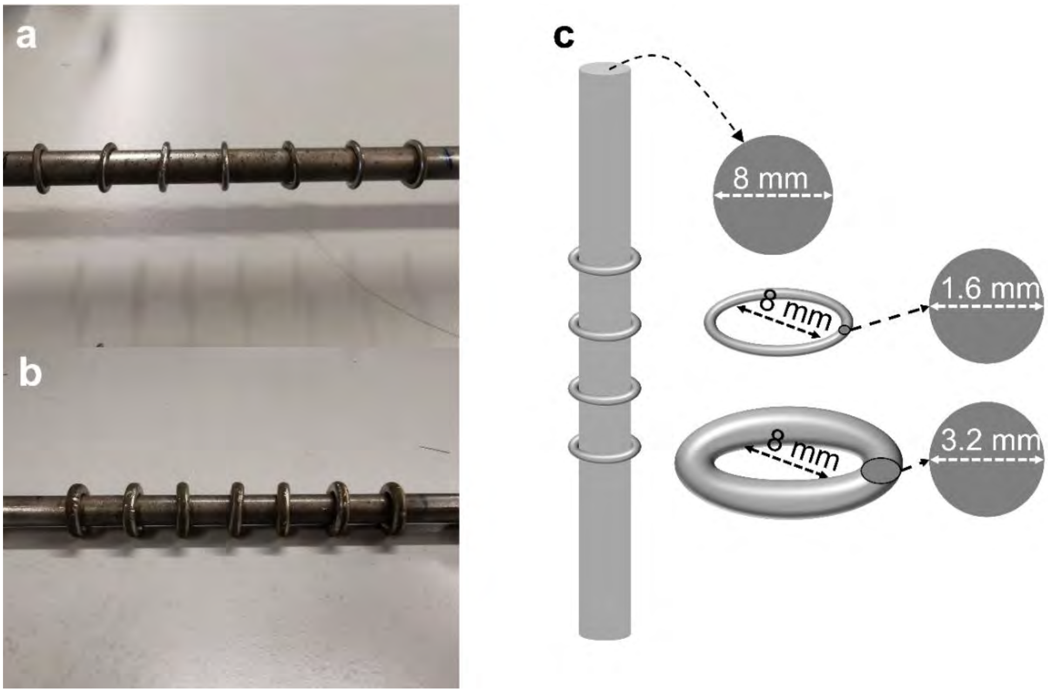

Figure 5.1. Photographs of the stainless steel rod inner electrode, with stainless steel rings with cross-sectional diameters of (a) 1.6 mm and (b) 3.2 mm. (c) Schematic diagram of stainless steel rod, stainless steel rings and their dimensions.

Figure 5.2 shows the whole set-up for the dry reforming experiments. The inner electrode was grounded. An alumina tube with an inner diameter of 17.4 mm and an outer diameter of 21.8 mm was coaxially placed over the inner electrode as a dielectric barrier, so the discharge gap of the ring-free reactor, which is the spacing between the 8 mm inner electrode and dielectric barrier, was about 4.7 mm. A stainless steel mesh tightly wound around the dielectric barrier tube was used as the external electrode. It was connected to high voltage supplied by a function generator (Tektronix, AFG 2021) and a high voltage amplifier (TREK, model 20/20C-HS). The length of the outer electrode was 100 mm, which defined the discharge length. According to the parameters of the reactor, the volume of the discharge zone was calculated to be 18.8 mL. A sinusoidal alternating input signal with a frequency of 3 kHz was provided by the function generator, and was then amplified by the amplifier. The voltage was measured by a high-voltage probe (Tektronix, P6015A), and the current was monitored by a Rogowski coil (Pearson 4100). A capacitor (10 nF) and a low-voltage probe (Picotech, TA150) connected in parallel with it were connected in series with the reactor to monitor the charge. The oscilloscope and connected PC collected and displayed all the electrical signals to calculate the power in real time. The power of the power supply was kept constant by adjusting the amplitude of the input signal from the amplifier according to the calculated power on the PC.

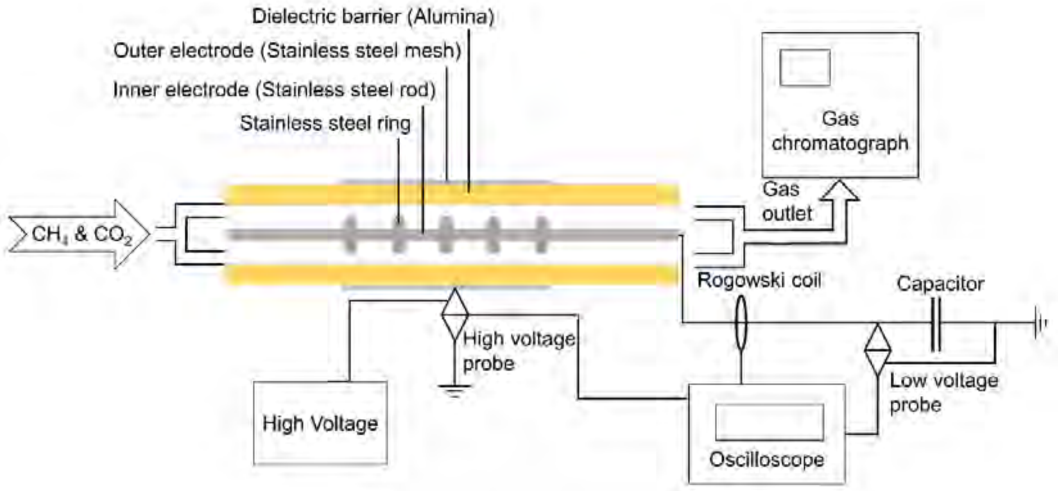

Figure 5.2. DBD plasma set-up and analytical system for the dry reforming experiments.

5.2.2 Performance of plasma-based dry reforming

The feed gas into the reactor was composed of 10 mL/min of CH_4 and 10 mL/min of CO_2 controlled by mass flow controllers (Bronkhorst EL-FLOW Select). Since the produced CO, H_2 and unknown amounts of various (oxygenated) hydrocarbons by the dry reforming reaction causes an unknown expansion coefficient and thus a possible pressure increase, while the GC always samples at a constant ambient pressure, the outlet gas composition analyzed by the GC would have systematic errors. Therefore, an internal standard gas, 10 mL/min of N_2, was added into the outlet gas to exclude these errors [18]. An online gas chromatograph (Trace GC 1310, Interscience) with a thermal conductivity detector (TCD) and a flame ionization detector (FID) was applied to analyze the composition and concentration of the outlet gas. The composition of the gas after the gas circuit was flushed for 30 minutes and before turning on the plasma, was denoted as $CO_{2,in}$ and $CH_{4,in,}$. The power was then turned on to generate plasma and maintained at a constant supplied power for 30 min. The outlet gases were analyzed and denoted with "out", i.e., $CO_{2,out}$, $CH_{4,out}$, CO_{out}, $H_{2,out}$ and $C_xH_yO_{z,out}$. The conversion of CO_2 and CH_4 were calculated by Eq. (1) and Eq. (2):

$$X_{CO_2}(\%) = \frac{CO_{2,in} - CO_{2,out}}{CO_{2,in}} \cdot 100\% \tag{1}$$

$$X_{CH_4}(\%) = \frac{CH_{4,in} - CH_{4,out}}{CH_{4,in}} \cdot 100\% \tag{2}$$

The (H-based) selectivity of H_2, and the C-based selectivity of CO and of the other chemicals were defined by Eq. (3) to Eq. (5):

$$S_{H_2}(\%) = \frac{H_{2,out}}{2(CH_{4,in} - CH_{4,out})} \cdot 100\% \tag{3}$$

$$S_{CO}(\%) = \frac{CO_{out}}{(CH_{4,in} - CH_{4,out}) + (CO_{2,in} - CO_{2,out})} \cdot 100\% \tag{4}$$

$$S_{C_xH_yO_z}(\%) = \frac{x \cdot C_xH_yO_{z,out}}{(CH_{4,in} - CH_{4,out}) + (CO_{2,in} - CO_{2,out})} \cdot 100\% \tag{5}$$

In this study, the energy yield (EY) of dry reforming was defined as the mmol of CO_2 and CH_4 that can be converted per kJ of supplied energy, as shown in Eq. (6):

$$EY\left(\frac{mmol}{kJ}\right) = \frac{V_{CO_2}X_{CO_2}+V_{CH_4}X_{CO_4}}{P_{sply}V_m} \cdot \frac{1000}{60}\left(\frac{Wmin}{kJ}\right) \tag{6}$$

Where V_{CO2} and V_{CH4} were the volumetric flow rate of CO_2 and CH_4 in the feed gas, respectively (in mL/min), and X_{CO2} and X_{CH4} are the conversion of CO_2 and CH_4, respectively. V_m is the molar gas volume (24.4 mL/mmol). It should be noted that P_{sply} in Eq. 6 is the supplied power (in W), and not the discharge power as used in most literature

[3,19]. If the discharge power is used to calculate the EY, we will get a larger value, about 1.5–2 times larger, than the EY presented in this chapter. However, we also want to include the effect of the reactor on the discharge power in the calculation of the energy yield. In this chapter, since two different values of the supplied power were applied, the conversion could not be directly compared between the reactor with two different supplied powers, and the energy yield was more important to reflect the performance.

5.2.3 Electrical characterization

To better understand the effect of adding the stainless steel rings on the reaction performance, we performed an electrical characterization of the plasma. The above-mentioned high voltage probe, low voltage probe, Rogowski coil and capacitor in the plasma set-up can collect the data of the voltage, current and charge during the discharge. The discharge power was calculated by voltage U and current I, via Eq. (7):

$$P_{\mathrm{sply}}(\mathrm{W}) = \int_0^{T} UI\,dt \tag{7}$$

The slopes of the Lissajous figures (dQ/dU) in this work were calculated by a Matlab script [16] to obtain the equivalent capacitance of the DBD reactor at different phases, since dQ/dU = C, as shown in Figure 5.3, a typical Lissajous figure in a DBD reactor. In the AB and CD phases when the reactor is not discharged, the slope of the AB and CD phases in the Lissajous figure is the capacitance of the capacitor formed by the dielectric barrier and the discharge gap in series, denoted by C_{cell}. Plasma occurs in the BC and DA phases. During the discharge, a part of the discharge gap behaves like a resistor due to the breakdown of the reactive gas, while the dielectric barrier and another part of the discharge gap (because the entire gap is not fully discharged in a DBD reactor) still behave as a capacitor. Therefore, the slope of the BC and DA phases, denoted by ζ, represents the capacitance including the dielectric barrier and the undischarged gap.

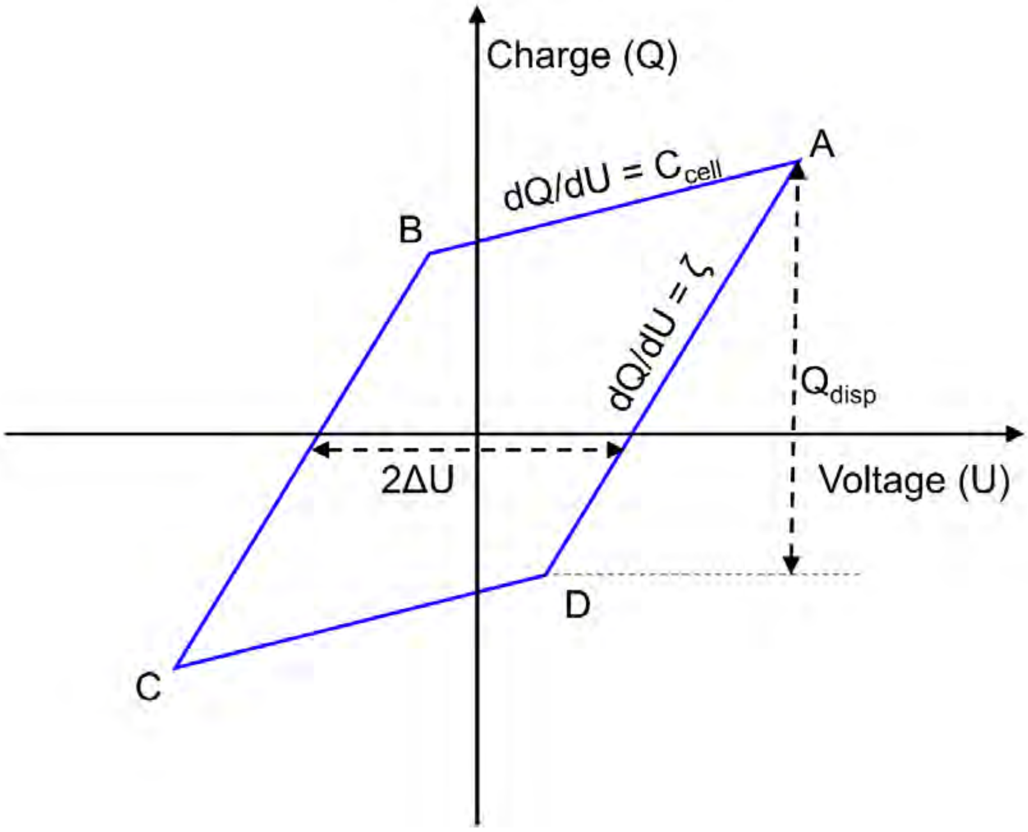

Figure 5.3. Typical Lissajous figure of a discharge in a DBD reactor.

The capacitance C_{diel} of the dielectric barrier alumina tube, used in this work, is 0.266 nF, which was measured in a previous study [16]. Using C_{cell}, ζ and C_{diel}, the discharging areal fraction, denoted as f, of the DBD reactor was calculated by Eq. 8 [20].

$$f = \frac{\zeta - C_{cell}}{C_{diel} - C_{cell}} \tag{8}$$

The burning voltage (U_{bur}) of the plasma in the reactor was calculated from C_{cell}, ζ, C_{diel} and the voltage at Q = 0 C in the Lissajous figures, i.e., ΔU, by Eq. 9 [20].

$$U_{bur} = \frac{1 - C_{cell}/C_{diel}}{1 - C_{cell}/\zeta} \Delta U \tag{9}$$

The charge difference between the points A and D in the Lissajous figure was the displaced charge in the DA discharge phase. It was divided by the number of micro-discharges counted in the current profile to get the average intensity of discharge filaments [16].

5.3 Results and discussion

The plasma-based dry reforming performance in a DBD reactor, with stainless steel rings over the inner electrode, was tested at 50 W and 30 W supplied power.

5.3.1 Plasma-based dry reforming at 50 W supplied power

5.3.1.1 Conversion and energy yield

Figure 5.4 illustrates the influence of placing stainless steel rings over the inner electrode rod on the CH_4 and CO_2 conversions and on the energy yield of plasma-based dry reforming at 50 W supplied power, for the rings with a cross-sectional diameter of 1.6 mm and 3.2 mm. The specific values for conversion and energy yield are in Appendix D, Table D.1. In addition to the EY calculated from the supplied power (as shown in Figure 5.4), the EY calculated from the plasma power is also listed in Table D.1. A difference in performance for the reactors with and without rings was observed, and also the number of rings had an effect. Since the supplied power could not be controlled precisely at 50 W all the time (see Table 5.1), sometimes changes in CH_4 and CO_2 conversions might be caused by supplied power fluctuations, which could not correctly reflect changes in reactor performance. The energy yield can reflect a more accurate trend of the performance. Since all experiments were performed at the same gas flow rate, and not the same space time, the specific input energy (SEI) was only related to the power, and the energy yield follows a similar trend as the conversion. As shown in Figure 5.4a, for 1.6 mm rings, the energy yield and the reactant conversions increase with the number of rings. However, they were always lower than in the reactor without rings. The rings with a cross-sectional diameter of 3.2 mm (Figure 5.4b) showed better performance and a similar but more pronounced increasing trend upon placing more rings. The reactors with only a few rings also had lower performance than the reactor without rings. However, the CO_2 conversion of the reactors with more than 10 rings exceeded that of the reactor with no rings, and the reactor with more than 15 rings also showed a higher energy yield. The DBD reactor with 20 rings with 3.2 mm cross-sectional diameter exhibited the best performance, although the improvement compared with the reactor without rings was limited.

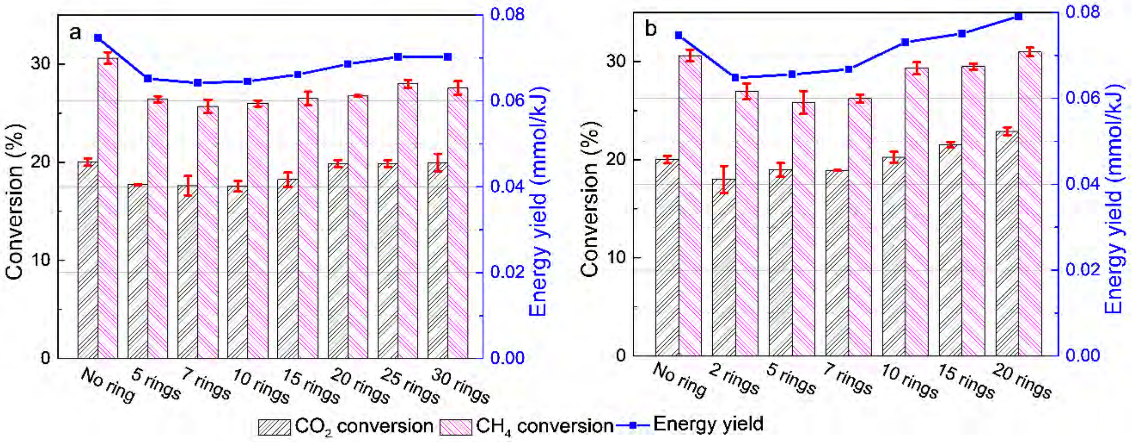

Figure 5.4. CH_4 and CO_2 conversion and energy yield of plasma-based dry reforming at 50 W supplied power, in a DBD reactor without rings, and with a varying number of stainless steel rings placed over the inner electrode, with cross-sectional diameters of (a) 1.6 mm and (b) 3.2 mm. The error bars were obtained from standard errors based on three repeat experiments with the rings kept in place.

Placing stainless steel rings over the inner electrode mainly has the following effects on the discharge in the DBD reactor. First of all, as introduced in the experimental section, the discharge gap between the inner electrode and the dielectric barrier was 4.7 mm (i.e., 17.4 mm − 8 mm, divided by 2). The metal rings reduced the discharge gaps at this location, to values of 3.1 mm and 1.5 mm, for the 1.6 mm and 3.2 mm rings, respectively (i.e., 17.4 mm – 11.2 mm, divided by 2; and 17.4 mm – 14.4 mm, divided by 2). The reduction in discharge gap causes a higher reduced electric field strength and power density at the metal rings, leading to more displaced charge per period (see section 3.1.2 below) and a higher electron energy. Therefore, more gas molecules can be hit by the discharge filaments [11], and more successful electron impact excitation can occur in the plasma [21]. These are the positive effects of the metal rings on the plasma behavior, which should increase the performance of the reactor [22]. The 3.2 mm rings exhibit better performance than the 1.6 mm rings due to the smaller discharge gap. However, these positive effects are not well reflected between reactors with and without rings in Figure 5.4, indicating the presence of negative effects, resulting in the majority of the ring-based configurations at 50 W supplied power being lower in performance than for the reactor without rings.

Secondly, the presence of rings in the discharge space of the DBD reactor reduces the available discharge volume. Since the same gas flow rate was applied in the experiments in Figure 5.4, the discharge volume reduction reduced the space time of plasma-based dry reforming. This is unfavorable to the conversion of CH_4 and CO_2. In previous studies on a micro-gap DBD reactor [16], the reduction in discharge volume resulted in a lower energy yield than reactors with larger discharge gaps, despite the stronger electric field in the micro-gap reactor. However, the metal rings in this study only occupy part of the discharge volume at the location where the rings were placed, which is much smaller than the drop in volume brought by reducing the entire discharge gap in the micro-gap reactors. Moreover, as observed in Figure 5.4, increasing the number or the cross-sectional diameter of the rings causes some improvement in conversion and energy yield (even when compared to the reactor without rings in some cases), although more rings means a larger discharge volume reduction. This suggests that although metal rings do reduce the discharge volume to some extent (~0.05 mL for each 1.6 mm ring and ~0.2 mL for each 3.2 mm ring), this is not the main negative factor that leads to the lower performance of the reactor with rings than the reactor without rings.

Finally, compared with the smooth and uniform surface of the inner electrode rod, discharges are more likely to take place on the metal rings with stronger reduced electric fields. This makes the discharge more stable and more uniform in intensity (see section 3.1.2 below), which may be beneficial to reduce the formation of by-products and improve the selectivity of the desired products [12]. However, the spatial distribution of the discharges becomes relatively non-uniform, as it is more difficult for the discharge to take place where no metal rings are present. This reduces the chance of gas molecules being hit by the discharges, resulting in an expected reduced conversion and energy yield [11]. Increasing the number of rings will reduce the distance between the rings, and is thus expected to improve the spatial uniformity of the plasma, in line with the trend in Figure 5.4 that the performance increases with the number of rings. This indicates that the non-uniform spatial distribution of the discharge is a more dominant negative effect of the stainless steel rings on the reactor performance compared to the reduction of the discharge volume. In addition, the existence of the rings might have an effect on the gas flow, such as turbulence, which could affect the mixing of the active species in the reactor.

5.3.1.2 Electrical characterization

Electrical characterization data of the above experiments were collected and calculated to better understand the effect of the stainless steel rings. The data that can be obtained directly from the raw measurement data or through simple calculations like averaging, are listed in Table 5.1. In most cases, the required applied peak-to-peak voltage (U_{pp}) to achieve a 50 W supplied power in the reactors with rings was smaller than in the reactor without rings. Moreover, the required U_{pp} decreased with the number of rings, while the root mean square current (I_{RMS}) of the generated plasma increased. Reactors with fewer than 15 rings with 1.6 mm diameter had a lower I_{RMS} than the ring-free reactor, while reactors with more than 15 rings with 1.6 mm diameter and all reactors with 3.2 mm rings had a higher I_{RMS} than the ring-free reactor. Only the U_{pp} trend of the reactors with 1.6 mm rings was not obvious when the number of rings was above 10. For the 3.2 mm rings, the U_{pp} was lower and the I_{RMS} was higher than for the same number of 1.6 mm rings, and the decrease in U_{pp} with the number of rings was more pronounced. The plasma power of the 1.6 mm rings did not show a clear trend, while the 3.2 mm rings showed a trend of decreasing plasma power with increasing number of rings, which is, in principle, negative to the performance of the reactor.

Table 5.1. Measured data from the input signals of the oscilloscope, including voltage, current, charge and power, for the DBD reactors without rings, and with stainless steel rings of varying number and two different cross-sectional diameters, at an almost constant supplied power of 50 W.

Cross-sectional diameter of rings	Number of rings	U_{pp} (kV)	I_{RMS} plasma (mA)	Plasma power (W)	Supplied power (W)	Displaced charge (nC/period)
Without rings	0	19.9	19.5	31.3	51.0	980
1.6 mm	5	19.4	16.8	32.0	50.4	1150
	7	18.5	18.3	32.2	50.2	1210
	10	17.7	18.8	32.7	50.2	1260
	15	17.1	19.7	32.7	50.3	1320
	20	17.2	21.8	33.0	50.6	1314
	25	17.2	22.1	32.3	50.7	1320
	30	17.4	22.4	31.9	50.3	1290
3.2 mm	2	20.2	20.0	30.8	51.6	1070
	5	19.2	21.4	29.0	51.1	1320
	7	18.2	22.6	28.5	50.3	1420
	10	17.4	24.5	28.1	50.5	1498
	15	16.7	25.1	27.9	50.5	1600
	20	16.7	24.9	26.7	50.6	1652

Figure 5.5 shows the fitted Lissajous figures (consisting of the calculated slopes) of the plasma at 50 W supplied power, in reactors with varying number and two different cross-sectional diameter of the stainless steel rings. The raw data of the Lissajous figures are shown in Figure D.1, in the Appendix D. Obvious differences can be observed from the Lissajous figures. First of all, the height of the Lissajous figure of the reactors with rings is higher than that of the reactor without rings, and it continues to increase as the number of rings increases. This indicates that the metal rings lead to more charge displacement within the plasma, which supports the aforementioned discharge promotion by the enhanced reduced electric field. The specific values of the displaced charges were calculated by taking the charge

difference between points A and D of the Lissajous figures, and are listed in Table 5.1. For the 1.6 mm rings, only the reactors with less than 15 rings showed an obvious trend of increasing the displaced charge with increasing number of metal rings, while the trend for the 3.2 mm rings is still relatively obvious until the maximum of 20 rings. Furthermore, the displaced charge in case of the 3.2 mm rings was always more than that of the 1.6 mm rings with the same number of rings, which should be one of the reasons why the reactors with 3.2 mm rings showed higher performance.

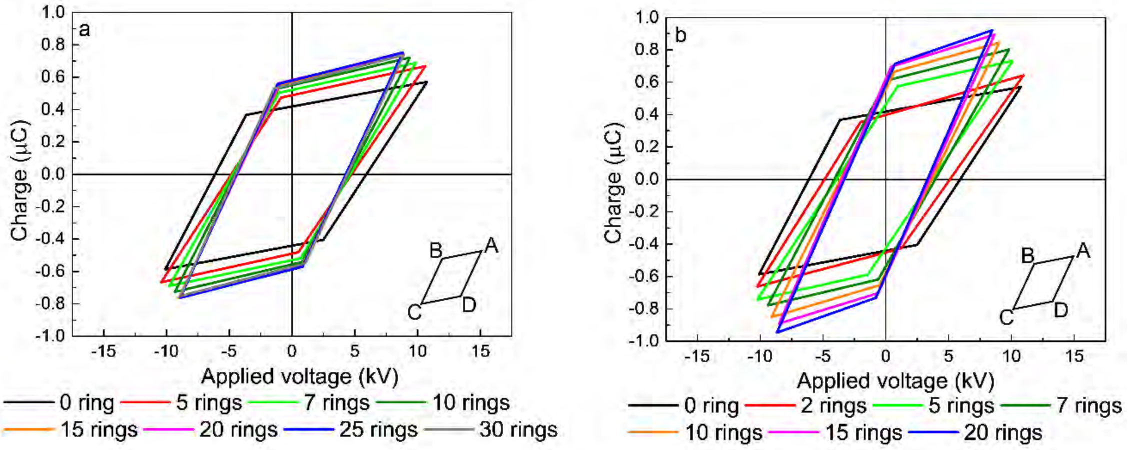

Figure 5.5. The fitted Lissajous figures (calculated by the MATLAB script) of plasma-based dry reforming at 50 W supplied power, in a DBD reactor without rings, and with varying number of stainless steel rings with cross-sectional diameters of (a) 1.6 mm and (b) 3.2 mm.

Secondly, the voltage at Q = 0 C in the Lissajous figures, which is related to the burning voltage (U_{bur}) of the plasma in the reactor, was changed by the rings. As shown in Table 5.2, after placing the stainless steel rings on the inner electrode, U_{bur} was significantly reduced. Furthermore, as the number of rings increases, U_{bur} shows a roughly decreasing trend. This suggests that the metal rings made it easier to ignite and sustain the plasma at relatively lower voltages. Moreover, the 3.2 mm rings lower the U_{bur} more than the 1.6 mm rings.

Finally, the slope of each side of the Lissajous figures also changes, indicating that the metal rings change the capacitance of the DBD reactor. The slope (capacitance of the entire reactor) C_{cell} of the undischarged phases and the slope ζ representative for the capacitance of the discharged phases are listed in Table 5.2. The capacitance C_{cell} of all the reactors with rings is always higher than that of the reactor without rings, because the discharge gaps are reduced by placing the metal rings. There seems to be a slightly rising trend of C_{cell} with the number of rings, but some cases do not follow it. On the other hand, ζ, has a clearly increasing trend with the number of rings. Since the DBD reactor was not fully discharged, the capacitance represented by ζ includes the capacitance of the undischarged gap and the dielectric barrier. The capacitance of the dielectric barrier is constant because the same barrier was used in all experiments. Therefore, the rise of ζ indicates that the undischarged fraction decreases upon increasing number of rings. The fractions of discharges (denoted by f) in the reactors, calculated from C_{cell} and ζ, are also listed in Table 5.2. For the 1.6 mm rings, the discharge fraction increases from 40.0% for 5 rings to 60.1% for 30 rings, while for the 3.2 mm rings, it increases from 38.7% for 2 rings to 62.9% for 20 rings, hence showing a larger increase rate. Since the gas flow rate was approximately constant and the plasma power was even reduced (at a constant supplied power) with the number of rings, the larger discharge fraction by the stainless steel rings was achieved without increasing the specific energy input. It needs to be noted that the plasma discharge fraction of the reactors with 5 rings or less, both for the 1.6 mm and 3.2 mm rings, was smaller than that of the reactor without rings, but as the number of rings increases, the discharge fraction becomes larger than in the reactor without rings. This is in line with the effect mentioned above: the metal rings can promote the discharge but will induce the discharge mainly taking place on the rings, resulting in a non-uniform spatial distribution of the discharge. The spacing between the rings, where it is more difficult for the discharge to take place, is large in reactors with fewer than five rings, and hence in this case the discharge fraction is even smaller than that of a reactor without rings. As the number of rings increases, the negative effect on the discharge fraction decreases and the positive effect increases, so the discharge fraction increases substantially.

Table 5.2. Calculated data derived from the raw data of electrical characterization, obtained by a MATLAB script, for the DBD reactors without rings and with stainless steel rings of varying number and two different cross-sectional diameters, at an almost constant supplied power of 50 W.

Cross-sectional diameter of rings	Number of rings	U_{bur} (kV)	C_{cell} (pF)	ζ (pF)	f (%)	Number of micro-discharges (a.u./T)	Average filament charge (nC/disch.)
Without rings	0	6.3	14.3	133.1	47.2	90	11
1.6 mm	5	5.2	16.9	116.5	40.0	75	15
	7	5.0	16.6	134.3	47.2	80	15
	10	4.7	18.2	149.7	53.1	81	16
	15	4.5	19.5	162.9	58.2	81	16
	20	4.5	18.8	165.7	59.4	96	14
	25	4.4	19.7	168.0	60.2	83	16
	30	4.6	20.1	167.8	60.1	93	14
3.2 mm	2	5.7	21.4	116.0	38.7	140	8
	5	4.1	17.3	116.2	39.8	126	10
	7	4.2	18.9	141.6	49.7	163	9
	10	3.9	22.2	155.9	54.8	150	10
	15	6.3	14.3	133.1	62.5	165	10
	20	5.2	16.9	116.5	62.9	135	12

Figure 5.6 shows the current profiles in the DBD reactors with varying number and two different cross-sectional diameters of the stainless steel rings. Although the difference in current profiles between the reactors with relatively more rings is not significant, comparing them with those reactors with no rings and fewer (≤ 5) rings shows the influence of the metal rings. The difference between current intensities in the reactor without rings is large, and it decreases as the number of rings increases. This confirms that the rings can make the discharge more uniform in intensity, which may change the selectivity of some products. The discharge onset in the reactors with rings is earlier, which is consistent with one of the conclusions of Figure 5.5 that the rings reduce the burning voltage of the plasma. The number of peaks in the current profiles is a measure for the number of micro-discharges in the plasma, this number is also listed in Table 5.2. The number of micro-discharges in the reactors with 1.6 mm rings is similar to that in the reactor without rings, while the number of micro-discharges in the reactor with the 3.2 mm rings is clearly higher (cf. Table 5.2).

Finally, the average filament charge of the micro-discharges can be obtained by dividing the displaced charge by the number of micro-discharges, and is a measure of the average discharge intensity. The average filament charge in case of the 1.6 mm rings is higher than that of the reactor without rings, while that of the 3.2 mm rings is similar to or even lower. Metal rings with both cross-sectional diameters improve the displaced charge within the plasma, as mentioned above, but the improvement for the 1.6 mm rings is on the average filament charge, or average discharge intensity, while the improvement for the 3.2 mm rings is on the number of micro-discharges. Hence, the change in discharge behavior caused by the stainless steel rings is different, possibly depending on the size of the remaining discharge gap between the metal and the dielectric barrier.

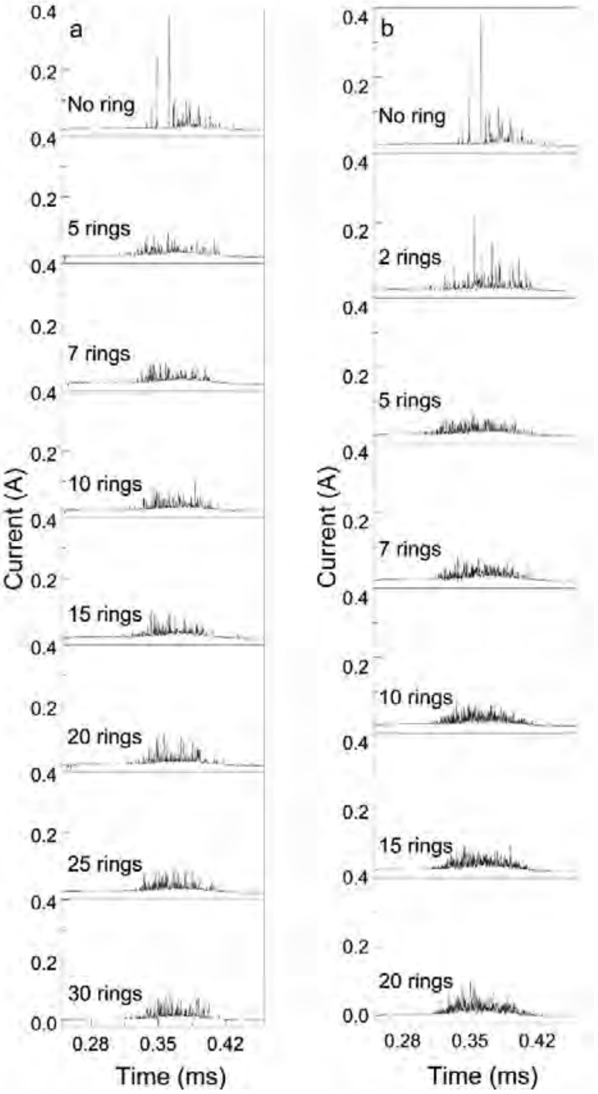

Figure 5.6. Current profiles of a discharge phase in DBD reactors at 50 W supplied power, without rings, and with a varying number of stainless steel rings with cross-sectional diameters of (a) 1.6 mm and (b) 3.2 mm.

5.3.1.3 Selectivity

Due to the limited surface area of the rings and the fact that a similar material was used as for the stainless steel inner electrode, we believe that the conversion and selectivity changes are mainly caused by the physical effect of the rings on the discharge. Figure 5.7 shows the selectivity of various products of the plasma-based dry reforming in the DBD reactor without rings and with varying numbers of stainless steel rings at 50 W supplied power, for both 1.6 mm and 3.2 mm rings. It needs to be noted that some possible liquid products and carbon deposits attached to the reactor, as well as other gaseous products not calibrated in the gas chromatograph, cannot be counted, and therefore, the carbon and hydrogen mass balance calculated from the product selectivity does not reach 100% (shown in Figure D.2 of the Supporting Information). As is clear from Figure 5.7, at 50 W supplied power, the placement of the metal rings and the number of rings only had a small effect on the selectivity of most products. The exception is that there is a slightly increasing trend for the selectivity of methanol with the number of rings, and the selectivity of ethane is more affected, although without a clear trend.

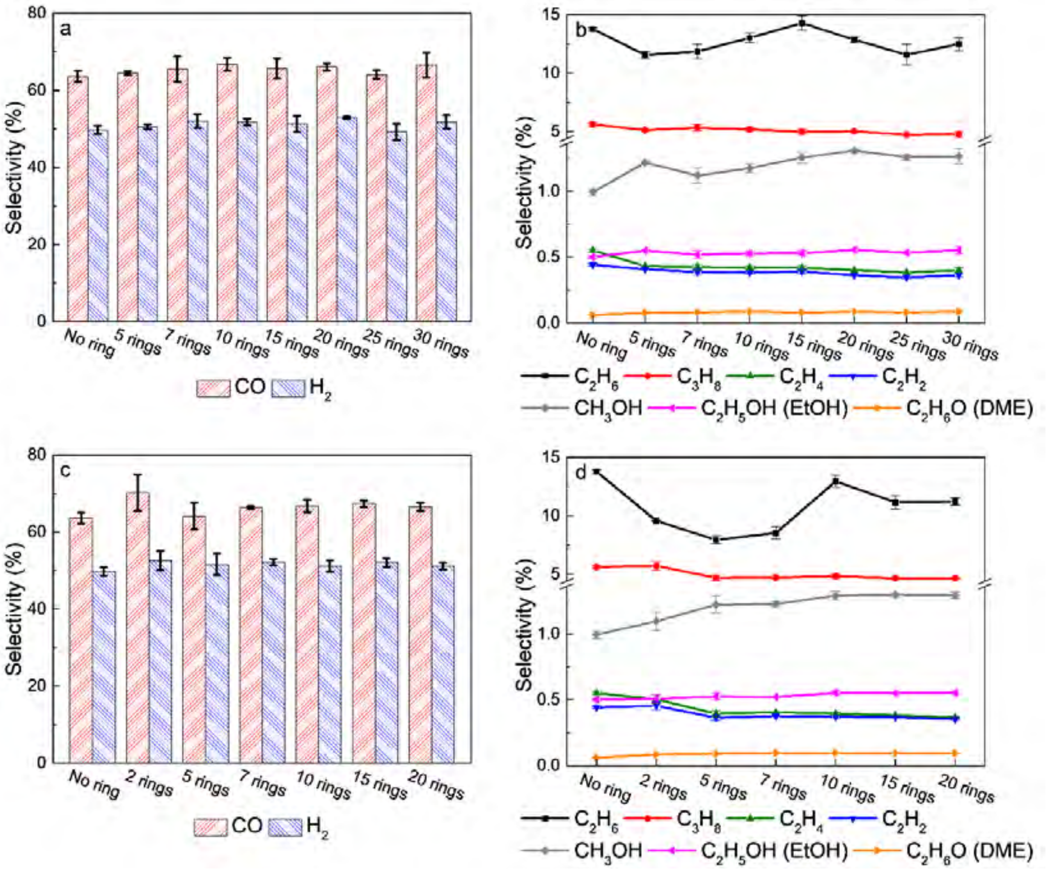

Figure 5.7. Selectivity of various products of plasma-based dry reforming at 50 W supplied power, in a DBD reactor without rings, and with varying number of stainless steel rings. (a) Syngas and (b) ethane, propane, ethylene, acetylene, methanol, ethanol (EtOH) and dimethyl ether (DME) selectivity in reactors with rings with a diameter of 1.6 mm. (c) Syngas and (d) ethane, propane, ethylene, acetylene, methanol, ethanol and dimethyl ether selectivity in reactors with rings with a diameter of 3.2 mm. The error bars were obtained from standard errors based on three repeat experiments with the rings kept in place.

5.3.2 Plasma-based dry reforming at 30 W supplied power

5.3.2.1 Conversion and energy yield

Figure 5.8 shows the influence of the same 1.6 mm and 3.2 mm rings on the CH_4 and CO_2 conversions and the energy yield of plasma-based dry reforming, but at 30 W supplied power. The effect of the rings is clearly different from the case at 50 W. At 30 W, the energy yields and reactant conversions in all reactors with the rings are higher than in the reactor without rings. There is also a clear effect of the number of rings to the conversion and energy yield, and the performance of the reactor with 3.2 mm rings has a tendency to increase with the number of rings. Compared with the reactor without rings, the increase of reactor performance resulting from the rings at 30 W supplied power is much greater than at 50 W. The DBD reactor with 20 rings with a 3.2 mm cross-sectional diameter has the best performance, with an energy yield double the value of the reactor without rings. It enhances the CO_2 conversion from 7.1% to 16.3 %, the CH_4 conversion from 11.9% to 22.5%, and the energy yield from 0.05 mmol/kJ to 0.1 mmol/kJ. As already mentioned above, the energy yield in this work was calculated from the supplied power, and the energy yield of the reactor with the best performance is 0.19 mmol/kJ if calculated from the plasma power as in most of the literature. Furthermore, compared to the reactors with the same number and diameter of rings at a supplied power of 50 W, although the CO_2 and CH_4 conversions are reduced due to the lower power, the energy yield is actually improved by 17% on average at 30 W, except for the reactor without rings.

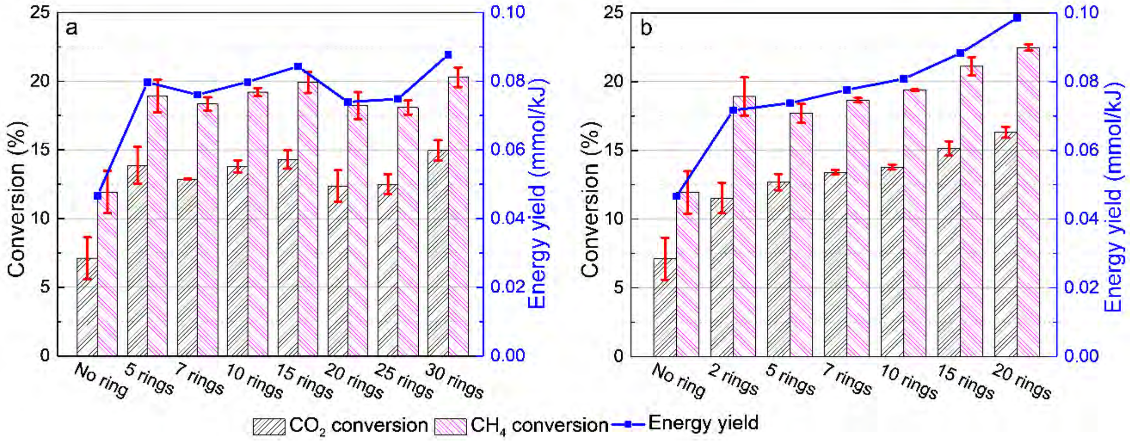

Figure 5.8. CH_4 and CO_2 conversion and energy yield of plasma-based dry reforming at 30 W supplied power, in a DBD reactor without rings, and with varying number of stainless steel rings with cross-sectional diameters of (a) 1.6 mm and (b) 3.2 mm. The error bars were obtained from standard errors based on three repeat experiments with the rings kept in place.

The effects of adding the stainless steel rings on the discharge has been described in section 3.1 above, and also apply here, i.e., a higher displaced charge, a larger discharge fraction, a higher discharge intensity, etc. In addition, the discharge in the reactor without rings is unstable at 30 W supplied power (see section 3.2.2 below), which is one of the reasons that the improvement of the reactor performance by the metal rings is so large at 30 W. On the other hand, the positive effects of the metal rings on the discharge is indeed greater at 30 W supplied power, as can be deduced below from the larger changes in parameters such as the discharge fraction and burning voltage.

5.3.2.2 Electrical characterization

Table 5.3 shows the collected and calculated electrical characterization data of the experiments in Figure 5.8, to better understand the effect of the stainless steel rings at 30 W supplied power. Similar to the case of 50 W, in most cases, the required applied U_{pp} to achieve a 30 W supplied power in the reactors with rings is smaller than in the reactor without rings. The required U_{pp} decreases again with the number of rings, while the I_{RMS} of the generated plasma increase again. The trend of U_{pp} and I_{RMS} of the reactors with 1.6 mm rings is not obvious when the number of rings is more than 10. For the 3.2 mm rings, the U_{pp}

is lower and the I_{RMS} was higher than for the same number of 1.6 mm rings, and the trend of U_{pp} with the number of rings was again more pronounced. However, different from the experiments at 50 W supplied power, the generated plasma power in all the reactors with rings is higher than in the reactor without rings. This is because the plasma in the reactor without rings is unstable, extinguishing or not discharging for some periods. As shown in Figure D.3 in the SI, in 6 periods of 2 ms, there was no discharge in 4 half periods. This is also one of the reasons for the poor performance of the reactor without rings at 30 W supplied power. Since the plasma power is calculated as the average power over all periods, including the phases without discharge, the plasma power in the reactor without rings is lower than in the other reactors.

Table 5.3. Measured data from the input signals of the oscilloscope, including voltage, current, charge and power, for the DBD reactors without rings and with stainless steel rings of varying number and two different cross-sectional diameters, at an almost constant supplied power of 30 W.

Cross-sectional diameter of rings	Number of rings	U_{pp} (kV)	I_{RMS} plasma (mA)	Plasma power (W)	Supplied power (W)	Displaced charge (nC/period)
Without rings	0	21.0	14.4	10.2	30.4	360
1.6 mm	5	17.9	13.9	16.4	30.6	700
	7	17.0	14.6	16.0	30.5	718
	10	16.1	17.2	18.0	30.8	780
	15	15.6	16.6	17.3	30.2	770
	20	15.9	17.7	17.4	30.8	790
	25	16.0	17.5	16.6	30.4	766
	30	15.9	17.8	16.1	29.9	734
3.2 mm	2	19.5	15.6	14.2	31.6	700
	5	16.6	16.4	15.4	30.7	850
	7	15.7	17.2	15.4	30.8	884
	10	15.0	18.2	15.7	30.5	930
	15	14.3	19.1	15.9	30.6	1000
	20	14.2	19.4	15.3	30.2	990

Figure 5.9 shows the fitted Lissajous figures of the plasma at 30 W supplied power, in the reactors without rings and with varying number and two different cross-sectional diameter

of the stainless steel rings. The raw data of the Lissajous figures are shown in Figure D.4. It should be noted that the Lissajous figure of the reactor without rings is only in the discharge phases, because the Lissajous figure could not be formed in the undischarged period. The Lissajous figures at 30 W exhibit more obvious differences between the reactors with and without rings than at 50 W supplied power. First of all, the height of the Lissajous figures, reflecting the displaced charge (see Table 5.3), follows the same trend, which is higher for the reactors with rings than for the reactor without rings, and increases with the number of rings. After placing a certain number of rings (e.g. 15 of 1.6 mm rings), a larger number of rings does not enhance the displaced charge anymore. The enhancement of displaced charge by the rings is more than double or even nearly triple that of the reactor without rings, indicating that the promotion of stainless steel rings on the plasma is greater at 30 W. Furthermore, the displaced charge of the 3.2 mm rings was also more than that of the 1.6 mm rings with the same number of rings at 30 W, so the reactors with 3.2 mm rings also yield a higher performance. Secondly, the U_{bur} reflecting the voltage for igniting and sustaining the plasma, calculated from the Lissajous figures, was reduced by the metal rings, in a similar trend as at 50 W. Finally, the capacitance of different phases of the DBD reactor, C_{cell} and ζ, calculated from the slope of the Lissajous figures, are listed in Table 5.4, as well as the discharge fractions, which are also calculated from them. The tendency of capacitance and discharge fraction due to the presence of the rings is the same as at 50 W. Thicker and more rings increase the capacitance and the discharge fraction. The 1.6 mm rings increase the discharge fraction from 30.0% for 5 rings to 44.7% for 30 rings, while the 3.2 mm rings increase the discharge fraction from 20.1% for 2 rings to 51.4% for 20 rings, with a larger increase rate. The discharge fraction of the reactors with relatively few (≤ 5) rings were smaller than that of the reactor without rings, probably because the rings induce the discharge to mainly take place on them, as mentioned above in section 3.1.2. The discharge fraction of the same reactor at 30 W was less than at 50 W. However, compared with the ring-free reactor, some plasma parameters, including the discharge fraction, burning voltage and displaced charge, were improved more by the presence of rings at 30W than at 50W, which is another reason why the reactor with stainless steel rings showed better performance at 30W.

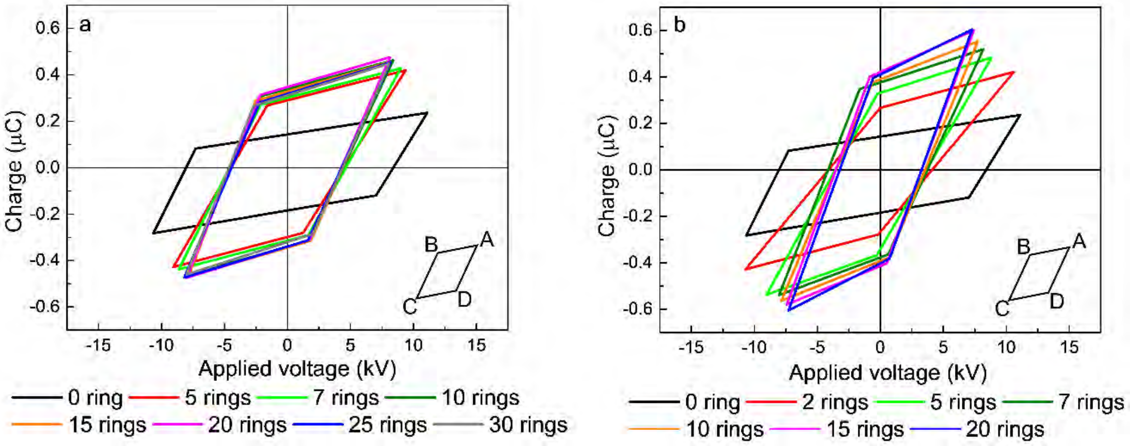

Figure 5.9. The fitted Lissajous figures (calculated by the MATLAB script) of plasma-based dry reforming at 30 W supplied power, in a DBD reactor without rings and with varying number of stainless steel rings with cross-sectional diameters of (a) 1.6 mm and (b) 3.2 mm.

Table 5.4. Calculated data derived from the raw data of electrical characterization, obtained by a MATLAB script, for the DBD reactors without rings and with stainless steel rings of varying number and two different cross-sectional diameters, at an almost constant supplied power of 30 W.

Cross-sectional diameter of rings	Number of rings	U_{bur} (kV)	C_{cell} (nF)	ζ (nF)	f (%)	Number of micro-discharges (a.u./T)	Average filament charge (nC/disch.)
Without rings	0	8.9	8.8	98.0	34.7	68	5
1.6 mm	5	5.1	14.0	89.7	30.0	97	7
	7	5.1	14.2	103.5	35.5	139	5
	10	4.8	15.0	122.6	42.8	110	7
	15	4.7	16	133.4	47.0	92	8
	20	4.6	16.3	129	45.2	99	8
	25	4.7	16.4	121.5	42.1	101	8
	30	4.7	17.2	128.5	44.7	117	6
3.2 mm	2	5.0	14.4	65.0	20.1	71	10
	5	4.2	18.3	95.9	31.3	107	8
	7	4.1	18.8	127.8	44.1	161	6
	10	3.9	21.5	131.2	44.9	135	7
	15	3.6	23.3	147.1	51.0	101	10
	20	3.6	27.2	149.9	51.4	124	8

Figure 5.10 shows the current profiles in the DBD reactors at 30 W supplied power. It should be noted that the current profile of the reactor without rings is selected from the stable discharge phases, and actually it is not discharged in some phases, as shown in Figure D.2. At 30 W supplied power, the stainless steel rings are again able to make the discharge more uniform in intensity, even with only 2 or 5 rings. The onset of the discharge was earlier in the reactors with rings due to the reduction in U_{pp}. The number of micro-discharges and average filament charge were calculated and listed in Table 5.4. Different from the experiments at 50 W, where the 1.6 mm rings or 3.2 mm rings can only increase either the average filament charge or the number of micro-discharges, at 30 W supplied power, both these parameters are higher in the reactors with rings than in the reactor without rings. The reason for the larger number of micro-discharges by the rings with both diameters is that the discharge in the reactor without rings at 30 W is unstable and extinguishes in some periods. Moreover, with a larger number of micro-discharges, the average displaced charge per discharge of the reactor with rings is still higher than that of the reactor without rings. This indicates again that at 30 W supplied power, the improvement of the discharge by the metal rings is greater than that at 50 W.

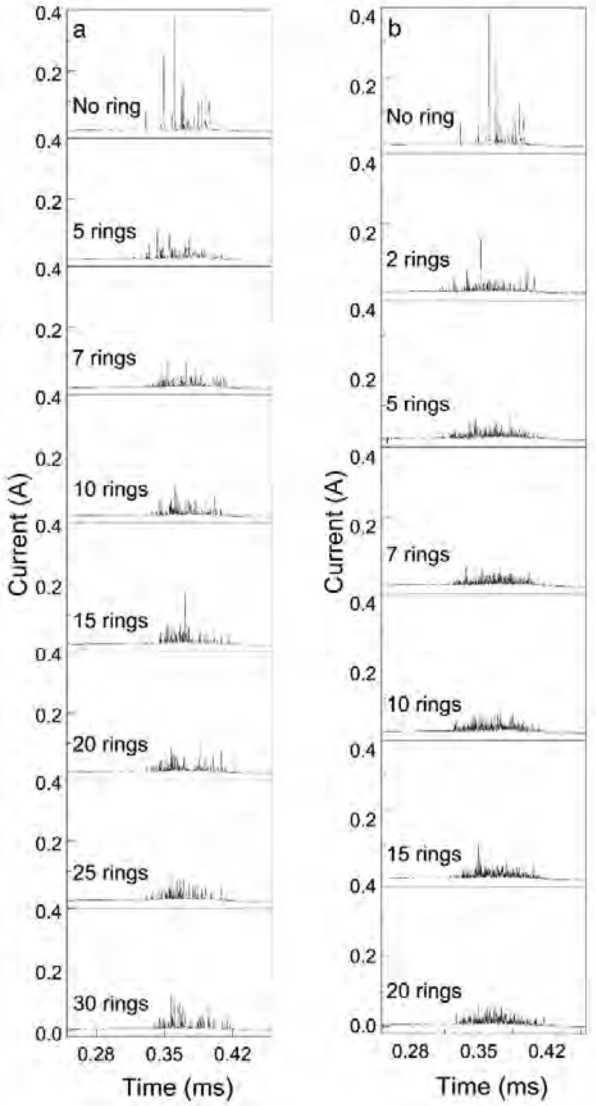

Figure 5.10. Current profiles of a discharge phase in DBD reactors at 30 W supplied power, for the reactor without rings and with varying number of stainless steel rings with cross-sectional diameters of (a) 1.6 mm and (b) 3.2 mm.

5.3.2.3 Selectivity

Figure 5.11 shows the selectivity of various products of the plasma-based dry reforming in DBD reactors with stainless steel rings at 30 W supplied power. In most cases, the syngas selectivity in the reactors with rings is slightly higher than in the reactor without rings. In fact, the higher selectivity resulting from the rings seems to be present at 50 W as well, but is less obvious. Figure D.5 shows the carbon and hydrogen atomic balance, plotted from Figure 5.11, and the atomic balance of the reactor with rings is higher than for the reactor without rings. This may be due to the fact that the products of plasma-based dry reforming were formed by the reaction of various radicals generated by the discharge, and the more uniform intensity of the discharge could reduce the types of formed by-products [12].

In addition, lower power seems to be favorable for improving the selectivity of some products. The selectivity of CO, H_2, ethylene, acetylene, methanol, and ethanol at 30 W was higher than at 50 W, while the selectivity of other products was not much different. Close observation and comparison of the selectivity at 30 W and 50 W shows similarities in the trend of selectivity of some products at different powers. This also proves that although there are mainly physical effects, the stainless steel rings can have a certain effect on the product selectivity as well.

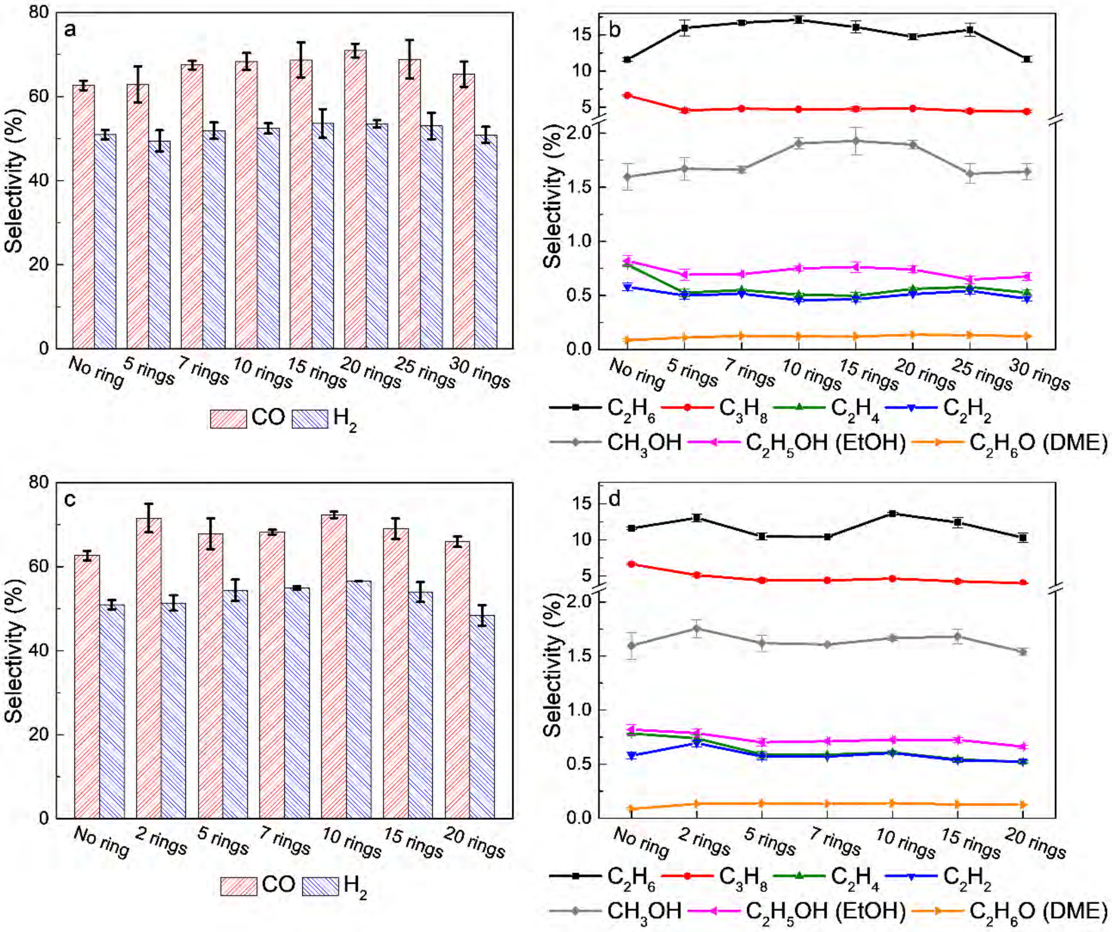

Figure 5.11. Selectivity of various products of plasma-based dry reforming at 30 W supplied power, in a DBD reactor without rings and with varying number of stainless steel rings. (a) Syngas and (b) ethane, propane, ethylene, acetylene, methanol, ethanol (EtOH) and dimethyl ether (DME) selectivity in reactors with rings with a diameter of 1.6 mm. (c) Syngas and (d) ethane, propane, ethylene, acetylene, methanol, ethanol and dimethyl ether selectivity in reactors with rings with a diameter of 3.2 mm. The error bars were obtained from standard errors based on three repeat experiments with the rings kept in place.

5.4 Conclusion

In this study, we put stainless steel rings over the inner electrode rod of a cylindrical DBD reactor, to change the local discharge gap and the electric field, and to study the dry reforming performance. A varying number of rings with cross-sectional diameters of 1.6 mm and 3.2 mm was used, and experiments were carried out at 50 W and 30 W supplied power. Since the rings are made of similar material as the inner electrode and with small surface area, we believe that the rings mainly cause physical effects on the discharge, and the catalytic effects are not considered. This study can therefore also provide a reference for the physical effects of catalysts with metal active components on the discharge behavior and reaction performance.

We found that at 50 W supplied power, the stainless steel rings mainly have negative effects on the performance relative to the reactor without rings. Only in a few cases the effects of the rings on the dry reforming performance are positive. However, at 30 W supplied power, the stainless steel rings greatly improve the performance, both in terms of reactant conversion and energy yield. The reactor with 20 rings with a 3.2 mm cross-sectional diameter showed the best performance. Compared to the reactor without rings, it increases the CO_2 conversion from 7.1% to 16.3 %, the CH_4 conversion from 11.9% to 22.5%, and the energy yield from 0.05 mmol/kJ to 0.1 mmol/kJ (0.19 mmol/kJ if it was calculated from the plasma power). All reactors with rings have higher energy yield at 30 W than at 50 W.

The difference in performance can be understood from studying the electrical characteristics. The presence of the stainless steel rings changes the electric field distribution in the reactor. The discharge gap is smaller where the rings are placed, increasing the local electric field. Through electrical characterization, it was found that the displaced charge and the discharge fraction, which can improve the conversion and energy yield of plasma-based dry reforming, increase with the number and the cross-sectional diameter of rings at the same energy input. This is the reason that the 3.2 mm rings always exhibit higher performance than the 1.6 mm rings. The non-uniform discharge gap caused by the rings makes the discharge more stable and more uniform in intensity, although its spatial distribution may be non-uniform. This spatial non-uniformity was reduced by placing more rings, while the positive effects such as displaced charge were enhanced, leading to better performance in reactors with more rings. Although the presence of metal rings reduces the discharge volume of plasma-based dry reforming and thus the space time, this negative effect was not significant in our study, since more rings and with larger diameter showed better performance in all experiments at the same gas flow rate. At 30 W supplied power, the metal rings can stabilize the discharge and have a greater improvement in the discharge (such as the number of micro-discharges, the average discharge intensity, and the discharge fraction) than at 50 W, and thus yield better performance. Moreover, the effect of the stainless steel rings on the discharge can also alter the selectivity of some products. The largest impact on selectivity is however caused by lowering the supplied plasma power to 30W, increasing the selectivity of e.g. methanol and ethane.

Besides dry reforming, the performance differences by placing metal rings in the DBD reactor to alter the discharge gap distribution may be applicable to other plasma-based processes as well. In addition, in plasma catalysis, the metal active components on the catalyst surface can also change the discharge gap and electric field distribution in the reactor, and the effects mentioned above might also play some role there. Catalyst studies to improve the conversion and selectivity of plasma reactions need to consider not only its catalytic activity, but also these effects on discharge behavior.

5.5 References

[1] Chung, W.-C.; Chang, M.-B. Review of catalysis and plasma performance on dry reforming of CH_4 and possible synergistic effects. *Renewable and Sustainable Energy Reviews* **2016**, *62*, 13-31.

[2] Khoja, A. H.; Tahir, M.; Amin, N. A. S. Recent developments in non-thermal catalytic DBD plasma reactor for dry reforming of methane. *Energy Convers. Manage.* **2019**, *183*, 529-560.

[3] Tu, X.; Whitehead, J. C. Plasma-catalytic dry reforming of methane in an atmospheric dielectric barrier discharge: Understanding the synergistic effect at low temperature. *Appl. Catal. B Environ.* **2012**, *125*, 439-448.

[4] Khoja, A. H.; Tahir, M.; Amin, N. A. S. Dry reforming of methane using different dielectric materials and DBD plasma reactor configurations. *Energy Convers. Manage.* **2017**, *144*, 262-274.

[5] Ozkan, A.; Dufour, T.; Bogaerts, A.; Reniers, F. How do the barrier thickness and dielectric material influence the filamentary mode and CO_2 conversion in a flowing DBD? *Plasma Sources Sci. Technol.* **2016**, *25*, 045016.

[6] Ozkan, A.; Dufour, T.; Silva, T.; Britun, N.; Snyders, R.; Bogaerts, A.; Reniers, F. The influence of power and frequency on the filamentary behavior of a flowing DBD—application to the splitting of CO_2. *Plasma Sources Sci. Technol.* **2016**, *25*, 025013.

[7] Vanraes, P.; Nikiforov, A.; Bogaerts, A.; Leys, C. Study of an AC dielectric barrier single micro-discharge filament over a water film. *Scientific Reports* **2018**, *8*, 10919.

[8] van 't Veer, K.; Engelmann, Y.; Reniers, F.; Bogaerts, A. Plasma-Catalytic Ammonia Synthesis in a DBD Plasma: Role of Microdischarges and Their Afterglows. *J. Phys. Chem. C* **2020**, *124*, 22871-22883.

[9] Andersen, J. A.; Christensen, J. M.; Østberg, M.; Bogaerts, A.; Jensen, A. D. Plasma-catalytic dry reforming of methane: Screening of catalytic materials in a coaxial packed-bed DBD reactor. *Chem. Eng. J.* **2020**, *397*, 125519.

[10] Snoeckx, R.; Aerts, R.; Tu, X.; Bogaerts, A. Plasma-Based Dry Reforming: A Computational Study Ranging from the Nanoseconds to Seconds Time Scale. *J. Phys. Chem. C* **2013**, *117*, 4957-4970.

[11] van 't Veer, K.; van Alphen, S.; Remy, A.; Gorbanev, Y.; De Geyter, N.; Snyders, R.; Reniers, F.; Bogaerts, A. Spatially and temporally non-uniform plasmas: microdischarges from the perspective of molecules in a packed bed plasma reactor. *J. Phys. D Appl. Phys.* **2021**, *54*, 174002.

[12] Ray, D.; Reddy, P. M. K.; Subrahmanyam, C. Ni-Mn/γ-Al_2O_3 assisted plasma dry reforming of methane. *Catal. Today* **2018**, *309*, 212-218.

[13] Bogaerts, A.; Centi, G. Plasma technology for CO_2 conversion: a personal perspective on prospects and gaps. *Frontiers in Energy Research* **2020**, *8*, 111.

[14] Ağıral, A.; Nozaki, T.; Nakase, M.; Yuzawa, S.; Okazaki, K.; Gardeniers, J. G. E. Gas-to-liquids process using multi-phase flow, non-thermal plasma microreactor. *Chem. Eng. J.* **2011**, *167*, 560-566.

[15] Sekiguchi, H.; Ando, M.; Kojima, H. Study of hydroxylation of benzene and toluene using a micro-DBD plasma reactor. *J. Phys. D Appl. Phys.* **2005**, *38*, 1722-1727.

[16] Uytdenhouwen, Y.; Van Alphen, S.; Michielsen, I.; Meynen, V.; Cool, P.; Bogaerts, A. A packed-bed DBD micro plasma reactor for CO_2 dissociation: Does size matter? *Chem. Eng. J.* **2018**, *348*, 557-568.

[17] Uytdenhouwen, Y.; Bal, K. M.; Michielsen, I.; Neyts, E. C.; Meynen, V.; Cool, P.; Bogaerts, A. How process parameters and packing materials tune chemical equilibrium and kinetics in plasma-based CO_2 conversion. *Chem. Eng. J.* **2019**, *372*, 1253-1264.

[18] Pinhão, N.; Moura, A.; Branco, J. B.; Neves, J. Influence of gas expansion on process parameters in non-thermal plasma plug-flow reactors: A study applied to dry reforming of methane. *Int. J. Hydrogen Energy* **2016**, *41*, 9245-9255.

[19] Chung, W.-C.; Pan, K.-L.; Lee, H.-M.; Chang, M.-B. Dry Reforming of Methane with Dielectric Barrier Discharge and Ferroelectric Packed-Bed Reactors. *Energy & Fuels* **2014**, *28*, 7621-7631.

[20] Peeters, F. J. J.; van de Sanden, M. C. M. The influence of partial surface discharging on the electrical characterization of DBDs. *Plasma Sources Sci. Technol.* **2014**, *24*, 015016.

[21] Aerts, R.; Somers, W.; Bogaerts, A. Carbon Dioxide Splitting in a Dielectric Barrier Discharge Plasma: A Combined Experimental and Computational Study. *ChemSusChem* **2015**, *8*, 702-716.

[22] Wang, B.; Yan, W.; Ge, W.; Duan, X. Kinetic model of the methane conversion into higher hydrocarbons with a dielectric barrier discharge microplasma reactor. *Chem. Eng. J.* **2013**, *234*, 354-360.

General summary

In this thesis, we studied the plasma-based dry reforming, which converts two greenhouse gases using electricity, which can in principle be obtained from renewable sources, to value-added chemicals and fuels, in a DBD reactor. This process is important to achieve sustainable goals and has a lot of advantages, such as low operating temperature and simple reactor design, however many challenges remain. It is often combined with catalysis to improve the performance, but the catalysts used in previous studies are still mainly catalysts for traditional thermal processes, which may be not suitable for plasma-based processes. Since the interactions between catalysts and plasma are complex, the properties required for specialized catalysts for plasma catalysis are still unclear. In addition, the DBD reactor itself also needs improvement due to its relatively low energy yield.

In order to study the effect of catalyst structure on plasma-based dry reforming, we performed a controllable synthesis of the morphology and structure of the catalysts. In Chapter 2, we studied the Stöber method to synthesize uniform silica spheres that can be used as catalyst supports or templates. The Stöber method is one of the most important and fundamental processes for the synthesis of inorganic (nano)materials, but has the drawback of using a large amount of organic solvent. We used ethanol as an example to explore the effect of the organic solvent, and found that ethanol increased the particle size of the obtained silica spheres and aided the formation of uniform silica particles rather than forming a gel. Nevertheless, we also found that an organic solvent in the initial synthesis mixture was not indispensable. An initially immiscible synthesis method was proposed, which can replace the organic solvent-based Stöber method to successfully synthesize silica particles with the same size ranges as the original Stöber process without addition of organic solvents. Moreover, this process can be of further value to be extended to the synthesis process of other materials based on the Stöber process.

The silica spheres synthesized by the new process in Chapter 2 were used as template to synthesize Cu and CuO catalysts with different pore sizes in Chapter 3. The effect of pore size on plasma catalysis is crucial but still unclear. Studies have shown plasma cannot enter micropores and mesopores, so catalysts for traditional thermocatalysis may not fit plasma catalysis. The 3D porous Cu and CuO prepared by uniform silica particles (10–2000 nm) here have uniform pore sizes and the same structure, and studying them can reveal the effect of catalyst pore size on the plasma-catalytic dry reforming. In most cases, the smaller the pore size, the higher the conversion of CH_4 and CO_2. Large pores reachable by more electrons did not improve the reaction efficiency. We attribute this to the small surface area and large crystallite size, as indicated by N_2-sorption, mercury intrusion and XRD. While the smaller pores might not be reachable by electrons, due to the sheath formed in front of them, as predicted by modeling, they can still be reached by radicals formed in the plasma, and ions may even be attracted into these pores. An exception are the samples synthesized from 1 μm silica, which show better performance. We believe this is due to the electric field enhancement for pore sizes close to the Debye length. The performance of CuO and Cu with different pore sizes can provide references for future research on oxide supports and metal components of plasma catalysts.

Besides the pore size, the particle diameter of the catalyst or packing is also one of the important factors affecting the interaction between plasma and catalyst. The improvement of catalysts or packing materials on the conversion of plasma-based dry reforming in existing research is limited, and some packings even reduce the conversion compared to an empty reactor. In Chapter 4, we used SiO_2 spheres (with or without supported metal) to study the effect of different support particle sizes on plasma-based dry reforming. We found that a uniform SiO_2 packing improves the conversion of plasma-based dry reforming. The metal loading does not necessarily improve the dry reforming performance of the material, but reduces the CH_4 and CO_2 conversion in most cases due to the interactions between metal and plasma. The conversion of plasma-based dry reforming first increases and then decreases with increasing particle size, due to the balance between the promoting and hindering effect of the particle filling on the plasma discharge. The best results were obtained with 740 nm SiO_2 packing with 5 wt % Ni loading, which improved the CO_2 and CH_4 conversion from 20% and 27%, respectively, in the empty reactor, to 44% and 55%, respectively. The particle size affects not only the conversion of dry reforming, but also the selectivity of various products. The effect on the selectivities could be attenuated by the metal loading. Finding a suitable packing diameter can thus be important for improving the conversion and product selectivity in plasma catalysis.

Chapter 5 is to improve the design of the DBD reactor itself, in order to try to increase its low energy yield. We put some stainless steel rings over the inner electrode rod of the DBD reactor to change the local discharge gap and electric field, and study the dry reforming performance. Compared to the original DBD reactor without rings, in most cases with 50 W supplied power, the metal rings have a negative impact on the performance of the reactor. This may be mainly due to the non-uniform spatial distribution of the discharges caused by the rings. However, at 30 W supplied power, the placement of the rings improves the performance of the reactor and the energy yield is higher than at 50 W. More rings and with a larger cross-sectional diameter can further improve the performance of the reactor. The reactor with 20 rings with a 3.2 mm cross-sectional diameter have the best performance in this study. Compared to the reactor without rings, it increases the CO_2 conversion from 7.1% to 16.3 %, the CH_4 conversion from 11.9% to 22.5%, and the energy yield from 0.05 mmol/kJ to 0.1 mmol/kJ (0.19 mmol/kJ if it was calculated from the plasma power), respectively. The presence of the stainless steel rings increases the local electric field, the displaced charges and the discharge fraction, and also makes the discharge more stable and with more uniform intensity. It also improves the selectivity of syngas. The performance improvement of placing stainless steel rings in this study may also be applicable to other plasma-based processes, and the physical effects of metals can provide references for the study of catalyst surface metals in plasma-catalytic processes.

Algemene samenvatting

In dit proefschrift hebben we de plasma-gebaseerde droge reforming bestudeerd, waarbij twee broeikasgassen met behulp van elektriciteit, die in principe uit hernieuwbare bronnen kan gehaald worden, werden omgezet in chemicaliën en brandstoffen met toegevoegde waarde, in een DBD-reactor. Dit proces is belangrijk om duurzame doelstellingen te bereiken en heeft veel voordelen, zoals een lage bedrijfstemperatuur en een eenvoudige reactoropstelling, maar er blijven nog veel uitdagingen. Het wordt vaak gecombineerd met katalyse om de prestaties te verbeteren, maar de katalysatoren die in eerdere onderzoeken zijn gebruikt, zijn nog steeds voornamelijk katalysatoren voor traditionele thermische processen, die mogelijk niet geschikt zijn voor plasma-gebaseerde processen. Omdat de interacties tussen katalysatoren en plasma complex zijn, zijn de eigenschappen die nodig zijn voor gespecialiseerde katalysatoren voor plasmakatalyse nog steeds onduidelijk. Daarnaast is ook de DBD-reactor zelf aan verbetering toe vanwege de relatief lage energie-efficiëntie.

Om het effect van de katalysatorstructuur op plasma-gebaseerde droge reforming te bestuderen, hebben we een controleerbare synthese van de morfologie en structuur van de katalysatoren uitgevoerd. In Hoofdstuk 2 hebben we de Stöber-methode bestudeerd om uniforme silicabolletjes te synthetiseren die kunnen worden gebruikt als katalysatordragers of sjablonen. De Stöber-methode is een van de belangrijkste en meest fundamentele processen voor de synthese van anorganische (nano)materialen, maar heeft als nadeel dat er veel organisch oplosmiddel wordt gebruikt. We gebruikten ethanol als voorbeeld om het effect van het organische oplosmiddel te onderzoeken en ontdekten dat ethanol de deeltjesgrootte van de verkregen silicabolletjes verhoogde en de vorming van uniforme silicadeeltjes promootte in plaats van een gel te vormen. Desalniettemin vonden we ook dat een organisch oplosmiddel in het initiële synthesemengsel niet onmisbaar was. Een aanvankelijk niet-mengbare synthesemethode werd voorgesteld, die de op organische oplosmiddelen gebaseerde Stöber-methode kan vervangen om met succes silicadeeltjes te synthetiseren met dezelfde groottebereiken als het oorspronkelijke Stöber-proces zonder toevoeging van organische oplosmiddelen. Bovendien kan dit proces van verdere waarde zijn om uit te breiden tot syntheseprocessen van andere materialen op basis van het Stöber-proces.

De silicabolletjes die met het nieuwe proces in Hoofdstuk 2 zijn gesynthetiseerd, werden in Hoofdstuk 3 als sjabloon gebruikt om Cu- en CuO-katalysatoren met verschillende poriegroottes te synthetiseren. Het effect van poriegrootte op plasmakatalyse is cruciaal, maar nog onduidelijk. Studies hebben aangetoond dat plasma geen microporiën en mesoporiën kan binnendringen, dus katalysatoren voor traditionele thermokatalyse passen mogelijk niet in plasmakatalyse. De 3D poreuze Cu en CuO bereid door uniforme silicadeeltjes (10-2000 nm) hebben hier uniforme poriegroottes en dezelfde structuur, en de studie ervan kan het effect van de poriegrootte van de katalysator op de plasma-katalytische droge reforming onthullen. In de meeste gevallen geldt: hoe kleiner de poriegrootte, hoe hoger de omzetting van CH_4 en CO_2. Grote poriën die door meer elektronen kunnen worden bereikt, verbeterden de reactie-efficiëntie niet. We schrijven dit toe aan het kleine oppervlak en de grote kristallietgrootte, zoals aangegeven door N_2-sorptie, kwikintrusie en XRD. Hoewel de kleinere poriën misschien niet bereikbaar zijn voor elektronen, vanwege de grenslaag die ervoor wordt gevormd, zoals voorspeld door modellering, kunnen ze nog steeds worden bereikt door radicalen die in het plasma worden gevormd, en ionen kunnen zelfs mogelijk in deze poriën worden aangetrokken door het elektrisch veld. Een uitzondering zijn de monsters die zijn gesynthetiseerd uit 1 µm silica, die betere prestaties vertonen. We denken dat dit te wijten is aan de verhoging van het elektrische veld voor poriegroottes die dicht bij de Debye-lengte liggen. De prestaties van CuO en Cu met verschillende poriegroottes kunnen referenties vormen voor toekomstig onderzoek naar oxidedragers en metaalcomponenten van plasmakatalysatoren.

Naast de poriegrootte is ook de deeltjesdiameter van de katalysator of pakking een van de belangrijke factoren die de interactie tussen plasma en katalysator beïnvloeden. De verbetering van katalysatoren of pakkingmaterialen op de conversie van plasma-gebaseerde droge reforming in bestaand onderzoek is beperkt, en sommige pakkingen verminderen zelfs de conversie in vergelijking met een lege reactor. In Hoofdstuk 4 hebben we SiO_2-bolletjes (met of zonder afgezet metaal) gebruikt om het effect van verschillende deeltjesgroottes op plasma-gebaseerde droge reforming te bestuderen. We ontdekten dat een uniforme SiO_2-pakking de conversie van plasma-gebaseerde droge reforming verbetert. De metaalbelading verbetert niet noodzakelijk de droge reforming-prestaties van het materiaal, maar vermindert in de meeste gevallen de CH_4- en CO_2-conversie vanwege de interacties tussen metaal en plasma. De omzetting van plasma-gebaseerde droge reforming neemt eerst toe en vervolgens af met toenemende deeltjesgrootte, vanwege de balans tussen het bevorderende en belemmerende effect van de deeltjesvulling op de plasmaontlading. De beste resultaten werden verkregen met 740 nm SiO_2-pakking met 5 gew.% Ni-belading, waardoor de CO_2- en CH_4-conversie verbeterde van respectievelijk 20% en 27% in de lege reactor naar respectievelijk 44% en 55%. De deeltjesgrootte beïnvloedt niet alleen de omzetting van droge reforming, maar ook de selectiviteit van verschillende producten. Het effect op de selectiviteiten zou kunnen worden afgezwakt door de metaalbelading. Het vinden van een geschikte pakkingsdiameter kan dus belangrijk zijn voor het verbeteren van de conversie en productselectiviteit bij plasmakatalyse.

Hoofdstuk 5 is om het ontwerp van de DBD-reactor zelf te verbeteren, om te proberen de lage energie-efficiëntie te verhogen. We hebben enkele roestvrijstalen ringen over de binnenste elektrodestaaf van de DBD-reactor geplaatst om de lokale ontladingsopening en het elektrische veld te veranderen, en de droge reformingprestaties te bestuderen. In vergelijking met de originele DBD-reactor zonder ringen, in de meeste gevallen met 50 W geleverd vermogen, hebben de metalen ringen een negatieve invloed op de prestaties van de reactor. Dit kan voornamelijk te wijten zijn aan de niet-uniforme ruimtelijke verdeling van de ontladingen veroorzaakt door de ringen. Bij 30 W geleverd vermogen verbetert de plaatsing van de ringen echter de prestaties van de reactor en is de energie-efficiëntie hoger dan bij 50 W. Meer ringen en een grotere diameter van de dwarsdoorsnede kunnen de prestatie van de reactor verder verbeteren. De reactor met 20 ringen met een doorsnede van 3,2 mm presteert het beste in deze studie. In vergelijking met de reactor zonder ringen verhoogt hij respectievelijk de CO_2-conversie van 7,1% naar 16,3%, de CH_4-conversie van 11,9% naar 22,5% en het energie-rendement van 0,05 mmol/kJ naar 0,1 mmol/kJ (0,19 mmol/kJ als het werd berekend op basis van het plasmavermogen). De aanwezigheid van de roestvrijstalen ringen verhoogt het lokale elektrische veld, de verplaatste lading en de ontladingsfractie, en maakt ook de ontlading stabieler en met meer uniforme intensiteit. Het verbetert ook de selectiviteit van syngas. De prestatieverbetering van het plaatsen van roestvrijstalen ringen in deze studie kan ook van toepassing zijn op andere plasma-gebaseerde processen, en de fysieke effecten van metalen kunnen referenties opleveren voor de studie van katalysatoroppervlaktemetalen in plasma-katalytische processen.

Future outlook

Undoubtedly, if the dry reforming process in a DBD reactor can be applied industrially, it may play a key role in sustainable energy and chemical production, i.e. providing another green and low energy consumption technology in this field. However, before we reach that state, the performance of dry reforming in DBD must be significantly improved, in terms of conversion and especially in energy yield and selective production. Furthermore, because a systematic theory which can guide the research has not been fully established yet, this process is currently only in the laboratory research and there is still some distance away from being economically viable for industrialization. Therefore, more in-depth and thorough studies are needed to promote the development of this area. Herein, improving the design of the reactor and combining it with catalysts/packing materials, both investigated in this PhD thesis, are two major research directions to promote the performance of this process, and thus will help and complement the relevant progress in this field.

From the perspective of catalysts and packing materials, we can see that the pore size of the catalyst has a significant effect on the conversion, which is different for materials with different properties. Macropores with specific pore size (at least several hundreds of nanometers) and micropores seem to be suitable pore sizes for dielectric supports and metal active components, respectively. Based on this finding, a lot of research should be carried out to select and design suitable materials. Therefore, future research in catalyst preparation needs to consider the effect of pore size to customize catalysts when different materials are applied. In addition, uniform and suitable particle sizes and packing densities of the packing/catalyst might improve the performance of plasma-based dry reforming further. Too large or too small particle sizes have negative impact on the plasma discharge. Hence, it is important to also take the effect of particle size into account and customize the catalysts for the reaction. The results in this PhD work will hopefully provide important references for future research on catalysts for plasma-based processes. How to achieve a synergistic effect of pore size and particle size will be crucial. Furthermore, since the interaction between plasma and catalyst is complex and has many influencing factors, as revealed by the existing research (both in literature and in this PhD work), further investigation of other physical and chemical properties of catalysts is highly needed, and the effects of both the discharge and the catalyst must be studied in more detail, through simulations and experiments, to find optimal catalysts and process parameters, to really make progress in this field.

From a reactor perspective, changes to the reactor design can also tailor the discharge, and further alter the dry reforming performance (such as in Chapter 5). Research on DBD reactors, although already at higher TRL for air cleaning applications, is still in its infancy for gas conversion applications, such as dry reforming. The design of the reactor will change the reaction parameters, e.g. the discharge uniformity in the reactor, which is closely related to the performance of the conversion process. Therefore, it will be interesting to investigate various reactor designs, and the relevant process parameters should be explored to more fully explore the role of the reactor. Based on this PhD work, we believe that the preparation of catalyst, reactor design and probably the combination of these two will be able to provide solutions in the future research directions. When more and more fundamentals and interacting aspects are being understood to assess how to make the mentioned parameters work together, the dry reforming performance and by extension also other plasma mediated CO_2 conversion processes will enhance.

Appendix A Supporting information for chapter 2

Amounts of reactants and characterization of obtained samples

Table A.1. The volumes and amounts of reactants of all the solvent-free syntheses in this work and the corresponding diameters of the obtained synthesized silica particles.

Entry number	Particle diameters	Volume of H_2O	Volume of ammonia solution (25%)	Molar amount of H_2O	Molar amount of ammonia	Volume of TEOS	Molar amount of TEOS
1	1312 nm	0 mL	55.78 mL	2.10 mol	0.74 mol	50 mL	0.23 mol
2	1325 nm	7.5 mL	55.78 mL	2.51 mol	0.74 mol	50 mL	0.23 mol
3	1407 nm	15 mL	55.78 mL	2.93 mol	0.74 mol	50 mL	0.23 mol
4	511 nm	30 mL	55.78 mL	3.76 mol	0.74 mol	50 mL	0.23 mol
5	1283 nm	0 mL	77.89 mL	2.93 mol	1.03 mol	50 mL	0.23 mol
6	1105 nm	7.5 mL	77.89 mL	3.34 mol	1.03 mol	50 mL	0.23 mol
7	1020 nm	15 mL	77.89 mL	3.76 mol	1.03 mol	50 mL	0.23 mol
8	792 nm	22.5 mL	77.89 mL	4.17 mol	1.03 mol	50 mL	0.23 mol
9	463 nm	30 mL	77.89 mL	4.59 mol	1.03 mol	50 mL	0.23 mol
10	774 nm	0 mL	100.00 mL	3.76 mol	1.33 mol	50 mL	0.23 mol
11	708 nm	15 mL	100.00 mL	4.59 mol	1.33 mol	50 mL	0.23 mol
12	376 nm	30 mL	100.00 mL	5.42 mol	1.33 mol	50 mL	0.23 mol
13	263 nm	45 mL	100.00 mL	6.25 mol	1.33 mol	50 mL	0.23 mol
14	783 nm	0 mL	122.11 mL	4.59 mol	1.62 mol	50 mL	0.23 mol
15	652 nm	15 mL	122.11 mL	5.42 mol	1.62 mol	50 mL	0.23 mol
16	434 nm	30 mL	122.11 mL	6.25 mol	1.62 mol	50 mL	0.23 mol
17	427 nm	45 mL	122.11 mL	7.08 mol	1.62 mol	50 mL	0.23 mol
18	232 nm	60 mL	122.11 mL	7.91 mol	1.62 mol	50 mL	0.23 mol
19	709 nm	0 mL	144.22 mL	5.42 mol	1.91 mol	50 mL	0.23 mol
20	653 nm	15 mL	144.22 mL	6.25 mol	1.91 mol	50 mL	0.23 mol
21	523 nm	30 mL	144.22 mL	7.08 mol	1.91 mol	50 mL	0.23 mol
22	386 nm	45 mL	144.22 mL	7.91 mol	1.91 mol	50 mL	0.23 mol
23	102 nm	60 mL	144.22 mL	8.75 mol	1.91 mol	50 mL	0.23 mol
24	361 nm	0 mL	100.00 mL	3.76 mol	1.33 mol	10 mL	0.045 mol
25	205 nm	15 mL	100.00 mL	4.59 mol	1.33 mol	10 mL	0.045 mol
26	47 nm	30 mL	100.00 mL	5.42 mol	1.33 mol	10 mL	0.045 mol
27	11 nm	45 mL	100.00 mL	6.25 mol	1.33 mol	10 mL	0.045 mol

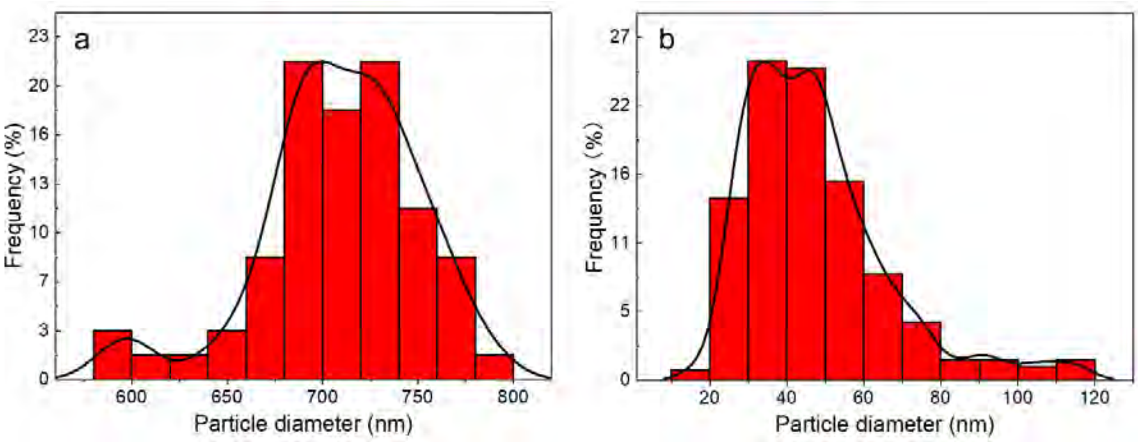

Figure A.1 Particle size distribution of silica synthesized by the solvent-free method, which is obtained by measuring and calculating the electron microscope images. (a) Size distribution of silica particles with an average diameter of ~710 nm. The amounts of reactants are 50 mL of TEOS (0.23 mol), 1.91 mol of NH_3 and 5.42 mol of H_2O. (b) Size distribution of silica particles with an average diameter of ~50 nm. The amounts of reactants are 10 mL of TEOS (0.045 mol), 1.33 mol of NH_3 and 6.25 mol of H_2O.

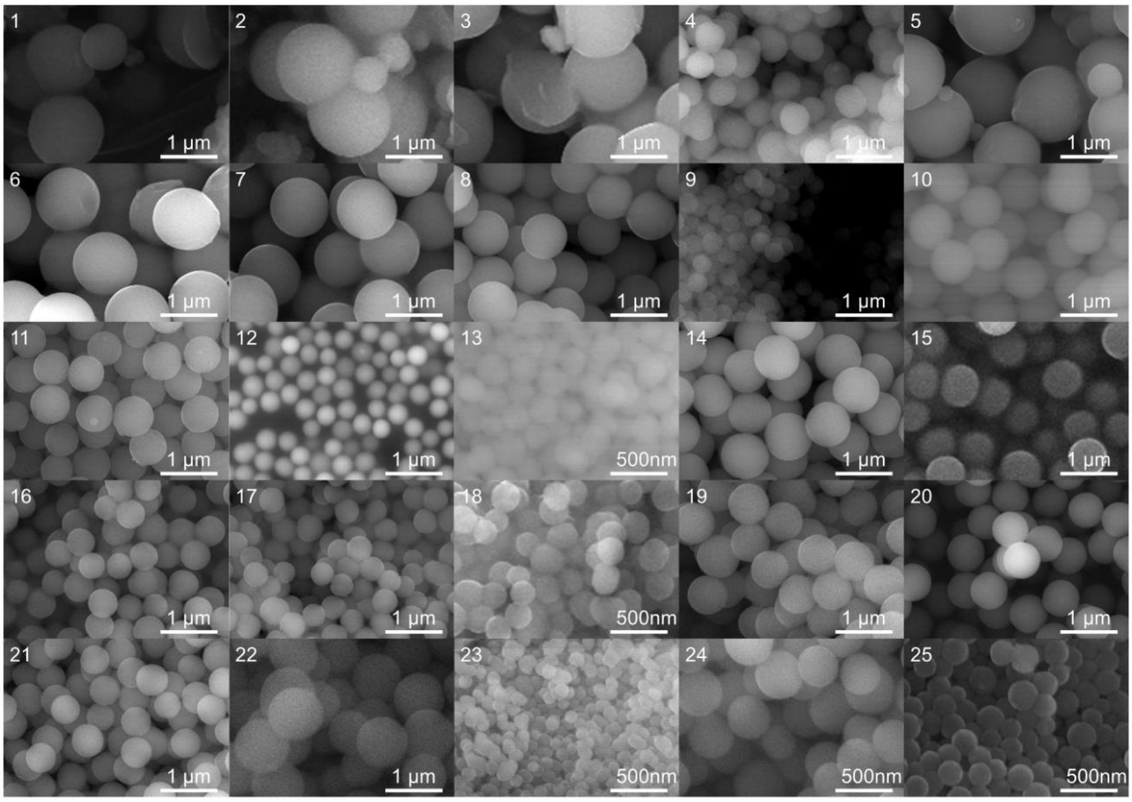

Figure A.2 SEM images of silica with different sizes prepared by the organic solvent-free method. The entry numbers of Table A.1 and Figure A.1 correspond to each other. (1) Silica particles with a diameter of ~1.3 µm. (2) Silica particles with a diameter of ~1.3 µm. (3) Silica particles with a diameter of ~1.4 µm. (4) Uniform silica spheres of ~510 nm. (5) Silica particles with a diameter of ~1.3 µm. (6) Uniform silica spheres of ~1.1 µm. (7) Uniform silica spheres of ~1 µm. (8) Uniform silica spheres of ~800 nm. (9) Uniform silica spheres of ~460 nm. (10) Uniform silica spheres of ~770 nm. (11) Uniform silica spheres of ~710 nm. (12) Uniform silica spheres of ~380 nm. (13) Uniform silica spheres of ~260 nm. (14) Uniform silica spheres of ~780 nm. (15) Uniform silica spheres of ~650 nm. (16) Uniform silica spheres of ~430 nm. (17) Uniform silica spheres of ~430 nm. (18) Uniform silica spheres of ~230 nm. (19) Uniform silica spheres of ~710 nm. (20) Uniform silica spheres of ~650 nm. (21) Uniform silica spheres of ~520 nm. (22) Uniform silica spheres of ~390 nm. (23) Uniform silica spheres of ~100 nm. (24) Uniform silica spheres of ~360 nm. (25) Uniform silica spheres of ~210 nm.

$$\mathrm{Si(OEt)_4 + nH_2O \rightleftharpoons Si(OEt)_{4\text{-}n}(OH)_n + n(EtOH)} \qquad \text{(Eq. 1)}$$

$$\mathrm{Si(OEt)_{4\text{-}n}(OH)_n + Si(OEt)_{4\text{-}m}(OH)_m \rightarrow (OH)_{n\text{-}1}(OEt)_{4\text{-}n}SiOSi(OEt)_{4\text{-}m}(OH)_{m\text{-}1} + H_2O} \qquad \text{(Eq. 2)}$$

$$\mathrm{Si(OEt)_{4\text{-}n}(OH)_n + Si(OEt)_{4\text{-}m}(OH)_m \longrightarrow (OH)_n(OEt)_{3\text{-}n}SiOSi(OEt)_{4\text{-}m}(OH)_{m\text{-}1} + EtOH} \qquad \text{(Eq. 3)}$$

Figure A.3 Equations of the Stöber method to synthesize silica. (Eq. 1) The hydrolysis of TEOS with $n \leq 4$. Silanol monomers and ethanol (EtOH) are the products. (Eq. 2) The dehydration condensation of two silanol groups to generate siloxane bonds. (Eq. 3) The dealcoholization condensation between silanol and ethoxy groups to generate siloxane bonds.

Table A.2. The volumes and amounts of chemicals of all the typical Stöber syntheses with ethanol in this work and the corresponding diameters of the obtained synthesized silica particles.

Entry number	Particle diameters	Volume of H_2O	Volume of ammonia solution (25%)	Molar amount of H_2O	Molar amount of ammonia	Volume of TEOS	Molar amount of TEOS	Volume of EtOH	Molar amount EtOH
28	705 nm	0 mL	100.00 mL	3.76 mol	1.33 mol	50 mL	0.23 mol	649.73 mL	11.14 mol
29	732 nm	15 mL	100.00 mL	4.59 mol	1.33 mol	50 mL	0.23 mol	634.73 mL	10.88 mol
30	722 nm	30 mL	100.00 mL	5.42 mol	1.33 mol	50 mL	0.23 mol	619.73 mL	10.63 mol
31	786 nm	45 mL	100.00 mL	6.25 mol	1.33 mol	50 mL	0.23 mol	604.73 mL	10.37 mol
32	663 nm	60 mL	100.00 mL	7.08 mol	1.33 mol	50 mL	0.23 mol	589.73 mL	10.11 mol
33	521 nm	90 mL	100.00 mL	8.75 mol	1.33 mol	50 mL	0.23 mol	559.73 mL	9.60 mol
34	763 nm	0 mL	100.00 mL	3.76 mol	1.33 mol	50 mL	0.23 mol	64.97 mL	1.11 mol
35	802 nm	15 mL	100.00 mL	4.59 mol	1.33 mol	50 mL	0.23 mol	63.47 mL	1.09 mol
36	677 nm	30 mL	100.00 mL	5.42 mol	1.33 mol	50 mL	0.23 mol	61.97 mL	1.06 mol
37	665 nm	45 mL	100.00 mL	6.25 mol	1.33 mol	50 mL	0.23 mol	60.47 mL	1.04 mol
38	652 nm	60 mL	100.00 mL	7.08 mol	1.33 mol	50 mL	0.23 mol	58.97 mL	1.01 mol
39	483 nm	90 mL	100.00 mL	8.75 mol	1.33 mol	50 mL	0.23 mol	55.97 mL	0.96 mol
40	504 nm	60 mL	55.78 mL	5.42 mol	0.74 mol	50 mL	0.23 mol	633.95 mL	10.87 mol
41	595 nm	45 mL	77.89 mL	5.42 mol	1.03 mol	50 mL	0.23 mol	626.84 mL	10.75 mol
42	791 nm	15 mL	122.11 mL	5.42 mol	1.62 mol	50 mL	0.23 mol	612.62 mL	10.51 mol
43	796 nm	0 mL	144.22 mL	5.42 mol	1.91 mol	50 mL	0.23 mol	605.51 mL	10.38 mol

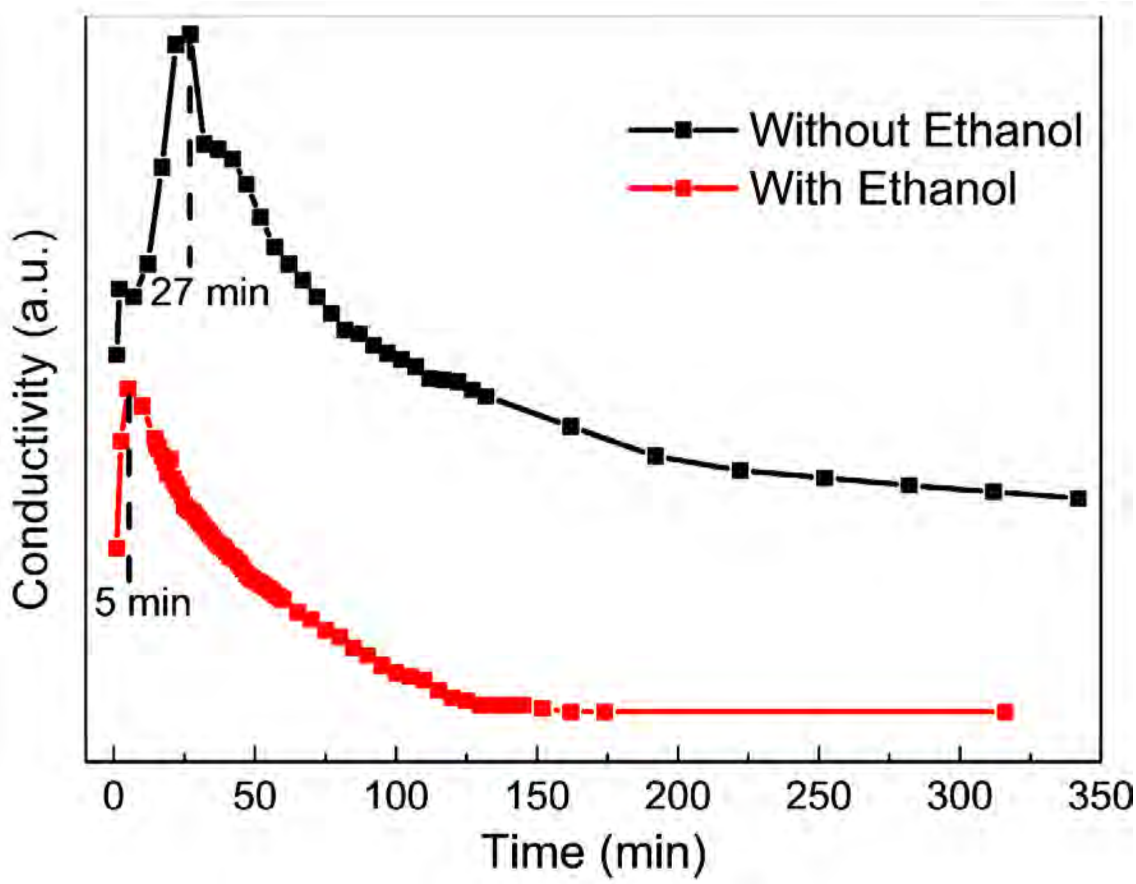

Figure A.4 Conductivity variation during the silica synthesis processes with ethanol and without ethanol. The amounts of reactants in both process are 50 mL of TEOS, 1.03 mol of NH_3 and 4.59 mol of H_2O. The amount of ethanol in the process with ethanol is to dilute the TEOS to 0.28 mol/L.

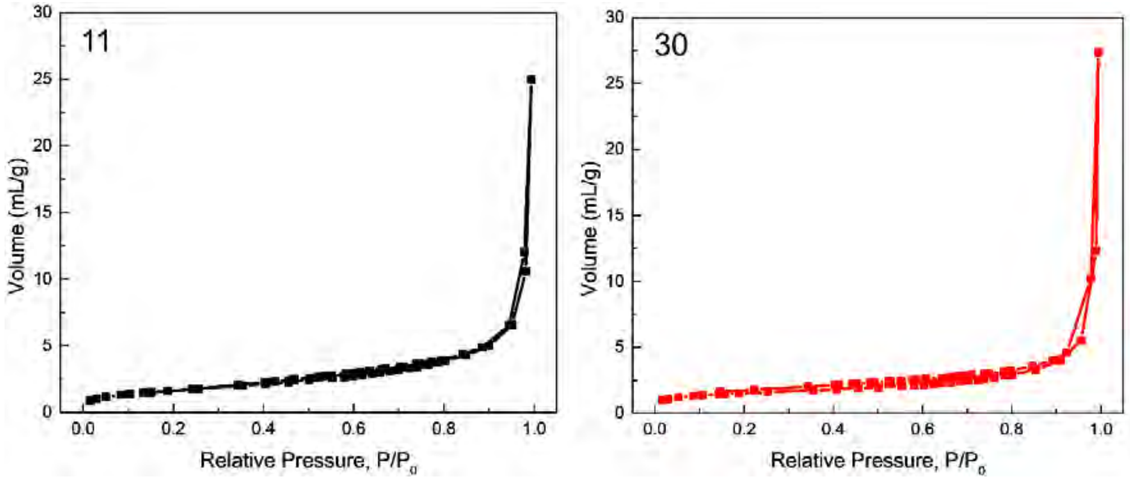

Figure A.5 N_2-sorption isotherms of silica spheres. (11) N_2-sorption isotherms of silica with an average diameter of ~710 nm, synthesized by the organic solvent-free process. (30) N_2-sorption isotherms of silica with an average diameter of ~720 nm, synthesized by the typical Stöber process.

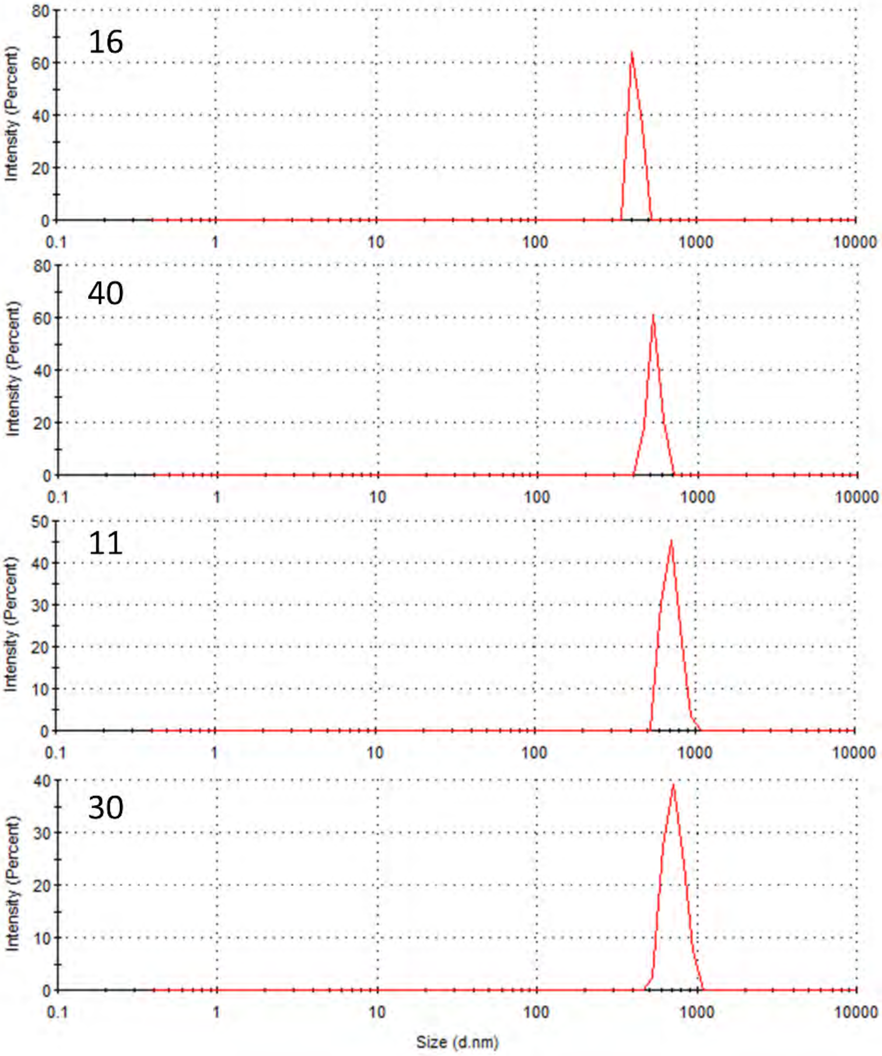

Figure A.6 Particle size distribution of silica spheres measured by DLS. (16) Particle size distribution of silica with an average diameter of ~430 nm as measured by SEM, synthesized by the organic solvent-free process. (40) Particle size distribution of silica with an average diameter of ~500 nm as measured by SEM, synthesized by the typical Stöber process. (11) Particle size distribution of silica with an average diameter of ~710 nm as measured by SEM, synthesized by the organic solvent-free process. (30) Particle size distribution of silica with an average diameter of ~720 nm as measured by SEM, synthesized by the typical Stöber process.

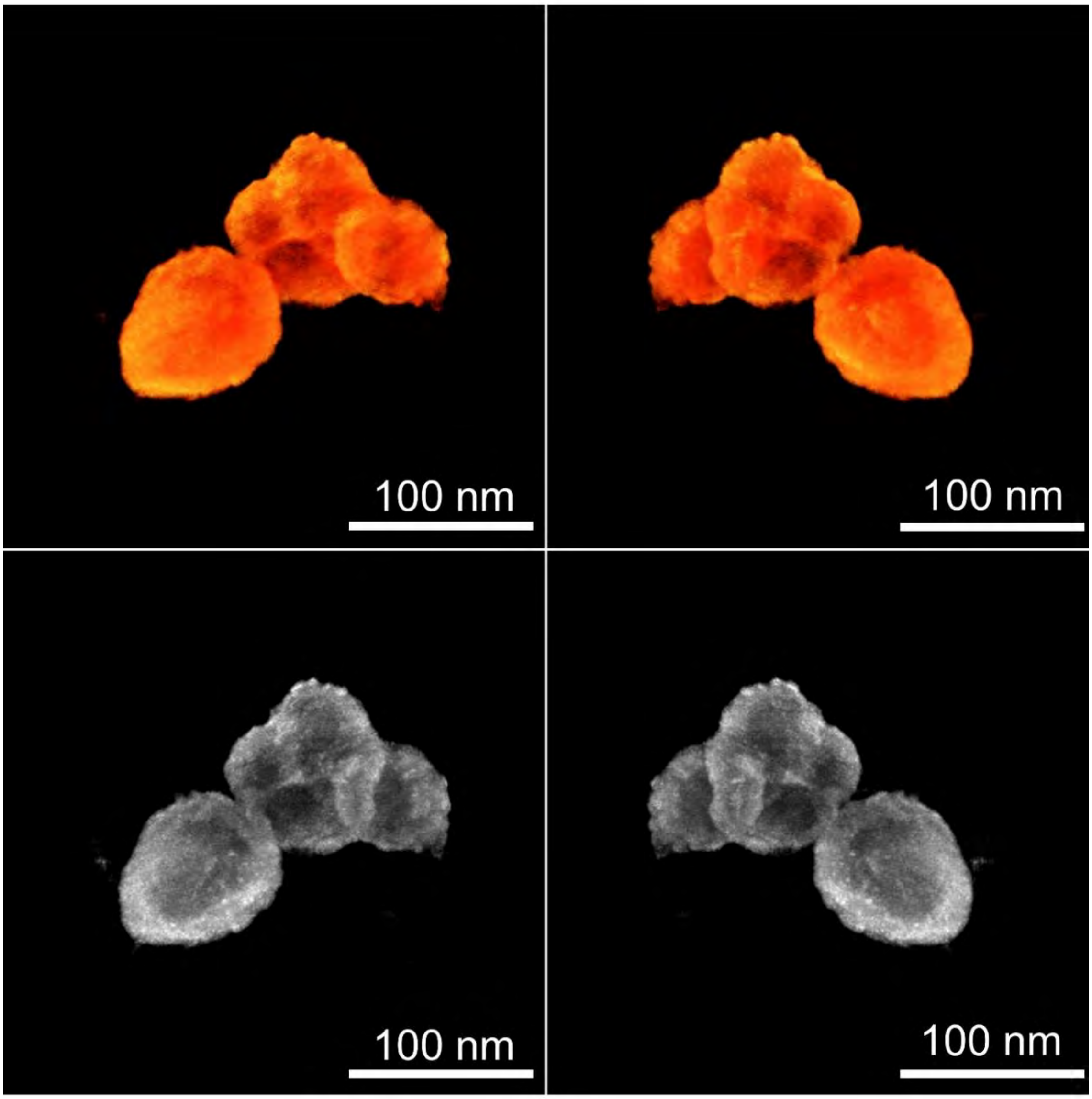

Figure A.7 3D visualization of electron tomography reconstructions of the particles with a diameter of about 50 nm. The amounts of reactants in the synthesis are 10 mL of TEOS, 1.33 mol of NH_3 and 5.42 mol of H_2O.

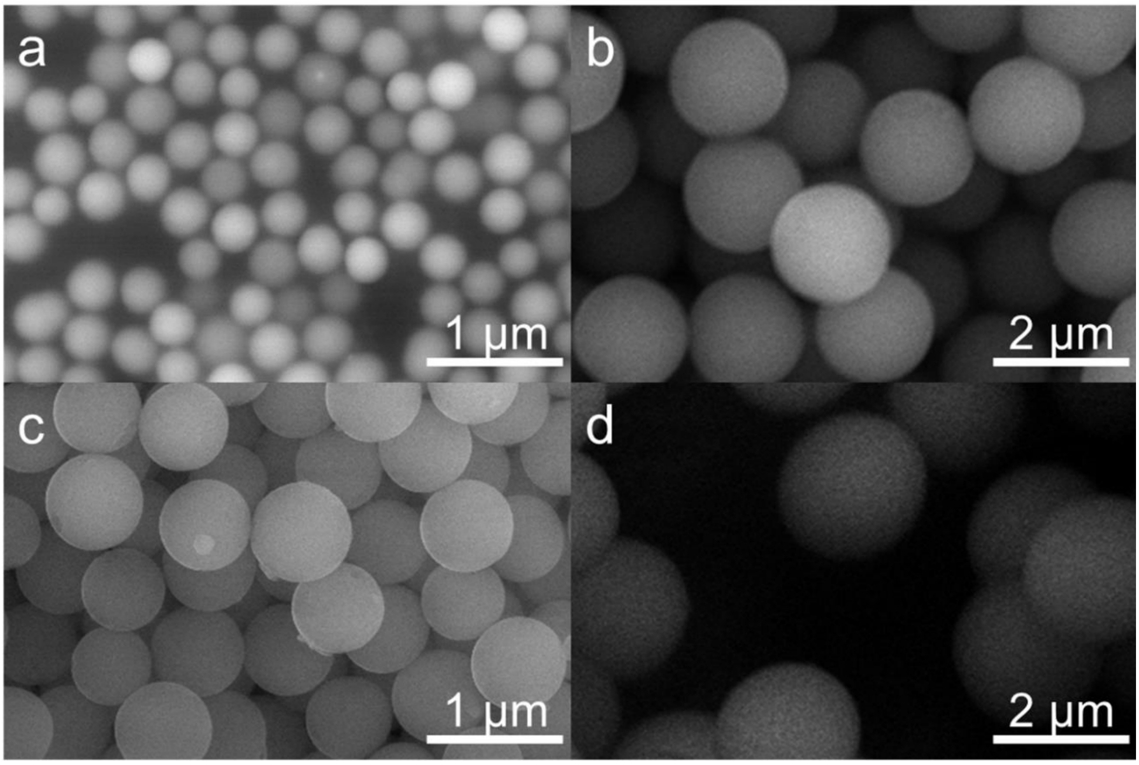

Figure A.8 SEM images comparison of silica spheres prepared by solvent-free method with $Cu(NO_3)_2$ and without $Cu(NO_3)_2$. (a) Silica particles with a diameter of about 380 nm, synthesized with 1.33 mol of ammonia, 5.42 mol of water and 50 mL of TEOS. (b) Silica particles with a diameter of about 1.8 µm, synthesized from the same amounts of reactants as Figure A.4a but with 0.1 g of $Cu(NO_3)_2 \cdot 3H_2O$ addition. (c) Silica particles with a diameter of about 710 nm, synthesized with 1.33 mol of ammonia, 4.59 mol of water and 50 mL of TEOS. (d) Silica particles with a diameter of about 2 µm, synthesized from the same amounts of reactants as Figure A.4c but with 0.1 g of $Cu(NO_3)_2 \cdot 3H_2O$ addition.

Appendix B Supporting information for chapter 3

Characterization and selectivity of the catalysts

Table B.1. Composition details of the CuO catalysts.

Samples	Al (wt%)	Si (wt%)	Ca (wt%)	Cu (wt%)
CuO-10		0.41	0.24	99.35
CuO-50	0.42	0.34	0.21	99.03
CuO-100	0.35	0.26	/	99.39
CuO-600	0.34	0.43	/	99.22
CuO-1000	/	0.31	/	99.69
CuO-2000	0.23	0.29	0.74	98.75

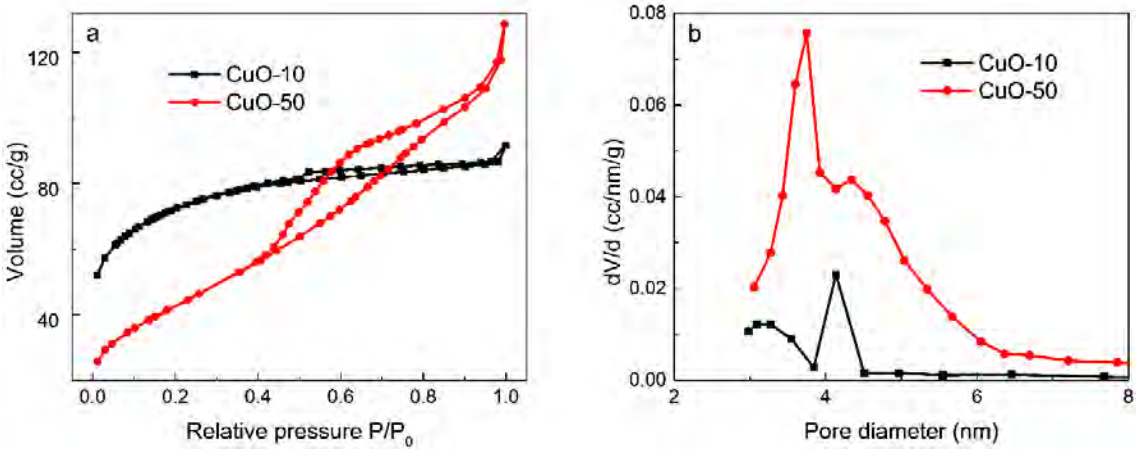

Figure B.1. (a) Isotherms of CuO-10 and CuO-50. (b) Pore size distribution of 3D porous CuO samples obtained by N_2-sorption (BJH desorption branch). It should be noted that the sharp pore size distribution peak around 4 nm of the CuO-10 sample in Figure B.1 (b) is a phantom peak.

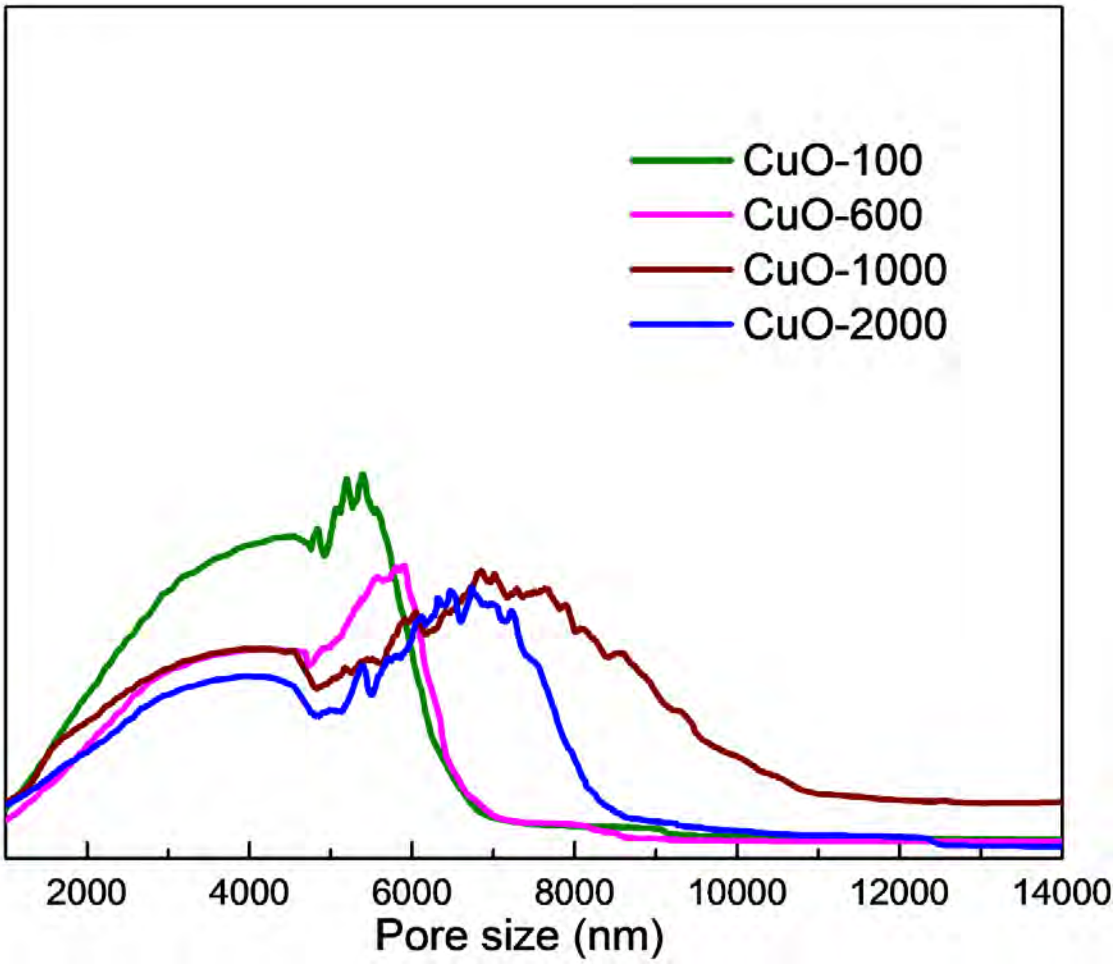

Figure B.2. Pore size distribution of 3D porous CuO-100, CuO-600, CuO-1000 and CuO-2000 obtained by mercury intrusion at the micrometer scale.

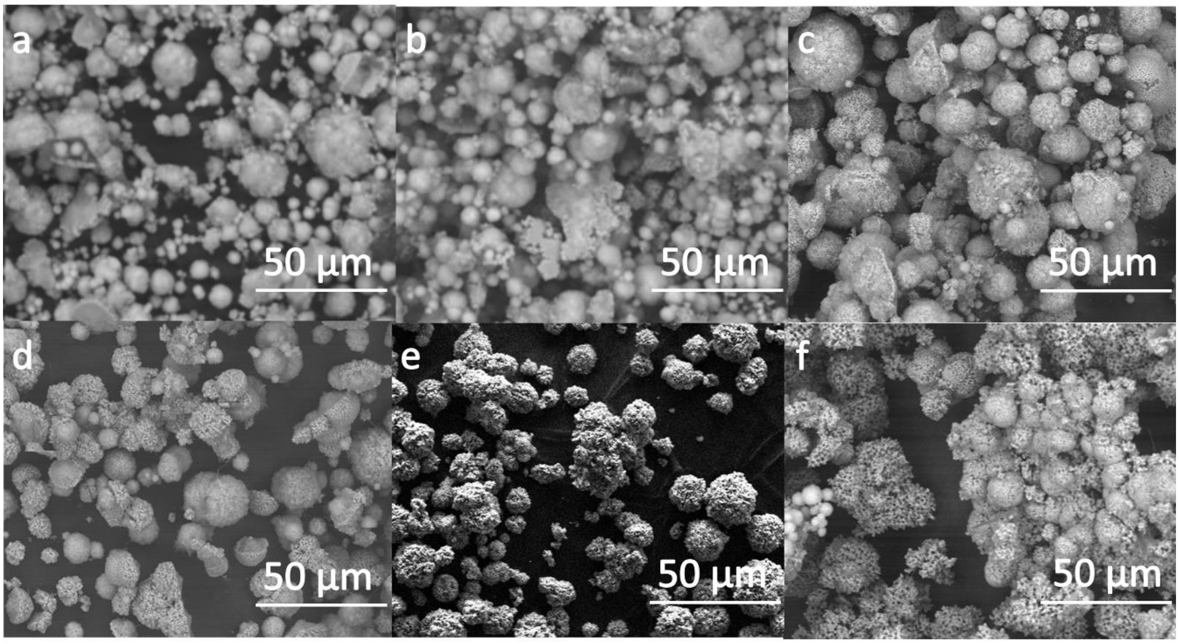

Figure B.3. SEM of 3D porous particles (a) CuO-10, (b) CuO-50, (c) CuO-100, (d) CuO-600, (e) CuO-1000, (f) CuO-2000.

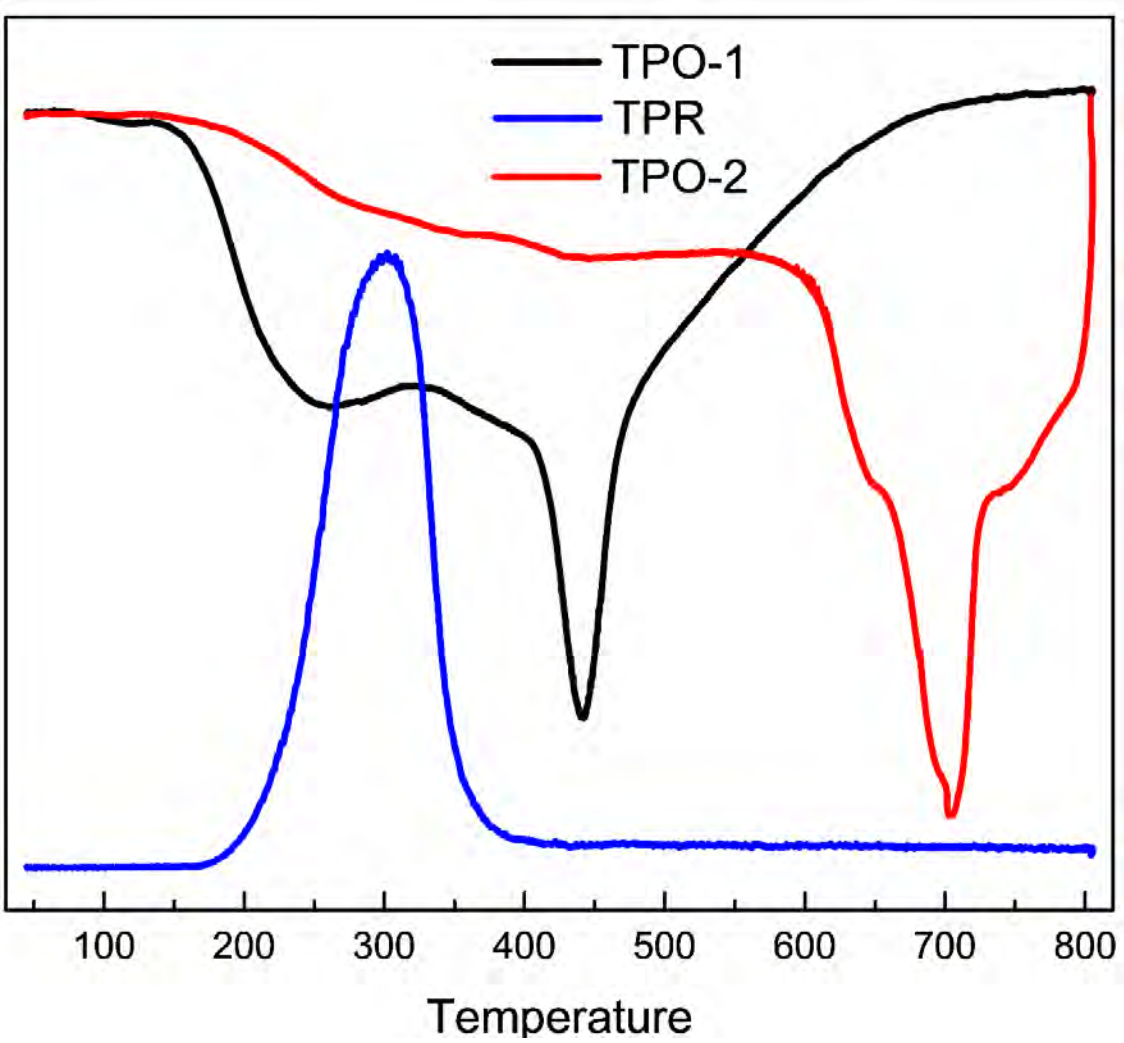

Figure B.4. Results of TPO-TPR-TPO of 3D porous samples after reduction in tube furnace at 450 °C.

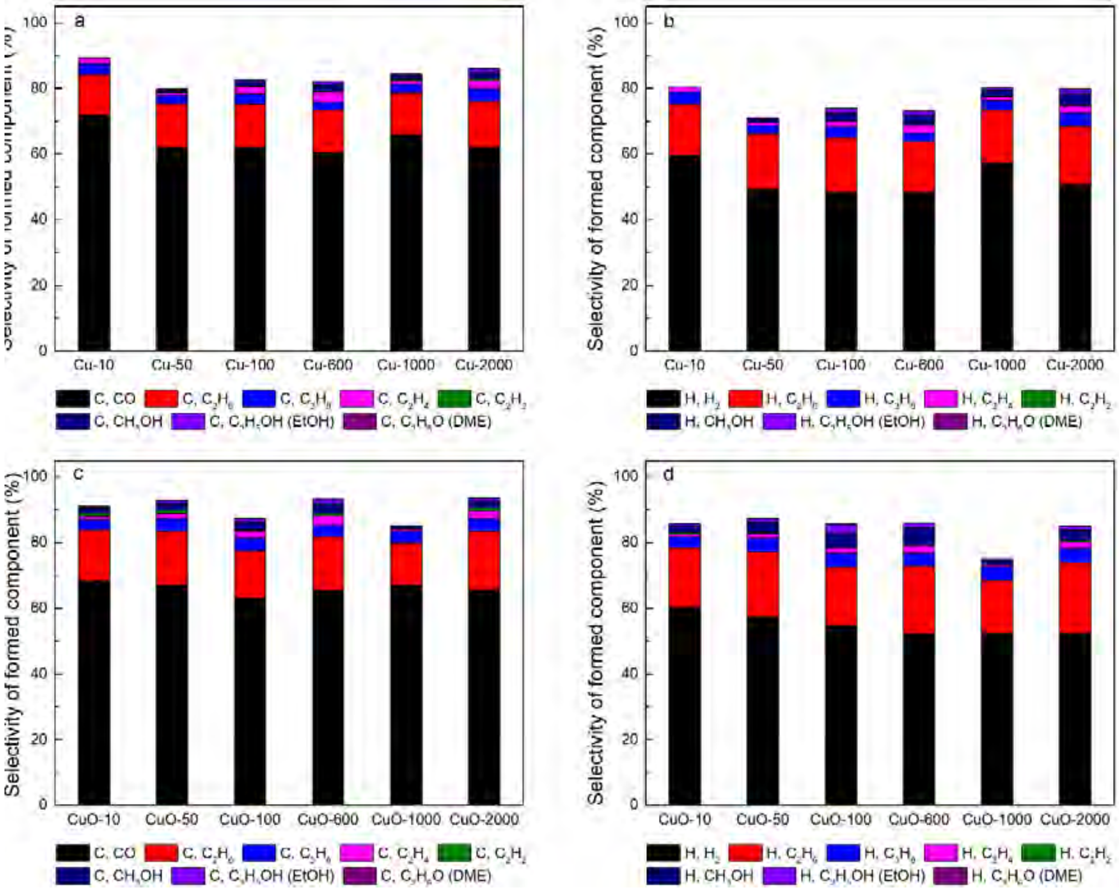

Figure B.5. Product carbon-based selectivities and carbon mass balance in plasma-catalytic dry reforming with different pore sizes of 3D porous Cu (a) and CuO (c) samples, and hydrogen-based selectivities and hydrogen mass balance in plasma-catalytic dry reforming with different pore sizes of 3D porous Cu (b) and CuO (d) samples.

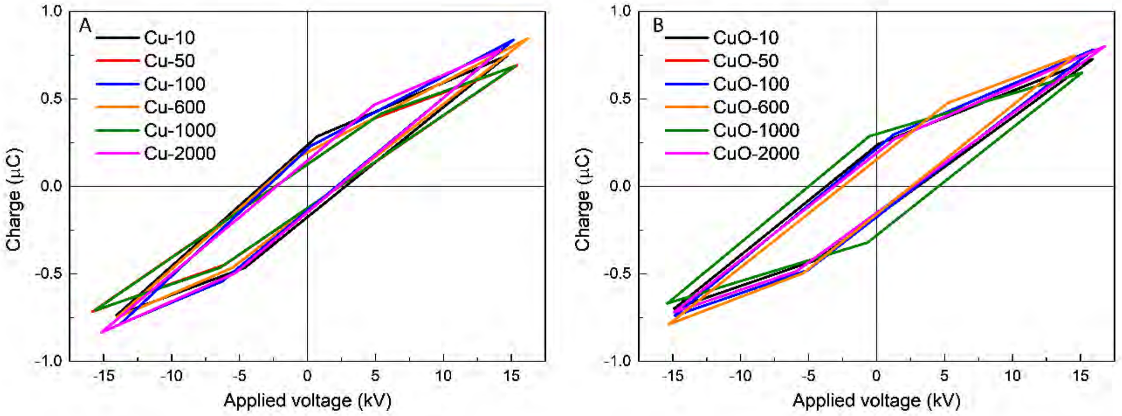

Figure B.6. The fitted Lissajous figures (calculated by a MATLAB script) of plasma-based dry reforming at 50 W supplied power, in a DBD reactor with 3D porous (a) Cu and (b) CuO.

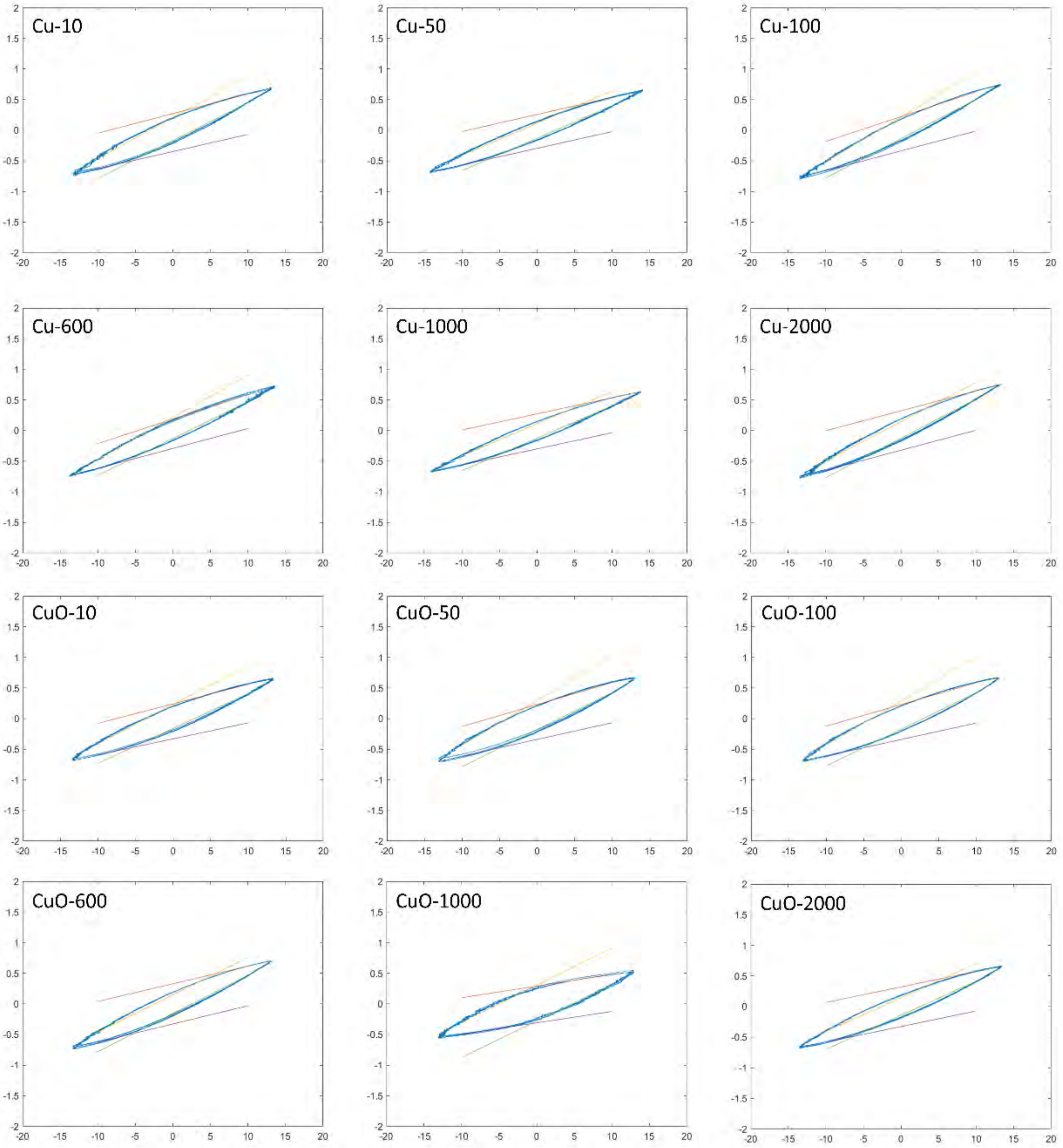

Figure B.7. Examples of raw data of Lissajous figures of plasma-based dry reforming at 50 W supplied power, in a DBD reactor with 3D porous Cu and CuO.

Appendix C Supporting information for chapter 4

Electrical characterization and selectivity of the catalysts

Table C.1. Conversion and energy yield of the dry reforming experiments with SiO_2 with different particle diameters.

	CO_2 conversion (%)	CH_4 conversion (%)	EY calculated from plasma power (mmol/kJ)	EY calculated from supplied power (mmol/kJ)
Empty reactor	19.65	26.90	0.116	0.063
Si-120	31.12	42.27	0.227	0.100
Si-460	35.38	49.27	0.213	0.115
Si-740	41.68	53.89	0.252	0.130
Si-810	40.53	52.14	0.232	0.125
Si-1130	33.25	42.08	0.176	0.103
Si-1800	24.05	32.98	0.125	0.077
Si-2390	20.25	27.99	0.106	0.066
Ni_5/Si-120	29.93	41.50	0.199	0.096
Ni_5/Si-460	40.75	53.10	0.239	0.127
Ni_5/Si-740	43.76	55.29	0.271	0.135
Ni_5/Si-810	36.58	47.51	0.215	0.114
Ni_5/Si-1130	25.09	35.70	0.150	0.083
Ni_5/Si-1800	25.48	34.23	0.135	0.081
Ni_5/Si-2390	18.10	24.93	0.097	0.059

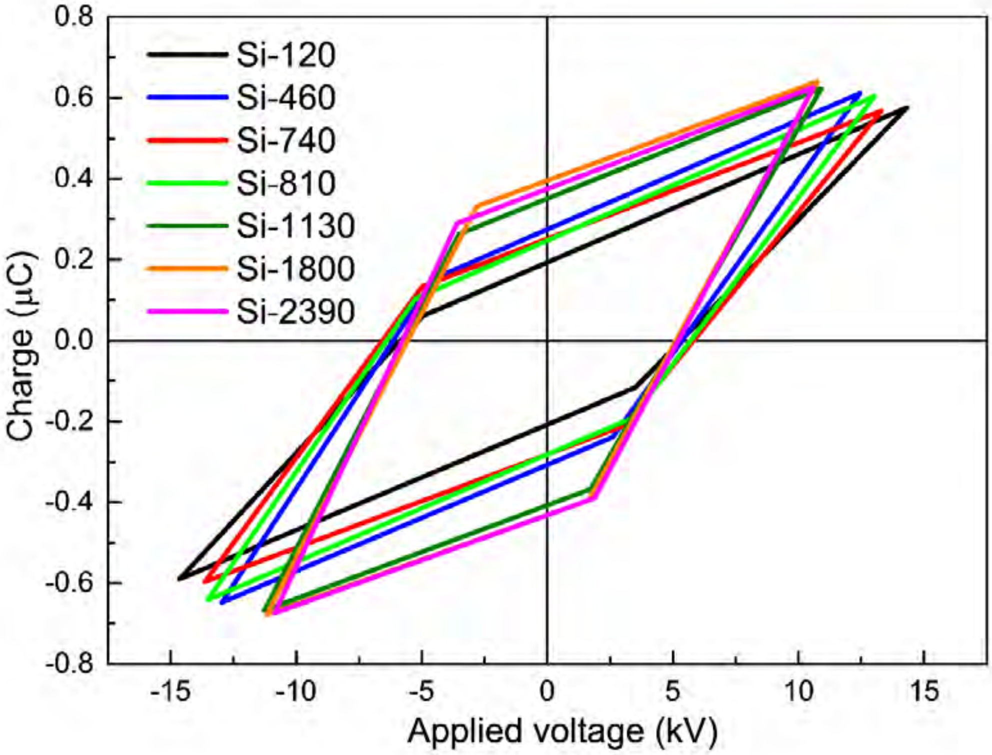

Figure C.1. The slopes of Lissajous figures of plasma-based dry reforming with different particle sizes of SiO_2.

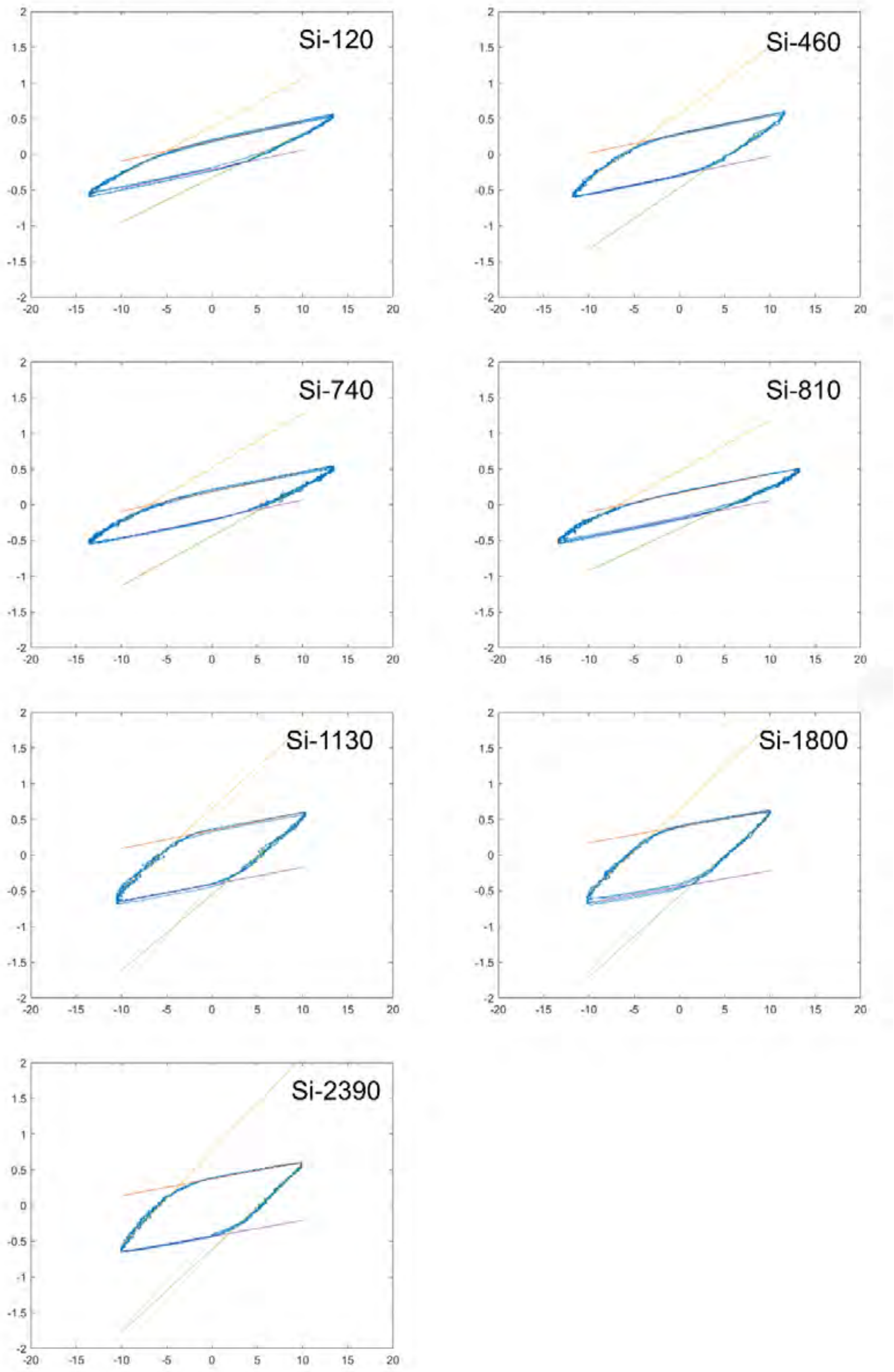

Figure C.2. The raw data of Lissajous figures of plasma-based dry reforming with different particle sizes of SiO_2.

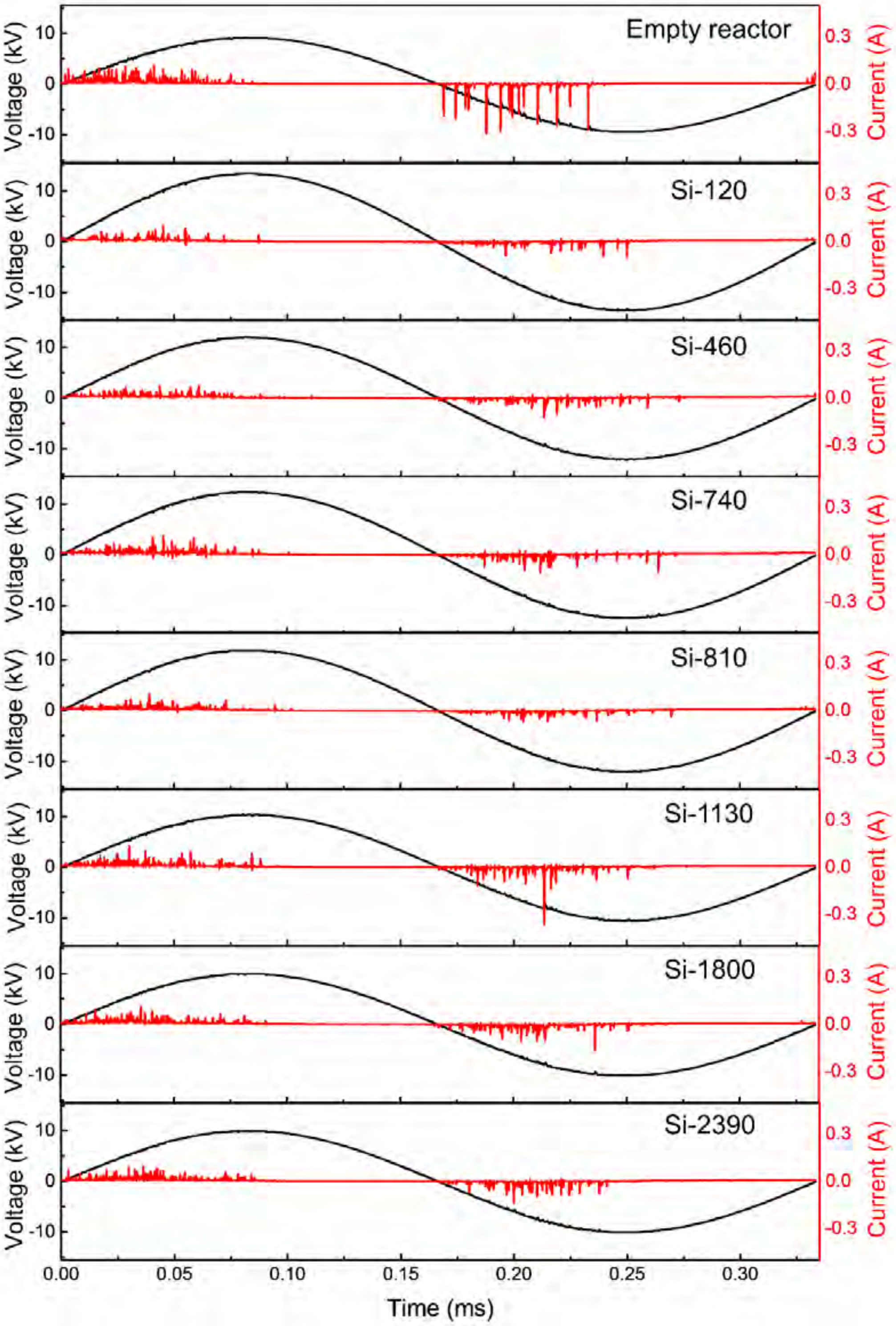

Figure C.3. The raw data of voltage (black curves) and current (red curves) profiles in a period of plasma-based dry reforming with different particle sizes of SiO_2.

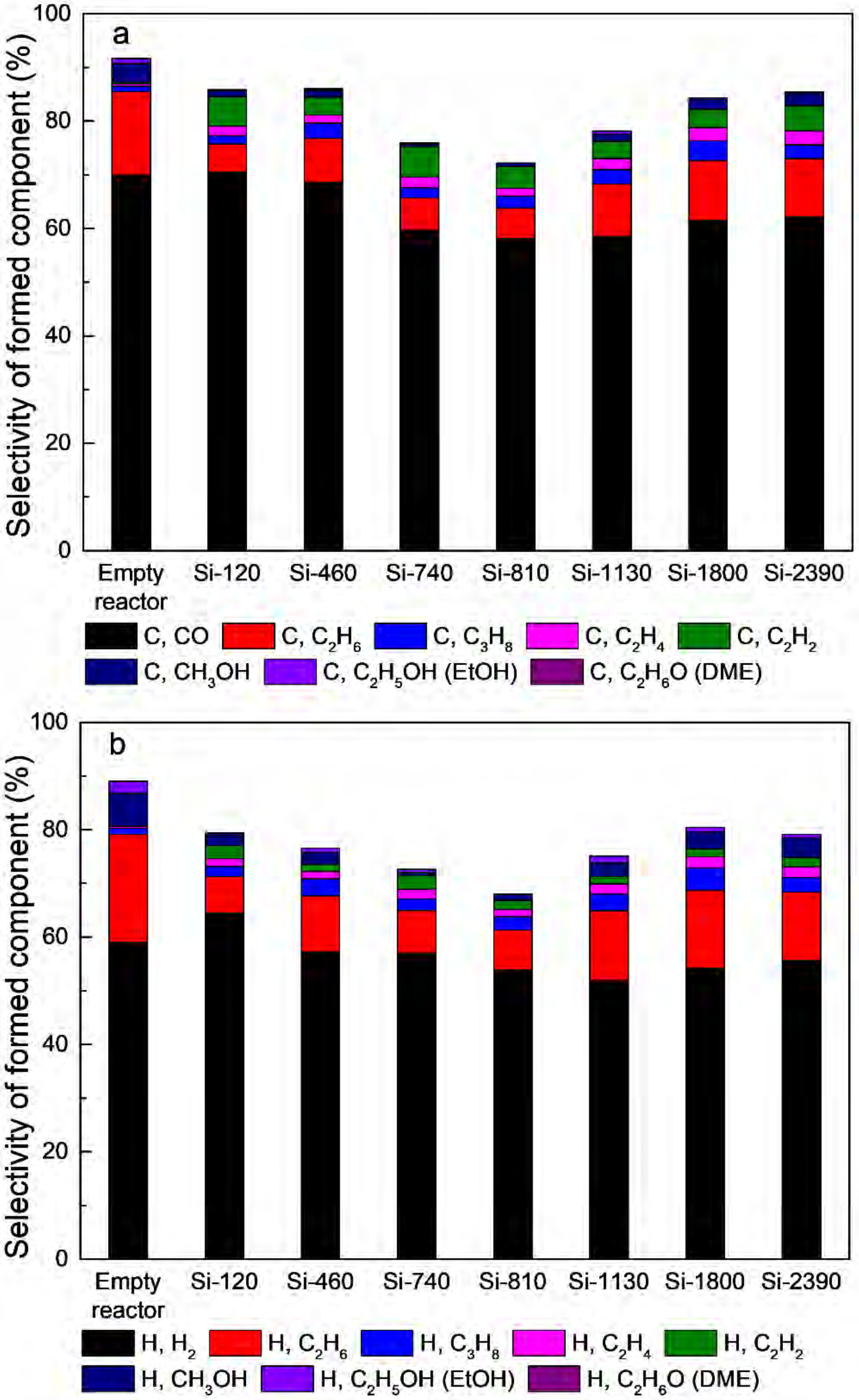

Figure C.4. Product carbon-based selectivities and carbon mass balance (a) and hydrogen-based selectivities and hydrogen mass balance (b) in plasma-based dry reforming, in the empty reactor and the packed reactor with different particle sizes of SiO_2.

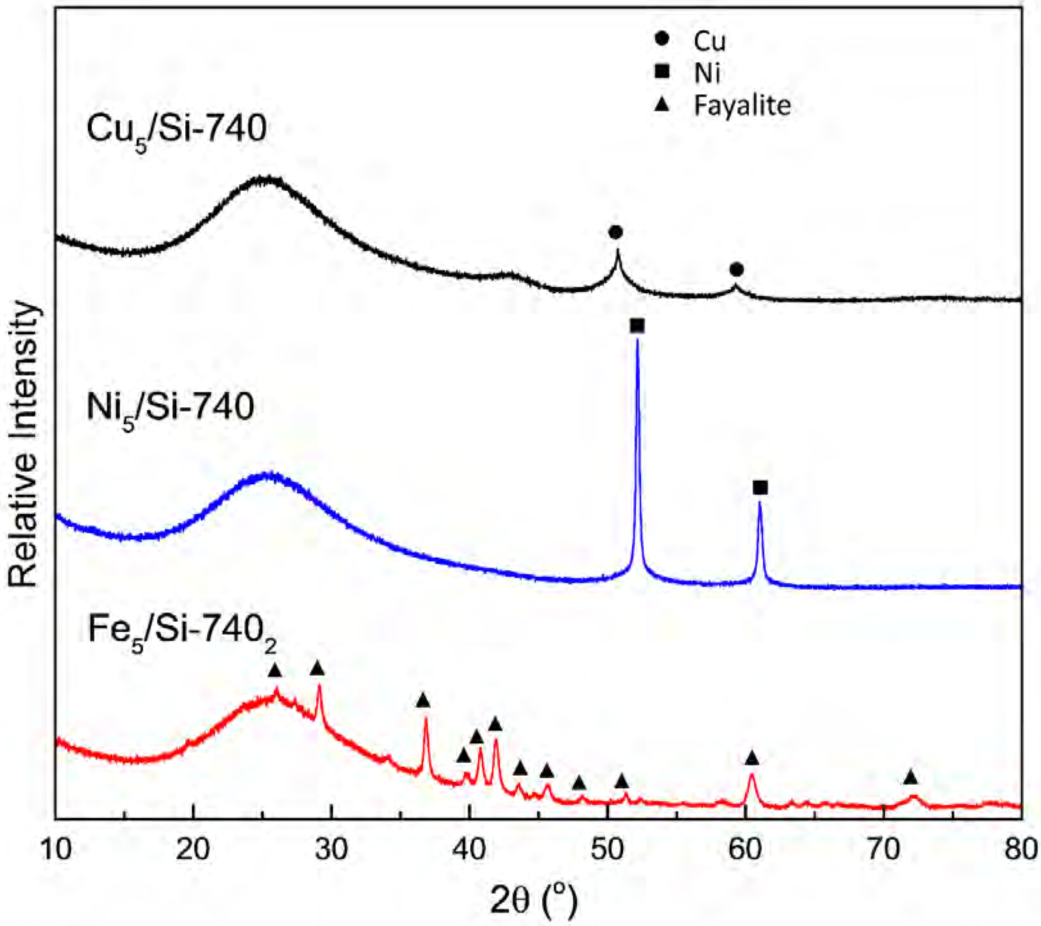

Figure C.5. XRD patterns of Cu_5/Si-740, Ni_5/Si-740 and Fe_5/Si-740 after 800 °C reduction. Position 2θ (°) from a cobalt (Co) tube.

It can be noticed from the XRD patterns that after reduction at 800 °C, metallic Cu and Ni supported on SiO_2 were successfully obtained, and Fe formed a fayalite solid solution with SiO_2 and a small amount of metallic Fe.

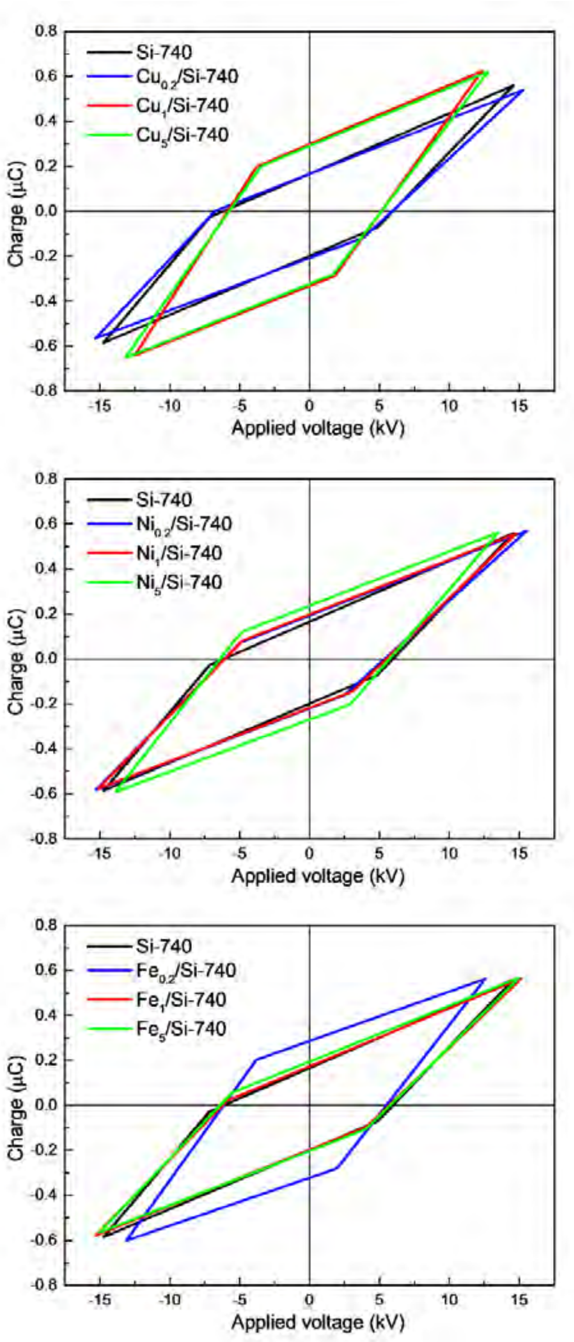

Figure C.6. The slopes of Lissajous figures in plasma-based dry reforming of Si-740 with different metals and loadings.

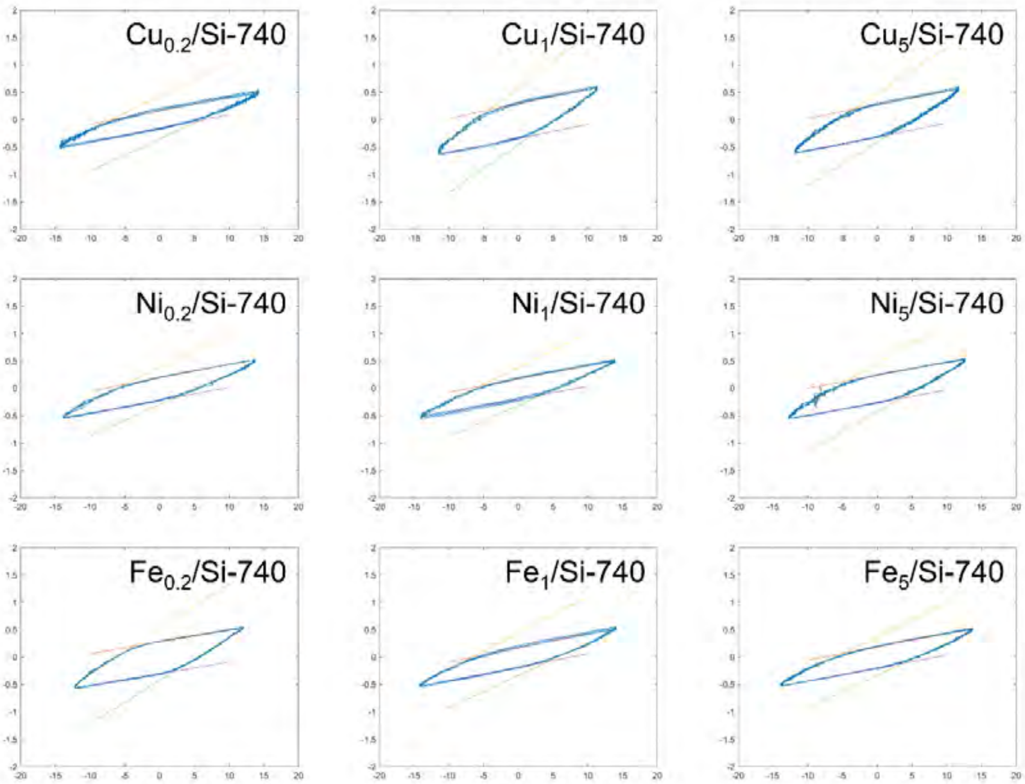

Figure C.7. The raw data of Lissajous figures of plasma-based dry reforming with different particle sizes of SiO_2.

Table C.2. Electrical characterization data measured and calculated from the recorded signals of the oscilloscope of the dry reforming experiments with Si-740 supporting different metals and loadings.

	Power source power (W)	Upp (kV)	Plasma power (W)	RMS Current plasma (mA)	Aver. number of µ disch. I graph	Aver. displ. Q per peak (nC/peak)
Si-740	50.31	24.84	25.95	12.45	69.81	7.67
$Cu_{0.2}$/Si-740	50.31	28.02	21.65	10.51	66.33	5.68
Cu_{1}/Si-740	50.50	22.76	27.21	12.78	74.29	8.52
Cu_{5}/Si-740	50.31	23.59	26.80	12.41	99.56	6.17
$Ni_{0.2}$/Si-740	50.89	27.67	22.66	11.01	70.25	5.88
Ni_{1}/Si-740	50.80	27.57	22.40	10.84	67.48	6.16
Ni_{5}/Si-740	50.04	25.35	24.97	11.38	79.33	6.40
$Fe_{0.2}$/Si-740	50.57	24.25	26.78	10.23	98.98	6.15
Fe_{1}/Si-740	50.36	27.99	21.78	9.49	67.46	5.52
Fe_{5}/Si-740	50.45	27.42	22.72	9.85	71.97	5.55

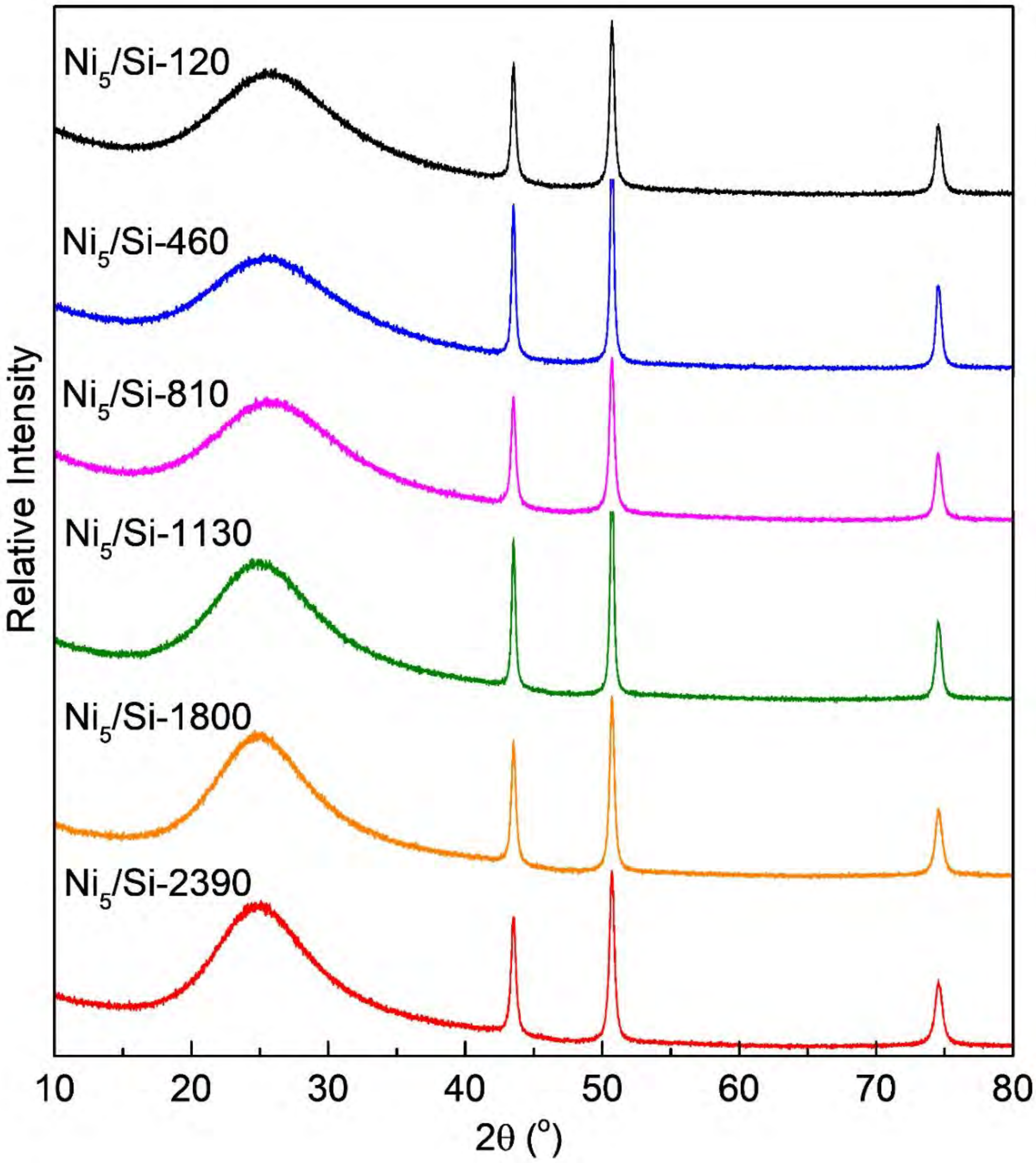

Figure C.8. XRD patterns of Ni$_5$/Si-120, Ni$_5$/Si-460, Ni$_5$/Si-810, Ni$_5$/Si-1130, Ni$_5$/Si-1800, and Ni$_5$/Si-2390 after calcination at 650°C in ambient air. Position 2θ (°) from a cobalt (Co) tube.

All peaks of the XRD patterns are attribute to NiO. These samples had been reduced, but were re-calcined and then measured by XRD to compare their oxides, to prevent differences in the samples due to surface oxidation caused by storage in air.

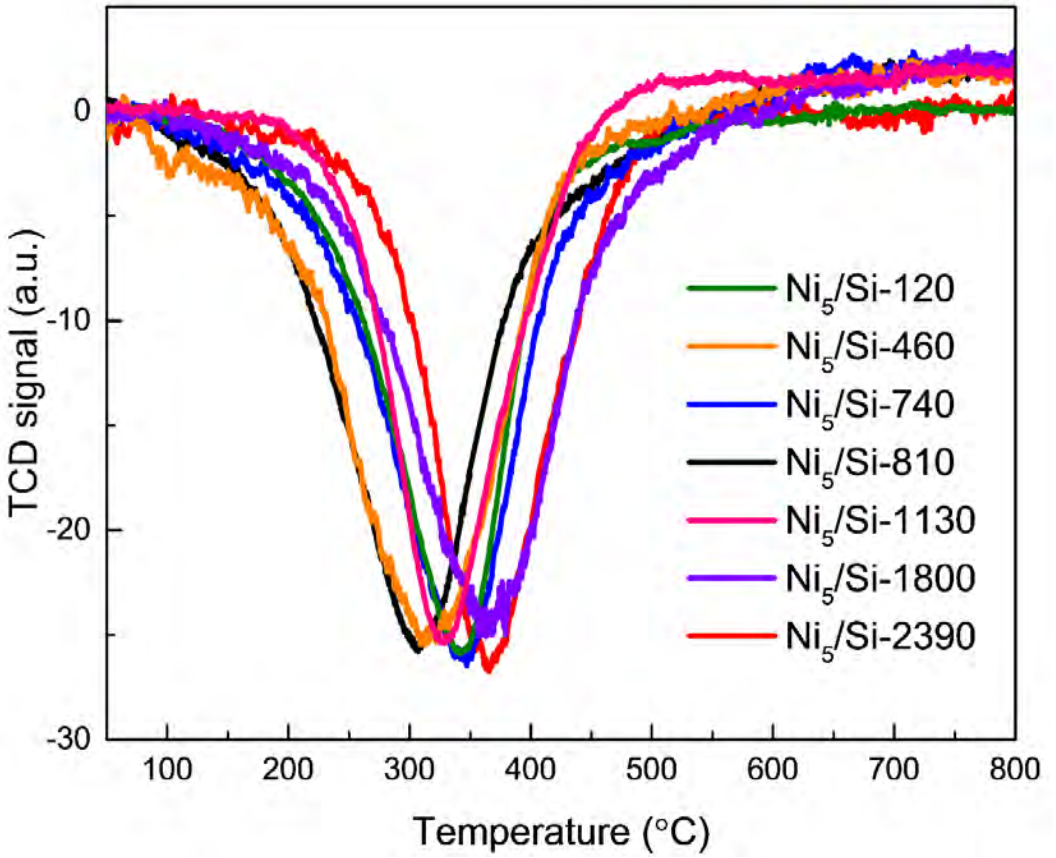

Figure C.9. O_2-TPO of reduced samples (SiO_2 with different particle sizes) with 5 wt % Ni loading.

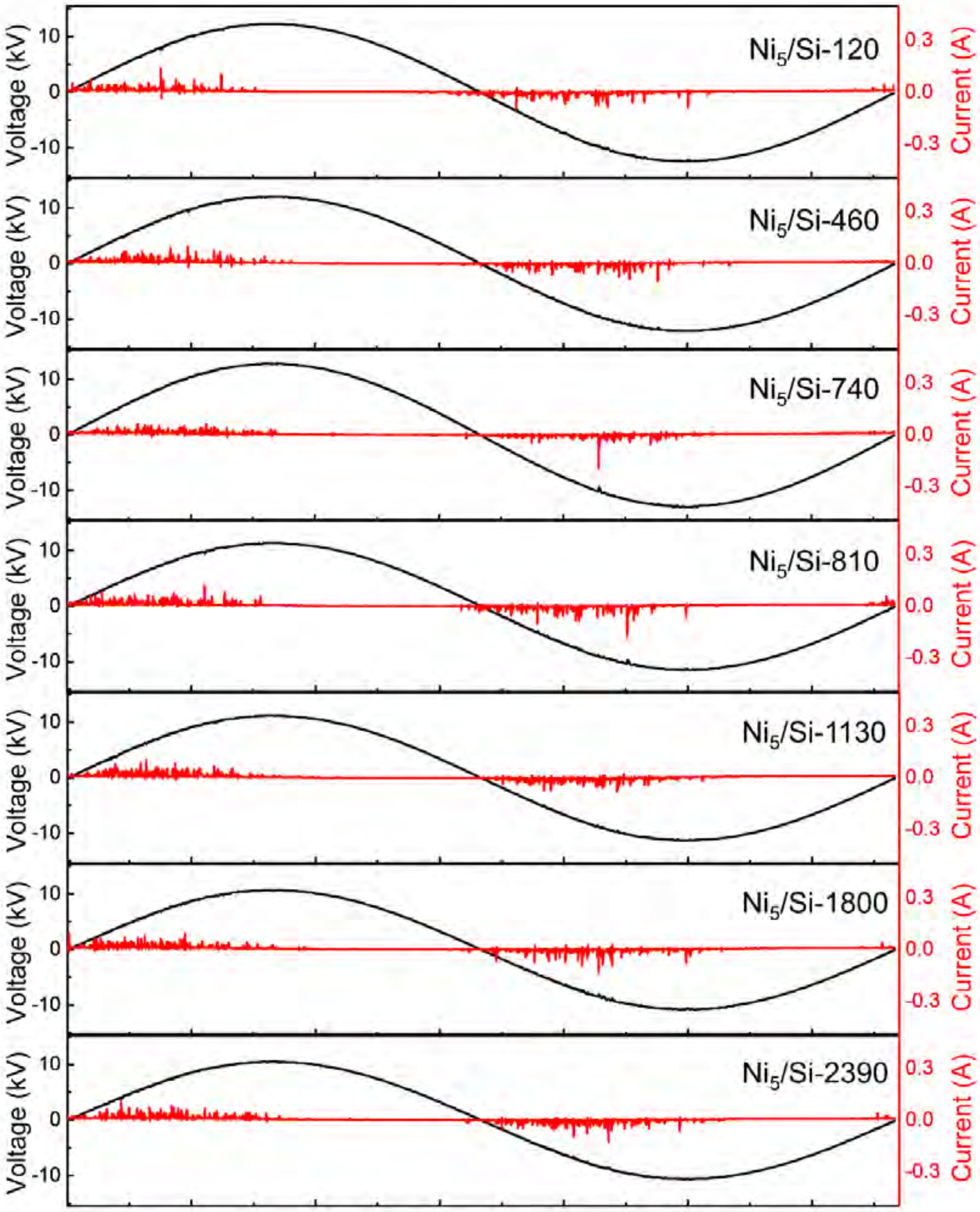

Figure C.10. The raw data of voltage (black curves) and current (red curves) profiles in a period of plasma-based dry reforming with 5 wt % Ni loading on different particle sizes of SiO_2.

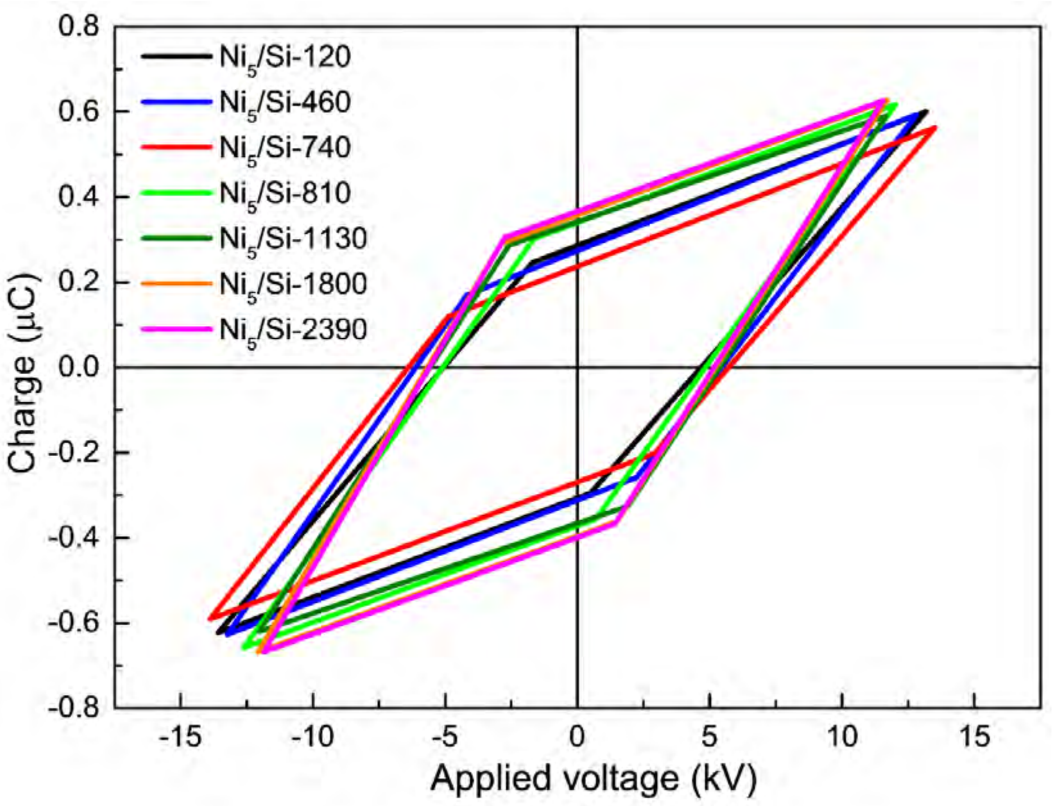

Figure C.11. The slopes of Lissajous figures in plasma-based dry reforming with 5 wt % Ni loading on different particle sizes of SiO_2.

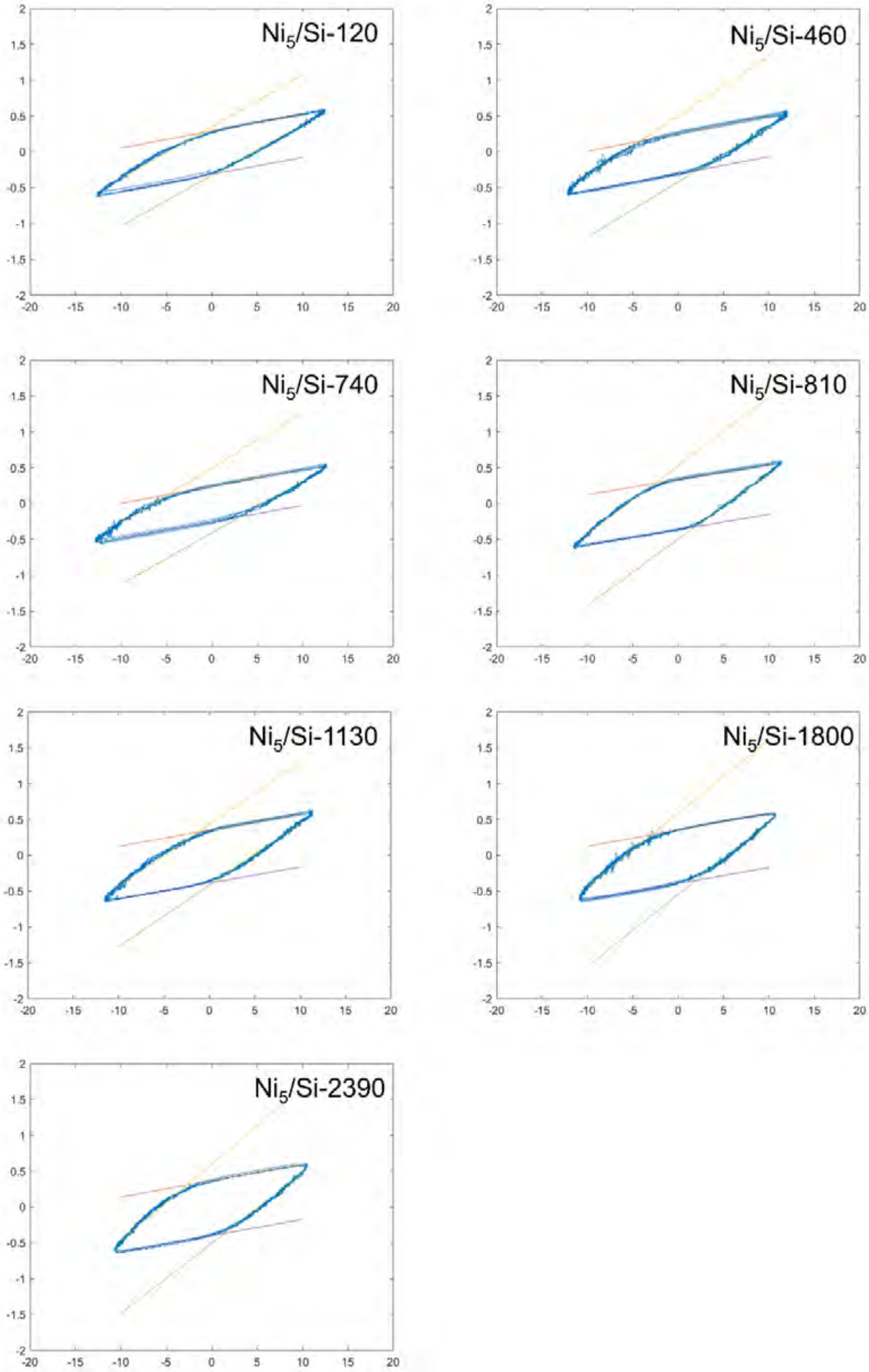

Figure C.12. The raw data of Lissajous figures of plasma-based dry reforming with 5 wt % Ni loading on different particle sizes of SiO_2.

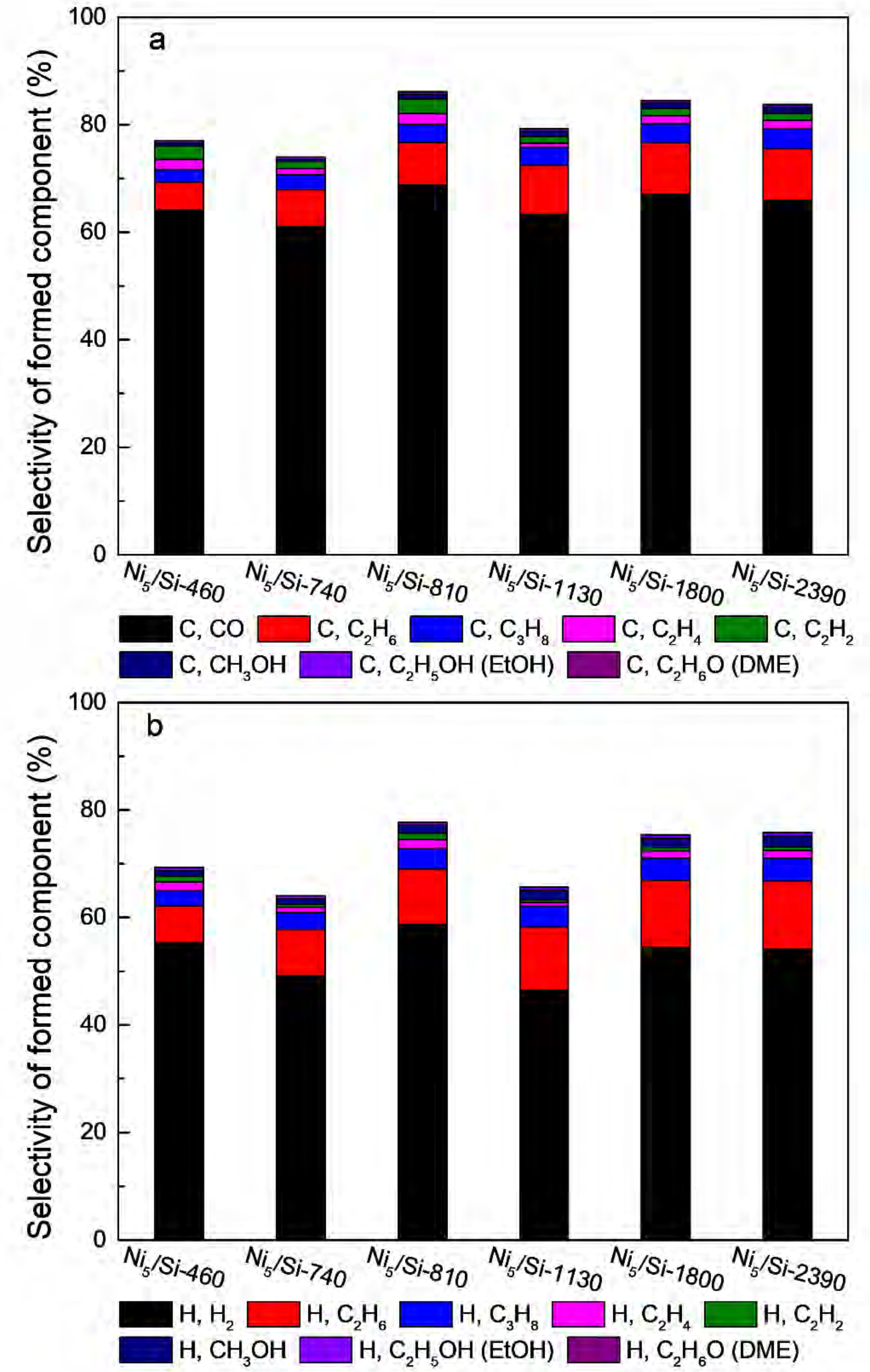

Figure C.13. Product carbon-based selectivities and carbon mass balance (a) and hydrogen-based selectivities and hydrogen mass balance (b) in plasma-based dry reforming with 5 wt % Ni loading on different particle sizes of SiO_2.

Appendix D Supporting information for chapter 5

Electrical characterization and selectivity of the reactors

Table D.1. Conversion and energy yield of the dry reforming experiments in DBD reactors with different number and cross-sectional diameters of rings.

Supplied power	Cross-sectional diameter of rings	Number of rings	CO_2 conversion (%)	CH_4 conversion (%)	EY calculated from supplied power (mmol/kJ)	EY calculated from plasma power (mmol/kJ)
50 W	Without rings	0	20.02	30.61	0.07	0.12
	1.6 mm	5	17.72	26.40	0.07	0.10
		7	17.61	25.69	0.06	0.10
		10	17.55	25.99	0.06	0.10
		15	18.23	26.48	0.07	0.10
		20	19.87	26.74	0.07	0.11
		25	19.87	28.00	0.07	0.11
		30	19.95	27.54	0.07	0.11
	3.2 mm	2	17.98	26.97	0.06	0.11
		5	18.94	25.82	0.07	0.11
		7	18.90	26.22	0.07	0.12
		10	20.26	29.31	0.07	0.13
		15	21.52	29.48	0.08	0.14
		20	22.89	30.97	0.08	0.15
30 W	Without rings	0	7.12	11.93	0.05	0.14
	1.6 mm	5	13.86	18.92	0.08	0.15
		7	12.87	18.34	0.08	0.15
		10	13.81	19.20	0.08	0.14
		15	14.29	19.90	0.08	0.15
		20	12.38	18.22	0.07	0.13
		25	12.50	18.09	0.07	0.14
		30	14.95	20.28	0.09	0.16
	3.2 mm	2	11.53	18.93	0.07	0.16
		5	12.70	17.69	0.07	0.15
		7	13.41	18.66	0.08	0.15

	10	13.79	19.39	0.08	0.16
	15	15.14	21.12	0.09	0.17
	20	16.32	22.48	0.10	0.19

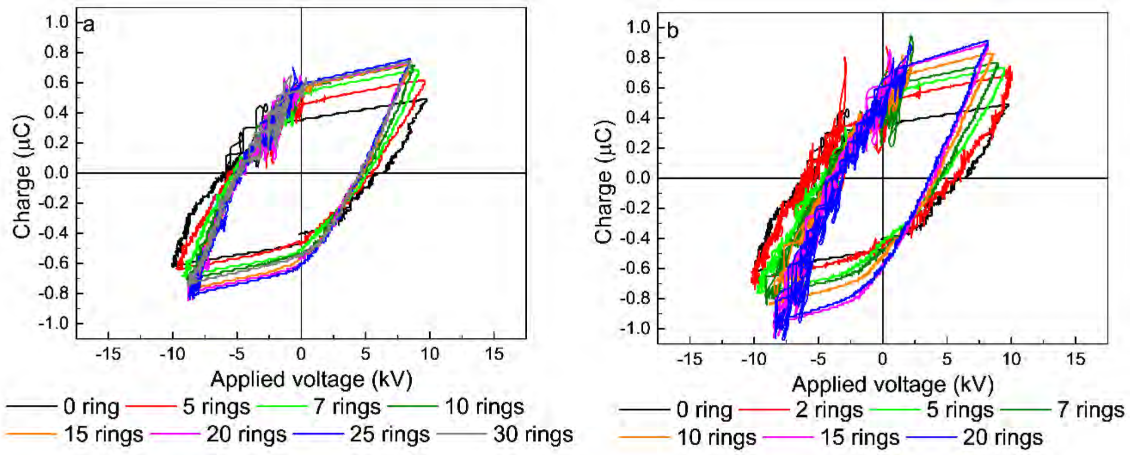

Figure D.1. The raw data of Lissajous figures for plasma-based dry reforming at 50 W supplied power, in a DBD reactor with varying number of stainless steel rings with cross-sectional diameters of (a) 1.6 mm and (b) 3.2 mm.

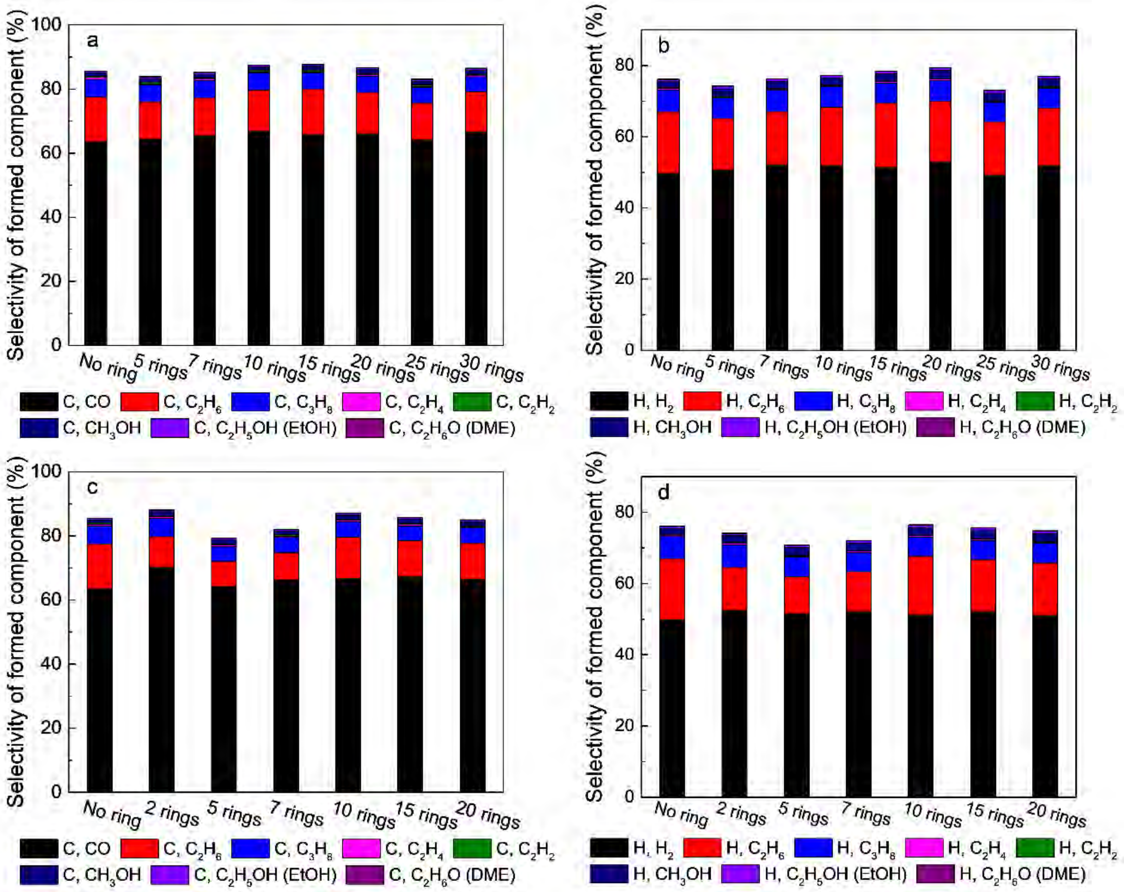

Figure D.2. (a) Carbon and (b) hydrogen atomic balance of plasma-based dry reforming in DBD reactors without rings, and with a varying number of rings with a diameter of 1.6 mm. (c) Carbon and (d) hydrogen atomic balance of plasma-based dry reforming in DBD reactors without rings and with a varying number of rings with a diameter of 3.2 mm. The plasma-based dry reforming was operated at 50 W supplied power.

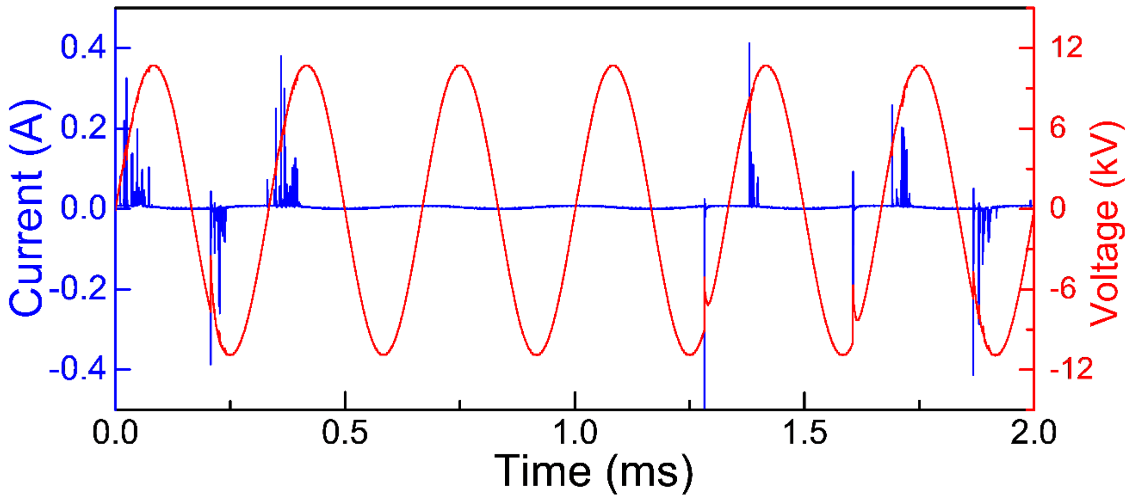

Figure D.3. Current and voltage profile in 2 ms for the reactor with no rings at 30 W supplied power.

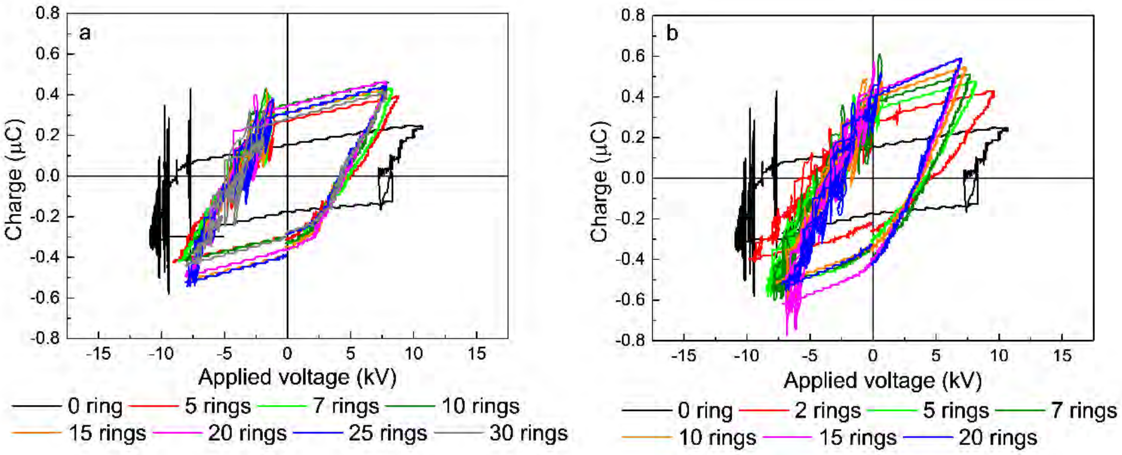

Figure D.4. The raw data of Lissajous figures for plasma-based dry reforming at 30 W supplied power, in a DBD reactor with varying number of stainless steel rings with cross-sectional diameters of (a) 1.6 mm and (b) 3.2 mm.

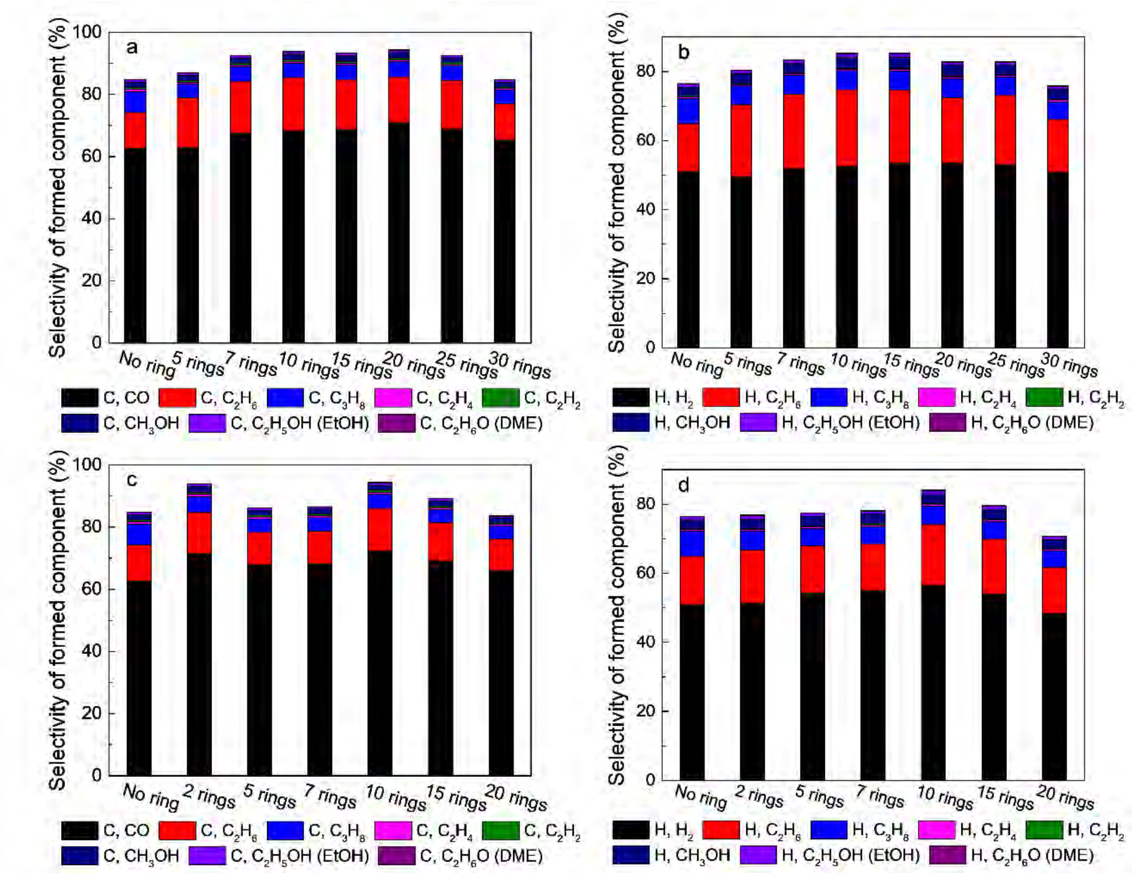

Figure D.5. (a) Carbon and (b) hydrogen atomic balance of plasma-based dry reforming in DBD reactors without rings and with a varying number of rings with a diameter of 1.6 mm. (c) Carbon and (d) hydrogen atomic balance of plasma-based dry reforming in DBD reactors without rings and with a varying number of rings with a diameter of 3.2 mm. The plasma-based dry reforming was operated at 30 W supplied power.

Appendix E List of publications and presentations

Publications

Modifying the Stöber Process: Is the Organic Solvent Indispensable?

Jinxin Wang, Kaimin Zhang, Safiyye Kavak, Sara Bals, Vera Meynen

Accepted manuscript for Chemistry—A European Journal
https://doi.org/10.1002/chem.202202670

3D porous Catalysts for Plasma-Catalytic Dry Reforming of Methane: How Does the Pore Size Affect the Plasma Catalytic Performance?

Jinxin Wang, Annemie Bogaerts, Vera Meynen

In revision at Chemical Engineering Journal

Plasma-based dry reforming of methane in a dielectric barrier discharge reactor with uniform (sub)micron packing/catalyst: The effect of particle diameter

Jinxin Wang, Kaimin Zhang, Annemie Bogaerts, Vera Meynen

In revision at Chemical Engineering Journal

Dry Reforming in a Dielectric Barrier Discharge Reactor with Non-uniform Discharge Gap: Effects of Metal Rings on the Discharge Behavior and Performance

Jinxin Wang, Kaimin Zhang, Annemie Bogaerts, Vera Meynen

In revision at Chemical Engineering Journal

Poster presentations

3D-macroporous Catalysts for Plasma-Catalytic Dry Reforming of Methane
Chemistry Conference for Young Scientists 2020, Blankenberge, Belgium, 19-21 February, 2020

3D-porous Catalysts for Plasma-Catalytic Dry reforming of Methane : How Does the Pore Size Affect the Plasma Catalytic Performance?
23rd Edition of the Netherlands' Catalysis & Chemistry Conference, Noordwijkerhout, Netherlands, 9-11 May, 2022

Modified Stöber Process: is the organic solvent indispensable?
Sol-Gel 2022, Lyon, France, 24-29 July, 2022

Does the Particle Diameter of a Catalyst/Packing Material Influence Plasma Dry Reforming of Methane?
8th ENMIX Nanoporous Materials Research in Europe, Thessaloniki, Greece, 6-7 October, 2022